



GEOTECHNOLOGIEN



GEO TECHNOLOGIEN

Science Report

Observation of the System
Earth from Space

Status Seminar
4 October 2010
Rheinische Friedrich-Wilhelms
Universität, Bonn

Programme & Abstracts

No. 17

GEOTECHNOLOGIEN

Science Report

Observation of the System
Earth from Space

Status Seminar
4 October 2010
Rheinische Friedrich-Wilhelms-
Universität Bonn

Programme & Abstracts

No. 17

Impressum

Editorship / Schriftleitung

Dr. Ute Münch, Werner Dransch

© Koordinierungsbüro GEOTECHNOLOGIEN, Potsdam 2010

ISSN 1619-7399

The Editors and the Publisher can not be held responsible for the opinions expressed and the statements made in the articles published, such responsibility resting with the author.

Die Deutsche Bibliothek – CIP Einheitsaufnahme

GEOTECHNOLOGIEN

Observation of the System Earth from Space

Status Seminar

4 October 2010

Rheinische Friedrich-Wilhelms-Universität Bonn

Programme & Abstracts –

Potsdam: Koordinierungsbüro GEOTECHNOLOGIEN, 2010

(GEOTECHNOLOGIEN Science Report No. 17)

ISSN 1619-7399

Distribution / Bezug

Koordinierungsbüro GEOTECHNOLOGIEN

Telegrafenberg

14473 Potsdam, Germany

Fon +49 (0)331-288 10 71

Fax +49 (0)331-288 10 77

www.geotechnologien.de

geotech@gfz-potsdam.de

Copyright Cover Picture / Bildnachweis Titel:

P. Carril / ESA

Preface

Observing the Earth from space has undergone a rapid development in recent years and today holds a prominent position in geo-related scientific research today. Research satellites are indispensable tools for studying processes on and inside the Earth system. The view from space allows the observation of the entire planet uniformly in near-real-time. Also the resulting time series of measurements allow the detection and monitoring of changes in this very complex system.

Satellites like CHAMP (Challenging Mini-satellite Payload), GRACE (Gravity Recovery and Climate Experiment) and GOCE (Gravity Field and steady state Ocean Circulation Explorer) measure the gravity and magnetic fields of the Earth with an unprecedented accuracy and resolution (in time and space) and provide the metrological basis for oceanography, climatology, glaciology, global change and geophysics in general.

The involvement of German scientists in these missions is strengthened by the R&D programme GEOTECHNOLOGIEN. The topic »Observation of the System Earth from Space« has been funded since 2001 by the Federal Ministry of Education and Research (BMBF) and the German Research Foundation (DFG). This substantial support is fully confirmed by the scientific and social relevance of this field of research and the unique insights in the system Earth gained in recent years.

Ute Münch
*(Head of the GEOTECHNOLOGIEN
coordination office)*

Gerhard Beutler
(Chair of the advisory committee)

Table of Contents

Scientific Programme »Observation of the System Earth from Space«	1
Progress Towards The New GFZ EIGEN-GRACE06S Gravity Field Time Series <i>Dahle Ch., Flechtner F., Neumayer K.H.</i>	3
Gravity Field Generation Applying the Integrated Approach <i>König D., Dahle C.</i>	7
Faster Reprocessing <i>Neumayer, K.H.</i>	13
Reprocessing of CHAMP and GRACE Observations for the Determination of Improved Static and Temporal Gravity Field Models with Regional Refinements (GREST-CHAMP/GRACE) <i>Shabanloui A., Schall J., Mayer-Gürr T., Eicker A., Kusche J., Kurtenbach E.</i>	22
Improved Acceleration Modelling and Level 1 Processing Alternative for GRACE <i>Peterseim N., Schlicht A., Flury J.</i>	31
GRIMM-2: The parent magnetic field model for an IGRF candidate model <i>Lesur V., Rother M., Hamoudi M., Wardinski I., Lühr H., Michaelis I., Rauberg J.</i>	35
Wavelet Correlation Analysis of CHAMP Magnetic Field Models – WACO CHAMP Results <i>Schachtschneider R., Hayn M., Holschneider M.</i>	42
Analysis and application of atmospheric data from CHAMP and GRACE <i>Heise S., Wickert J., Arras C., Beyerle G., Haser A., Schmidt T., Zus F.</i>	46
GOCE gravity gradients: a new satellite observable <i>Bouman J., Stummer C., Murböck M., Fuchs M., Rummel R., Pail R., Gruber T., Bosch W., Schmidt M.</i>	52
GOCE gravity field determination by means of rotational invariants: first experiences <i>Cai J., Baur O., Sneeuw N.</i>	62
Stochastic model refinements for GOCE gradiometry data <i>Krasbutter I., Brockmann J.M., Kargoll B., Schuh W.-D.</i>	70

GLOBAL gravity field determination with REGIONAL refinements by the analysis of GOCE level-1b data (GLOREGOCE)	77
<i>Shabanloui A., Schall J., Mayer-Gürr T., Eicker A., Kusche J., Kurtenbach E.</i>	
Modelling topographic effects in GOCE gravity gradients	84
<i>Grombein T., Seitz K., Heck B.</i>	
Quality Assessment of GOCE Gradients	94
<i>Brieden P., Müller J.</i>	
Inferring the mean dynamic topography by using GOCE geoid information in ocean state estimations	101
<i>Siegismund F., Köhl A., Stammer D.</i>	
Validation of GOCE products by terrestrial data sets in Germany	106
<i>Voigt C., Rülke A., Denker H., Ihde J., Liebsch G.</i>	
High-resolution global gravity fields by combining GOCE, GRACE and terrestrial dataFirst results from the REAL GOCE project	112
<i>Shako R., Förste C., Abrikosov O., Bruinsma S., Dahle C., Flechtner F., Neumayer K.H., Marty J.-C.</i>	
Constraints for Future Missions	118
<i>Doll B., Sand R.</i>	
Quick-look gravity field analysis of formation scenarios selection	126
<i>Reubelt T., Sneeuw N., Iran-Pour S.</i>	
The mission option OPTIMA – novelties and benefit	134
<i>Brieden P., Müller J., Flury J., Heinzel G.</i>	
Optimized Gravity Field Determination from Future Satellite Missions	140
<i>Elsaka B., Kusche J.</i>	
Numerical Simulations of new Gravity Mission Concepts	146
<i>Raimondo J.-C., Neumayer K.-H., Flechtner F.</i>	
Inertial Sensing for Future Gravity Missions	152
<i>Hirth M., Brandt N., Fichter W.</i>	

Laser interferometry for future satellite gravimetry missions	
<i>Sheard B., Dehne M., Mahrtdt C., Gerberding O., Müller V., Heinzel G., Danzmann K.</i>	160
New concepts for high precision laser based space metrology	
<i>Klein V., Bedrich S.</i>	167
High Accuracy Long Distance Measurement with Frequency Combs	
<i>Lezius M., Steinmetz T., Holzwarth R.</i>	172
Quantum sensors for Earth observation	
<i>Gilowski M., Rasel E.M.</i>	178
Environmental Disturbance Modelling for Future Gravity Missions	
<i>Pelivan I., Theil S.</i>	185
Authors Index	193
GEOTECHNOLOGIEN Science Reports – Already published/Editions	197

Scientific Program

Status Seminar »Observation of the System Earth from Space« 4 October 2010,

Rheinische Friedrich-Wilhelms-Universität Bonn

4. October 2010

10:45 – 11:15	Welcome
11:15 – 12:45	Projekt Lotse-CHAMP/GRACE
11:15 – 11:30	Überblick – CHAMP/GRACE Status
11:30 – 11:45	LOTSE - CHAMP/GRACE Statusbericht
11:45 – 12:00	Thema Reprozessierung Schwerefeldmodelle
12:00 – 12:15	Thema Reprozessierung Magnetfeldmodelle
12:15 – 12:30	Thema Reprozessierung Atmosphärenparameter
12:30 – 12:45	Ausblick und Anwendungspotentiale
<i>12.45 - 14.00</i>	<i>Lunch</i>
14.00 – 15.30	Projekt REAL-GOCE
14:00 – 14:15	REAL-GOCE Statusbericht
14:15 – 14:45	Thema Gradientenanalyse und Schwerefeldberechnung
14:45 – 15:15	Thema Validation & Kombination
15:15 – 15:30	GOCE-Status, Ausblick und Anwendungspotentiale
<i>15.30 - 16.00</i>	<i>Coffee Break</i>
16.00 – 17.30	Projekt Future Gravity Mission
16:00 – 16:15	Überblick – Gesamtstatus
16:15 – 16:30	Future Gravity Mission Statusbericht
16:30 – 16:50	Thema 1: Geodäsie
16:50 – 17:10	Thema 2: Sensoren und Systeme
17:10 – 17:30	Ausblick und Anwendungspotentiale
17:30 – 18:30	Poster session and exhibits
18:30 – 19:00	Final Discussion
<i>ca. 19.00</i>	<i>Dinner</i>

Progress Towards The New GFZ EIGEN-GRACE06S Gravity Field Time Series

Dahle Ch., Flechtner F., Neumayer K.H.

Helmholtz Centre Potsdam, GFZ German Research Centre for Geosciences,

Correspondence to: Ch. Dahle (dahle@gfz-potsdam.de)

1. Introduction

Since end of 2006, GFZ as part of the GRACE Science Data System is routinely processing EIGEN-GRACE05S (or RL04 in the SDS nomenclature) monthly gravity field solutions (*Flechtner et al., 2010*). Up to now, this time series comprises nearly 8 years and allows for investigation of various time-varying mass variation signals in the system Earth such as the continental hydrological cycle, surface and deep ocean currents, ice mass change in Antarctica and Greenland or secular effects induced by GIA.

As a matter of fact, the error level of the RL04 time-series is still about a factor of 15 above the pre-launch simulated baseline accuracy caused by inaccurate background models, instrument data or processing standards. Most evidently, this becomes visible by spurious striping artefacts in the monthly solutions, which have to be filtered by the users before further analysis. In the framework of the GEOTECHNOLOGIEN Project »TOBACO CHAMP/GRACE«, GFZ will reprocess the whole GRACE mission to get a consistent and more precise new EIGEN-GRACE06S (RL05) time series using improved background models, reprocessed Level-1B instrument data and upgraded processing standards. An overview of these upgrades is given in Chapter 2. Chapter 3 describes first results of one year (2008) of preliminary RL05 solutions and their improvements compared to RL04. Conclusions and an outlook on the remaining issues to get a final RL05 series for the complete GRACE mission period are summarized in Chapter 4.

2. Models, Instrument Data and Processing Standards for Reprocessing of the EIGEN-GRACE06S Time Series

In order to derive a consistently reprocessed EIGEN-GRACE06S time series we have applied improved observation and background models, reprocessed instrument data and upgraded processing standards which are described in the following.

2.1. Observation Models and Instrument Data

For RL05 we have improved our GPS data processing by adding GPS phase windup corrections and absolute phase center variations and derived our own GPS azimuth/elevation dependent masks for both GRACE satellites. These improvements, plus use of ITRF2008 instead of ITRF2005 station coordinates, have also been used to reprocess all GPS constellations (orbits and clocks). In order to reduce geographically correlated elimination for K-band range-rate (KBRR) data (e.g. in the Amazon region due to large mass variation signals) we have applied a 5-sigma (instead of 3-sigma) elimination criterion and a time-variable part of the static background model (derived from the RL04 time series, see below). Additionally we now analyze more KBRR data as due to a previous misinterpretation of the L1B Product User Handbook (*Case et al., 2010*) we eliminated in RL04 KBRR data with low but valid signal-to-noise ratio. Finally we used a preliminary version of recomputed Level-1B star camera and KBRR instrument data (V.02), resulting in more precise KBRR phase center corrections.

2.2. Background Models

The static gravity model has been upgraded to EIGEN-51C, a combination of CHAMP and GRACE (Bruinsma et al., 2010). We have also estimated trend and seasonal (annual, semi-annual) signals from re-parameterized GRACE RL04 normal equation systems. Here we used only coefficients which passed a significance test. This time-variable model has been added to the static field during gravity field determination, but has been restored to the solved monthly model in order to guarantee the same model output philosophy than in previous releases. One effect is that the number of eliminated KBRR residuals has been much reduced (see Figure 1) by this approach. Finally, we used the preliminary ocean tide model EOT10a, which is an update of EOT08a (Savcenko and Bosch, 2008). All other background models, e.g. to de-alias non-tidal short-term mass variations or to correct for Solid Earth and pole tides, remained unchanged.

2.3. EPOS Environment and Standards

Thanks to the various improvements to reduce the computation time to calculate and solve monthly GPS and GRACE normal equation systems (see Neumayer, this issue) the processing of a monthly gravity field up to degree and order 150 is now approximately a factor of two faster than for RL04. We have tested the influence of the arc length which was 24 hours for RL04. The arc length is always a compromise between »short« to avoid the accumulation of data and modeling errors during numerical integration and »long« to retain resonant longer-period gravitational perturbations. We

found a considerable improvement when using 6-hourly arcs which is mainly due to the fact that we then use in principal a much denser parameterization of accelerometer parameters (biases and scales). Therefore we stayed with 24 hours arcs (in order not to increase computation time and disk space for four times more normal equation systems), but introduced 6-hourly accelerometer along-track scales and biases for along-track, cross-track and radial directions. The contribution of GPS observations to the gravity field solution was reduced by limiting the maximum degree and order in the combination of GPS and KRR normal equations to 80 for GPS.

3. Results of 1 Year of preliminary EIGEN-GRACE06S Gravity Field Solutions

The positive effect of reprocessed GPS constellations for the year 2008 becomes visible when looking at the 3D RMS w.r.t. IGS which was reduced from 7.2 to 5.1 cm and is now much more homogeneous (without jumps and seasonal signals, see Figure 2).

As a result of the upgrades mentioned in Chapter 2 the pre-fit GPS and KRR residuals for 2008 decreased from 7.4 to 6.2 mm and from 0.36 to 0.27 $\mu\text{m/s}$, respectively (not shown). Most important, the formal and calibrated errors of the RL05 monthly solutions could be significantly improved (Figure 3). The overall level of the calibrated errors is now only a factor of 11 above the GRACE baseline, which is an improvement w.r.t. RL04 of approximately 25%.

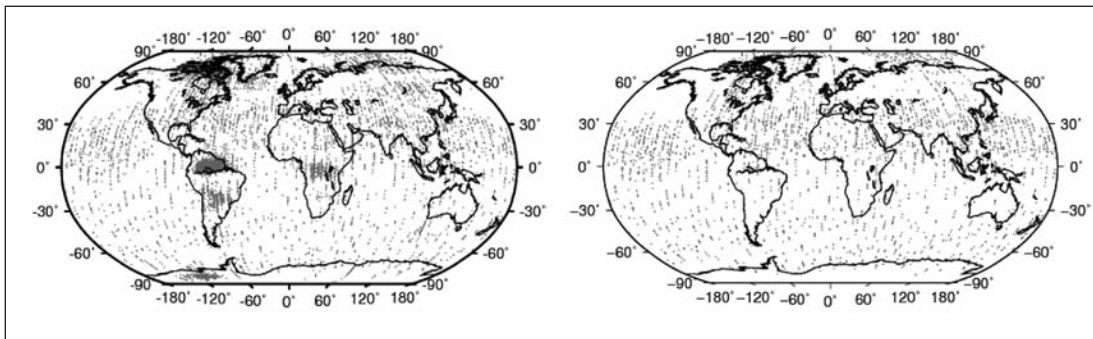


Figure 1: Eliminated KBRR data in RL04 (left) and RL05 (right)

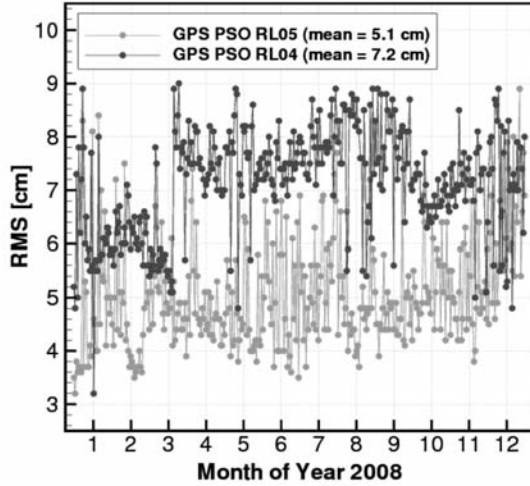


Figure 2: 3D position RMS of RL04 and RL05 constellations [cm] w.r.t. IGS

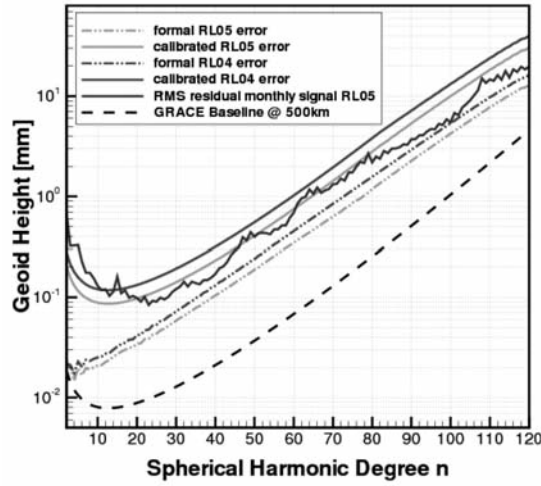


Figure 3: Formal and calibrated errors of RL04 and RL05 monthly solutions of year 2008 w.r.t. the GRACE baseline.

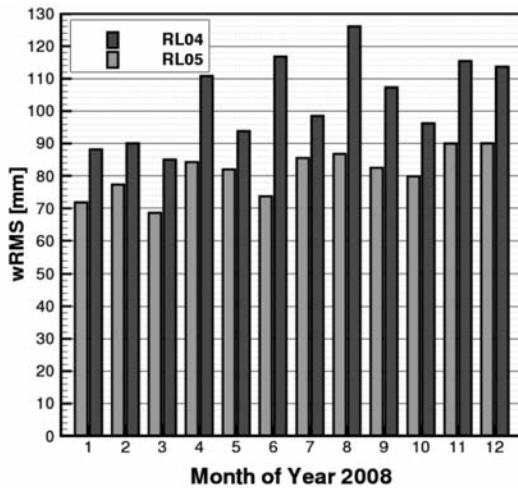


Figure 4: RMS of unfiltered monthly gravity models w.r.t. the static EIGEN-GRGS.RL02 in terms of geoid height [mm] up to degree and order 120

The resulting RL05 monthly fields show reduced horizontal (due to the improved L1B data and better KBRR phase center corrections) and meridional striping. As an example the RMS of the unfiltered monthly solutions in terms of geoid height w.r.t. the static EIGEN-GRGS.RL02 (*Bruinsma et al., 2009*) field up to degree and order 120 for April 2008 reduced from 111 to 83 mm, an improvement of 33% which is typical for all other monthly models (Figure 4). Also the scatter of these RMS values is now much smaller. The filtered solutions using the *Kusche et al. (2009)* approach still show an improvement of some percent for small wavelengths (240km, DDK3) over the oceans (not shown). Finally, the RL05 mean static field for 2008 shows considerable improvement above degree 90 when analyzing SLR residuals of low Earth Orbiting Satellites (LEO) such as GFZ-1 and GOCE, which is a further indication of the quality of our reprocessed time series.

4. Conclusions and Outlook

We have reprocessed a first version of RL05 (EIGEN-GRACE06S) monthly gravity field models using improved background and observation models, instrument data and processing standards for 2008. The overall calibrated error could be reduced from a factor of 15 (RL04) to 11, showing that these new models are now much closer to the GRACE baseline. These new models have been preliminary validated and show reduced horizontal and meridional striping, e.g. visible in reduced RMS when comparing unfiltered RL04 and RL05 solutions to a static gravity field. Also the static field for 2008 shows considerable improvements when comparing SLR residuals of various LEO satellites such as GFZ-1 or GOCE.

Within the next few months we will test and add several upgraded models (e.g. the final EOT10a) and data (e.g. final L1B V.02) or the influence of new IERS2010 processing standards. Also the combination of GRACE with LAGEOS is planned as some 2008 GRACE monthly solutions still show degradation in the degree 2 co-

efficients. We are optimistic that we can gain further improvements and that the full GRACE mission will be reprocessed in spring 2011 and provided to the user community.

Savcenko R., Bosch W.: EOT08a – empirical ocean tide model from multi-mission satellite altimetry. DGFI Report No. 81, Deutsches Geodätisches Forschungsinstitut (DGFI), München, 2008

Acknowledgements

The project TOBACO-CHAMP/GRACE is funded within the BMBF R&D-Programme GEOTECHNOLOGIEN with FKZ 03G0728A.

We would like to thank the German Space Operations Center (GSOC) of the German Aerospace Center (DLR) for providing continuously and nearly 100% of the raw telemetry data of the twin GRACE satellites.

References

Bruinsma S., Lemeoine J.-M., Biancale R., Vales N. (2009): CNES/GRGS 10-day gravity field models (release 2) and their evaluation, Adv. In Space Res., doi 10.1016/j.asr.2009.10.012

Bruinsma S.L., Marty J.C., Balmino G., Biancale R., Foerste C., Abrikosov O. and Neumayer H. (2010), GOCE Gravity Field Recovery by Means of the Direct Numerical Method, presented at the ESA Living Planet Symposium 2010, Bergen, June 27 - July 2 2010, Bergen, Norway

Case K., Kruizinga G., Wu, S.C. (2010): GRACE Level-1B Data Product User Handbook, GRACE Project Document 327-733, Rev. 1.3

Flechtner F., Dahle, Ch., Neumayer, K.H., König R., Förste, Ch. (2010): The Release 04 CHAMP and GRACE EIGEN Gravity Models, Flechtner et al. (eds.), System Earth via Geodetic-Geophysical Space Techniques, Adv. Technologies in Earth Sciences, Springer-Verlag Berlin Heidelberg 2010, doi 10.1007/978-3-642-10228-8_4

Kusche J., Schmidt R., Petrovic S., Rietbroek R. (2009): Decorrelated GRACE time-variable gravity solutions by GFZ, and their validation using hydrological model, J. Geod., doi 10.1007/s00190-009-0308-3

Gravity Field Generation Applying the Integrated Approach

König D., Dahle Ch.

Helmholtz Centre Potsdam, GFZ German Research Centre for Geosciences

Introduction

The generation of gravity fields at GFZ based on precise orbit determination using the L1B instrument data of the GRACE mission is currently done applying the conventional two-step method where GPS orbits and clock parameters are introduced as fixed being produced in a preceding step. That way the real-world scenario is split into two separate steps meaning that important correlations between the GPS ground stations, the GPS satellites and the GRACE Low Earth Orbiters on the other hand are neglected. In order to better describe the real world it is strived for carrying out the gravity field processing applying the integrated approach (see *Zhu et al., 2004*) where all relevant observations are processed within one step thus considering all correlations. In particular, benefits for estimating gravity field coefficients following the integrated approach have been demonstrated in *König et al. (2005)*.

In a first attempt two solutions for gravity field harmonic coefficients up to degree and order 10 are computed applying the integrated approach, and, for comparison purposes, they are as well computed applying the two-step method following the routine GRACE gravity field processing (*Flechtner et al., 2010*). The solutions obtained are of daily resolution covering the period of April 2004 with two days missing (2004/04/05 and 2004/04/26). By accumulating the daily normal equations for both cases two monthly solutions are derived.

Processing

The data comprise GPS observations of selected GPS ground stations (GPS/ground), GPS-SST measurements (GPS/SST) taken on-board each GRACE Low Earth Orbiter (LEO), and K-band range-rate data (KBRR) measured between the LEOs. The GPS measurements have got a time spacing of 30s, and they are processed as L3 ionosphere-free linear combinations. The KBRR observations are provided as preprocessed L1B data by JPL at intervals of 10s. Overall, the processing standards and background models mainly follow the GRACE release 04 standards (*Flechtner et al., 2010*). In order to keep pace with recent developments in modeling some updates are introduced: IGS absolute phase center corrections are applied to GPS/ground measurements, and a GFZ-derived correction mask is applied to GPS/SST phase measurements.

As a basis for both the integrated approach as well as the two-step method GPS constellations, i.e. orbits and clock parameters of the GPS satellites, are generated by means of precise orbit determination (POD) of the GPS satellites using the GPS/ground data. In this step also the GPS/ground data is cleaned from outliers. The length of each arc is 24h with about 50 ground stations involved.

In order to further prepare the integrated approach the GPS/SST data as well as the KBRR data are cleaned from outliers by means of POD of the GRACE LEOs using the produced GPS constellations as fixed. Independently, the two-step method is carried out using the same fixed GPS constellations. Here, as well, the nominal arc length is 24h but can be shorter if e.g. instrument data are missing or not usable.

In this investigation this is only the case for the arc on day 2004/04/09 (length: 0.375d).

Finally, the integrated approach is performed by simultaneous POD of the GPS satellites and the GRACE LEOs using the cleaned GPS/ground, GPS/SST, and KBRR data.

Results

The quality assessment is concentrated here on the estimated gravity field coefficients (GFCs). They are evaluated regarding their a posteriori standard deviations, some difference degree variances and the series of their daily estimates.

The a posteriori standard deviations, i.e. the formal errors, are almost the same for both solutions in C00 and the degree-one coefficients. There are significant differences for the GFCs from degree two on with the coefficients coming from the two-step method revealing standard deviations surprisingly half an order of magnitude smaller than those coming from the integrated approach. On the other hand both solutions show the same structure of a posteriori sigmas: the higher the order the higher the sigma. But there still remains the question whether these differences in a posteriori sigmas are yet significant. Considering e.g. that the calibrated release 04 errors result

from multiplying the original formal errors by a factor of approximately 10 it is also possible that the integrated approach gives more realistic formal errors. Therefore no interpretation is given at this early stage of investigation.

The degree variances are determined for the difference between each solution with respect to EIGEN-51C (*Bruinsma et al., 2010*) as well as for the difference between both solutions. As can be seen in Figure 1 the degree variances of the difference between both solutions are above the calibrated release 04 error meaning that the differences are too high as to represent an improvement towards the GRACE baseline. Forming the degree variances of the differences of each solution with respect to EIGEN-51C represents a comparison to an external reference. Again, smaller difference degree variances mean a greater significance of the changes towards the GRACE baseline. For the degrees equal to and larger than four the degree variances of the differences to EIGEN-51C are approximately the same for both solutions. Regarding degree three these degree variances are slightly smaller for the integrated approach whereas they are smaller for the two-step method at degree two. This is most probably due to an outlier in the daily estimates on day 2004/04/09 (year 2004.27049)

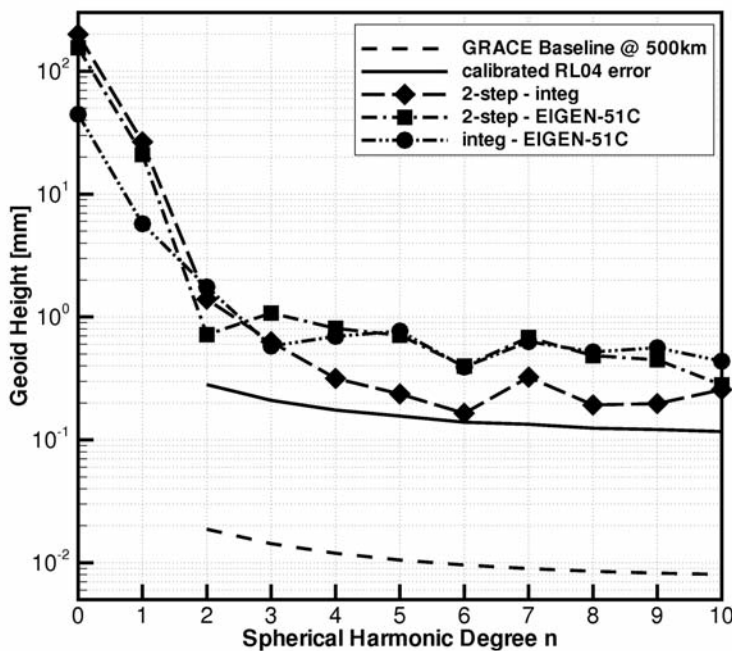


Figure 1: Difference degree variances for various solutions.

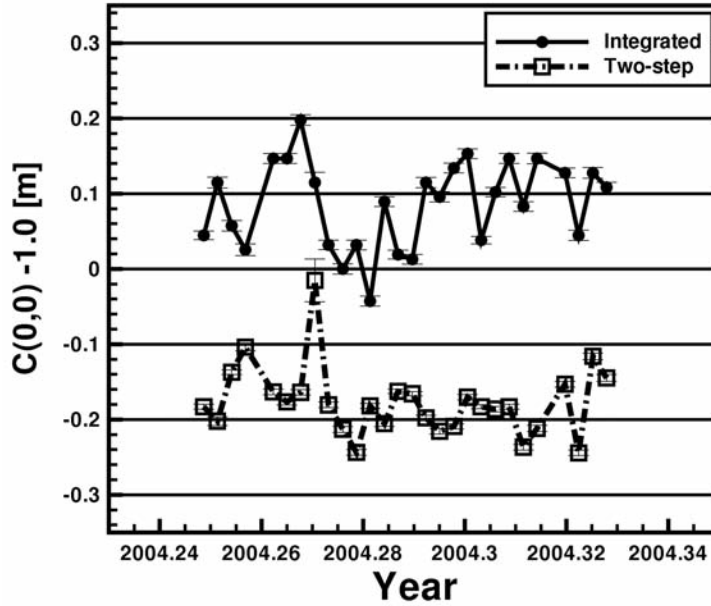


Figure 2: Daily estimates of C00-1.0, rescaled to metric distance on the Earth surface; mean \pm standard deviation [m]: $+0.0862\pm0.0579$ m (integrated), -0.1768 ± 0.0467 (two-step).

which is the day of the short arc: regarding the degree-two terms the integrated approach is affected, in case of the degree-three terms there is at least an outlier in C30 for the two-step method. On the other hand it is known that in general estimating C20 from GRACE data is not reliable. At degrees zero and one there are significantly smaller difference degree variances for the integrated approach indicating a better quality of the solved-for parameters.

Estimating C00 is a good indicator for revealing the reliability of a solution as there is no physical reason for this parameter to deviate from its expectation value of one. As visualized by Figure 2 the scatter of each series is roughly the same while the mean differs significantly. In case of the integrated approach the time series is nearer to its expectation with a mean of 0.0862m whereas in case of the two-step method the mean is -0.1768m. This means that the integrated approach is more reliable regarding the scale of the gravity field.

The dynamic geocenter which is the center of mass of the Earth is represented by the GFCs C11, S11, and C10 referring to the x-, the y-, and the z-coordinate, respectively. Short-term mass variations are modeled here using the AOD1B product that does not contain hydro-

logy; but effects of hydrology on geocenter variations are expected to be less than a millimeter. That way any larger bias as well as larger scatter of the series indicate reduced quality. The time series of the daily solutions reveal lower mean values and lower standard deviations in all three components for the integrated approach, see Figure 3. This is especially pronounced in C10, the z-component. Thus, it can be stated that applying the integrated approach better daily estimates of the coordinates of the dynamic geocenter are obtained than applying the two-step method.

Regarding C20 there is much higher scatter in case of the integrated approach but the trend for both solutions is the same. On the other hand C20 estimates derived by GRACE are currently not accepted to be trustful leading to the GRACE Project recommendation to exchange GRACE-derived estimates of C20 by SLR-derived values provided in the GRACE Technical Note #05 (see GRACE Project Document). As C20 is a geophysically interesting parameter future research will certainly focus on improving the integrated approach for estimating this parameter.

The series of the daily estimates of C21, S21, and of S22, see Figure 5, reveal only a small

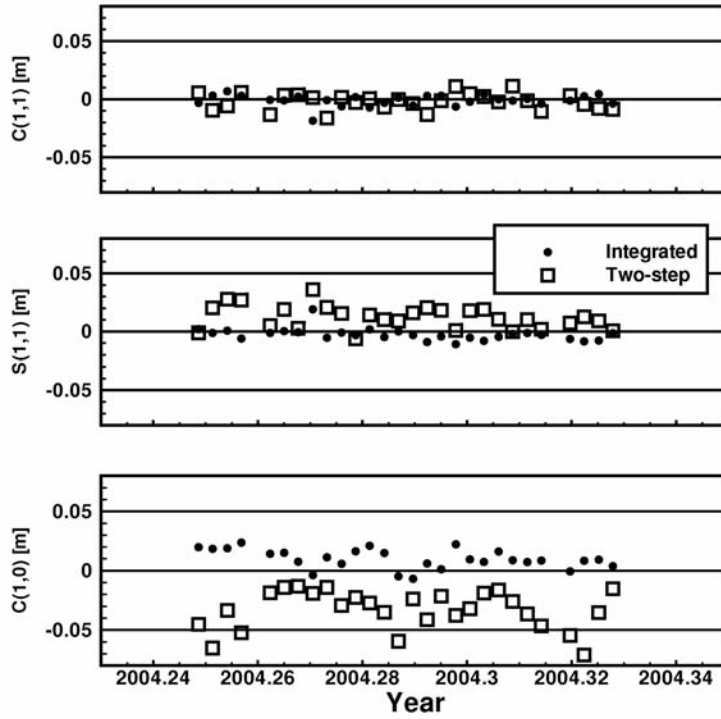


Figure 3: Daily estimates of dynamic geocenter coordinates, rescaled to metric distance; mean \pm standard deviation [m]:

C11: -0.0010 ± 0.0050 (integrated), -0.0019 ± 0.0071 (two-step),
 S11: -0.0027 ± 0.0055 (integrated), $+0.0123 \pm 0.0099$ (two-step),
 C10: $+0.0100 \pm 0.0082$ (integrated), -0.0331 ± 0.0163 (two-step).

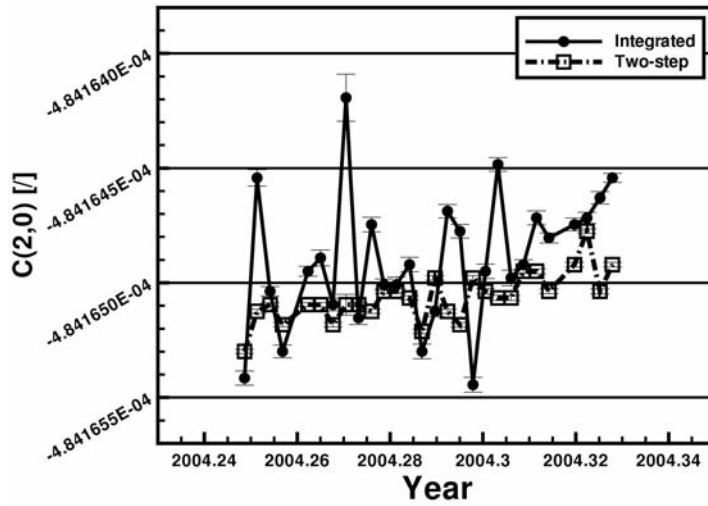


Figure 4: Daily estimates of C20.

bias of less than a millimeter between both approaches. Also the standard deviations differ by less than a millimeter. Nonetheless the integrated approach seems to be sensitive with respect to outliers in the data and therefore needs careful processing.

Concerning the zonal terms (order = 0) of degree ≥ 3 there is only some detectable difference between both approaches for C30 with higher scatter in case of the integrated approach

and a visible trend in case of the two-step method. It is interesting to see that the outlier on 2004/04/09 as well occurs more pronounced in the series of the two-step method.

Conclusions

In order to improve current GRACE-based gravity fields it is investigated whether the integrated approach leads to better results than the currently followed two-step method. For

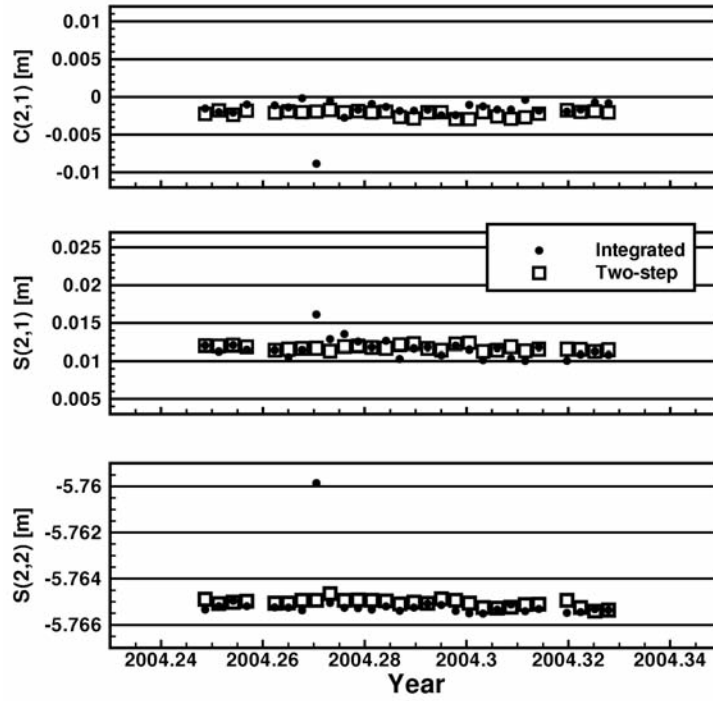


Figure 5: Daily estimates of degree-two terms, rescaled to metric distance on the Earth surface; mean \pm standard deviation [m] (without outlier on 2004/04/09):

C21: -0.0015 ± 0.0006 (integrated),
 -0.0022 ± 0.0004 (two-step),
 S21: $+0.0114 \pm 0.0009$ (integrated),
 $+0.0117 \pm 0.0003$ (two-step),
 S22: -5.7653 ± 0.0001 (integrated),
 -5.7650 ± 0.0002 (two-step).

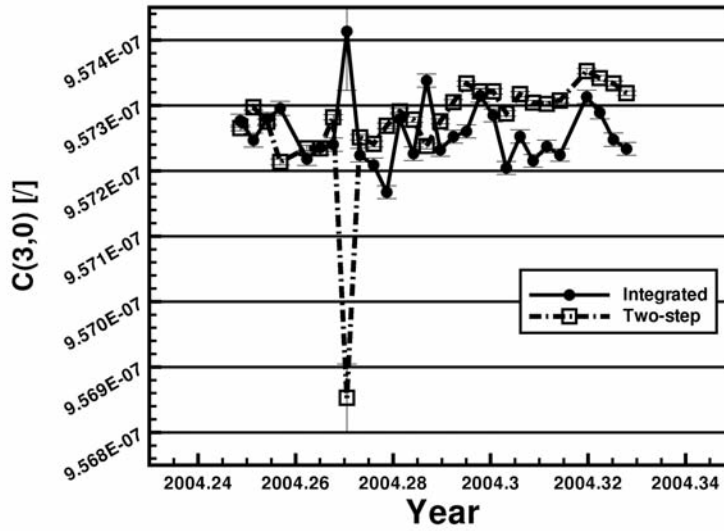


Figure 6: Daily estimates of C30.

getting a first comparison of both approaches gravity field coefficients up to degree and order ten are estimated by either approach with daily resolution covering one month of data. The degree variances of the differences between either monthly solution and EIGEN-51C show better agreement of the integrated approach with this EIGEN field for degrees zero, one, three, and four.

Lower biases and lower scatter of the series of the daily estimates show that the integrated

approach delivers better solutions of C00 and the coordinates of the dynamic geocenter (C11, S11, C10). Smaller degree variances of the difference between the integrated solution and EIGEN-51C as well indicate a better quality of those coefficients compared to the two-step method. But there still remains the question whether it is reasonable to estimate these coefficients or to keep them fixed. While the two-step method resolves C20 with much lower day-to-day scatter, there is almost no dif-

ference in C21, S21, and S22. Concerning the zonal terms from degree three on there is only significant difference in C30.

It should be emphasized that the work presented here is only a first step towards generating satellite gravity fields applying the integrated approach. The integrated approach has got the potential to deliver better qualities, however some open issues still need to be resolved.

Acknowledgments

The project TOBACO-CHAMP/GRACE is funded within the BMBF R&D-Programme GEOTECHNOLOGIEN with FKZ 03G0728A.

We would like to thank the German Space Operations Center (GSOC) of the German Aerospace Center (DLR) for providing continuously and nearly 100% of the raw telemetry data of the twin GRACE satellites.

References

Bruinsma SL, Marty JC, Balmino G, Biancale R, Förste C, Abrikosov O and Neumayer H (2010) GOCE Gravity Field Recovery by Means of the Direct Numerical Method, presented at the ESA LivingPlanet Symposium 2010, Bergen, June 27 - July 2 2010, Bergen, Norway

Flechtner F, Dahle Ch, Neumayer KH, König R, Förste Ch (2010) The Release 04 CHAMP and GRACE EIGEN Gravity Model. Flechtner et al. (eds.), System Earth via Geodetic-Geophysical Space Techniques, Adv. Technologies in Earth Sciences, Springer-Verlag Berlin Heidelberg 2010, doi 10.1007/978-3-642-10228-8_4.

GRACE Project Document: GRACE Technical Note #05, <http://isdc.gfz-potsdam.de/>

König R, Reigber Ch, Zhu S (2005) Dynamic model orbits and Earth system parameters from combined GPS and LEO data. *Advances in Space Research* 36, doi: 10.1016/j.asr.2005.03.064, pp. 431-437.

Zhu S, Reigber Ch, König R (2004) Integrated Adjustment of CHAMP, GRACE and GPS Data. *Journal of Geodesy*, Vol. 78, No. 1-2, pp. 103-108.

Faster Reprocessing

Neumayer K.H.(1)

(1) Helmholtz Centre Potsdam, GFZ German Research Centre for Geosciences,

Correspondence to: K.H. Neumayer (neumayer@gfz-potsdam.de)

1. Introduction

Reprocessing a gravity field involves a lot of experimenting. Background models have to be evaluated and tested, data pre-processing methods have to be analysed, different processing strategies have to be weighted against each other. Applying a method to one day or one week of test data does often not show if it works or not. In order to obtain a meaningful static gravity field it is necessary to process consecutive data of one month at least, often more. Annual time variability shows on a time scale of years, not of months. Thus when a reprocessed gravity field is finally offered to the community then it has, in fact, not been reprocessed once but many times. It is therefore vital that the technical part of the processing is reliable and fast. Hardware has to be chosen in a manner that it helps the task, and developed software has to exhaust all the possibilities of existing hardware. Software development must include all possible tools of parallelization and efficient computation. The design and management of processing chains has to be optimized. Modularity is a necessity if several persons are involved in the development process. In the following we present what has been achieved here so far.

2. Established Processing Strategy

Gravity fields are adjusted from normal equations obtained from batches of consecutive measurement data. The typical time horizon for a gravity field that is considered to be a static one is one month (at least what concerns GRACE processing). Data that go into the adjustment are, in the case of GRACE, GPS code and phase measurements as well as inter-

satellite tracking data in the form of microwave range rate. Furthermore, on-board accelerometer measurements and star-tracker attitude quaternions give non-conservative accelerations and satellite body orientation. The parameters that are adjusted are - apart from the Stokes coefficients of the gravity field and (optionally) the expansion coefficients of the ocean tides - daily initial positions and velocities of all satellites, calibration factors and biases of the measured surface accelerations and empirical parameters that model errors in the inter-satellite tracking link. Finally, there are GPS phase ambiguities and offsets of the GPS on-board receiver clock.

The comprehensive normal equation is not computed in one sweep from the entire data set, but the original time interval is chopped into batches of (typically) one day length. Normal equations are computed for those smaller data batches, they are then added up to one global equation, which is finally solved for all parameters. The processing along these lines is done in several consecutive steps.

In the first step, the gravity field we start from, and also the ocean tides, if present, are not estimated. For every day of the month, the satellite orbits are adjusted as good as possible to the measurement data by varying the rest of the parameters. This is commonly called *screening*.

In the second step, the expansion coefficients of the gravity field (and possibly those of the ocean tides) are added to the set of solve-for parameters, and for all one-day sub-arcs, the design equations are computed and stored.

In the third step, normal equations are computed from the design equations.

Those normal equations are then added up and solved. Depending on the problem at

hand, a parameter reduction is applied.

Experience has shown that the above-mentioned third step, which essentially amounts to the apparently trivial task of multiplying large matrices, is the most time-consuming of all. As a rule, it makes almost no sense to attempt a speedup of the rest if that bottleneck is not widened.

The screening part is done on a Linux cluster. The daily jobs of one month are simultaneously started on different nodes of the network, so the amount of time the screening of all arcs takes is effectively the time to do the screening for one day only. Steps two and three are performed on interconnected shared memory workstations that run the Unix operating system.

To accelerate processing in step two, the design equation is not created in one piece. A technique is applied that is called *parameter chunking*: Not one, but several instances of the satellite integration and adjustment program are started in parallel at the same time. Their controlling input files are almost identical. The difference between them is the flagging of parameters as free or as solve-for. Typically, depending on the capacity of the underlying hardware, 20-40 such processes are started in parallel, having mutually disjoint sets of free parameters, and the union of the free parameters over all jobs give the set of desired parameters that are to be adjusted altogether. In technical terms, this amounts to partitioning the design equation matrix into 20-40 column blocks. The format of the output files gives a well-defined interface for subsequent processing. Experience shows that a considerable speedup is achieved by this fragmenting policy, and it is more straightforward and much simpler than to spend time on parallelizing the orbit adjustment program proper. Speedup may also be due to effects in the operating system having to do with memory management and array addressing which seem to favour processes that occupy small portions of the RAM.

The largest part of the third step, creating normal equations from design equations, is the computation of normal equation matrices from design matrices. This is achieved, at the level of the underlying fortran programs, with

MPI (message passing interface).

The subsequent adding, parameter reduction and solution of the normal equations is done with the in-house TOTSOL processing environment. It features tools that look like Unix/Linux commands, with command line parameters and option switches. To the user they are essentially black boxes.

The orbit integration and adjustment program that is used for steps one and two bears the name EPOS-OC, and this abbreviation will be used in the following.

3. Parallelization from the Viewpoint of Hardware and Software

The acceleration of processing, for our purposes, is mainly achieved by parallelization. There are two essentially different approaches depending on the underlying computational hardware.

A cluster environment with physically distributed memory hardware features a large number (up to several thousands) of computation nodes, where the resources of the individual node, like number of processors or RAM (random access memory) size, are small. Effectiveness is achieved by breaking down the task into a very large number of subtasks that are distributed over the nodes to be run in parallel. That distribution can be done by hand with commands like rsh (remote shell) or ssh (secure shell), but in most cases it involves a queuing system. A typical tool for parallel programming at source code level is MPI (message-passing interface). Shared-memory optimization, like OpenMP (open multi-processing), is a concept that applies to a different type of hardware, featuring CPU arrays (typical 16, 24) that share one and the same large RAM (up to 128 GB). It is activated by inserting dedicated directives into the source code of programs that are written in computer languages like fortran or C adopted for numerical high-performance computing.

Distributed memory parallelization at the level of program source code is much more difficult to implement. The MPI communication protocol e.g. basically amounts to calling a collection of subroutines from the respective high-

level language, and the distribution of data to computation nodes and their collection has to be programmed by hand. An easier, brute force alternative is to do the distribution at the level of the shell. Programs that are treated as »black boxes« for dedicated tasks are invoked on the computation nodes via the queuing system, and they communicate with the help of files. Those data files are either copied to and from the local disks of the nodes, or they are read from and written to a storage location that is visible from all nodes.

The limiting factor of distributed memory computation is the transport of data between the nodes and, as a consequence, the network load.

In shared memory-machines, by contrast, the data is already »in place« for all CPUs and needs not to be transported or written. The limiting factor here is the number of CPUs on the machine.

At the GFZ in Potsdam, we have a distributed memory cluster with a central RAID (redundant array of independent disks) system with a total capacity of some 90 TB of disk space. The current usage is such that some 20-25 TB are permanently free. The controlling central access node has 12 CPUs with 800 MHz each, sharing 16 GB RAM. At the moment (September 2010) 202 computation nodes are accessible via a load sharing facility (LSF). The individual computation nodes are such that there are 33 with 2 CPUs, 114 with 4 CPUs and 42 with 8 CPUs. In theory there are 858 processors accessible altogether. The binding of the users to dedicated processing queues as well as frequently occurring hardware problems restrict the number of CPUs available to the gravity field processing group to about 90 at most. The individual nodes are »small« according to the standards of today, we have 2-8 GB RAM per node with the understanding that »GB RAM equals number of processors«, i.e. if we have 8GB RAM on a node then 8 processors have to share it. The tact frequency of the individual processors ranges between 1 GHz and 2.8 GHz. The cluster is continuously updated and expanded, thus the number of nodes changes.

Interesting for the shared-memory approach,

on the other hand, is the recent acquisition of two Linux workstations with 24 GB RAM each, having 16 and 24 processors respectively with 2.4 and 2.6 GHz tact frequency.

4. A Description of some File Interfaces

Design equation files are produced by EPOS-OC in the above-mentioned second processing step. Some remarks on the structure of those files are in order. Let n_{par} be the number of solve-for parameters, and let m_{obs} be the number of observations. Then the ensuing file has a size of $8 \cdot (m_{\text{obs}} + 2) \cdot (n_{\text{par}} + 10)$ bytes. The file format is binary and direct access. The individual file record length is $8 \cdot (n_{\text{par}} + 10)$.

Record numbers 3 to $m_{\text{obs}} + 2$ are used for the design equation proper. In the first record, three integers n_{par} , m_{obs} and l_{amb} are stored, where the first two have already been explained and the third one is, in the case of GPS measurements present, the number of GPS phase ambiguities. The second data record contains intelligence on a-priori parameter sigmas and is not of interest here.

The entries from record number three onward we symbolically write as

`ctyp, kep, j1, j2, res(1:4), pois(1:4), pard(1:nobs)`

with the following meaning: `ctyp` is a 4-character string, with the fourth character always a space, the first three designating the observation type, like GPS, KRR, POS, VEL, ... for GPS code/phase, k-band range rate, satellite positions, satellite velocities, and so forth. The 4-byte integer `kep` is the epoch number in case of GPS measurements; it is typical for GPS that we have more than one observation per epoch, and the epoch counter shows which measurements belong to the same epoch. In case of non-GPS measurements this entry either has no meaning, or it is used as an auxiliary parameter e.g. for data filtering. The integers j_1 , j_2 are the indices of the sender and receiver clock parameter for GPS, otherwise they are dummies. The following 8-byte real numbers `res(1:4)` are measurement residuals. In case of GPS measurements, `res(1:2)` are

code and phase residuals, for non-GPS measurements, only $\text{res}(1)$ is used; $\text{res}(3:4)$ are dummy entries reserved for future measurement types. The same philosophy applies to the observation weights $\text{pois}(1:4)$, with $\text{pois}(1:2)$ being used for the GPS case, and $\text{pois}(1)$ for all others. The 8-byte real numbers in the vector $\text{pard}(1:n_{\text{obs}})$ are the partial derivatives of the observation with respect to the parameters, where the simultaneous treatment of code/phase observation pairs in case of GPS (which will not be explained here) demands that the last l_{amb} parameters are the phase ambiguities. It should be remembered that, due to parameter chunking, EPOS-OC started in parallel produces not one but between 20 – 40 such design equation files, thus realising a block-column partitioning of the design equation matrix. Normal equations are produced hereof in the above-mentioned third step. The adopted way to store them is a pair of two files, a HEADER and a BINARY body.

The HEADER contains intelligence on the types of measurements processed for the normal equation, the number of solve-for parameter, the number of observations and the number of reduced parameters. Furthermore, the ITPI (sum of the weighted squares of the residuals) per measurement type is stored. The starting values for the parameters reside here as well as a mapping of the parameter numbers to the parameter names.

The BINARY body file contains the system matrix of the normal equation, its right-hand side vector and the sum of the weighted squares of the observation residuals (ITPI). As with the design equations, the file format is binary and direct access. If we have n_{par} solve-for parameters, then the record length of that direct-access file is $8 \cdot (n_{\text{par}} + 2)$ bytes: The first 8-byte real in every record is the respective entry of the normal equation right-hand side vector, followed by the n_{par} elements of the normal equation matrix row. The last 8 bytes are dummies. This structure applies to records 1 to n_{par} . Record number $n_{\text{par}}+1$ is essentially empty, only the first 8-byte real is the target functional ITPI. Consequently, the size of the BINARY file is $8 \cdot (n_{\text{par}}+1) \cdot (n_{\text{par}}+2)$.

5. Re-ordering of the Parameters

In a typical scenario most of the parameters are Stokes coefficients of the gravity field. Thus the *parameter chunking* explained above traditionally means a chunking of the gravity field parameters alone. Let us explain this with an example. Imagine we had a day for which we want to generate the design equations, and we make 30 chunks of free parameters. Then chunk numbers 1 to 29 contain gravity field parameters. Chunk number 30 however contains a problematic mixture of parameters that are specific to the arc, like orbit elements, accelerometer calibration factors and k-band parameters, but also global parameters like the ocean tides and those gravity field coefficients that are not contained in chunks 1 to 29. A considerable performance improvement was achieved by slightly changing the chunking policy: Not only the gravity field parameter vector now is chopped up into handy pieces, but also the vector of ocean tide coefficients, and the last chunk contains no global, but only arc-specific parameters. To make an example, chunks 1 to 30 contain the gravity field, chunk 31 and 32 the ocean tides and chunk 33 the parameters that describe the satellite orbits of the specific day and data calibration factors, and nothing else. The performance improvement has to do with the logistics of operations that follow later like the reduction of arc-specific parameters and the adding of normal equations, which were traditionally taken care of by commands of the TOTSOL chain that assume no structure of the normal equation matrices whatsoever and therefore perform a lot of now redundant operations like permuting the parameter vector before a reduction and re-mapping of initial parameter values before an adding and a re-sizing of the matrix and vector dimensions. In the novel form, the global parameters (gravity and ocean tides) are already sorted to the front of the parameter vector, therefore reduction and adding becomes almost trivial. The saving in the processing time is around four hours for that processing step.

Furthermore, a consequent migration of the second processing step to the distributed-

memory cluster environment allows an almost unlimited number of chunks per arc and a processing of several arcs at the same time in a batch.

As an example, the accumulation of the design equations of a test model problem with a gravity field of degree and order 90 took 2 hours 47 minutes with the new method, compared to 7 hours when it is done the traditional way. On the Linux cluster, the processing time essentially scales with the number of computation nodes available.

6. Novel Methods for the computation of Normal Equations

6.1. Fragmented Normal Equations on the Distributed Memory Cluster

A first attempt to port the traditional MPI approach more or less unchanged to the Linux cluster was not satisfactory. On the one hand there were spurious errors of the MPI subsystem on the connected Linux machines. On the other hand, a scaling of the performance with the number of computation nodes was not achieved. A possible reason is the »smallness« of the individual cluster node, with respect to the number of CPUs (2,4 and 8) and the limited size of the RAM (2 to 8 GB). Despite the fact that MPI seems to be tailored for applications with distributed memory, the physical distribution of the latter causes a lot of overhead in process communication, and a considerable part of the whole time MPI is running it is occupied with copying data from one processor node to the other.

It was therefore decided to

- Dispense with MPI for the time being
- Maintain the concept of computing the normal equation as lower block-triangular matrix, in a chess-board pattern, but to do this by fragmenting the BINARY body into files
- Not to re-assemble the BINARY file from the fragments for subsequent processing, but to re-implement the operations like adding of normal equations and reduction of

arc-specific parameters for the normal equation in fragmented form.

How this approach has been realized is best explained by making an example.

GRACE gravity fields are typically computed from one or more months of data. The sub-arcs of such a campaign have a length of one day. It has been established to designate an arc, and its derived normal equation by begin and end date in civilian notation, e.g.

20040301.000000__20040302.000000

or, with symbolic parameters

yyyymmdd.hhnnss__yyyymmdd.hhnnss

where yyyy/mm/dd are the dates of begin and end, and hh:nn:ss is the time of the day at a granularity of seconds. Furthermore, it makes sense to accumulate normal equations for different data types separately, identifying the kind of measurements used by a three-character string like GPS, KRR, SLR, POS, VEL etc. for GPS code/phase, k-band range rate, satellite laser ranging, satellite positions, satellite velocities etc.. Thus, for every type of measurement, there is a pair of HEADER/BINARY files

20040301.000000__20040302.000000.GPS.h,

20040301.000000__20040302.000000.GPS.b,

20040301.000000__20040302.000000.KRR.h,

20040301.000000__20040302.000000.KRR.b,

and so forth that, when obtained, is fed into subsequent processing.

In our new approach, the BINARY parts, i.e. the files with the extension *.b for the individual measurement type, do no longer exist. They have been replaced with a directory

20040301.000000__20040302.000000.d

that contains binary direct-access files


```
GPS_001_001.b
GPS_002_001.b  GPS_002_002.b
GPS_003_001.b  GPS_003_002.b  GPS_003_003.b
....
```

```
KRR_001_001.b
KRR_002_001.b  KRR_002_002.b
KRR_003_001.b  KRR_003_002.b  KRR_003_003.b
....
```

where the meaning of GPS, KRR (as an example) has already been explained, and the three-digit indices like ..._003_002 etc. are the numbers of block-row and block-column of the fragmentation.

If n_1, n_2, n_3, \dots are the number of parameters in block 1, 2, 3, etc. then the off-diagonal blocks, like e.g. (5,3), see to GPS_005_003.b, KRR_005_003.b etc. contain the $n_5 \cdot n_3$ normal equation matrix elements and nothing else. The size of such a binary file is therefore $8 \cdot n_5 \cdot n_3$ bytes.

However, the diagonal blocks, like

```
GPS_001_001.b, GPS_002_002.b, GPS_003_003.b, ...
KRR_001_001.b, KRR_002_002.b, KRR_003_003.b, ...
```

have the same internal structure as the BINARY file explained in section 4, i.e. for the block number (e.g.) 5, GPS_005_005.b contains not only the elements of the sub-matrix of dimension n_5 , but also the respective sub-section of the right-hand side vector as well as the ITPI (which is the same for all blocks). Thus, the files GPS_005_005.b, KRR_005_005.b etc are all of the same size $8 \cdot (n_5+1) \cdot (n_5+2)$ bytes.

As the structure of the diagonal blocks is the same as the one of the original, complete normal equation, all the well-established tools of the TOTSOL chain may be applied, a fact that considerably facilitates operations with such normal equation fragments.

The development of faster processing chains is not a task that is achieved by one person alone. It does not only involve the numerical programming part, but also experiments to determine the optimal sequence of operations like adding of normal equations, reduction and solving. It is therefore vital that the software is modular and easy-to-use even for the non-expert. Therefore, the purely numerical part of

the individual processing steps has been encapsulated in a hierarchy of shell scripts that are reminiscent of ordinary Unix/Linux commands. For example, the fortran programs

```
sub_verbgl_2_ngl_gps
sub_verbgl_2_ngl_ngp
f90_verbgl_2_ngl_gps_two_inputs
f90_verbgl_2_ngl_ngp_two_inputs
```

that realize the computation of the normal equation fragments from one (diagonal block) or two (non-diagonal block) of design equation files are in turn called by a shell script

```
submit_neq_block_350.sh
```

that submits the computation of dedicated normal equation fragments to the processing queue. That command, in turn, is called by

```
distributed_verbgl_2_ngl_350.sh
```

that establishes the normal equation fragments of all measurement types for a given arc, and the latter command is repeatedly called by

```
distributed_verbgl_2_ngl_4_arc_list_on_cluster.sh
```

that computes the arc-wise normal equations for the whole campaign.

In a likewise manner, all following processing steps have been implemented. For example,

```
add_mtyps_of_fragmented_NEQ_350.sh
```

realizes the addition of the individual measurement types (GPS, KRR etc.) for a given arc, and

```
reduce_mtyp_of_fragmented_NEQ_350.sh
```

reduces the arc-specific parameters for the fragmented normal equation, like satellite orbit elements, accelerometer calibration factors, ambiguities etc., so that only the global parameters – gravity field and ocean tides – remain.

6.2. Shared Memory Processing speedup with OpenMP

OpenMP (open multi-processing) is a tool for parallel operations on machines with a large number of processor cores that use one and the same large RAM. It is activated by placing a standardized set of dedicated compiler directives directly into the source code of the numerical computation part at places that are time-critical, like matrix-matrix and matrix-vector multiplication. As already mentioned, the most time-consuming part in our processing chain is the computation of normal equations from design equations, which basically amounts to matrix multiplications. The computer language our numerical computations are implemented in is fortran 95, here the OpenMP directives look like comments. An example of such a directive would be

```
!$OMP PARALLEL DO FIRSTPRIVATE(K) PRIVATE(I,f,z)
SHARED(N) SCHEDULE(dynamic)
  DO I = 1,k
    DO f = 1,k
      .....
      .....
!$OMP END PARALLEL DO
```

This instrument is obviously simple to use, the distribution of the work to the processors is not the concern of the program developer, as it is in the distributed memory case. It is entirely taken care of by the compiler and the runtime environment. This, however, is also a restriction; OpenMP cannot be used in a meaningful way on a computation cluster with many physically separated nodes where each node has only limited resources of memory and processors.

Thus both approaches, the one with fragmented normal equations and the one with OpenMP, do not exclude, but rather complement each other.

Normal equation computation goes in two steps; first design equations are to be computed, then normal equations from the design equations. In the shared-memory environment, the first of the two steps is implemented, just as in the distributed-memory case, by parame-

ter chunking and starting as many EPOS-OC integrator runs as there are nodes on the respective shared-memory machine. It is just as in the distributed memory case, but the EPOS-OC runs are not sent to individual computation nodes with a queuing system, but started on one and the same machine in parallel. No OpenMP is involved here.

The following step – computation of the normal equations – is encapsulated with several hierarchies, just as in the distributed-memory case. The command the user has to issue is

```
shared_memory_verbgl_2_ngl_350.sh
```

and the OpenMP functionality is activated with the optional switch `-omp`. Control is passed to two fortran programs featuring OpenMP

```
f90_verbgl_2_ngl_gps_omp
f90_verbgl_2_ngl_ngp_omp
```

where the first one computes GPS normal equations from the design equation files, and the second one does the same for the non-GPS case. If the optional switch `-omp` is omitted, `shared_memory_verbgl_2_ngl_350.sh` queries for an usable MPI system on the local machine and uses that if it exists, thus we have backward compatibility.

The shell script looks and behaves like a standard Linux/Unix command. The behaviour is controlled by dedicated switches like `-omp`, `--omp_stack_size` etc., hiding cumbersome details entirely from the user, thus enhancing modularity and facilitating the development of processing chains if several people work together.

7. The Speedup Achieved in Figures

A model problem, for a GRACE-like scenario was used as a test case. A relatively small gravity field of degree and order 90 was adjusted. 28 days of GPS code/phase as well as inter-satellite tracking data were used. Processing was done in data batches of one day length, yielding 2·28 normal equation matrices (for every day, there is one for GPS and one for the

inter-satellite link) that were added up and solved. In the following table we have the results for the processing time bottlenecks described above:

	Conventional	Distributed memory	OpenMP
Design equations	7 hours	2.5 hours	3.8 hours
Normal equations	5.2 hours	4.5 hours	3.3 hours

The first line is the time spent for the computation of the design equations for the whole 28 days using parameter chunking and simultaneous EPOS-OC runs, the second line is the time for computing all $2 \cdot 28 = 56$ normal equations from the design equations. The column »conventional« refers to the established method described in section 2 above, namely MPI on a shared-memory Unix workstation with 128 GB RAM and 16 CPUs of 1.8 GHz tact frequency each. The columns »distributed memory« stands for the strategy with the fragmented normal equations described in section 6.1, realised on the Linux cluster described in section 3. Finally, the last column gives the results for the OpenMP parallelization of section 6.2, realized on one of the Linux shared memory workstations mentioned at the end of section 3. Both the novel methods need, in sum, some 7 hours compared to the 12.5 hours of the older method. It has to be kept in mind that the results of the first row grow linear with the number of parameters, the ones in the second row grow with the square of that number. Furthermore, to allow an interleaving style of processing, it was necessary in the »distributed memory« case to keep the design equation files for the whole four weeks on mass storage. For our example, we had $n_{\text{par}} = 9345$ solve-for parameters and some $m_{\text{obs}} = 1.57$ million observations for 28 days, which amounts to about 100 GB of storage space according to the formula

$$\text{storage space/GB} = 8 \cdot (n_{\text{par}} + 10) \cdot (m_{\text{obs}} + 2) / 1024^3$$

explained at the begin of section 4. Fortunately this is easy to handle on the 90 TB RAID system

of the Linux cluster. It should be noted that the number of parameters of the adjustment problem grows approximately with the square of the maximal degree and order of the adjusted gravity field, thus degree and order 150 instead of 90 transform those 100 to almost 300 GB.

8. Conclusions

Various methods have been combined to significantly reduce the computation time for the gravity field processing of GRACE-like satellites. A re-ordering of the parameter vector facilitates the adding of normal equations and reduction of arc-specific parameters, thereby saving up to four hours of processing time for a monthly gravity field.

Parameter chunking not only for the gravity field expansion coefficients, but also for the ocean tides accelerates the computation of design equations.

In the distributed memory environment, fragmentation of normal equations in a lower triangular-block wise manner, and for the subsequent processing keep the normal equations fragmented. No high-level protocol mechanism like MPI was used.

All programming was kept modular, the individual tasks are called in the same manner as Unix commands with a parameter list and various options, so that for the experimenter and the designer of a processing environment or a processing chain, the implemented shortcuts are employed automatically (i.e. the user activates OpenMP by throwing the `-omp` switch, he has not to fiddle with parameters). Layered encapsulation, the task distribution and process management is achieved by a

hierarchy of shell scripts, the purely numerical work is done with specialized f95 programs that are very simple in most cases.

For the model problem presented, the computation of design equations and, subsequently, the normal equations, can be accelerated by a factor of two at least.

Acknowledgements

The project TOBACO-CHAMP/GRACE is funded within the BMBF R&D-Programme GEOTECHNOLOGIEN with FKZ 03G0728A.

We would like to thank the German Space Operations Center (GSOC) of the German Aerospace Center (DLR) for providing continuously and nearly 100% of the raw telemetry data of the twin GRACE satellites.

Reprocessing of CHAMP and GRACE Observations for the Determination of Improved Static and Temporal Gravity Field Models with Regional Refinements (GREST-CHAMP/GRACE)

Shabanloui A., Schall J., Mayer-Gürr T., Eicker A., Kusche J., Kurtenbach E.

Astronomical, Physical and Mathematical Geodesy Group, Institute of Geodesy and Geoinformation, University of Bonn, Nussallee 17, D-53115 Bonn, Germany, E-Mail: shabanloui@geod.uni-bonn.de

1. Abstract

The analysis of the GRACE (Gravity Recovery And Climate Experiment) gravity field observations has already proved the feasibility to determine mass variations especially with respect to continental hydrology in different geographical regions. Daily and monthly solutions of the gravity field have been determined, showing clearly temporal gravity field variations closely correlated to the hydrological water cycle and other time dependent processes in the Earth system. In the following, the GRACE gravity field model ITG-Grace2010 will be presented. It has been determined using the short arc method and consists of three parts: ITG-Grace2010s as static Earth's gravity field solution up to degree 180, unconstrained monthly GRACE solution up to degree 120 and daily snapshots based on Kalman smoother up to degree 40.

2. Precise Orbit Determination (POD) Technique

The interest in a Precise Orbit Determination (POD) of Low Earth Orbiters (LEOs) especially in pure geometrical mode using GNSS observations has grown rapidly. Conventional GNSS-based strategies rely on the GNSS observations from a terrestrial network of ground receivers (IGS network) as well as the GNSS receiver on -

board the LEO in double difference (DD) or in triple difference (TD) data processing modes. With the advent of precise orbit and clock products at centimeter level accuracy provided by the IGS (International GNSS Service) centers, the two errors associated with broadcast orbits and clocks can be significantly reduced. Therefore, higher positioning accuracy can be expected even when only a single GNSS receiver is used in a zero difference (ZD) procedure (*Shabanloui, 2008*). Along with improvements in the International GNSS Services (IGS) products in terms of GPS satellite orbits and clock offsets, the Precise Point Positioning (PPP) technique based on zero differenced carrier phase observations has been developed in recent years. In this paper, the zero difference procedure has been applied to the GRACE high-low Satellite to Satellite Tracking (hl-SST) observations, then the solution has been denoted as Geometrical Precise Orbit Determination (GPOD). The estimated GPOD GRACE results are comparable with results of other groups e.g. A. Jäggi at Bern (*Jäggi, 2009*); but because of different outliers detection and data processing strategies, the GPOD results presented here are more or less different than the other groups' results. It should be mentioned that the estimated geometrical orbit of the twin satellite mission GRACE is point-wise and its accuracy relies on the geometrical status of the

GNSS satellites and on the number of the tracked GNSS satellites as well as on the GNSS measurement accuracy in the data processing. The position accuracy of 2-3 cm of twin GRACE satellites based on high-low GPS carrier phase observations with zero difference procedure has been achieved. These point-wise absolute positions can be used to estimate kinematical orbit of the LEOs. Nowadays, limiting factor for LEO POD is mainly encountered with the modeling of the carrier phase SST observations, where a precise knowledge of the phase center location of the GNSS antennas in a pre-requisite for a precise orbit determination. Since GPS week 1400, the absolute phase center location instead of relative values are adopted for GNSS transmitter and receiver antennas. Based on robot calibration, the absolute phase center for a number of GNSS receiver antennas is determined. For the GNSS transmitter antennas, the absolute phase center are estimated based on GNSS data processing. However, consistent GNSS receiver antenna models for twin satellite GRACE, which are equipped with non-geodetic receiver antenna, are available since a short time from robot calibration method. Therefore, the GPS SST data of twin GRACE satellite are used to estimate empirical antenna phase center variations (PCV). It should be mentioned that near field multipath and cross talk with active GPS occultation antennas are main sources for

systematic carrier phase observation errors which are encountered in the actual GRACE environments. Based on independent K-band low-low SST (ll-SST) observations and estimated empirical antenna phase center variations (PCVs) with residual approach, the GRACE orbits are improved with the zero differenced high-low SST observations. Fig. 1 shows the estimated phase center variation patterns for twin GRACE satellites based on residual analysis pattern.

3. Representation of Earth's gravity field

The innovative character of GRACE is due to the highly precise line of sight (LOS) range and range-rate K-band measurements between the twin satellites. In addition, the surface forces acting on the twin GRACE satellites are measured by a 3D accelerometer and can be removed properly during the recovery procedure. The classical approach of satellite geodesy in gravity field recovery consists basically in deriving the spherical harmonic coefficients representing the gravitational potential from an analysis of accumulated orbit perturbations of the satellites. In this approach, it is an indispensable requirement to analyze medium long satellite arcs covering at least one day or more in order to cover the characteristic periodic and secular disturbances caused by the small corrections to the approximate force

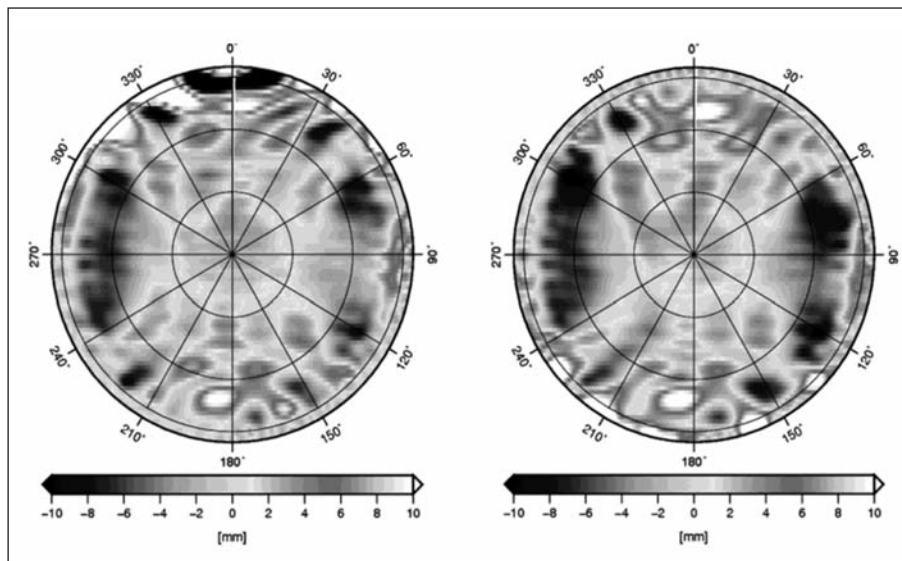


Figure 1: Phase center variations (PCV) for GRACE A (left) and GRACE B (right) GPS antennas.

function. In the short arc approach, this requirement is not necessary anymore for the new generation of dedicated gravity satellites like GRACE (*Illk. et al. 2006*). The principal characteristic of the method presented in this paper based on the use of short arcs of the satellite orbits in order to avoid the accumulation of modeling errors and a rigorous consideration of correlations between the range observations in the sub-sequent adjustment procedure. Further details to the physical model of the gravity field recovery technique based on GRACE observations can be found in *Mayer-Gürr 2010 and Kurtenbach et.al. 2009*. As a result of the dedicated spaceborne gravity field mission GRACE, ITG-Grace2010 has been derived which consists of three parts: daily solutions estimated using Kalman filter smoothing, unconstrained monthly solutions and a high resolution long-time mean.

4. Daily solutions with Kalman filtering

For more than 7 years, the twin GRACE satellites have measured the Earth's gravity field and its temporal variations. The official product of the GRACE project to describe these temporal variations is a series of monthly mean Earth's gravity field solutions. This concept has the disadvantage that these monthly gravity fields are not able to represent the Earth's gravity field variations within a monthly time span. This leads to aliasing errors due to unmodeled high frequency gravity field changes resulting in the wellknown error strip pattern. Furthermore, these aliasing errors are accepted to be one of the reasons that the predicted accuracy of the GRACE mission (baseline) has not been achieved yet. Several analysis centers try to overcome this drawback by reducing the time span to 10-daily (*Lemoine et al. 2007*) or even weekly (*Flechtner et al. 2009*) batches. An increase in temporal resolution results in less observations per time span and therefore a reduced redundancy in the Earth's gravity field representation parameters. This leads to a decreasing accuracy of the estimated unknown parameters with decreasing time span. When processing individual batches, no further infor-

mation about temporal behavior of the Earth's gravity field is exploited. However, it can be assumed that the gravity field does not change arbitrarily from one epoch to the next one. Therefore, the Earth's gravity field variations can be considered as a dynamic process. Based on this knowledge, the temporal resolution can be enhanced without losing spatial information with the goal to calculate daily solutions.

The processing of GRACE measurements e. g. hl-SST, K-band and acceleration observations, for one day can be formulated in a Gauss-Markov model as,

$$\mathbf{l}_t = \mathbf{A}_t \mathbf{x}_t + \mathbf{v}_t \quad (1)$$

where $\mathbf{l}_t, \mathbf{x}_t$ are the GRACE observation and the Earth's gravity field representation vectors, and $\mathbf{A}_t, \mathbf{v}_t$ are the design matrix and the observation residual vector for each day t , respectively. To obtain a reasonable gravity field model from one day of GRACE data, additional information is required. Up to now, no temporal correlations have been introduced into the processing strategy. But it can be safely prescribed that the estimate of the gravity field will not change arbitrarily from one day to the next, therefore a simple constraint can be introduced by stating

$$\mathbf{x}_t = \mathbf{B} \mathbf{x}_{t-1} + \mathbf{w}. \quad (2)$$

This represents a prediction of the gravity field coefficients from day $t-1$ to the current day t . The prediction is characterized by the matrix of the process dynamic \mathbf{B} . The normally distributed noise vector $\mathbf{w}(\mathbf{w} \sim N(0, \mathbf{Q}))$ with the covariance matrix \mathbf{Q} represents the accuracy of the prediction. Here a stationary, unbiased and first order Markov process in time is assumed. In the following section a process model expressed by \mathbf{B} and \mathbf{Q} is derived.

In *Kurtenbach et al. (2009)* the simple assumption, that there are no changes between two states ($\mathbf{B}=\mathbf{I}$) with a covariance matrix \mathbf{Q} derived from the hydrological model WGHM (*Döll et al., 2003; Hunger and Döll, 2008*), was introduced.

ced. Hereby a stationary, homogeneous and isotropic process on the sphere was assumed. In this section an improved version will be presented which takes into account the full correlation structure between two subsequent days, represented by the covariance matrix

$$C \begin{Bmatrix} \mathbf{x}_t \\ \mathbf{x}_{t-1} \end{Bmatrix} = \begin{pmatrix} \Sigma & \Sigma_\Delta \\ \Sigma_\Delta^T & \Sigma \end{pmatrix}. \quad (3)$$

Let Eq. (2) be a stationary, unbiased first order Markov process in time with the auto-covariance matrix

$$\Sigma := C\{\mathbf{x}_t, \mathbf{x}_t\} \quad (4)$$

and the cross-covariance matrix

$$\Sigma_\Delta := C\{\mathbf{x}_t, \mathbf{x}_{t-1}\}. \quad (5)$$

Then a linear predictor

$$\hat{\mathbf{x}}_t = \mathbf{B}\mathbf{x}_{t-1} \quad (6)$$

can be found, such that the prediction error $\mathbf{w} = \mathbf{x}_t - \hat{\mathbf{x}}_t$, has minimum variance. According to *Moritz (1980)* this predictor can be obtained by

$$\mathbf{B} = \Sigma_\Delta \Sigma^{-1} \quad (7)$$

with the covariance matrix of the prediction error \mathbf{w} ,

$$\mathbf{Q} = \Sigma - \Sigma_\Delta \Sigma^{-1} \Sigma_\Delta^T. \quad (8)$$

In practice, the matrices (4) and (5) of the Earth's gravity field are unknown and therefore an empirical version of these matrices has to be derived, which can be calculated using the output of geophysical models.

The Kalman smoother approach described above was applied to calculate daily gravity field solutions from GRACE level-1B data, covering the time span 2002-08 to 2009-08. For each day a set of spherical harmonic coefficients was derived for degrees $n=2 \dots 40$ as differences to the static gravity field ITG-Grace2010s, using the standard background

models described in *Mayer-Gürr et al. (2010)*. The models used to build the process model are the Water GAP Hydrology Model (*Döll et al., 2003; Hunger and Döll, 2008*), the ocean circulation model OMCT (*Dobslaw and Thomas 2007*), and the atmospheric data provided by the European Centre for Medium-Range Weather Forecasts (Research Department ECMWF, 2008). In order to guarantee that the GRACE solutions are not biased towards the model values themselves but that only the stochastic behavior is exploited, the model output from the years 1976-2000 (i.e. outside the GRACE time span) was used. These daily solutions are part of the GRACE gravity field model ITG-Grace2010 (*Mayer-Gürr et al., 2010*) and can be downloaded at <http://www.igg.uni-bonn.de/apmg/index.php?id=itg-grace2010>. To evaluate the information content of the daily GRACE models, they were compared to independent data sets as described below.

5. Comparison with ocean bottom pressure (OBP) data

Ocean bottom pressure recorders represent an independent type of measurement for the integrated mass column of oceanic and atmospheric variations. Therefore, they can be used as a validation tool for the mass variations derived from GRACE.

In Fig. 2 the black line shows the temporal evolution of the data observed by an OBP recorder located in the northern Atlantic provided by *Macrander et al. (2010)*. These in-situ measurements are compared to the atmosphere and ocean de-aliasing product (AOD1B, gray line) used in the GRACE L1B data analysis (*Flechtner, 2007*) and to the daily GRACE models obtained by the Kalman smoother approach (dark-gray line) described here. The AOD1B model represents the knowledge of the temporal high-frequent mass variations on a global scale without the use of GRACE. It can be seen that the daily GRACE solutions show better agreement to the independent OBP data set than the modeled atmospheric and oceanic

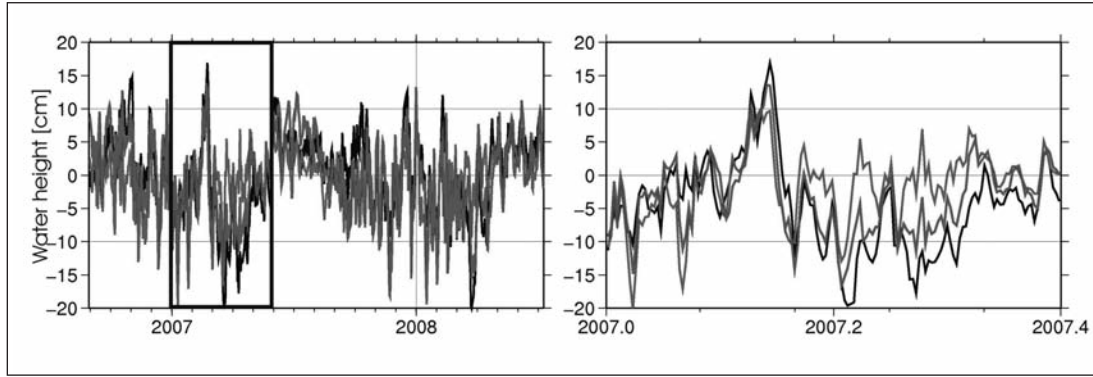


Figure 2: Left: OBP recorder observations in the northern Atlantic ocean (black), daily GRACE solutions (dark-gray) and AOD1B model (gray). Right: zoom-in on a smaller time span.

variations of AOD1B. Further investigations will include a larger number of OBP recorders.

6. Comparison with GPS station movements

Mass variations at the Earth's surface result in geometrical deformations of the Earth's crust which can be measured by GPS receivers. Therefore, the global network of permanent GPS stations delivers a further set of independent observations which can be used as comparison for GRACE gravity field models. The vertical station displacements of the reprocessed time series of the International GNSS Service, see *Steigenberger et al. (2006)*, were compared to the GRACE Kalman solutions on a daily basis.

The results are displayed in Fig. 3. The large figure shows the percentage of the signal of each of the stations that can be explained by the GRACE observations, i.e. it illustrates the reduction of the RMS values of the GPS observations when the GRACE solutions are subtracted. The smaller figures on top show the time series for two exemplary GPS stations. The in-situ GPS observations are given by the black curve, the GRACE time series by the dark-gray curve and as a comparison the AOD1B model is plotted in the gray line as well. The right figure represents an example for a station with very good agreement (NRIL, Norilsk). It is situated in northern Siberia, where the data coverage by GRACE is very

good and the daily signal of the radial displacements is large due to strong atmospheric mass variations. In contrast to this, the correlation of the time series is very poor in the left figure (both for the Kalman solutions and for the AOD1B product) which shows a station near the equator in the Pacific ocean (GLPS, Puerto Ayora). Here the signal itself is very small and the data coverage by GRACE is less dense.

7. Monthly Earth gravity field representation

The daily GRACE snapshots as described in Sec. (4) guarantee an optimal extraction of information in time and space. However, they are difficult to interpret due to the implicit spatial and temporal filtering that is applied during the Kalman smoother process. Therefore, it is convenient to publish additional monthly solutions as they represent the standard product of temporal gravity variations. The problem with calculating monthly mean solutions, however, is given by the fact that variations within the monthly span are not modeled. This leads to aliasing effects resulting in the well-known error stripe pattern. Therefore, the temporal high-frequent variations are generally subtracted during the analysis process using geophysical models. In general these models comprise the tidal effects caused by the sun and the moon, the Earth and ocean tides, non-tidal atmospheric and ocean variations. But nevertheless there are still model errors cau-

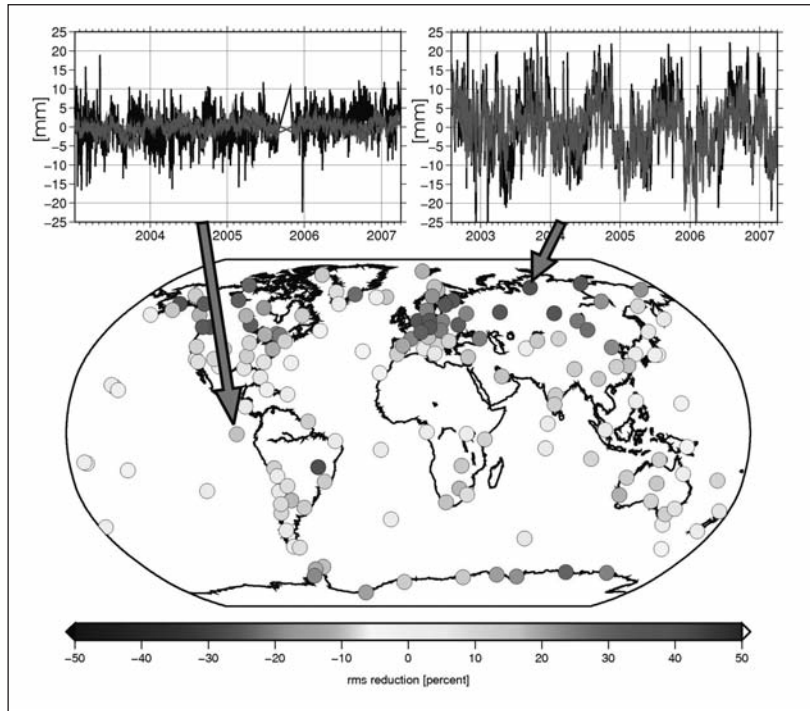


Figure 3: Comparison daily GRACE solutions with radial GPS station movements. Large figure: amount of the GPS signal that can be explained by GRACE- Top figures: Comparison of time series for individual stations for GPS (black), GRACE (dark-gray) and AOD1B (gray), left: GLPS (Puerto Ayora), right: NRIL (Norilsk).

sing aliasing and there are geophysical phenomena such as hydrology, that have so far not been considered in the de-aliasing products. There are two different possibilities that can be applied. The first one is to include the hydrological model in addition to the atmospheric and oceanic variations into the de-aliasing procedure. The second idea uses the daily Kalman solutions as improved de-aliasing product.

De-aliasing using the total water storage output of the WGHM model

In order to investigate the possibility to apply the total water storage as provided by the WGHM as an additional de-aliasing product for GRACE, the daily WGHM model values are reduced from the observations. This is an addition to the standard de-aliasing procedure, which takes into account the oceanic, atmospheric, and tidal variations. Monthly global GRACE solutions were then calculated and compared to monthly solutions determined without using the WGHM as de-aliasing model. The results were evaluated by comparison with the long-term mean GRACE solution which serves as pseudo-real comparison due to the

larger amount of data included. There are a few months where the approach does not lead to any improvements, but in the majority of the solutions the de-aliasing using the WGHM model helped to improve the solution. These results were presented by *Eicker et al.* (2009-04, talk at EGU General Assembly). Nevertheless, the use of temporal high-resolution (daily) GRACE models calculated with hydrological prior information for the de-aliasing of longer temporal means (monthly) has shown to have a significantly larger impact. Therefore, the direct use of the hydrology model itself has been abandoned.

ITG-Grace2010 unconstrained monthly solutions:

Improved de-aliasing using daily GRACE solution. The daily Kalman solutions are very well suited to model the temporal high-frequency signals provided by GRACE. But besides being used as individual product, they can also be applied to significantly improve the calculation of monthly GRACE solutions. In this context, the daily time series was used as additional de-aliasing model to reduce the high-frequency temporal variations before calculating monthly

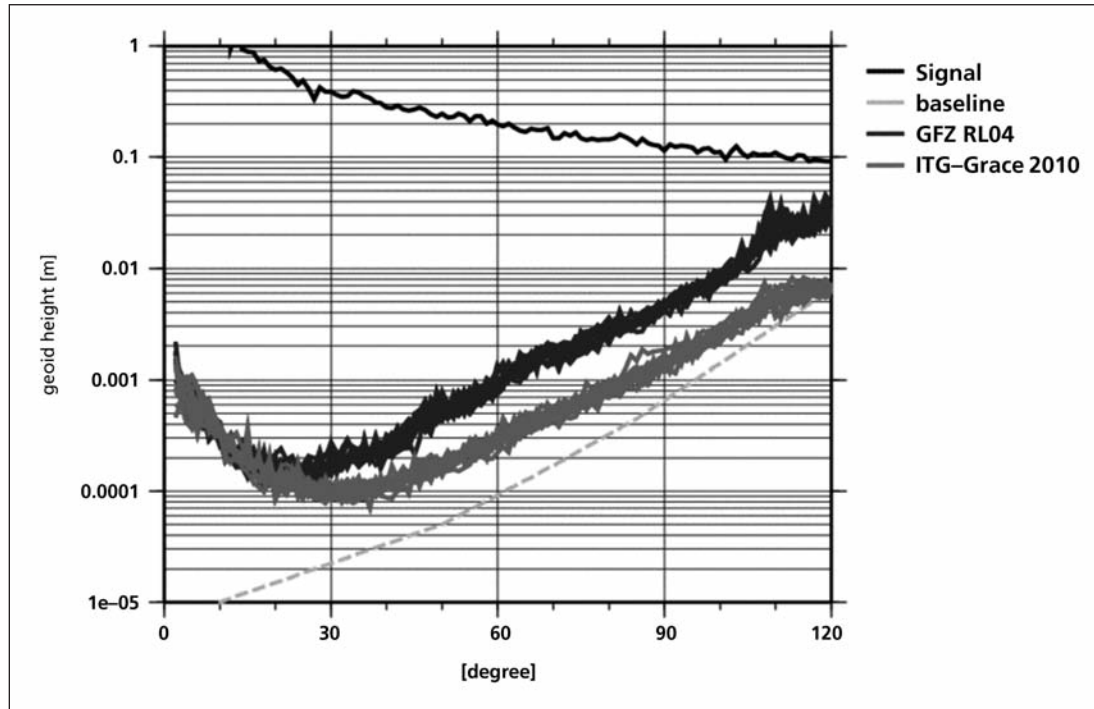


Figure 4: Errors of different monthly gravity field solutions compared to static field ITG-Grace2010s. The impact of the improved de-aliasing using the daily Kalman solutions leads to an improvement of the GRACE monthly solutions (gray) compared to the GFZ-RL04 solutions (dark-gray).

mean fields. Afterwards the monthly mean of the daily solutions is restored to receive the complete monthly signal. This procedure was applied in the reprocessing of the complete GRACE data, leading to the monthly solutions of the ITG-Grace2010 time series, as described in *Mayer-Gürr et al. (2010)*. Fig. 4 shows the improvements that were possible to achieve with this approach. The dark-gray lines show the differences in terms of degree variances of each monthly GFZ-RL04 solution (*Flechtner et al., 2010*) for the year 2008 compared to the static field ITG-Grace2010s. This long-term mean serves as pseudo-real comparison due to the larger amount of data included. The differences represent the quality that was achieved in the current releases before the reprocessing. Without the improved de-aliasing using the daily Kalman solutions, the ITG monthly errors are in the same range as the GFZ-RL04. But the application of the daily solutions as improved de-aliasing product has led to an improvement by a factor of three, the errors being illustrated by the gray lines. Especially in the higher degrees the errors are reduced, which corresponds

to an increase in spatial resolution. These solutions are published in *Mayer-Gürr et al. (2010)*.

8. Static Earth gravity field representation

The ITG-Grace2010 is a long term mean gravity field model covering the time span 2002-08 to 2009-08 calculated from GRACE data only up to degree and order 180. The solution is based on integral equation approach using short arcs with a maximum length of 60 min (*Mayer-Gürr, 2010*), the K-band range rates with a sampling rates of 5 s and kinematical orbits with a sampling rate of 30 s were used as (pseudo) observations. It should be mentioned that some background models e.g. IERS 2003 for Earth rotation and EOT08a for ocean tide etc. were used during GRACE data processing. For more details refer to *Mayer-Gürr (2010)*. In addition to the background models, the daily Kalman solutions were used as improved de-aliasing product. The mean of the AOD1B product and of the daily solutions was restored afterwards. Therefore, ITG-Grace2010s contains the complete gravity field signal inclu-

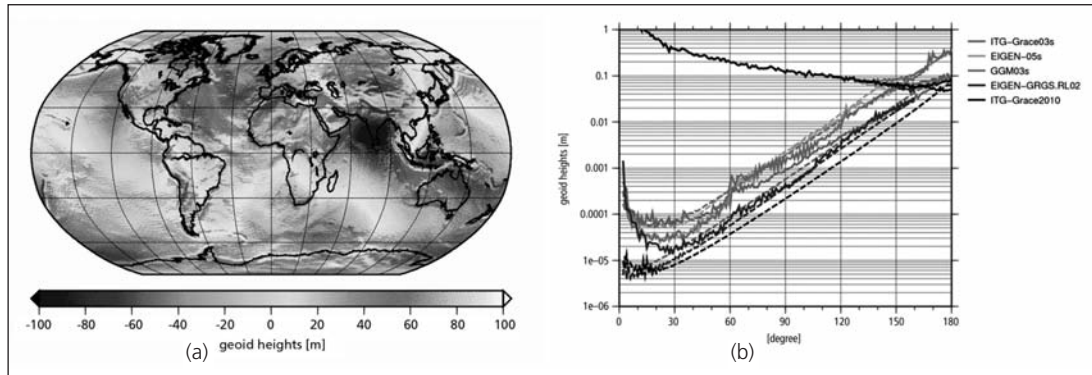


Fig. 5 (a): Static gravity field solution ITG-Grace2010 up to degree 180 in terms of geoid undulations. (b) Differences of ITG-Grace 2010 to the other released static GRACE solutions (solid lines) and formal errors (dotted lines).

ding atmosphere and ocean masses. The reference epoch of this mean gravity field model is 1 January 2005. A full variance-covariance matrix is provided for the static solution. During the estimation process of the monthly gravity fields 32760 unknown gravity field parameters were estimated. The full variance-covariance matrix has a size of about 8 GB memory. To simplicity, the matrix is split up into smaller files and only the upper triangle of the matrix is stored. Further information is provided in Mayer-Gürr (2010). Fig. 5(a) illustrates the static part of ITG-Grace2010s in terms of geoid undulations up to degree 180 resulting in 32760 unknown gravity field parameters. Fig. 5(b) shows the differences of ITG-Grace2010 to the other static GRACE solutions (solid lines) and formal errors (dotted lines).

9. Conclusions

In this paper, the Earth's gravity field model ITG-Grace2010s with its three parts, static high resolution model up to degree 180, monthly Grace solution up to degree 120 and daily solution based on Kalman smoother up to degree 40 with full variance-covariance matrix was presented. These models have been estimated using an house developed software GROOPS.

10. Acknowledgements

The financial support by BMBF (Bundesministerium für Bildung und Forschung) within the

frame of the Geotechnologien-Programm is gratefully acknowledged.

11. References

- Dobslaw, H., Thomas, M. (2007): Simulation and observation of global ocean mass anomalies. *Journal of Geophysical Research* 112.
- Döll, P., Kaspar, F., Kaspar, B. (2003): A global hydrological model for deriving water availability indicators: model tuning and validation. *Journal of Hydrology* 270, 105-134.
- Eicker, A. (2008): Gravity field refinements by radial basis functions from in-situ satellite data, dissertation, Institute for Geodesy and Geoinformation, University of Bonn, Germany.
- Flechtner, F. (2007): AOD1B Product Description Document for Product Releases 01 to 04, Tech. Rep., Geoforschungszentrum Potsdam, 2007.
- Flechtner, F., Dahle, C., Neumayer, K. H., König, R. and Förste, C. (2009): The release 04 CHAMP and GRACE EIGEN gravity field models, in *Satellite Geodesy and Earth System Science Observation of the Earth from Space*, edited by F. Flechtner et al., Springer, Berlin, in press.
- Flechtner, F., Dahle, C., Neumayer, K.H., König, R. and Förste, C. (2010), The Release 04 CHAMP and GRACE EIGEN Gravity Field Models, In: F. Flechtner, T. Gruber, A. Güntner, M. Manda, M. Rothacher, T. Schöne and J. Wickert (Eds.):

- System Earth via Geodetic-Geophysical Space Techniques, Springer, ISBN 978-3-642-10227-1, DOI 978-3-642-10228-8, pp 41 - 58, 2010.
- Hunger, m., Döll, P. (2008): Value of river discharge data for global scale hydrological modeling. *Hydrology and Earth System Sciences* 12, 841861. <http://www.hydroearth-sci.net/12/841/2008/>.
- Jäggi, A., Dach, R., Montenbruck, O., Hugentobler, U., Bock, H., Beutler, G. (2009): Phase center modeling for LEO GPS receiver antennas and its impact on precise orbit determination. *Journal of Geodesy*, vol. 83(12), pp. 1145-1162, DOI 10.1007/s00190-009-0333-2.
- Kurtenbach, E., Mayer-Gürr, T. and Eicker A. (2009): Deriving daily snapshots of the Earth's gravity field from GRACE L1B data using Kalman filtering, *Geophys. Res. Lett.*, 36, L17102, doi:10.1029/2009GL039564.
- Kurtenbach, E., Eicker, A., Mayer-Gürr, T., Holschneider, M., Hayn, M., Fuhrmann, M., Kusche, J. (2010): Improved daily GRACE gravity field solutions using Kalman smoother, submitted to *Journal of Geodynamics*.
- Ilk, K.H., Löcher, A., Mayer-Gürr, T. (2006): Do we need new gravity field recovery techniques for the new gravity field satellites? *Proceeding of the VI Hotine-Marussi Symposium of the Theoretical and Computation Geodesy: Challenge and Role of Modern Geodesy*, May 29 – June 2, 2006, Wuhan, China.
- Lemoine, J.-M., Bruinsma, S., Loyer, S., Biancale, R., Marty, J.-C., Perosanz, F. and Balmino G. (2007): Temporal gravity field models inferred from GRACE data, *Adv. Space Res.*, 39, 1620– 1629, doi:10.1016/j.asr.2007.03.062.
- Macrander, A., Böning, C., Böbel, O., Schröter, J. (2010): Validation of GRACE Gravity Fields by in-situ Data of Ocean Bottom Pressure, in: F. Flechtner, T. Gruber, A. Guentner, M. Manda, M. Rothacher, T. Schöne, J. Wickert (Eds.), *System Earth via Geodetic-Geophysical Space Techniques*, Springer, ISBN (Print) 978-3-642-10227-1, DOI: 10.1007/978-3-642-10228-8, 2010.
- Mayer-Gürr, T. (2006): *Gravitationsfeldbestimmung aus der Analyse kurzer Bahnbögen am Beispiel der Satellitenmission CHAMP und GRACE*, dissertation, Institute for Geodesy and Geoinformation, University of Bonn, Germany.
- Mayer-Gürr, T., Kurtenbach, E., Eicker, A. (2010): ITG-Grace2010 gravity field model. <http://www.igg.uni-bonn.de/apmg/index.php?id=itg-grace2010>.
- Mayer-Gürr, T., Eicker, A., Kurtenbach, E., Ilk, K.-H. (2010): ITG-GRACE: Global Static and Temporal Gravity Field Models from GRACE Data., in: F. Flechtner, T. Gruber, A. Güntner, M. Manda, M. Rothacher, T. Schöne, J. Wickert (Eds.), *System Earth via Geodetic-Geophysical Space Techniques*, Springer, ISBN (Print) 978-3-642-10227-1, DOI: 10.1007/978-3-642-10228-8, 2010.
- Moritz, H. (1980): *Advanced Physical Geodesy*. Wichmann, Karlsruhe.
- Research Department ECMWF (2008): *Iifs documentation – part iii: Dynamics and numerical procedures (cy33rl)*. <http://www.ecmwf.int/research/iifsdocs>.
- Shabanloui, A. (2008): *A new approach for a kinematic-dynamic determination of Low satellite orbits based on GNSS observations*, dissertation, Institute for Geodesy and Geoinformation, University of Bonn, Germany.
- Steigenberger, P., Rothacher, M., Dietrich, R., Fritsche, M., Rulke, A., Vey, S. (2006): Reprocessing of a global GPS network, *Journal of Geophysical Research* 111, doi:10.1029/2005JB003747g.

Improved Acceleration Modelling and Level 1 Processing Alternative for GRACE

Peterseim N. (1), Schlicht A. (2), Flury J. (3)

(1) Institut für Astronomische und Physikalische Geodäsie, Technische Universität München, Arcisstr. 21, 80333 München, nadja.peterseim@bv.tum.de

(2) Forschungseinrichtung Satellitengeodäsie, Technische Universität München, Arcisstr. 21, 80333 München, schlicht@bv.tum.de

(3) Institut für Erdmessung / Centre for Quantum Engineering and Space-Time Research QUEST, Universität Hannover, Schneiderberg 50, 30167 Hannover, flury@ife.uni-hannover.de

1. Introduction

GRACE is a dual satellite mission for measuring the gravity field of the earth and its temporal changes. The spacecrafts follow each other about 220 km apart on a near circular and polar orbit. The satellites are interconnected by a K-band microwave link measuring the exact separation distance and its rate of change to an accuracy of about $1\mu\text{m/s}$. In order to take into account all non-gravitational forces, both spacecrafts are equipped with accelerometers. The accuracy of these sensors is 2 magnitudes better than in the previous mission CHAMP. However, maybe because of the sensitivity of these sensors, the observed signal contains several effects which are not sufficiently understood. Some of them are related to switching events in electric circuits, like heater switching and current changes in magnetic torquers. Other signatures, so called »twangs«, could up to date not be clearly resolved or correlated with any switching process. However, investigation and discussions are ongoing whether clanks or vibrations are the cause for these signatures.

2. Modelling of accelerometer spikes due to current changes in the magnetic torquers

If a source of a signature is identified, the spikes on the accelerometer can be modelled by superimposing the 10Hz accelerometer signal of many of these events and fitting the signal

waveform. This procedure is allowed because the timing of the original signal is known and the 10 Hz measuring rate matches to the transfer function. This approach has already been used for heater switching events and is now translated to the current changes in the magnetic torquer coils.

The magnetic torquers are used for attitude control and maintenance of the satellite. In combination with the cold-gas thrusters and a processing unit onboard of the satellite the Attitude and Orbit Control System (AOCS) is formed. By changing the amplitude of the current through the magnetic coil of the magnetic torquer the magnetic moment evoked by the torquer is changed and the torsional moment acting upon the spacecraft in combination with earth magnetic field is varied.

With a significant quantity of both accelerometer and magnetic torquer data the spikes in the accelerometer data evoked by current changes in the torquer can be empirically modelled. For each current step a model needs to be determined – in our case we chose to round the currents given before and after the current change to the nearest integer milliampère in order to keep the number of models manageable. With these models a time-series of spikes evoked by magnetic torquer current changes can be computed. The computed time-series can be used to reduce these spikes in accelerometer (cf. section 4).

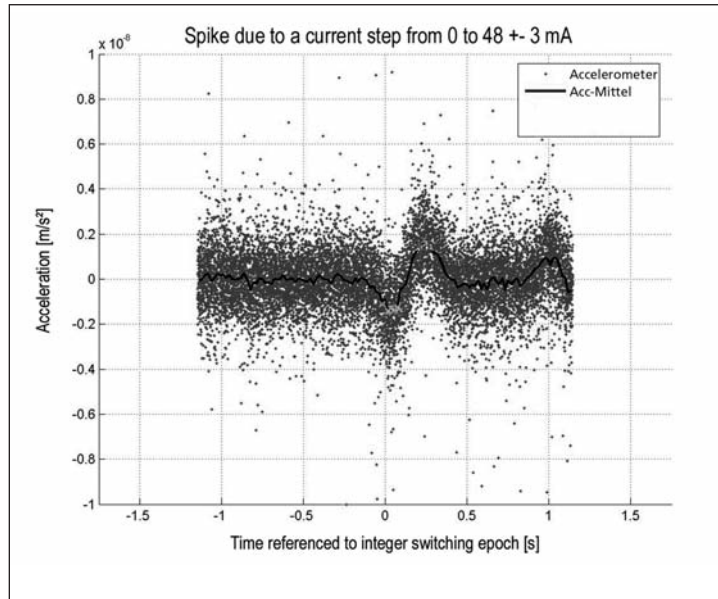


Figure 1: Spike in along track accelerometer data due to current change from 0 to 48 mA in magnetic torquer 1 (Peterseim 2010).

Figure 1 shows an accelerometer signal of GRACE A concerning to a typical current step in magnetic torquer 1 (oriented along track) from 0 to 48 mA. The red dots are the superimposed accelerometer data referenced to the integer switching epoch given in the magnetic torquer data. A spike typically consists of two peaks, whereas the order is reversed for negative current changes.

3. Characterisation of twangs

As the cause for the occurrence of twangs is not known up to now, we began our study of these accelerometer spikes by a characterisation of their signal form and their spatial and temporal occurrence.

We identify a twang in accelerometer data by computing the ratio of the RMS of a 10s interval in accelerometer data with the RMS of the following 10s interval. If the ratio exceeds a set threshold, which is 1.4 in our case, we assume that there must be a twang in accelerometer data. We proceeded with this approach in 1s steps. Any data that could be affected by thruster activation was not considered as twang.

If a significant time-span of accelerometer data is considered, geographical correlation become

obvious (cf. figure 2). Furthermore either the season, the local time, the orbit, or all have a significant impact onto the distribution of twangs. In figure 2, the twangs as occurring in the winter months of 2008 (January, February, November and December) at GRACE B are shown. Geographical correlations, and some correlation with earth magnetic field in the northern hemisphere, are obvious. The red dots are twangs where the first peak is negative, the white dots are twangs where the first peak is positive. Some signatures, with respect to the orientation of the first peak of the spike, appear to be distinct and clearly separated from each other. Here it is already obvious that there are different types of twangs involved, which can be correlated to the spatial occurrence.

Investigation concerning the correlation, distribution and origin of twangs are still ongoing.

4. Level 1 processing alternative

In this part of the project, we want to answer the questions which amplitudes and frequencies of these effects mentioned in the previous sections remain after the pre-processing and filtering applied in the Level 1 accelerometer processing (Wu *et al.* 2006), and whether the remaining amplitudes affect the gravity field results.

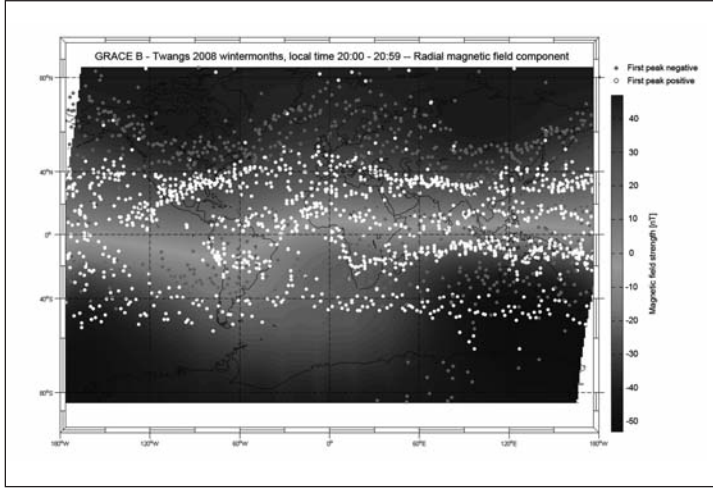


Figure 2: Twangs in winter 2008 in GRACE B vs. radial component of magnetic field of earth determined by GRACE onboard magnetometer.

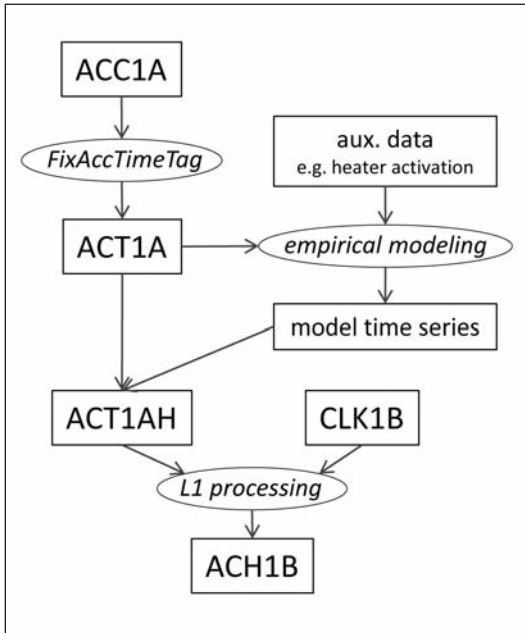


Figure 3: Modified Level 1 accelerometer data processing sequence taking into account empirically modelled time series of satellite-induced effects.

The general method is the following (see Fig. 3): we take effects for which empirical modeling at the epochs of 10 Hz Level 1a accelerometer data is available. The modeling results are subtracted from a time-tag corrected intermediate Level 1A product named ACT1A (Kruizinga 2010). Then, Level 1 processing is applied to the reduced data using software described in Frommknecht et al. (2006), see also Frommknecht and Schlicht (2010). The resulting alternative Level 1b accelerometer data are examined, and introduced in the gravity field estimation process.

To date, the procedure has been applied to compute Level 1b accelerometer data reduced for heater switching spikes for a period of 4 months (January to April 2008). Results are named ACH1B data. An example of a short time series is shown in Fig. 4.

5. Conclusion

We are now able to provide an alternative accelerometer level 1B dataset where the heater spikes are eliminated. As soon as the modelling of the accelerometer signals due to current changes in the magnetic torquer on GRACE B is done a dataset with reduced magnetic torquer spikes can be prepared.

Furthermore, we showed that the spatial distribution of twangs appear to follow significant patterns, which vary with respect to the local time and season or orbit. Once the cause for some or all twangs is known, depending on how many types of twangs can be clearly identified and associated, it might be possible to model some twangs. The models can then be used like the models in accelerometer data for spikes due to heater and magnetic torquer switching events.

Acknowledgements

The authors would like to thank the GRACE Science Team for overall support, and the Center for Space Research (CSR), University of Texas, as well as the GeoForschungsZentrum

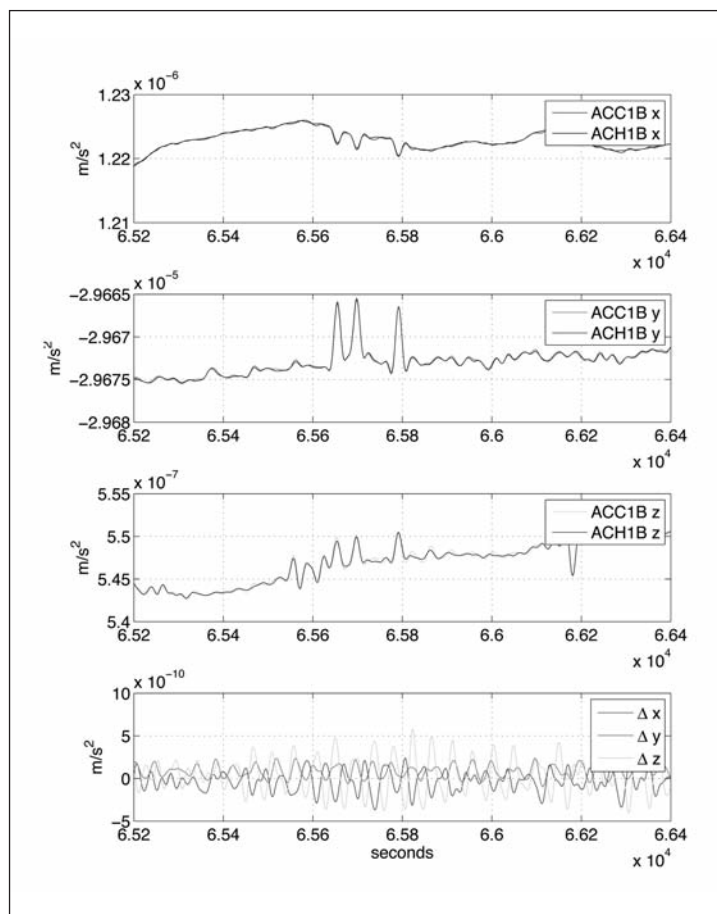


Figure 4: ACH1B acceleration data obtained by reducing heater switching spikes are smoother than the original ACC1B data. The upper three panels show the three accelerometer axes, referring to Science Reference Frame. Differences ACH1B-ACC1B (bottom panel) are typically up to $5 \times 10^{-10} \text{ m/s}^2$. The larger peaks in the middle of the example time series are due to thruster activations. Data are from GRACE A, 2007-07-15

Potsdam (GFZ) for providing the data our studies are based upon. Furthermore, we would also like to thank GSOC. The Bundesministerium für Bildung und Forschung (BMBF, German Federal Ministry of Education and Research) is acknowledged for the financial support of this research within the Lotse-CHAMP/GRACE project (03G0728C) of the GEOTECHNOLOGIEN Programme.

References

Flury J, Bettadpur S, Tapley BD (2008) Precise accelerometry onboard the GRACE gravity field satellite mission, *Adv Space Res* 42:1414–1423, DOI: 10.1016/j.asr.2008.05.004
 Frommknecht B, Schlicht A (2010)

Frommknecht B, Fackler U, Flury J (2006): Integrated Sensor Analysis GRACE, in: Flury J, Rummel R, Reigber C, Rothacher M, Boedeker G, Schreiber U (eds.), *Observation of the Earth System from Space*, pp. 99-114

Hudson D (2003): In-Flight Characterization and Calibration of the SuperSTAR Accelerometer, Master Thesis, Center for Space Research, The University of Texas at Austin

Kruizinga G (2010) personal communication

Peterseim N (2010): Acceleration Disturbances onboard of GRACE Satellites due to Magnetic Torquers; Diploma thesis, Institut fuer Erdmessung, Leibniz Universitaet Hannover

Wu SC, Kruizinga G, Bertiger W (2006) Algorithm Theoretical Basis Document for GRACE Level-1B Data Processing V1.2, NASA/JPL GRACE 327-741

GRIMM-2: The parent magnetic field model for an IGRF candidate model

Lesur V., Rother M., Hamoudi M., Wardinski I., Lühr H., Michaelis I., Rauberg J.

Helmholtz Centre Potsdam, GFZ German Research Centre for Geosciences

Abstract

The International Geomagnetic Reference Field (IGRF) is a very frequently used model of the Earth's main magnetic field by both the science community and the industry. This model is updated every five years. We present here the second generation of the GRIMM magnetic field model that was derived to contribute to the IGRF-11. The model has been developed from a newly, reprocessed CHAMP satellite data set covering nearly 10 years. It has a temporal and spatial resolution significantly improved compared to previous models.

1. Introduction

The CHAMP satellite has provided very high quality vector measurements of the Earth's magnetic field, which have led into numerous studies about its external and internal sources. In 2009, the satellite has been orbiting at very low altitude (around 320km), and, because the external magnetic field perturbations have been small due to a very long period of low solar activity, this has been particularly beneficial for studies of internal fields. Furthermore, fully processed CHAMP vector data have been made available up to 2009.5, in order to provide the best possible data set for the preparation of the 11th version of the International Geomagnetic Reference Field, IGRF (*Finlay et al., 2010*).

The IGRF is a model of the main Earth's magnetic field that is made of a series of single epoch snapshot models, five years apart, and a predictive Secular Variation (SV) model. For the preparation of the new version of the IGRF, different institutes over the world have been pro-

posing candidates to the 2005 and 2010 snapshot field models and for the SV predictive model covering the epochs 2010-2015. In our case, these candidates have been derived from a parent model: the second version of the GFZ reference internal magnetic model --GRIMM-2 (*Lesur et al., 2010*).

The Earth's core magnetic field is the most significant source of the Earth's main field. The contribution from the large-scale lithospheric field, although it cannot be separated from the core field contribution by analyzing magnetic data alone, is generally assumed to be negligible for the largest wavelength of the observed field. In the following we will therefore not distinguish between »core« and »main« magnetic fields.

We present in this manuscript some aspects of the second generation of the GRIMM model and the associated candidates to the IGRF. The main difficulty in building models of the Earth's main magnetic field is to deal with the other source contributions to the data. For main field modeling, these contributions are mainly those of the large-scale external field of magnetospheric origin, and the field generated at high latitudes in the polar ionosphere. The fields generated at mid latitudes in the dayside ionosphere are vanishing at night time (their induced internal counterparts are however persisting during the night). These mid-latitude ionospheric fields can therefore being ignored if night time data are used. To avoid as much as possible the leakage of other ionospheric and magnetospheric contributions into core magnetic field models, the only solution lies in

a careful data selection and appropriate modeling techniques. The GRIMM magnetic field model is based on a new approach of the data selection that has proved to lead to robust model of the Earth's main magnetic field.

We start in the next section in presenting some aspects of the data processing and its recent developments. Then, in the third section, elements of the GRIMM-2 model are presented. Finally, the fourth section is dedicated to the derivation of the IGRF candidates. We conclude in the last section.

2. Developments in the CHAMP magnetic field data processing

The main developments in terms of data processing have been made to improve the algorithm for the precise attitude determination of the magnetometers. In order to take full advantage of the fluxgate resolution, attitude knowledge with an arc-second precision is required. The scheme can be divided into three parts: First, the initial In-flight-Calibration procedure and the Star Camera (ASC) standard processing have been partly recoded, migrated to a new operating system, and upgraded by correlating irregularities with satellite house-keeping readings and other recorded external events. Second, the transformation routine from satellite into the Earth-Centered-Earth-Fixed (ECEF) NEC (North-East-Center) system has been improved, and validated. Last, the time series describing the observed bending of the optical bench (i.e. variation of the Euler Angles between magnetometer and ASC reference frame) has been validated by an independent modeling approach that co-estimates the time dependent Euler Angles and magnetic model coefficients. Further details are given below.

The original standard version of the ASC processing is leading to the CH-ME-2-ASC-BOOM products. The improvement of this ASC processing is still ongoing, but re-coding and migration to a new platform is finished. Additionally, considering data from the second pair

of ASC sensors in CHAMP's body, during this ASC processing, permits most of the time to control the results, but sometimes also filling the data gaps.

A validation of the initial transformation from the ASC-sensor to the ECEF coordinate system by an alternative computing path using an external astronomical library -- the »SOFA« library (IAU SOFA Center, 2010) -- was successfully done. Another step towards a robust processing to hold the precision of the attitude information was to overcome the discontinuation of the Bulletin B of the International Earth Rotation and Reference Systems Service (IERS Message 144). The integration of slightly different earth rotation parameters from the Bulletin B into the processing was done and was adopted as new standards.

For the validation of the time dependent Euler Angle a new, quaternion based, approach where a magnetic field model and the angles are co-estimated, was developed, coded, and tested on synthetic data. The approach has been also tested on real CHAMP data products and compared with solutions from other modeling groups. The new approach has proved to converge faster than an algorithm directly based on the angles. The quaternion-based algorithm benefits from the fairly simple form of the Hessian matrix. The field-modeling algorithm, on which this approach was developed, is the GRIMM inversion family algorithm.

Figure-1 shows that the GRIMM based Euler Angle estimation provide consistent results for various evaluation window lengths and data sets (i.e. either complete data set or selected data set). These results are also inside the expected deviation from the Euler Angle reference. This agreement is somewhat weakened for the early, more disturbed periods (see left frame in Figure-1 where a phase shift appears. This phase shift is not yet well understood and is under further investigation).

The determination of Euler Angle rotations in the framework of the CHAMP data processing

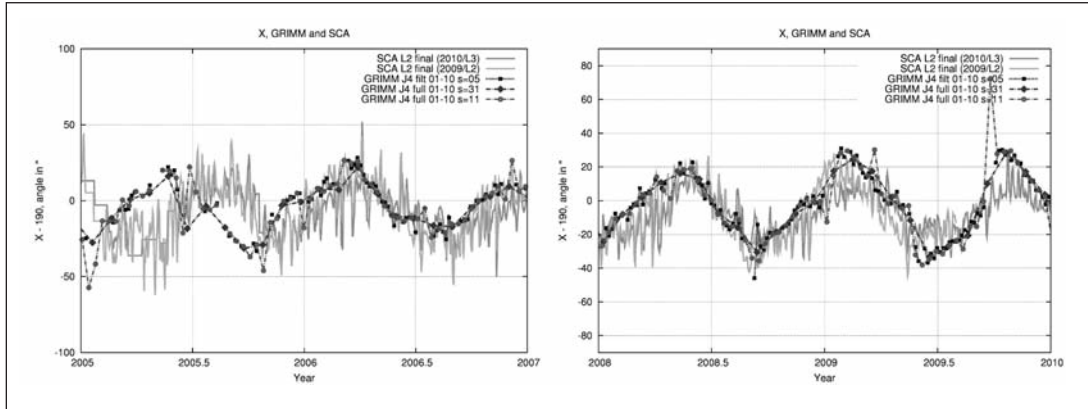


Figure 1: Late period of CHAMP mission period with SCA (POMME family based, personal communication with Stefan Maus) Euler Angle estimation (Gray, 2009 and 2010 version) compared with the newly developed, GRIMM based approach with various window sizes.

is a decisive step towards the challenging data processing of the multi-satellite ESA mission Swarm. The implementation can take data from other sources than CHAMP readings into account, either observatory data, as already tested, or other satellites (as required option for the multi-satellite Swarm project ahead).

The end of the active mission of CHAMP in September 19, 2010 triggered the preparations for the first full reprocessing of the vector magnetic field data with the currently available stage of the processing functionality.

3. The GRIMM-2 model

The model GRIMM-2 has been built from CHAMP satellite magnetic vector data only, and observatory hourly mean vector data. The version 51 Level-2 CHAMP satellite data set has been used. It spans the epochs 2001.0 to 2009.58 and includes improved time dependent FGM-ASC orientation corrections (i.e. orientation of the fluxgate magnetometers relative to the reference frame defined by the star cameras). The observatory hourly mean data have been used only up to 2009.0.

The data selection process differs depending on the data latitude. At mid and low latitudes, data are selected for magnetically quiet times as characterized by magnetic indices, night times, and X,Y components only in the Solar-Magnetic (SM) system of coordinates. At high

latitudes, the magnetic data are selected also for magnetically quiet periods, but at all local times, and for all three components in the usual North, East, Down (NEC) system of coordinates. It has been shown that such a selection technique leads to robust models of the core magnetic field. The underlying ideas are:

- 1) Not to use, at mid latitudes, data along the magnetic dipole axis (Z-SM axis) in order to avoid the magnetospheric dominant contributions generally attributed to the ring current.
- 2) Using all local time data at high latitudes to avoid large data gaps associated with the 6 month long summer day-light periods over the auroral regions.

The model parameterization includes a large-scale field of internal origin – i.e. the core field, the lithospheric field up wavelengths around 800km, and a large-scale external field with its associated induced counterpart. The core field is parameterized in time using B-splines of order six. The lithospheric field is assumed constant in time whereas the external field is parameterized in time by piece-wise linear polynomials, with knots three months apart. This is completed, for the rapid temporal variations of the external field and their induced counterparts, by a parameterization based on the VMD index (Thomson and Lesur, 2007).

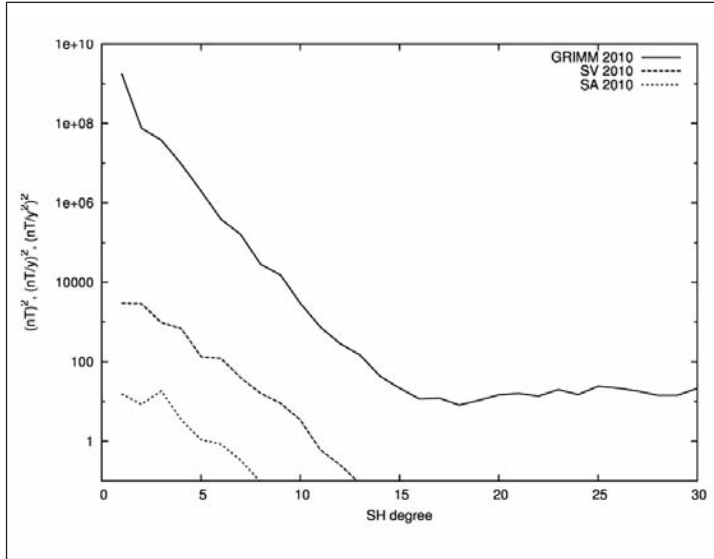


Figure 2: Power spectra of the GRIMM-2 magnetic field calculated at the Earth's reference radius for year 2010. Presented are the spectra of the core field snapshot, its SV and acceleration.

The model inversion process has been regularized by minimizing a measure of the model third temporal derivative. This is compatible with the order six B-spline representation used. In order to improve the robustness of the model near the end of the data time span, the second temporal derivative has been minimized at the model end points. These constraints have been applied at the core-mantle boundary such that the derived model is optimized there. This point is one of the significant differences with the first version of the GRIMM model. With these constraints the GRIMM-2 model presents a relative smooth temporal behavior.

Overall, the data set represents more than 7 millions data values, and the model itself consists of around 6300 parameters. To solve this problem, a code has been developed over several years in a parallel computing environment, nonetheless several days are required to derive a model using the iterative re-weighted least squares approach.

Figure 2 presents the magnetic field energy of the static core field, its SV and acceleration, as a function of the Spherical Harmonic (SH) degree, all calculated at the Earth reference radius (6371.2 km). All present the expected converging spectra. Above SH degree 13, the SV is very small and cannot be resolved. The static

field spectra flatten because of the contribution of the lithospheric field. Although the magnetic field and its SV are not changing too rapidly with time, it has been observed that the acceleration evolved rapidly on annual time scales. This causes significant difficulties for predicting the SV evolution for the coming five years.

Figure 3 presents the vertical down component of the core magnetic field, out of the GRIMM-2 model, calculated at the Earth surface for year 2010. In Figure 3 the magnetic equator where the vertical component vanishes is clearly visible. Also visible is the weakness of the field in the Southern part of the Atlantic Ocean and South America. This feature is associated at the core-mantle boundary with a patch of reverse flux. In Figure 4, one can see that the SV is the largest at mid latitudes. The strength of the vertical down component decreases rapidly in the eastern part of the Atlantic Ocean, while it increases in the north of the Indian Ocean. The SV is weak over the Pacific Ocean.

3. IGRF candidates

Three contributions were required for the IGRF candidates:

- 1) a snapshot of the field for year 2005,
- 2) a snapshot of the field for year 2010,

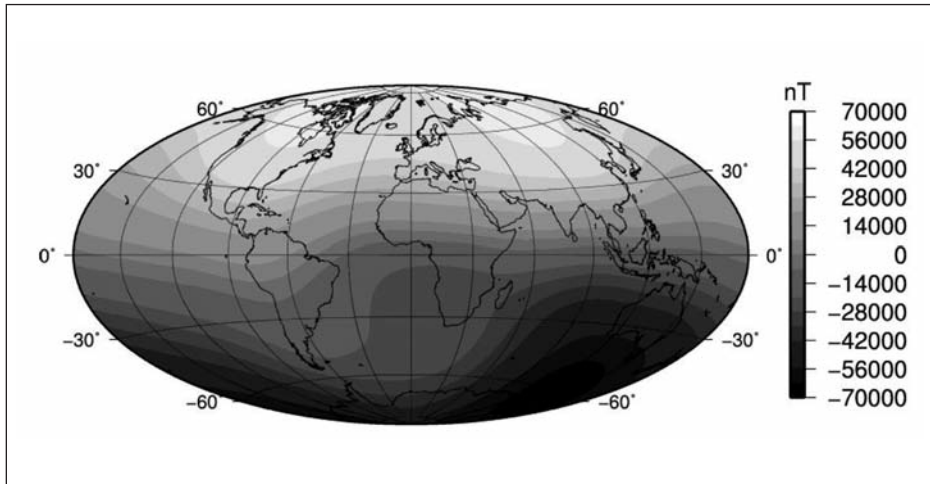


Figure 3: Vertical down component of the main magnetic field estimated using GRIMM-2 model, for the year 2010 and at the Earth's surface.

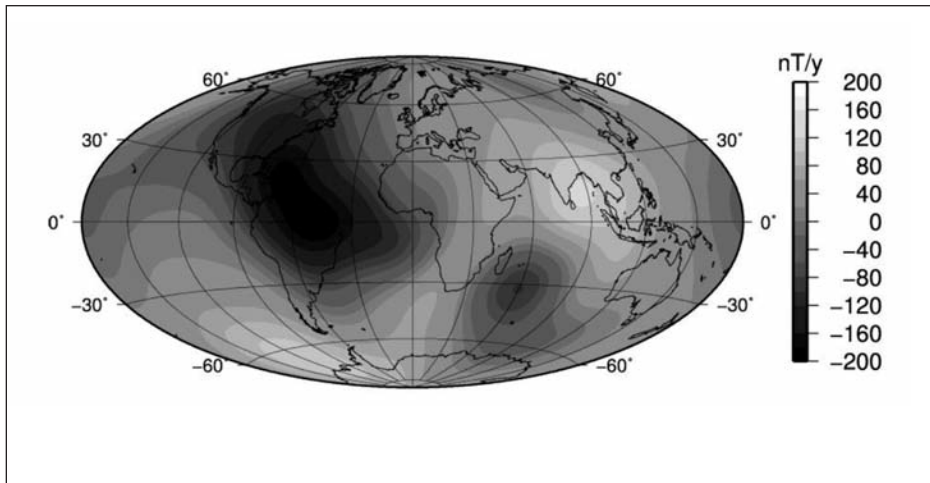


Figure 4: Vertical down component of the main magnetic field secular variation estimated using GRIMM-2 model, for the year 2010 and at the Earth's surface.

3) a predictive SV variation for 2010-2015. Because the data set used in the GRIMM-2 model extend only up to 2009.5, it has been necessary to extrapolate the model in order to derive the 2010 snapshot and the 2010-2015 SV models. A short description is given below.

A candidate for the Definitive Geomagnetic Reference Field (DGRF) model for epoch 2005.0 has been derived by averaging the GRIMM-2 model between 2004.5 and 2005.5. This was done in order to improve the robustness of the Gauss coefficient estimates. The

resulting model has been truncated to SH degree 13. Compared with the GRIMM-2 model at epoch 2005, the DGRF candidate does not differ by more than 0.25nT for any of the Gauss coefficients. The maximum difference is reached for the coefficient g_1^1 .

A candidate model for the IGRF for epoch 2010 has been derived by extrapolating the GRIMM-2 Gauss coefficients for year 2009 using the SV values at the same epoch – i.e. the acceleration between 2009 and 2010 has been simply ignored. This approach was used because the

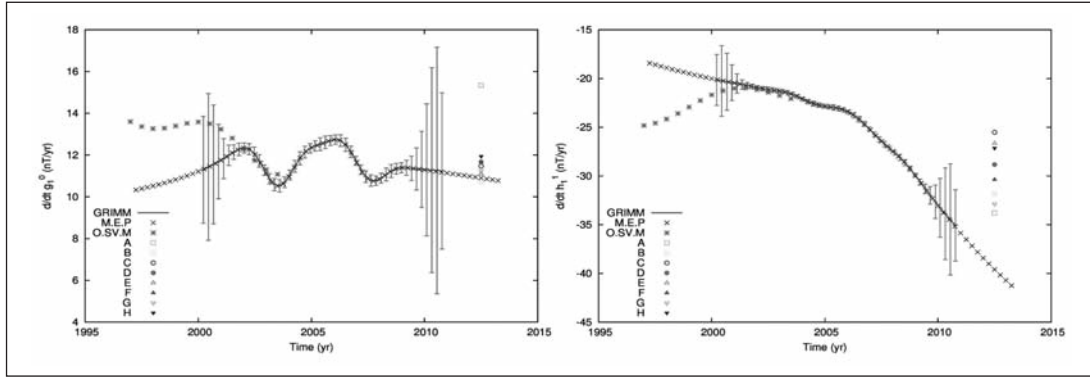


Figure 5: SV coefficients g_1^0 and h_1^1 as estimated by various field models, candidates and extrapolation processes where: GRIMM are the estimated coefficients with error-bars as obtained by the »GRIMM-2« parent model, »M.E.P« are the estimates obtained by applying the maximum entropy method, »O.S.V.M« are the coefficients as obtained from a 50 years field model derived from monthly mean observatory data. The candidate estimates are labeled from »A« to »H«.

GRIMM-2 acceleration model after 2009 is not robust due to the lack of data after 2009.5. Compared with the model directly estimated from GRIMM-2, the IGRF candidate differs by 1.5 nT for the Gauss coefficient h_1^1 . The differences stay below 1nT for any other coefficients.

Regarding the SV predictive model, SV Gauss coefficients variation estimates were derived by linearly interpolating the individual Gauss SV coefficients given by GRIMM-2 over the 2001, 2009.5 periods. These linear interpolations were used to extrapolate the SV coefficients from 2009 to epoch 2012.5.

Figure 5 illustrates the difficulties in predicting the SV over a five-year period. Although the SV is robustly estimated when data are available, the error-bars on GRIMM-2 Gauss coefficients show large uncertainties in these estimates as soon as they are associated with an extrapolation process. The Maximum Entropy Prediction technique (MEP) is often considered as the most reliable extrapolation technique, but when compared with true estimates coming from another model – here the OSVM model (Lowes, 2004) – it is clear from the Figure 5, that the MEP technique may fail. The candidate models, numbered from A to H, differ significantly from each other. Our candidate derived from GRIMM-2 is the G model.

Information about candidate models submitted to DGRF (2005), IGRF (2010) and predictive-SV (2010 to 2015) can be downloaded from the websites:

<http://www.ngdc.noaa.gov/AGA/vmod/candidatemodels.html>

<http://www.ngdc.noaa.gov/AGA/vmod/igrf.html>

4. Conclusion

We have briefly presented some of the developments associated with the processing of the CHAMP magnetic vector data. The main progresses have been made in improving the processing of the ASC data. The re-estimation of the Euler Angles using a new independent algorithm shows a good agreement between the different estimates of these angles. The remaining differences are only minor and well inside the expected accuracy of the angles.

We have also presented the second generation of the GFZ Reference Internal Magnetic Model (GRIMM-2). As for the first generation, the model has been derived to provide an accurate description of the core field, its temporal behavior and in particular of the secular acceleration. The GRIMM-2 model has been compared and tested again a direct concurrent – CHAOS-2 (Olsen et al., 2009) — and proves to be robust. The model is accurate over the data

time span, but may not be an accurate representation of the Earth's main field outside this time period. The GRIMM-2 model was used as a parent model to derive the GFZ candidate to the IGRF-11.

Acknowledgments

We would like to acknowledge CHAMP mission operated and supported by GFZ German Research Centre for Geosciences, Potsdam, the German Aerospace Center (DLR) and German Federal Ministry of Education and Research (BMBF) and to thanks the institutes and observatories providing data and indices. This work was done with the financial support of GEOTECHNOLOGIEN project 03G0728A.

References

Finlay, C. C., S. Maus, C. D. Beggan, T. N. Bondar, A. Chambodut, T. A. Chernova, A. Chulliat, V. P. Golovkov, B. Hamilton, M. Hamoudi, R. Holme, G. Hulot, W. Kuang, B. Langlais, V. Lesur, F. J. Lowes, H. Luehr, S. Macmillan, M. Manda, S. McLean, C. Manoj, M. Menvielle, I. Michaelis, N. Olsen, J. Rauberg, M. Rother, A. Tangborn, L. Tøffner-Clausen, E. Thebault, A. W. P. Thomson, I. Wardinski, Z. Wei and T. I Zvereva, International Geomagnetic Reference Field: The Eleventh Generation, *Geophys. J. Int.*, 2010, accepted.

Lesur, V., Wardinski, I., Manda, M. GRIMM: the GFZ Reference Internal Magnetic Model based on vector satellite and observatory data, *Geophys. J. Int.*, 173, 2, 382-394, 2008.

Lesur, V., I. Wardinski, M. Hamoudi and M. Rother, The second generation of the GFZ Reference Internal magnetic Model: GRIMM-2, *Earth Planets Space*, 2010, accepted.

Lowes, F. J., and N. Olsen, A more realistic estimate of the variances and systematic errors in spherical harmonic geomagnetic field models, *Geophys. J. Int.*, 157, 1027-1044, doi: 10.1111/j.1365-246X.2004.02256.x, 2004.

Olsen, N., M. Manda, T. J. Sabaka, and L. Tøffner-Clausen, CHAOS-2 -- a geomagnetic field model derived from one decade of continuous satellite data, *Geophys. J. Int.*, 1, doi: 10.1111/j.1365-246X.2009.04386.x, 2009.

SOFA, Standards of Fundamental Astronomie, IAU SOFA Center, STFC Rutherford Appleton Laboratory, Harwell Science and Innovation Campus, Didcot, Oxfordshire, OX11 0QX, United Kingdom.

Thomson, A. W. P., and V. Lesur, An improved geomagnetic data selection algorithm for global geomagnetic field modelling, *Geophys. J. Int.*, 169, 951-963, doi: 10.1111/j.1365-246X.2007.03354.x, 2007.

Wavelet Correlation Analysis of CHAMP Magnetic Field Models – WACO CHAMP Results

Schachtschneider R., Hayn M., Holschneider M.

University of Potsdam

Introduction

The purpose of the project »Wavelet Correlation Analysis of CHAMP magnetic Field Models (WACO-CHAMP)« is the calculation of the correlations for magnetic field models obtained from CHAMP magnetic field data. In a first step we developed a family of directional wavelets on the sphere that are suitable for directional analysis of geomagnetic field components (WP240). With the help of these wavelets we calculate a covariance matrix for a satellite data based geomagnetic field model to show the correlations between the data (WP250). The third task is to improve geomagnetic field modeling by using the knowledge about the correlations and filter artifacts from satellite tracks, thereby reducing the noise level of the model (WP260).

Spherical Directional Poisson Wavelets

The basic idea of Spherical Directional Poisson Wavelets (SDPWs) is to take a horizontal derivative of a symmetric function on the sphere (for details see Hayn & Holschneider, 2009). The function chosen here is the Poisson kernel.

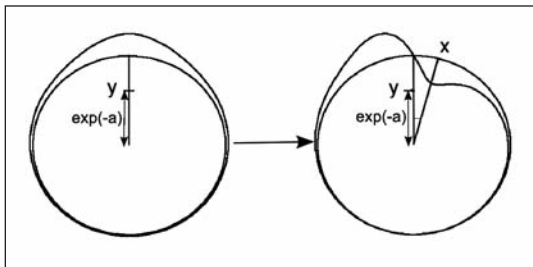


Figure 1: Simplified idea of the wavelet construction. The wavelets are lateral derivatives of a symmetric kernel on the sphere.

Figure 1 shows the principle in 2D. On the left panel is the Poisson kernel on the sphere. The right panel shows the horizontal derivative.

On the Sphere the derivative direction determines the direction that can be analyzed with the resulting wavelet; it is perpendicular to the direction of the derivation. The wavelet is then rotated on the sphere to the location that is to be analyzed using Euler rotations. It is defined as

$$g_a^{\rho, n}(\vec{x}) = a^n \partial_\theta^n (R_{\vec{y}}(\theta, \rho) P^{\text{int}})(\vec{x}, \vec{y})_{\vec{y} = e^{-\rho} \vec{e}_z}$$

where a is the scale, n is the order of the wavelet, θ is the direction of the derivative, ρ is the axis of rotation for the Euler-rotation of the wavelet to the point of analysis, and P^{int} is the Poisson kernel defined as

$$P^{\text{int}}(\vec{x}, \vec{y}) = (2\Psi_{\vec{y}}^1 + \Psi_{\vec{y}}^0)(\vec{x})$$

with

$$\Psi_{\vec{y}}^0(x) = \frac{1}{|\vec{x} - \vec{y}|},$$

$$\Psi_{\vec{y}}^1(\vec{x}) = |y| \frac{P_1(\widehat{\vec{x} - \vec{y}} \cdot \hat{y})}{|\vec{x} - \vec{y}|^2} = \frac{(\vec{x} - \vec{y}) \cdot \vec{y}}{|\vec{x} - \vec{y}|^3}.$$

With the help of the SDPWs the wavelet transform of a signal can be calculated as

$$W_{[g_a, \xi]} s(a, \xi) = \langle g_{a, \xi} | s \rangle.$$

The directional wavelet transform delivers information about the alignment of structures of an investigated field for a certain scale, i.e. the part of the signal that is aligned in a certain direction at the investigated scale. The inverse transform is defined as

$$M_{[g_a]} r = \int_0^\infty \frac{da}{a} \int_{SO(3)} d\Sigma(\xi) r(a, \xi) g_{a, \xi}$$

where r are the wavelet coefficients and $SO(3)$ is the group of rotations in R^3 .

Directional Wavelet Decomposition

With the help of the newly developed directional Poisson wavelets we performed a decomposition of the radial component of a preliminary HIREMAG lithospheric model of the geomagnetic field (Figure 2). We chose scales between 0.005 and 0.1 and decomposed the model for directions between 0 and 170 degree at 10 degrees steps. Figure 3 shows three examples of wavelet transforms at different scales and directions: scale 0.1 and direction 0 degrees (top panel), scale 0.02 and direction 90 degrees (middle), and scale 0.02 and direction 50 degrees (bottom panel). Especially the north-south striking field components (90 degrees wavelet transform) is contaminated by satellite track artifacts. In the southern regions at the transition between different data types the model is very noisy.

This wavelet decomposition is the basis for the design of a filter module on the one hand and the calculation of the full covariance matrix on the other hand. These steps are described in the following sections.

Design of a filter module

When modeling the lithospheric field up to a high spherical harmonic degree the noise in the satellite data becomes a serious problem. The amplitude of the amplified noise eventually reaches magnitudes of the signal itself and there is a well known patterns of stripes along the satellite tracks. They result from unmodeled ionospheric sources. Especially field aligned currents near the poles produce noise that is problematic in inversion. In order to improve high resolution lithospheric field modeling these artifacts have to be removed. As they appear along satellite tracks and thus are aligned in a certain direction they can be separated from the signal by extracting the according direction in the wavelet transform. As the wavelet transform is a local analysis tool it is also possible to filter only those regions that are contaminated by noise. This is useful since the noise contamination is different in different areas of the globe and different data sets are used in mid latitudes and near the poles.

The Covariance Matrix for a Field Model

It is the aim of this work to analyze correlations in a field model that was computed from CHAMP geomagnetic satellite data. Therefore we chose the MF4 model for our calculations. This model represents the visible part of the

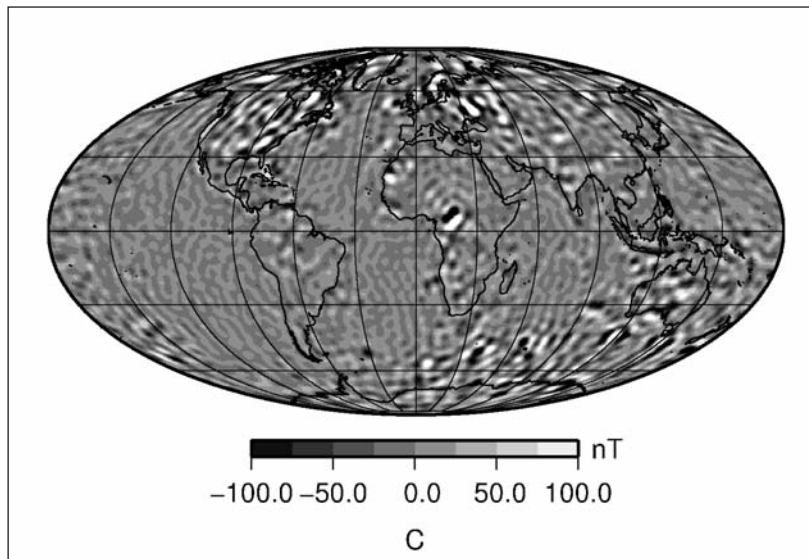


Figure 2: Preliminary HIREMAG lithospheric field model of spherical harmonic degree 16-75 used for wavelet decomposition.

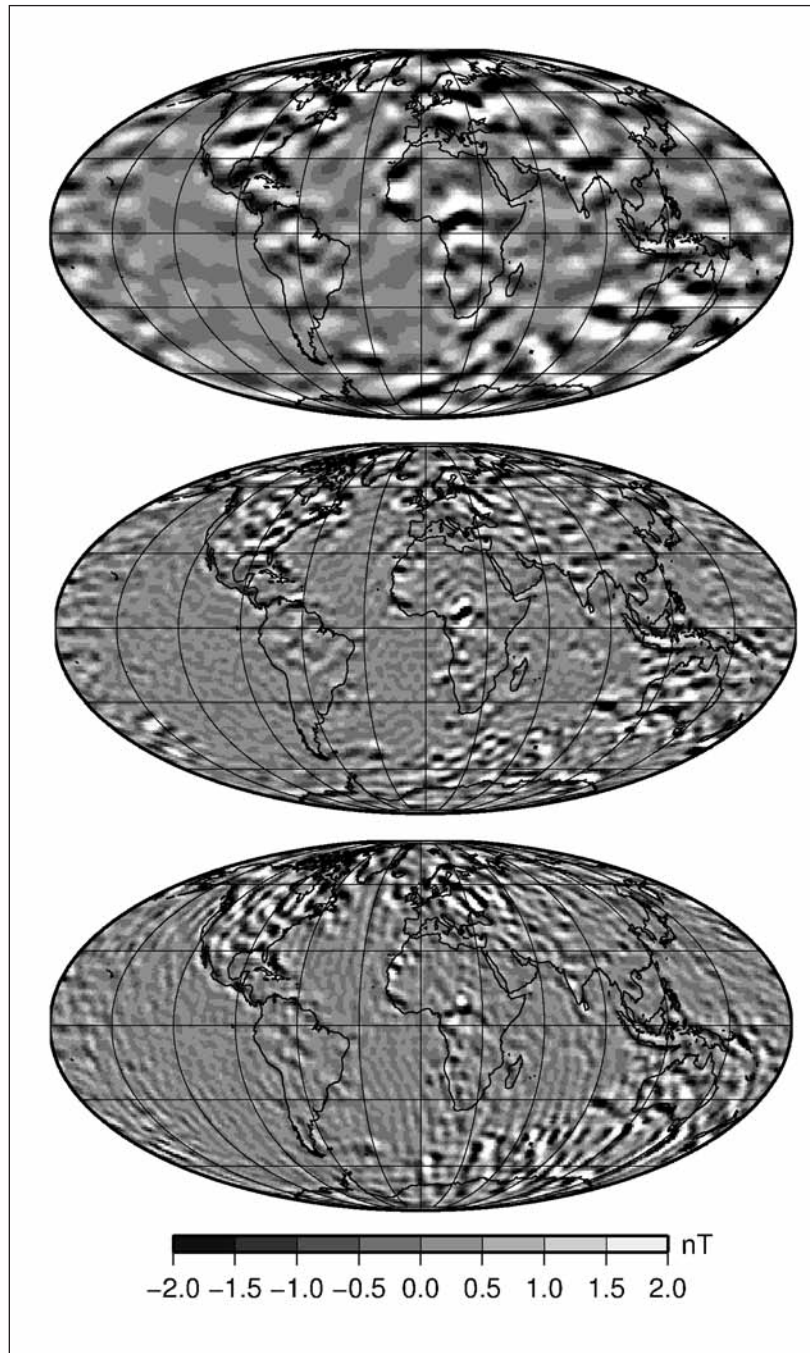


Figure 3: Examples of the wavelet decomposition for different scales and directions. For details see the text.

crustal magnetic field. It is derived from CHAMP measurements of the period August 9th, 2000 to April, 2005 and is given as spherical harmonic coefficients ranging from degree 16 to 90. The coefficients 1-15 are set to zero since the crustal field is masked by the core field for those degrees.

When trying to obtain the covariance matrix for a field model one faces the obstacle that

there is only one realization of the investigated random process. From that limited data no covariances can be calculated. One advantage of the wavelet transform is its finite correlation length. Wavelet coefficients with a distance greater than the correlation length are statistically independent. Therefore we can divide the wavelet transform into independent subdomains (Figure 4). These subdomains are taken as surrogates for independent realizations of the

stochastic process with which we can calculate covariances for the geomagnetic field model.

For each scale and direction a separate covariance matrix is obtained. These are combined to a comprehensive covariance matrix C_w in wavelet space. That comprehensive matrix in wavelet space has to be transformed back to physical space by

$$C_p = M_g C_w M_g^T,$$

where M_g is the discretized inverse directional wavelet transform operator and superscript T denotes the transposed matrix.

High-resolution modeling

The covariance matrix obtained in WP250 contains information about the correlation of the geomagnetic data in the lithospheric field model. These informations can be used as Bayesian priors for inversions of the geomagnetic field. Instead of assuming isotropic data the covariance matrix can introduce the obtained information about the anisotropy of the field. Therefore in the inversion scheme with Tikhonov regularization (Engl *et al.*, 1996)

$$\vec{m}^{est} = (A^T A + \Gamma^T \Gamma)^{-1} A^T \vec{b}$$

the Tikhonov matrix Γ is replaced by the covariance matrix C_p thus introducing the obtained a priori information.

Conclusions and Outlook

We have constructed a family of functions on the sphere that are admissible as wavelets and have directional properties. With these directional Poisson wavelets we have decomposed a preliminary geomagnetic lithospheric field model of the HIREMAG work package. We have demonstrated that noise contamination along satellite tracks can be extracted with this decomposition. We have shown a possibility to calculate the covariance matrix of the data in wavelet space for a single realization of the stochastic process by taking advantage of the

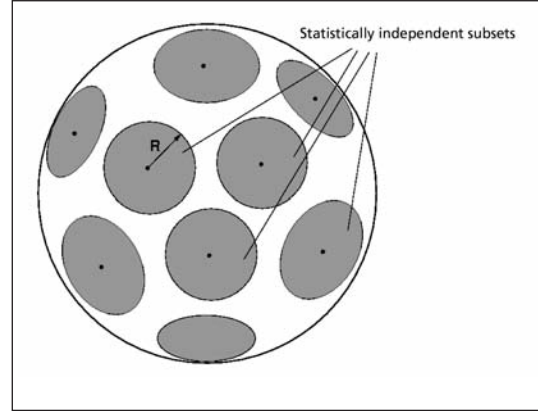


Figure 4: Scheme for the division of the wavelet transform on the sphere into independent subsets. The subsets are statistically independent if the radius, R , is larger than the correlation length of the reproducing kernel of the wavelet transform.

finite correlation length of the reproducing kernel of the wavelet transform. With these results we can calculate the covariance matrix in physical space and design a filter that helps to improve geomagnetic lithospheric field modeling by reducing the artifacts of the satellite tracks.

Acknowledgements

The project WACO-CHAMP is part of the R&D-Programme GEOTECHNOLOGIEN. GEOTECHNOLOGIEN is funded by the German Ministry of Education and Research (BMBF) and the German Research Foundation (DFG), Grant (03G0728D) WACO-CHAMP of project LOTSE-CHAMP/GRACE).

References

- Hayn, M. and Holschneider, M., 2009, Directional spherical multipole wavelets, J. Math. Phys. 50(7), doi:10.1063/1.3177198
- Holschneider, M., 1995, Wavelets: An Analysis Tool, Oxford University Press
- Engl, Heinz W. and Hanke, Martin and Neubauer, Andreas, 1996, Regularization of Inverse Problems, Kluwer Academic Publishers

Analysis and application of atmospheric data from CHAMP and GRACE

Heise S., Wickert J., Arras C., Beyerle G., Haser A., Schmidt T., Zus F.

GFZ German Research Centre for Geosciences, Potsdam, Germany

Abstract

The German geoscience satellite CHAMP (CHALLENGING Minisatellite Payload) has collected the currently longest available time series of GPS radio occultation (RO) data comprising nearly eight years. Around 570,000 occultation measurements were performed between Feb. 2001 and Oct. 2008. This time series is continued by the U.S./German GRACE (Gravity Recovery And Climate Experiment) mission. To generate a homogeneous and high quality long-term set of GPS-RO data for climatological applications and trend analyses, a consistent reprocessing is needed. Major objectives of the GEOTECHNOLOGIEN research project ATMO-CHAMP/GRACE therefore are: a) improvement of the scientific GPS RO processing software, b) consistent reprocessing of the CHAMP/GRACE GPS-RO long-term data set applying this improved software and c) the demonstration of climatological applications for the long-term data set. In this paper the status of the CHAMP/GRACE processing is overviewed and climatological applications regarding

global temperature and tropopause trends and irregularities of the ionospheric E-region are demonstrated.

1. Introduction

The GPS radio occultation (RO) remote sensing technique (e.g., Kursinski *et al.*, 1997, Yunck *et al.*, 2000) exploits atmospheric (neutral atmosphere and ionosphere) refraction and delay of GPS signals observed aboard Low Earth Orbiting (LEO) satellites (Fig.1). Observed phase path delays can be inverted to vertical profiles of bending angle, refractivity and meteorological quantities (temperature, humidity, e.g. Heise *et al.*, 2008). Main properties of the calibration-free RO technique are insensitivity to clouds and rain, global coverage and high vertical resolution. Currently, CHAMP provides the longest available consistent time series of GPS RO measurements comprising nearly eight years (e.g., Wickert *et al.*, 2009). This data set allows for the first climatological investigations based on GPS radio occultation measurements

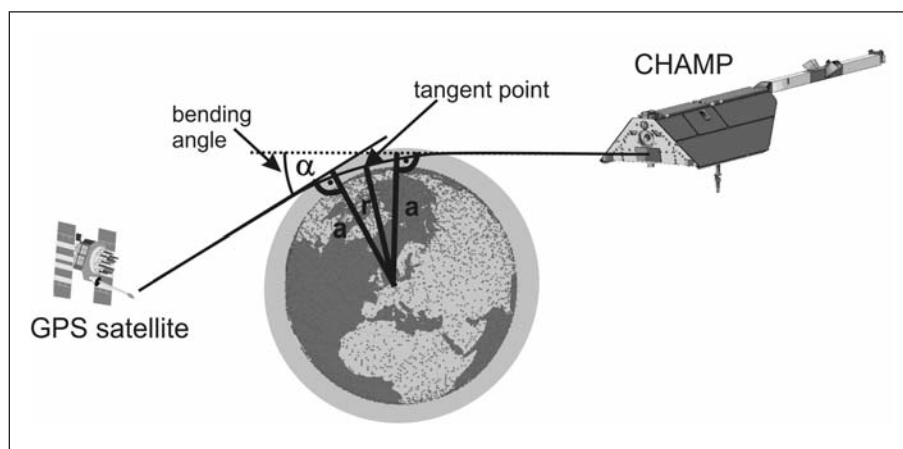


Figure 1: GPS radio occultation principle.

and is continued by GRACE-A and several following GPS RO missions (FORMOSAT-3/COSMIC, Metop, TerraSAR-X, TanDEM-X). The reprocessing activities and climatological investigations presented here are funded within the research project »Analysis of atmospheric data from CHAMP/GRACE and application for climatological investigations« (ATMO-CHAMP/GRACE) of the GEOTECHNOLOGIEN programme of the German Ministry for Education and Research.

2. Status of CHAMP and GRACE radio occultation processing

While the CHAMP mission came to its fiery end on September 19, 2010, last occultation measurements were recorded on October 4, 2008. About 570,000 GPS occultations were observed since February 2001 (see Fig.2). GRACE-A occultations are continuously activated since 2006 and are provided in near-real time to several weather services (e.g., UK MetOffice, ECMWF, NCEP, DWD) to improve their global forecasts. These activities were started within the GEOTECHNOLOGIEN research project Near-Real Time Radio Occultation (NRT-RO, Wickert, 2010). In preparation of the reprocessing of the large CHAMP/GRACE data set, the computation time has been reduced significantly by adaption of the GFZ RO analyses soft-

ware for application on Linux platforms. As a precondition for the improvement of the GPS RO processing software comprehensive inter-comparisons with analyses results from other RO processing centres (e.g. UCAR, JPL) and with independent meteorological data (e.g. ECMWF analyses or radiosonde observations) were performed. In this context, GFZ was involved in an intercomparison study of several CHAMP RO data processing centres (*Ho et al., 2009*; see Fig. 3 left). While the GFZ atmospheric products from CHAMP are in excellent agreement with other processing results (e.g. UCAR) especially in the altitude range between 10 and 25 km, a positive refractivity bias is observed above 25 km (Fig. 3). This bias will be investigated in more detail in the further course of the ATMO-CHAMP/GRACE project. Results will flow in the improved GFZ RO analyses software. Since a software change related inhomogeneity in the GFZ CHAMP atmospheric data set could be detected, a preliminary reprocessing was performed to provide a consistent CHAMP RO data set for further climatological investigations of atmospheric parameters (e.g. temperature, tropopause altitude).

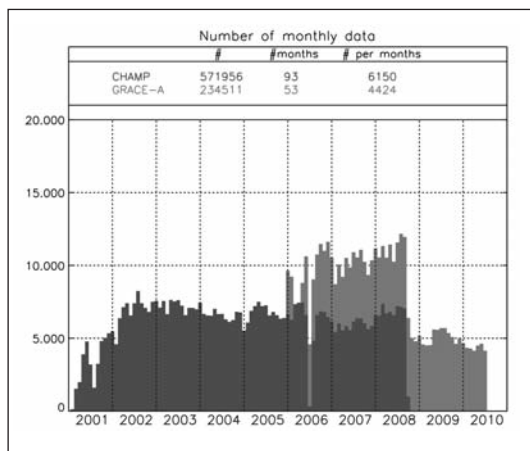


Figure 2: GFZ CHAMP/GRACE-A occultation data processing statistics 2001-2010.

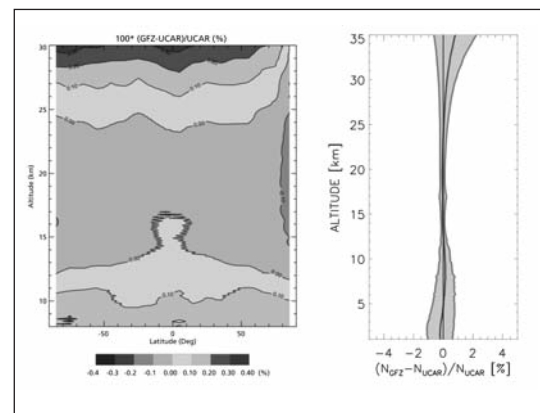


Figure 3: Left: Mean zonal refractivity difference between 2006 CHAMP results from GFZ and UCAR, from *Ho et al., 2009*; Right: Mean global difference and standard deviation between CHAMP refractivity results from GFZ and UCAR for January/February 2006.

3. Applications of atmospheric data from CHAMP and GRACE

3.1. Global temperature and tropopause trends

The upper troposphere and lower stratosphere (UTLS) is one of the key regions of the atmosphere with significant importance for the stratosphere-troposphere exchange as well as climate research. The determination of UTLS temperature and tropopause height trends are crucial for the monitoring of climate change processes. Global high-resolution temperature observations are only available from GPS radio occultation (RO) data, whereas the CHAMP mission has generated the first long-term RO data set (2001-2008) that is continued from GRACE since 2006.

De-seasonalized global monthly anomalies of tropopause heights from CHAMP/GRACE are the basis for linear trend analyses considering also Quasi Biennial Oscillation (QBO) effects and El Niño-Southern Oscillation (ENSO) signals. An increase of the global tropopause height of about 60 m over the time period 2001-2010 is observed (Fig. 4, solid line), see also *Schmidt et al. (2008)*. The associated temperature trend pattern is shown in Fig. 5. There is an overall slightly warming in the upper troposphere (from 5 km to the tropopause) with strongest signals in the subtropical region of both hemis-

pheres. In the lower stratosphere from the tropopause up to 25 km predominant negative temperature trends (cooling) are detected.

3.2. Irregularities of the ionospheric E-region

Sporadic E layers (Es) are defined as thin sheets of enhanced electron density that form in the ionospheric E region, preferably in the midlatitudes of the summer hemisphere between 80 and 120 km altitude. Fig. 6 gives an overview on the global distribution of sporadic E layers during the seasons of the year 2008. Highest Es rates are found in the midlatitudes on the respective summer hemisphere. During winter and in polar regions Es rates are generally low. Moderate Es activity is observed during equinox seasons in lower latitudes. In equatorial regions, a slim line of nearly no observed Es events appear during all seasons. This line follows exactly the magnetic equator. Also the minimum in Es occurrence rates in the South Atlantic region that correlates well with the minimum in the Earth's magnetic field's intensity suggests a close connection of both parameters.

Currently, CHAMP provides the longest available consistent time series of GPS RO measurements comprising nearly eight years. Figure 7 shows the time series of latitude dependent monthly Es rates measured by CHAMP bet-

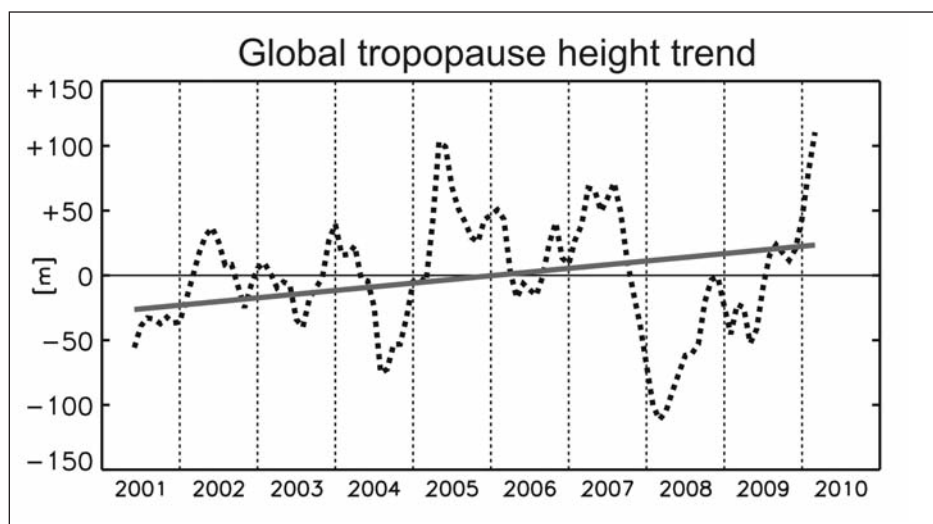


Figure 4: Global tropopause height trend (solid line) based on CHAMP and GRACE (2001-2010).

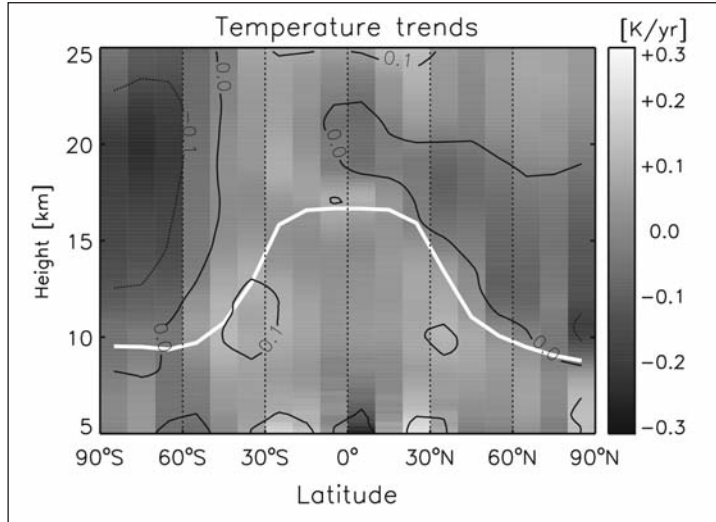


Figure 5: Global temperature trends in the upper troposphere and lower stratosphere based on CHAMP and GRACE (2001-2010), see Schmidt et al., 2010. The solid white line denotes the tropopause height.

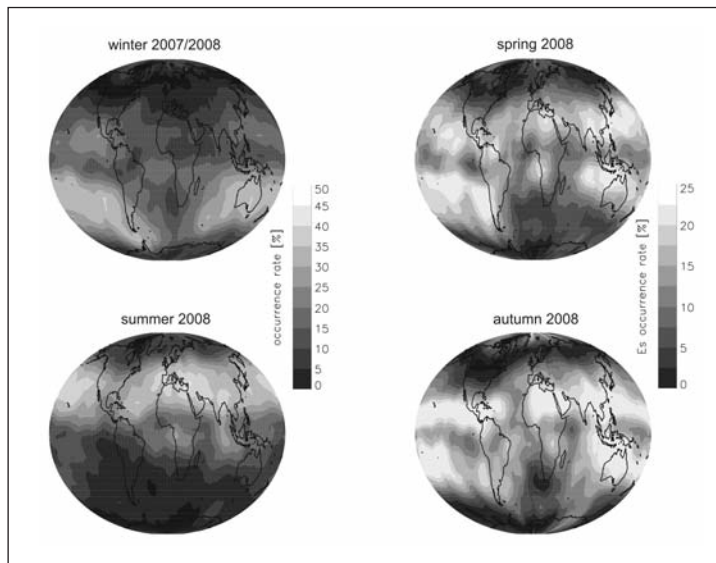


Figure 6: Seasonal global distribution of sporadic E occurrence rates in 2008 derived from CHAMP, GRACE and COSMIC GPS RO data. Each plot contains measurements collected during three months; winter (December 2007, January and February 2008), spring (March, April, May 2008), summer (June, July, August 2008) and autumn (September, October, November 2008) in a 5° x 5° resolution.

between January 2002 and October 2008. The expected summer maximum alternating between the northern and southern hemisphere is clearly visible. The individual summer maxima are interrupted by very low Es rates in spring and autumn. Weak secondary maxima are found at low latitudes on the winter hemisphere. In general, the Es rates in the southern hemisphere are apparently reduced by 25% compared to the northern hemisphere. The summer maxima vary in intensity, duration and dimension. But usually values around 40% (30%) in Es occurrence frequency are observed in the northern (southern) hemisphere. For more comprehensive results of Es investiga-

tions with GPS radio occultation data from CHAMP, GRACE and FORMOSAT-3/COSMIC see Arras (2010).

4. GPS radio occultation with TerraSAR-X and TanDEM-X

The German TerraSAR-X satellite was launched on June 15, 2007 and since June 21, 2010 its twin satellite TanDEM-X is in orbit. Main purpose of the two-satellite-mission is the generation of a high resolution Earth surface elevation model using a new generation X-band radar. The occultation instrumentation consists of two occultation antennas (forward- and aft-

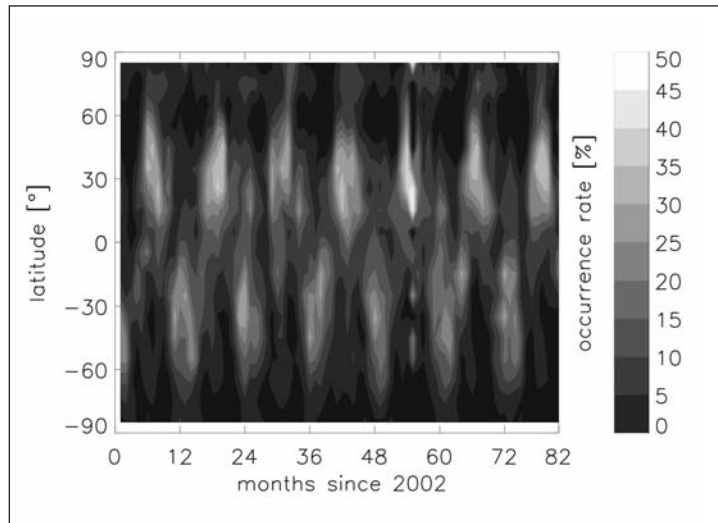


Figure 7: Time series of monthly latitude dependent (10° resolution) sporadic E rates between 2002 and 2008 derived from CHAMP GPS radio occultation data.

looking) and the Integrated GPS Occultation Receiver (IGOR) providing dual frequency GPS RO observations for atmospheric remote sensing. GPS radio occultation measurements onboard TerraSAR-X are continuously activated since February 2009. On August 30 and 31 of 2010 the TanDEM-X occultation receiver was successfully activated for the first time. The operational GFZ orbit and occultation analysis system has successfully been used for near-real time processing of CHAMP RO data and is currently in use for processing of GRACE RO observations. In contrast to the BlackJack RO receivers aboard CHAMP and GRACE, the IGOR receiver applies the open-loop tracking technique to improve GPS signal tracking in the lower troposphere. The operational GFZ RO analysis system has been upgraded for processing of open-loop RO data. This also includes the handling of navigation bit data (needed for open-loop data correction) which are collected by GFZ's global »NavBit« monitoring ground network. Continuous provision of TerraSAR-X near-real time atmospheric data for numerical weather prediction is currently in preparation. For more details on initial TerraSAR-X occultation results see *Beyerle et al. (2010)*.

5. Summary and Outlook

In order to reduce computation time and improve sustainability, the GFZ RO analysis software has been adapted for application on LINUX platforms. Comprehensive intercompari-

sons of GFZ analyses results with other processing centres (e.g. UCAR) have been accomplished revealing excellent agreement up to 25 km altitude but a positive refractivity bias above. This bias has to be solved in further course of the ATMO-CHAMP/GRACE project. A preliminary consistent reprocessing of the CHAMP long-term data set was already performed to remove software change related inhomogeneities. The CHAMP/GRACE long-term data set is successfully used for several atmospheric applications such as temperature and tropopause trends, gravity wave activity and occurrence of sporadic E-layers. Currently GFZ operationally provides GRACE-A data for numerical weather prediction centres (e.g., UK MetOffice, ECMWF, NCEP, DWD). It is planned to extend this near-real time activities by TerraSAR-X and TanDEM-X data.

Acknowledgements

The authors are grateful to the CHAMP, GRACE, TerraSAR-X and TanDEM-X teams for their efforts to maintain the availability of GPS radio occultation data. The German Ministry for Education and Research supported this work within the GEOTECHNOLOGIEN programme (research project ATMO CHAMP/GRACE).

References

- G. Beyerle, L. Grunwaldt, S. Heise, W. Köhler, R. König, G. Michalak, M. Rothacher, T. Schmidt, B. Tapley, J. Wickert, First results from the GPS atmosphere sounding experiment TOR aboard the TerraSAR-X satellite, *Atmospheric Chemistry and Physics*, subm., 2010.
- C. Arras, A global survey of Sporadic E Layers based on GPS radio occultations by CHAMP, GRACE and FORMOSAT-3/COSMIC, PhD thesis, University Leipzig, 2010.
- S. Heise, J. Wickert, G. Beyerle, T. Schmidt, H. Smit, J.-P. Cammas, M. Rothacher, Comparison of water vapour and temperature results from GPS radio occultation aboard CHAMP with MOZAIC aircraft measurements, *IEEE Transactions on Geoscience and Remote Sensing*, 46, 11, 3406-3411, doi:10.1109/TGRS.2008.920268, 2008.
- S. Ho, G. Kirchengast, S. Leroy, J. Wickert, A. J. Mannucci, A. Steiner, D. Hunt, W. Schreiner, S. Sokolovskiy, C. Ao, M. Borsche, A. v. Engeln, U. Foelsche, S. Heise, B. Iijima, Y.-H. Kuo, R. Kursinski, B. Pirscher, M. Ringer, C. Rocken, T. Schmidt, Estimating the Uncertainty of using GPS Radio Occultation Data for Climate Monitoring: Inter-comparison of CHAMP Refractivity Climate Records 2002-2006 from Different Data Centers, *J. Geophys. Res.*, 114, D23107, doi:10.1029/2009JD011969, 2009.
- E. R. Kursinski, G. A. Hajj, K. R. Hardy, J. T. Schofield, R. Linfield, Observing Earth's atmosphere with radio occultation measurements using the Global Positioning System, *J. Geophys. Res.*, 102, 23429-23465, 1997.
- J. Wickert, Near-real-time provision and usage of global atmospheric data from CHAMP and GRACE (NRT-RO): Motivation and Introduction, In: Flechtner, F., Gruber, T., Güntner A., Mandea, M., Rothacher, M., Schöne T., Wickert, J., (Eds.), *System Earth via Geodetic-Geophysical Space Techniques*, Springer, ISBN 978-3-642-10227-1, DOI 10.1007/978-3-642-10228-8, Berlin, Heidelberg, pp 429-432, 2010.
- J. Wickert, G. Michalak, T. Schmidt, G. Beyerle, C.Z. Cheng, S.B. Healy, S. Heise, C.Y. Huang, N. Jakowski, W. Köhler, C. Mayer, D. Offiler, E. Ozawa, A.G. Pavelyev, M. Rothacher, B. Tapley, C. Arras, GPS radio occultation: Results from CHAMP, GRACE and FORMOSAT-3/COSMIC, *Terrestrial, Atmospheric and Oceanic Sciences (TAO)*, 20, 35-50, doi: 10.3319/TAO.2007.12.26.01, 2009.
- T. Schmidt, J. Wickert, G. Beyerle, S. Heise, Global tropopause height trends estimated from GPS radio occultation data, *Geophys. Res. Lett.*, 35, L11806, doi:10.1029/2008GL034012, 2008.
- T. Schmidt, J. Wickert, A. Haser, Variability of the upper troposphere and lower stratosphere observed with GPS radio occultation bending angles and temperatures, *Adv. Space Res.*, doi:10.1016/j.asr.2010.01.021, 2010.
- T. P. Yunck, C. H. Liu, R. Ware, A history of GPS sounding, *Terr. Atmos. and Oceanic Sci.*, 11(1), 1-20, 2000.

GOCE gravity gradients: a new satellite observable

Bouman J. (1), Stummer C. (2), Murböck M. (2), Fuchs M. (1), Rummel R. (2), Pail R. (2), Gruber T. (2), Bosch W. (1), Schmidt M. (1)

(1) Deutsches Geodätisches Forschungsinstitut, München

(2) Institut für Astronomische und Physikalische Geodäsie, Technische Universität München

Introduction

The GOCE satellite was launched on March 17, 2009. It is the first mission of ESA's Living Planet Programme and the first satellite with a gravitational gradiometer. GOCE aims at the determination of the stationary part of the Earth's gravity field and geoid with maximum accuracy and spatial resolution (ESA 1999). The gradiometer data are essential to achieve this aim. Thus, the first step in GOCE data analysis should be to look into the characteristics of this new data type. Our goal therefore is to obtain a comprehensive understanding of signal and error characteristics of the individual measured gravitational gradients (GGs). This should be the basis of their use in science and application.

In order to get a full understanding of the signal and error characteristics of the GOCE gravity gradients they are studied at four different levels. The first one is gradiometer internal calibration as a pre-requisite in the further processing of the gradiometer data. Once calibrated measurements are available they can be analyzed spectrally and gravity field analysis can be performed. The second level is therefore analysis of the gradiometer data. The GOCE gravity gradients are given in the instrument frame. The analysis of the gravity gradients may require rotation of the GOCE GG to other local reference frames, which represents the third level. This is done with GOCE data only and - in order to strengthen the long wavelength parts - with a combination of recent GRACE gravity models. The goal must be minimum loss of

accuracy due to the contribution from the weaker gradient components. The fourth level is gravity gradient validation with satellite altimetry. The high precision and high sample rate of satellite altimeter data permits comparison of gravity gradients derived from satellite altimetry and GOCE gravity gradients.

Gradiometer internal calibration

Gravitational gradiometry based on the principle of differential accelerometry requires the six three-axis accelerometers to have the same scale and to be perfectly aligned. The real instrument can approximate this ideal at most up to a high level of accuracy. Thus, calibration is the central condition for any correct use and interpretation of the gradiometric measurements. Calibration on ground is difficult due to the presence of g . Therefore calibration is carried out using random shaking of the instrument by a set of cold gas thrusters, (Cesare and Catastini 2008), which is called in-flight or internal calibration. Two algorithms have been developed to retrieve the calibration parameters, one by ALENIA and an alternative one by engineers of ESA-ESTEC (Cesare and Catastini 2008, Lamarre 2008). Both algorithms determine the calibration parameters iteratively and rely on semi-empirical processing steps that are not fully understood (Bouman et al. 2008).

In the nominal processing, the inverse calibration matrices (ICMs) determined by the ESA-ESTEC method from the previous shaking are applied. It was found that some elements of

the ICM from two consecutive shakings (e.g. the shakings of October 2009 and of January 2010) show a significant variation with time. In addition, one observes a slight degradation in time (from October 2009 to January 2010) of the gravity gradient performance when analysing the GGT trace.

To check whether it is possible to avoid this degradation of the GGT trace performance with time, four simulation scenarios have been performed. Since in particular the differential scale factor of accelerometer pair 25 in Y-direction (dSF25y) shows a significant variation with time, the effect of linear interpolating the corresponding ICM element is investigated. Moreover the impact an alternative method for angular rate reconstruction (ARR, *Stummer et al. 2010*) is analysed. For each of the four scenarios, the GGs from 31 October to 31 December 2009 have been reprocessed, using an autonomous implementation of the nominal EGG Level 1b processor:

- 1) As reference, the original GGs have been reprocessed with the nominal method for ARR and using the nominal (previous) ICM.
- 2) As 1) but with interpolation of the ICM element corresponding to dSF25y.
- 3) Instead of the nominal method for ARR, the Wiener ARR method was used. The nominal ICMs have been applied.
- 4) Again, the Wiener method for ARR was used, but this time with interpolation of the ICM element corresponding to dSF25y

Figure 1 illustrates the trace performance of the four sets of gravity gradients from scenarios 1) to 4) at a day (27 December 2009) that is far away in time from the October calibration and thus the variation of dSF25y with respect to this calibration is expected to be large.

One can notice that:

- When using the nominal ARR method, there is only a small improvement of the GGT trace performance due to ICM interpolation

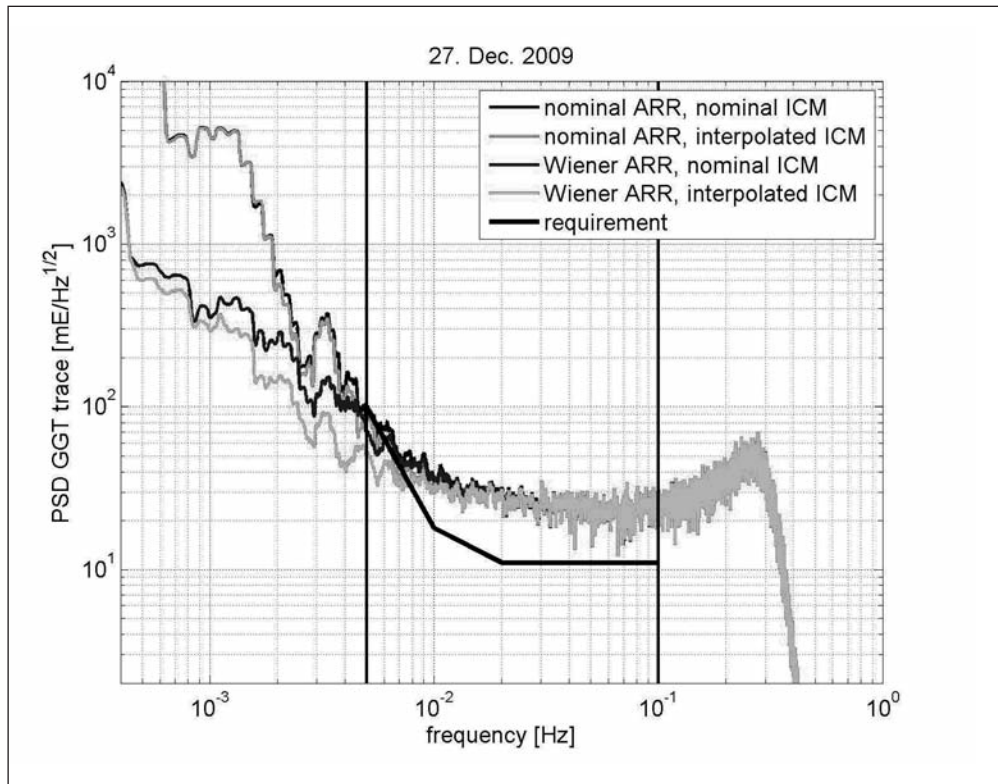


Figure 1: PSD of GGT trace, effect of ICM interpolation (dSF25y) using nominal and Wiener method for ARR

(upper black vs. grey curves) for frequencies at the lower end of the MBW (5 mHz).

- With the Wiener method for ARR (using nominal ICM, lower black curve), the GGT trace performance improves significantly with respect to the nominal ARR method (two upper curves). The improvement is largest for low frequencies and is to a smaller extent still present for frequencies up to 7 mHz.
- The GGT trace performance is best when the Wiener method for ARR is used and the ICM element corresponding to dSF25y is interpolated (lower grey curve).

Thus, it is confirmed that a change of an accelerometer scale factor can have a significant impact on the accuracy of the gravity gradients. Moreover, it is possible to compensate for this effect to some extent by linear interpolation of the corresponding ICM element using the Wiener method for ARR. When the nominal method for ARR is used this positive effect of ICM interpolation cannot be achieved.

Analysis of the gradiometer data

Since GOCE is the first satellite mission ever with a gradiometer on board, the analysis of these data with noise is very important. The spectral characteristics of the gradiometer measurements can be analyzed in several ways. One option is to use the redundancy within the accelerometers and the gradiometer as a whole, to check the individual components against each other. Each of the 6 three-axis GOCE accelerometers has two ultra-sensitive (US) axes and one less sensitive (LS) axis. The two US axes measure the Control Voltages (needed to keep the accelerometers proof mass stable) with 2 electrode pairs, the LS axes have 4 electrode pairs. Therefore, in total there are $6 \cdot 8 = 48$ electrode-pairs.

To check the performance of each of these electrode pairs, the nominal GOCE Level 1b processing has been rerun, replacing the measurements of one specific electrode pair with the measurements of the corresponding pair along the same axis. In Figure 2 the impact of

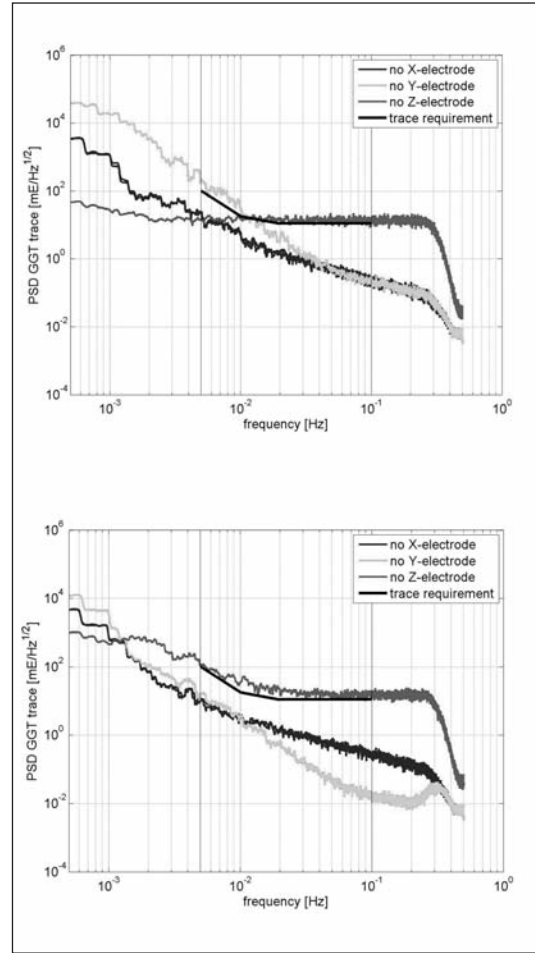


Figure 2: Impact on GGT trace due to the replacement of individual Control Voltages of accelerometer 1 (top) and of accelerometer 2 (bottom)

the replacement on the GGT trace is shown. For a better visualisation, always the PSD of the difference between the specific new GGT trace and the nominal one (using all measurements) has been computed. One can notice two things. First, the replacement of measurements along one specific axis always causes a similar impact on the GGT trace. Therefore, it can be excluded that there is one electrode with a particular bad performance. Second, the impact on the GGT trace depends on the axis on which the replacement is done. E.g. the replacement of a Z-electrode (in the Accelerometer Electrode System Reference Frame (AESRF), red curves) has a significant impact on the GGT trace throughout the complete gradiometer measurement band width (MBW). Table 1 gives a detailed overview of the impact of electrode replacements on the individual gradients.

Table 1: Impact on gradients due to replacement of Control Voltages

Sensi- tivity	Arrange- ment	ACC	Axis in AESRF	Axis in GRF	Impact on	Frequency range
US	In-line	1/4	Z	X	V_{xx}	Within MBW
		2/5	Z	Y	V_{yy}	
		3/6	Z	Z	V_{zz}	
US	Trans- versal	1/4	Y	Z	$\dot{\omega}_y$	Lower MBW
		2/5	Y	X	$\dot{\omega}_z$	Not significant
		3/6	Y	X	$\dot{\omega}_y$	Lower MBW
LS	Trans- versal	1/4	X	Y	$\dot{\omega}_z$	Not significant
		2/5	X	Z	$\dot{\omega}_x$	
		3/6	X	Y	$\dot{\omega}_x$	

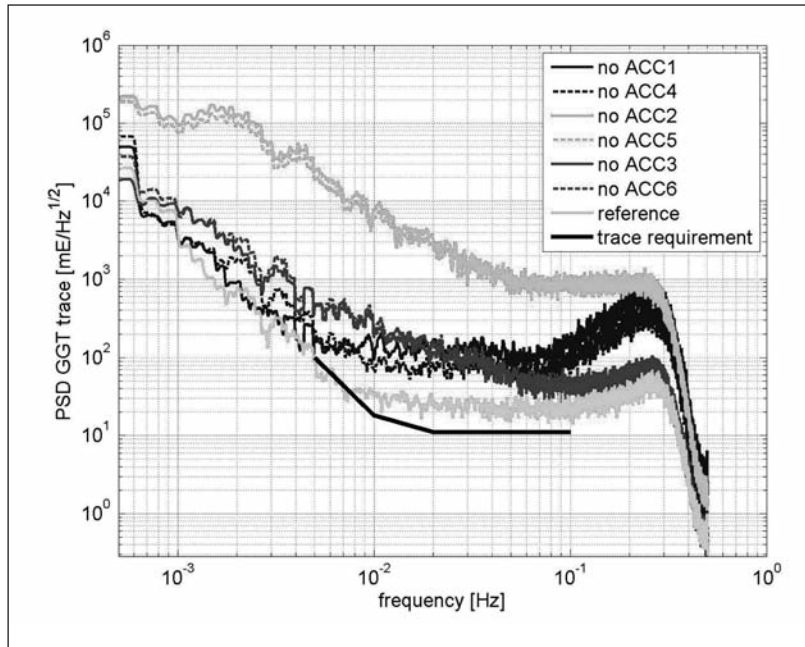


Figure 3: Impact on GGT trace due to replacement of complete accelerometers

Additionally, 6 sets of GGs have been computed, replacing one accelerometer by a virtual accelerometer, which is formed by the common-mode accelerations of the corresponding remaining accelerometers. In Figure 3 the PSDs of the GGT trace for all six cases of accelerometer replacement are shown. Again, one can notice two things. First, the impact on the GGT trace is similar for the accelerometers on the same gradiometer arm. Second, the impact is depending on the axis on which the replacement is done. The GGT trace degrades most, if

an accelerometer on the Y-axis, accelerometer 2 or 5 (two upper curves), is replaced, because these accelerometers are the only ones with US axes in Y direction, which is the main measurement direction in this case. Therefore, the Y-direction of the corresponding virtual accelerometer can only be built from LS measurements.

Spectral characteristics of the diagonal gradiometer components

Theoretically the gravity gradients individually

as well as certain well defined combinations show typical spectral characteristics, see e.g. (Rummel and van Gelderen 1992, Rummel 1997). In reality these theoretical properties will only be met to a certain extent. This is due to measurement noise, imperfect calibration, less sensitive accelerometer components and to rotational effects. Thus, these spectral characteristics are an important tool for the assessment of the quality of measured gradients. Further insight in the GOCE gravity gradient characteristics is obtained by their global behaviour in terms of spherical harmonic coefficients by the semi-analytic method (Sneeuw 2000, Pail and Plank 2002, Wermuth et al. 2006, Pail et al. 2007). It is feasible to use single gravity gradient components as well as various combinations of gravity gradient components for global spectral analysis, for the first time using real data.

Each individual gradiometer component has its own spectral strength and weakness. The actual spectral characteristics are analyzed, employing spherical harmonic (SH) analysis on the three diagonal components. The observations used are GOCE data from November and December 2009. A semi-analytical approach leads iteratively to a consistent adjustment resulting in SH coefficients and a Block-Diagonal Variance-Covariance matrix. The estimated standard deviations of this solution can be seen in Figure 4 (top) in the spherical harmonic (SH) domain. Typical SH error characteristics of GOCE GG can be seen. The inclined orbit, which provides no observations over the poles, leads to large errors around the zonal coefficients. The sensitivity for lower degrees is quite low and a near isotropic behaviour can be observed in the higher degrees (i.e. main dependency of the errors of the SH degree and not of the SH order). Bright stripes around multiples of the SH order 16 for low degrees are noticeable as well, which are characteristic for high noise at multiples of the orbit frequency. It is useful to compare the estimated standard deviations with the differences of the estimated SH coefficients and the coefficients of an existing gravity field model (here EIGEN-5C)

(Fig. 4 middle). These coefficient differences lead to comparable SH structures. A different look at this comparison is provided by the median per SH degree of these two SH spectra (Fig. 4 bottom). The median is used because it is not sensitive to the very high errors around the zonals affected by the polar gap. As EIGEN-5C is a combined model from five years GRACE and LAGEOS data we assume it to be better in the lower degrees than GOCE. Therefore the differences in these degrees can

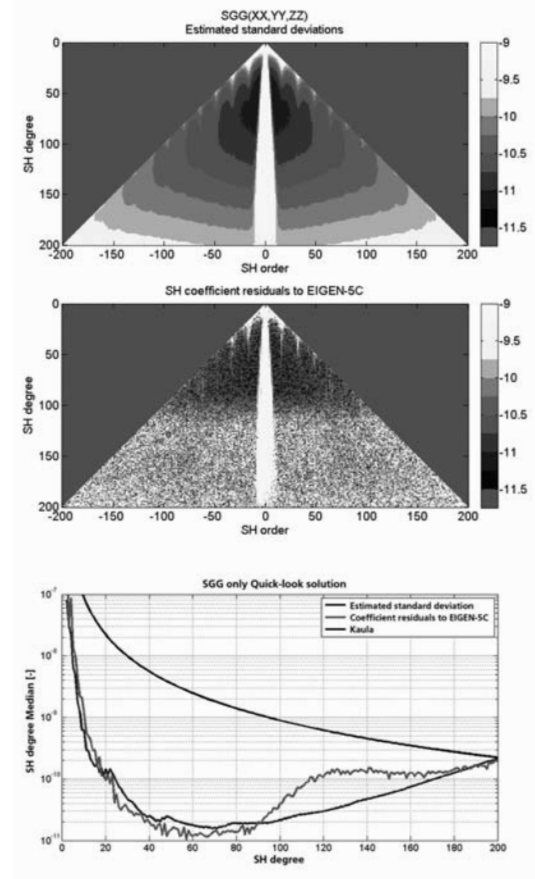


Figure 4: Top: estimated standard deviations of a semi-analytical gravity field estimation of GOCE's GGs of November and December 2009 (log10). Middle: Differences between the estimated SH coefficients and the coefficients of EIGEN-5C Bottom: SH degree median of the two upper SH coefficients

be assumed to be mainly errors. As the median of the estimated standard deviations is quite close to the median of the coefficient differences it can be assumed that the observations are processed consistently and lead to realistic errors for GOCE's GGs.

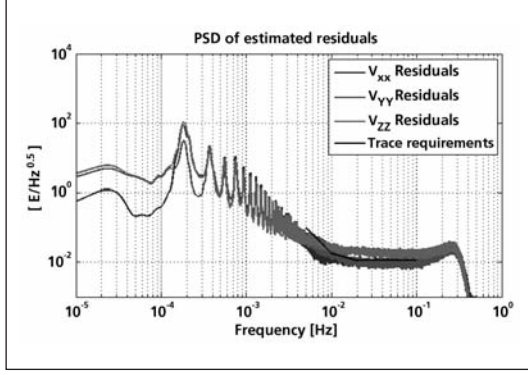


Figure 5: PSD of the estimated residuals of the three diagonal components

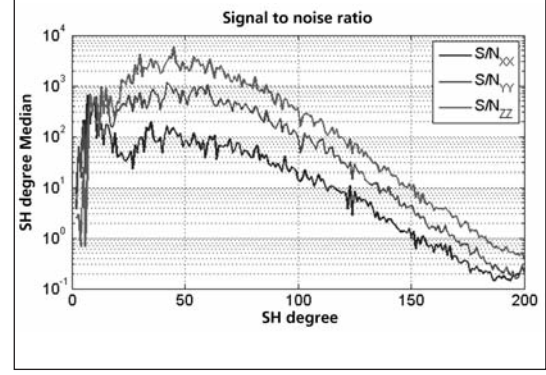


Figure 7: SH degree median of the signal to noise ratio of the three diagonal components

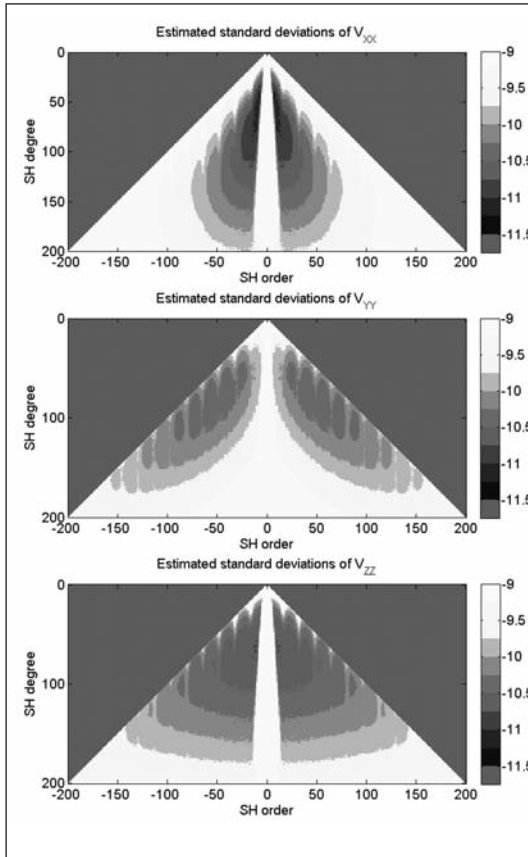


Figure 6: SH error spectra of the three diagonal components (top: XX, middle: YY, bottom: ZZ) (log10)

This analysis provides the estimates of the observation residuals as well. A spectral representation of these residuals shown in Figure 5 as PSDs. Derived from a consistent processing of the combination of the three diagonal components of GOCE's GGs to SH coefficients, these PSDs gives a realistic error characteristic of each of the 3 components in the frequency

domain. One can notice two things. All 3 components show similar noise behaviour with frequency. Large peaks occur at multiples of the orbit frequency. The noise level for frequencies above 10 mHz is nearly constant (white noise) and around 10 mE/Hz^{0.5}. Nevertheless some differences can be observed. The noise level of V_{zz} in the upper frequency range is nearly two times larger than the other two components. At around 10 mHz the V_{xx} component seems to have a lower noise level than the others.

By propagating this noise PSDs in a semi-analytical way onto the SH spectrum one gets the noise behaviour in the SH domain (Figure 6). The peaks in the PSDs are mapped on multiples of the SH order 16 and are visible in bright stripes as in the combined solution. The theoretical characteristics remain in this realistic case. These are the large errors around the zonals (polar gap) and the typical sensitivities for V_{xx} (around the zonals), V_{yy} (sectorials) and V_{zz} (near isotropic). Dividing these errors by the SH coefficients of the estimated signal a signal to noise ratio in the SH domain arises. Its median per SH degree can be seen in the right Figure 7. The V_{zz} -component has the highest S/N ratio for all SH degrees, the V_{xx} -component the smallest.

Rotation of the gravity gradient tensor

The calibrated gravity gradients, as derived from the GOCE gradiometer, are given in the GRF, the Gradiometer Reference Frame, which

co-rotates with the satellite in its orbit. The GRF is approximately oriented in the radial, along-track, cross-track direction and is governed by the attitude control system. While the location of the measurements is determined using GPS orbit determination, the orientation in inertial space relies on the star sensors. In principle it is therefore possible to rotate the measurements to a local geographical frame. Such a representation would allow a more general analysis and interpretation of the measurements independent of satellite orbit and satellite position.

There are, however, two problems in the transformation of the gravity gradients from the GRF to other frames. First, the rotation of the gravitational tensor from one orthonormal frame to another requires the pre- and post-multiplication of the tensor with a corresponding rotation matrix. Consequently, the tensor components in the rotated system are linear combinations of the components in the original system. Because two of the non-diagonal tensor components are much less accurate than the other components, a rotation to another frame will also make the diagonal components in the transformed frame less accurate (*Müller 2003*). Secondly, the accurate gravity gradients do have high accuracy in the MBW (Measurement Bandwidth), but the error increases for low frequencies. This error tends to leak into the MBW while transforming from GRF to other local frames (*Bouman 2007*).

An algorithm has been developed and implemented to prevent gravity gradient deterioration in the frame transformation. The GOCE gravity gradient signal below the MBW is replaced by signal from a global model to prevent leakage, for example a GRACE or a GOCE quick-look model (*Foerste et al. 2007, Pail and Wermuth 2003*). In addition, the two less accurate gravity gradients in the GRF are replaced by gravity gradients which have been computed from a quick-look GOCE gravity field model.

Dependent on the gradiometer performance the spectral limit of model information and

measured GGs has been evaluated using a trade off between signal bandwidth, signal energy and measurement noise. This limit, which is assigned by the filter cut-off frequencies, is important because it gives a value for the long wavelength quality of GOCE data. Due to the impact of rotational effects on the rotated GGs, the cut-off frequency is being derived in the rotated reference frame by an analysis aiming for an optimal ratio between signal and noise energy of the derived GGs. With this analysis the low frequency spectral gradiometer performance can be tested and evaluated.

The tensor rotation of GOCE GGs mixes components derived from model information and measurements which depends on the rotational angle, the spectral signal strength, the gradient axes and the orbit height. The amount of GOCE information in the rotated gradients is an important quantity for local analysis. Two frames are of special interest: the local orbital reference frame (LORF) and the local north oriented frame (LNOF). The LORF X-axis is aligned with the velocity vector of the satellite, the Z-axis is in almost radial direction in the orbital plane and Y-axis complements the right-handed frame. The X-axis of the LNOF points North, the Y-axis West and the Z-axis radial outward.

The ratio of model and GOCE GGs has been used to evaluate the model content present in the rotated gravity gradients in different reference frames. The amount of model information in the rotated gradients is shown in Figure 8 for V_{yy} (LNOF & LORF). As the GRF is aligned within a few degrees with the LORF, the rotations from GRF to LORF are small, whereas the rotation about the yaw axis can be large going from GRF to LNOF. The mean model content in the rotated gradients is summarized in Table 2.

The rotated gravity gradients can be used to validate and evaluate global gravity field models at the GOCE orbit in the LNOF. Especially for the fine scale structures in common global gravity field models such as e.g. the EGM2008 or the EIGEN5C differences are seen globally and particular in regions such as South America,

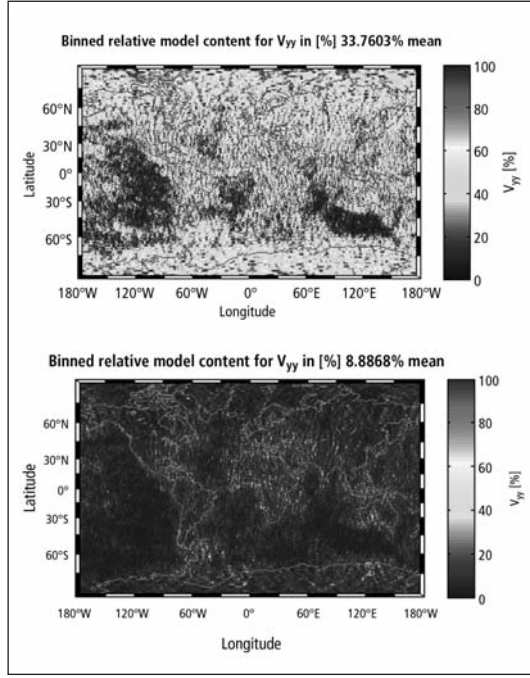


Figure 8: Relative model content in V_{YY} LNOF (top) and LORF (bottom)

Table 2: Mean relative model content in rotated gravity gradients in LNOF and LORF)

GG	LNOF	LORF
V_{XX}	20.8 %	2.6 %
V_{YY}	33.8 %	8.9 %
V_{ZZ}	1.1 %	2.0 %
V_{XZ}	14.2 %	4.2 %

Africa or South Asia, see Figure 9. The measurement anomalies in V_{YY} south of Australia and Northern Canada are a non gravity related GOCE feature, which is probably related to a drift in the gradiometer differential scale factors (see section on gradiometer internal calibration).

Gravity gradient validation with satellite altimetry

Since many years satellite altimetry provides measurements of mean sea level (MSL). MSL nearly coincides with an equipotential surface of the Earth gravity field, the geoid. Deviations between mean sea level and geoid, known as dynamic ocean topography (DOT) are caused by external forcing and remain below ± 1 -2 m. The mean curvature of the geoid is proportional to the radial gravity gradient of the distur-

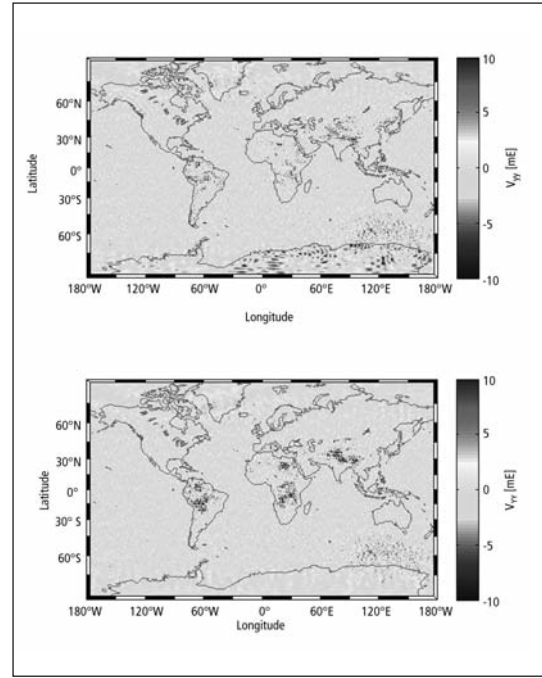


Figure 9: V_{YY} binned averaged differences 31 October 2009 – 11 January 2010: GOCE - EIGEN5C (top), GOCE - EGM2008 (bottom)

bing potential (*Heiskanen and Moritz 1967*). It can be shown that the mean curvature of the mean sea level is a very precise measure of the curvature of the geoid (*Bosch 2003, Bouman et al. 2010*). Thus, from the geometry of the mean sea level one can infer the second radial derivative of the disturbing potential. This opens the possibility to use satellite altimetry for the validation of gradients.

GGs may be transformed to any arbitrary reference frame and therefore also to a reference frame aligned with satellite altimeter ground tracks. This opens the possibility to use the single gravity gradient components for modelling and comparison with along track gravity gradient profiles as derived from satellite altimetry, cf. (*Rummel and Haagmans 1991, Khafid 1993*). In addition, at crossover points of altimeter ground tracks the second radial derivative of the gravitational potential can be determined using the along track gravity gradient profiles of ascending and descending tracks (*Rummel and Haagmans 1991*). At crossover points altimetric gravity gradients (radial component) may therefore be used to validate the GOCE radial gravity gradients.

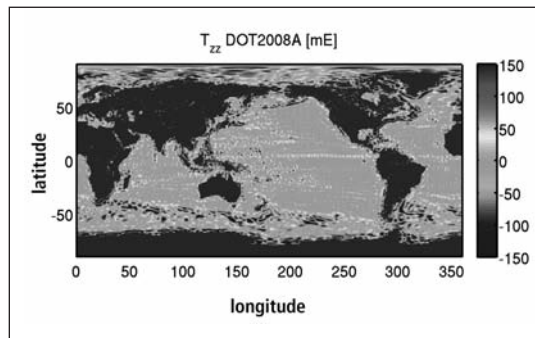


Figure 10: DOT TZZ signal at the Earth's surface computed with DOT2008A

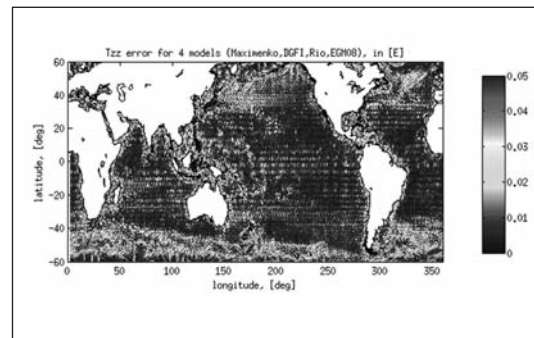


Figure 11: T_{ZZ} RMS differences for 4 different DOT-models

We assessed how large the influence is of neglecting the DOT and thus assuming that MSL is an equipotential surface. The DOT model DOT2008A has been expanded in spherical harmonics (Pavlis *et al.* 2008) and the coefficients have been used to compute the vertical GG with respect to a reference ellipsoid. This DOT TZZ signal is shown in Figure 10 where the colour bar has been set to ± 150 mE. For reference: the error in the accurate GOCE gravity gradients is 10 – 20 mE for medium resolutions. The DOT can therefore not be neglected.

Because the DOT cannot be neglected it must either be modeled or estimated simultaneously with, for example, a regional gravity field when satellite altimeter data and GOCE gravity gradients are combined. Different models for the DOT exist and we computed the differences between 4 models. The RMS of these differences, in terms of vertical gravity gradient, is shown in Figure 11. Clearly, the differences between the DOT models are large in regions with the major currents. There are however also regions, such as the Pacific, where the differences between the DOT models are small. Satellite altimeter data in these regions could be used for GOCE validation if the altimeter data are corrected for DOT.

Acknowledgements

This work was sponsored by the German Department for Education and Research (Bundesministerium für Bildung und Forschung) as part of the GEOTECHNOLOGIEN program. Josef

Sebera provided the figure on DOT differences.

References

- Bosch W (2003) On the combination of altimetry and satellite derived gravity field models. Presented at the IUGG General Assembly, Sapporo, Japan
- Bouman J (2007) Alternative method for rotation to TRF. GO-TN-HPF-GS-0193, issue 1.0
- Bouman J, Catastini G, Cesare S, Jarecki F, Müller J, Kern M, Lamarre D, Plank G, Rispens S, Veicherts M, Tscherning CC, Visser P (2008) Synthesis analysis of internal and external calibration. GO-TN-HPF-GS-0221, Issue 1.0
- Bouman J, Bosch W, Sebera J (2010) Assessment of systematic errors in the computation of gravity gradients from satellite altimeter data. Accepted for publication in Marine Geodesy
- Cesare S, Catastini G (2008) Gradiometer on-orbit calibration procedure analysis. Issue 4, GO-TN-AI-0069, Alenia Spazio, Turin
- ESA (1999) Gravity Field and Steady-State Ocean Circulation Mission. Reports for mission selection; the four candidate earth explorer core missions, ESA SP-1233(1)
- Foerste C, Schmidt R, Stubenvoll R, Flechtner F, Meyer U, Koenig R, Neumayer H, Biancale R, Lemoine JM, Bruinsma S, Loyer S, Barthelmes F, Esselborn S (2007) The GeoForschungsZen-

- trum Potsdam / Groupe de Recherche de Géodésie Spatiale satellite-only and combined gravity field models: EIGEN-GL04S1 and EIGEN-GL04C. *J Geod.* doi: 10.1007/s00190-007-0183-8
- Heiskanen W, Moritz H (1967) *Physical geodesy*. W.H. Freeman and Co.
- Khafid (1993) Filtering of satellite altimetry data with optimal smoothing cubic splines. Master's thesis, Faculty of Geodetic Engineering, Delft University of Technology
- Lamarre D (2008) Algorithm description: retrieval of gradiometer parameters. Version 2.0 draft, 23/APR/08
- Müller J (2003) GOCE gradients in various reference frames and their accuracies. *Adv Geosci* 1:33–38
- Pail R, Plank G (2002) Assessment of three numerical solution strategies for gravity field recovery from GOCE satellite gravity gradiometry implemented on a parallel platform. *Journal of Geodesy*, 76:462–474
- Pail R, Metzler B, Preimesberger T, Lackner B, Wermuth M (2007) GOCE Quick-Look Gravity Field Analysis in the Framework of HPF. In *Proceedings of the 3rd International GOCE User Workshop*. ESA-ESRIN, Frascati, Italy, 6-8 November 2006, ESA SP-627
- Pail R, Wermuth M (2003) GOCE SGG and SST quick-look gravity field analysis. *Advances in Geosciences*, 1:5–9
- Pavlis DE, Holmes SA, Kenyon SC, Factor JK (2008) An Earth Gravitational Model to Degree 2160: EGM2008, Presented at EGU General Assembly 2998, Vienna, Austria
- Rummel R (1997) Spherical spectral properties of the earth's gravitational potential and its first and second derivatives. In F. Sansò and R. Rummel, editors, *Geodetic Boundary Value Problems in View of the One Centimeter Geoid*, volume 65 of *Lecture notes in earth sciences*, pages 359–404. Springer, Berlin
- Rummel R, Haagmans R (1991) Gravity gradients from satellite altimetry. *Marine Geodesy*, 14, 1–12
- Rummel R, van Gelderen M (1992) Spectral analysis of the full gravity tensor. *Geophysical Journal International*, 111:159–169
- Sneeuw N (2000) A semi-analytical approach to gravity field analysis from satellite observations. Reihe C No. 527, Deutsche Geodätische Kommission
- Stummer C, Fecher T, Pail R (2010) Improved method for angular rate determination within the GOCE gradiometer processing. Submitted to *J Geod*
- Wermuth M, Rummel R, Földvary L (2006) Mission Simulation and Semi-Analytical Gravity Field Analysis for GOCE SGG and SST. In J. Flury, R. Rummel, C. Reigber, M Rothacher, G. Boedecker, and U. Schreiber, editors, *Observation of the Earth System from Space*, pages 193–208. Springer

GOCE gravity field determination by means of rotational invariants: first experiences

Cai J., Baur O. and Sneeuw N.

Stuttgart University

1. Introduction

Launched on 17 March 2009, ESA's Gravity field and steady-state Ocean Circulation Explorer (GOCE) will revolutionize our understanding of one of Earth's most fundamental forces – gravity. Commonly, GOCE gradiometry analysis relates the single gravitational gradients to the unknown gravity field parameters. For its application, the orientation of the gravitational tensor relative to the reference frame of gravity field modeling is of prime importance. Hence, the orientation information quality strongly influences the accuracy of the entire analysis procedure. Gravity field recovery based on the rotational invariants of the gravitational tensor avoids any orientation concerns. For this reason, the invariants representation constitutes an alternative and independent procedure for GOCE data analysis. Within the support programs GOCE-GRAND I and II [12], the methodological fundamentals were established to apply the invariants approach to gradiometer data. Most notably, in this context, the algorithms have been implemented on high performance computing platforms and have been tested successfully within the framework of comprehensive numerical simulation studies. The major objective of this work package is the application of the existing routines to GOCE real data. The final outcome is an Earth's gravity field solution based on the invariants representation.

In case of full tensor gradiometry all second-order derivatives of the geopotential, denoted as gravitational gradients (GGs) V_{ij} , $i, j = 1, 2, 3$ can be derived. They are summarized in the symmetric gravitational tensor, or Eötvös ten-

sor [3]. Due to technical reasons (ground calibration), for GOCE two of the off-diagonal elements V_{12} and V_{23} are reduced in accuracy by several orders of magnitude, hence can be considered as unobserved.

Typically, gradiometer data analysis is performed at the level of individual GGs, in particular the main diagonal elements of the gravitational tensor. This approach embraces a variety of methods commonly attributed to the space-wise or time-wise methods [10]. Here we present an alternative analysis concept. It is based on gravitational tensor rotational invariants [1].

As invariants are composed of gravitational gradients products, the alternative representation yields a non-linear least-squares minimization problem requiring iterative model parameter estimation. Moreover, invariants are composed of all individual GGs. Thus, GGs accuracies must be compatible, which is only ensured by full tensor gradiometry.

In brief, the pros and cons of the invariants representation can be summarized as follows:

Pros of the invariants representation:

- scalar-valued gravity field functionals
- independent of the gradiometer orientation in space
- independent of the orientation accuracy
- independent of reference frame rotations / parameterization

Cons of the invariants representation:

- non-linear observables
- gravitational gradients required with com-

patible accuracy (full tensor gradiometry)

- more complex stochastic model handling
- iterative parameter estimation, huge computational costs

In this contribution, we present strategies to overcome the difficulties of the invariants representation in the context of GOCE data analysis and first experiences incorporating GOCE real data. The proposed methods are a tailored combination of (i) linearization in terms of a perturbation theory approach, (ii) synthesis of GGs for full tensor gradiometry reconstruction, (iii) error propagation in order to derive the stochastic model of invariants, and (iv) implementation of the algorithms on high performance computing platforms.

2. Invariants representation

The basic observation equation in satellite gradiometry reads [9]

$$\underline{\Gamma} = -\underline{V} + \dot{\underline{\Omega}} + \underline{\Omega}^2. \quad (1)$$

The observation tensor $\underline{\Gamma}$ is the sum of the gravitational tensor \underline{V} and rotational parts, i.e., the Euler tensor $\underline{\Omega}$ and the centrifugal tensor $\underline{\Omega}^2$. The rotational parts occur due to the rotation of the gradiometer reference frame relative to inertial space; they have to be reduced from the observation tensor prior to data analysis. For GOCE the separation is achieved by gradiometer observations (splitting the observation tensor into its symmetric and antisymmetric part) in combination with star tracker measurements. We denote the coefficient matrix of \underline{V} as $\mathbf{V}=[V_{ij}]$. The properties $V_{11}+V_{22}+V_{33}=0$ and $V_{ij}=V_{ji}$ hold true, i.e., \mathbf{V} is a trace-free symmetric matrix.

A tensor itself is independent of orthogonal transformations. This does not hold for its coefficient matrix. The individual components vary according to their projection on the base coordinate axes. Scalar-valued tensor invariants, however, are independent of frame rotations and thus independent of the reference base. A

second order tensor in three-dimensional Euclidean space (such as the Eötvös tensor) is characterized by three independent invariants [6], constituting a so-called complete invariants system. Invariants systems can be defined in various ways; transformation relations allow to transfer them to each other [5, 4].

The two most prominent invariants systems result from the eigenspace representation of \mathbf{V} , i.e., from the solution of the general eigenvalue problem of the tensor coefficient matrix. The characteristic equation $\det(\mathbf{V}-\lambda\mathbf{I}_3)$ yields the cubic polynomial

$$\lambda^3 - I_1\lambda^2 + I_2\lambda - I_3 = 0. \quad (2)$$

The roots of the characteristic equation are well-known as the eigenvalues λ_i , $i=1, 2, 3$ of \mathbf{V} . They constitute the complete invariants system $\{\lambda_1, \lambda_2, \lambda_3\}$. As the eigenvalues are invariants, according to Eq. (2) the polynomial coefficients I_i , $i=1, 2, 3$ form an invariants system too, denoted as $\{I_1, I_2, I_3\}$. As a function of the eigenvalues it reads

$$\begin{aligned} I_1 &= \lambda_1 + \lambda_2 + \lambda_3, \\ I_2 &= \lambda_2\lambda_3 + \lambda_1\lambda_3 + \lambda_1\lambda_2, \\ I_3 &= \lambda_1\lambda_2\lambda_3. \end{aligned} \quad (3)$$

In terms of GGs (symmetric and trace-free coefficient matrix \mathbf{V}) the I_i become [9]

$$I_1 = \text{tr } \mathbf{V} = 0, \quad (4a)$$

$$I_2 = -\frac{1}{2}\text{tr } \mathbf{V}^2 = -\frac{1}{2}(V_{11}^2 + V_{22}^2 + V_{33}^2 - V_{12}^2 - V_{13}^2 - V_{23}^2), \quad (4b)$$

$$I_3 = \det \mathbf{V} = V_{11}V_{22}V_{33} + 2V_{12}V_{13}V_{23} - V_{11}V_{23}^2 - V_{22}V_{13}^2 - V_{33}V_{12}^2. \quad (4c)$$

The invariant I_1 equals the trace and I_3 the determinant of the tensor coefficient matrix. I_2 is the sum of the coefficient matrix principal minor determinants by deleting one row and column.

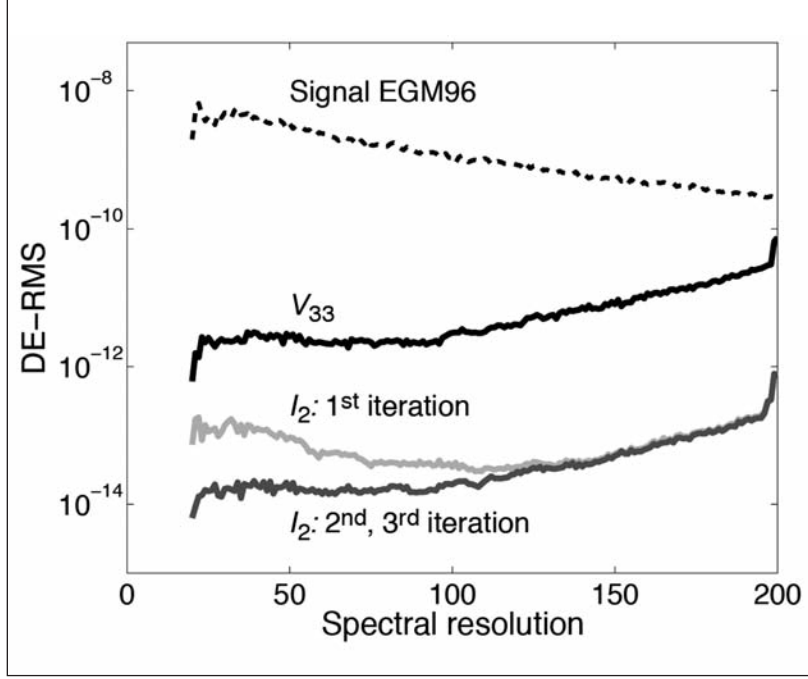


Figure 1: Invariant I_2 , linearization performance in terms of degree-error RMS values. Closed-loop simulation with initial linearization model OSU86F. The invariants solutions are relative to the V_{33} base-line accuracy.

In case of a nadir-pointing gradiometer of GOCE type the invariants system $\{I_1, I_2, I_3\}$ is particularly suited for gravity field recovery. Within this contribution we restrict ourselves on the invariant I_2 . The results and conclusions hold for I_3 accordingly. Analysis of the invariant I_1 , yields the trivial solution, however, might be used as constraint within the parameter estimation process. The superiority of the system $\{I_1, I_2, I_3\}$ is due to the minor effect of the (unobserved) off-diagonal tensor elements on the overall invariants computation, as will be discussed in Sect. 4.

3. Linearization

We achieved efficient linearization of the functional model (4b) by the calculation of perturbations relative to an a priori known reference solution according to

$$\delta I_2 = I_2 - I_2^{\text{ref}} \quad (5)$$

where I_2^{ref} indicate synthesized invariants from reference GGs U_{ij} , $i, j = 1, 2, 3$. The U_{ij} are approximations to the real GGs and thus $V_{ij} = U_{ij} + \delta V_{ij}$ holds true with δV_{ij} the (incremental) corrections to the a priori values. Neglecting all non-linear incremental correction terms, the linearized perturbation of I_2 becomes

$$\delta I_2 = -U_{11}\delta V_{11} - U_{22}\delta V_{22} - U_{33}\delta V_{33} - 2(U_{12}\delta V_{12} + U_{13}\delta V_{13} + U_{23}\delta V_{23}). \quad (6)$$

Linearization induces an iterative processing scheme. To start the iterative potential parameter estimation process, external information in terms of reference gradients U_{ij} is necessary. From the second iteration on, the actual result is used to set up the linearized functional model. The synthesis of the U_{ij} is done within the initialization phase of each iteration.

In order to demonstrate the performance of the proposed procedure we conducted a series of (error-free) closed-loop simulation studies. The GOCE-like synthetic test data set consists of 518400 samples using the EGM96 gravity field model [7] up to degree and order 300. Figure 1 highlights results adopting the gravity field model OSU86F [8] as initial a priori information. In Figure 1, the invariants estimates are displayed relative to the V_{33} reference solution (deviation of invariants analysis from V_{33} analysis, hence a relative measure), i.e., the V_{33} degree-error RMS curve serves as baseline accuracy.

The iterative process can be terminated after only two iterations, demonstrating the linearization error to be small. Moreover, further experiments showed that the linearization per-

formance is insensitive towards the a priori linearization field.

4. Full tensor gradiometry reconstruction

Exemplary for an arbitrary day of GOCE data registration, Figures 2 and 3 present the invariant I_2 on November 2, 2009. The comparison of forward modeled invariants (based on GGs derived from an a priori reference gravity field) with real data clearly reveals the destructive impact of the inaccurate GGs V_{12} and V_{23} on invariants computation. Neglecting the off-diagonal elements in Eq. (4b) yields values that are close to the reference invariants. Consequently, V_{12} and V_{23} have a minor effect on the overall invariants computation.

The same conclusion is also supported by the power spectral densities in Figures 4 and 5. Considering the off-diagonal GGs provided by GOCE results in a noise level well above the reference invariants signal (noise is defined here as the difference between the real and reference signal). Neglecting V_{12} and V_{23} , on the other hand, decreases the noise level below the reference signal.

For the invariant I_3 , the similar conclusion can be drawn from Figures 6, 7, 8 and 9, i.e., V_{12} and V_{23} have a minor effect on the overall invariants computation and neglecting V_{12} and V_{23} , decreases the noise level below the reference signal.

The geographical distribution of the invariant I_2 derived from the main diagonal GGs along the GOCE ground tracks for November and December 2009 is shown in Figure 10.

For GOCE data analysis, we propose to replace the elements V_{12} and V_{23} by forward modeled GGs. In each iteration step the actual estimate is used for the evaluation of V_{12} and V_{23} . Based on these values, invariants computation is straightforward and thus the solution of the linearized observation model. To start the iterative process, initial values have to be provided in terms of external information. Since the con-

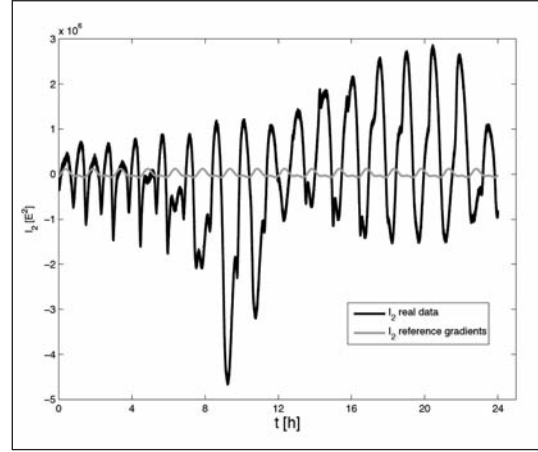


Figure 2: Invariant I_2 , 2. November 2009: real data, all GGs (black line); forward modeled reference invariants, all GGs (gray line).

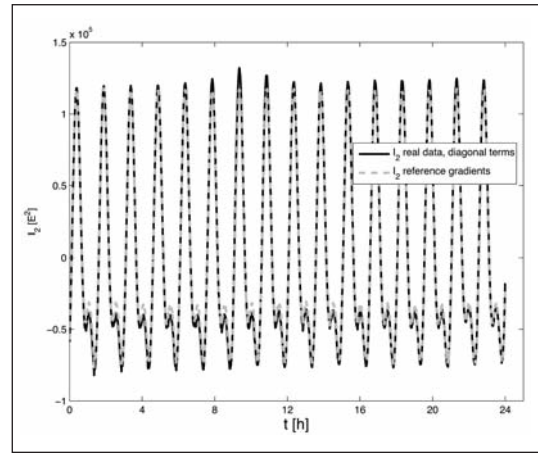


Figure 3: Invariant I_2 , 2. November 2009: real data, main diagonal GGs only (black line); forward modeled reference invariants, all GGs (gray dashed line).

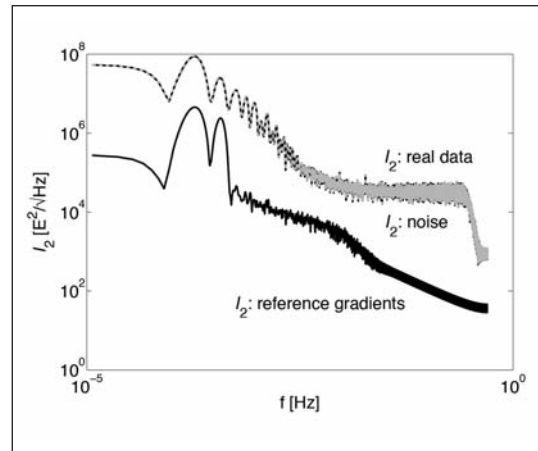


Figure 4: Invariant I_2 , 2. November 2009: real data, all GGs (black dashed line); forward modeled reference invariants, all GGs (black solid line); noise (gray solid line).

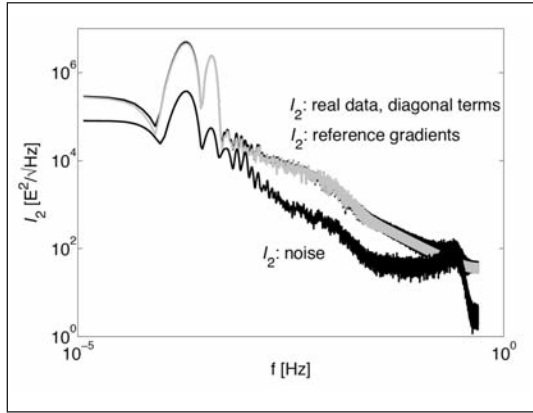


Figure 5: Invariant I_2 , 2. November 2009: real data, main diagonal GGs only (black dashed line); forward modeled reference invariants, all GGs (gray solid line); noise (black solid line).

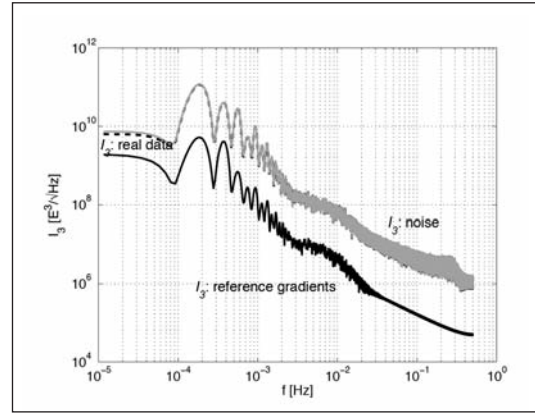


Figure 8: Invariant I_3 , 2. November 2009: real data, all GGs (black dashed line); forward modeled reference invariants, all GGs (black solid line); noise (gray solid line).

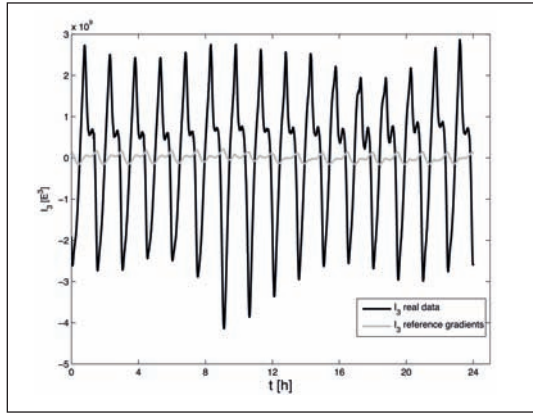


Figure 6: Invariant I_3 , 2. November 2009: real data, all GGs (black line); forward modeled reference invariants, all GGs (gray line).

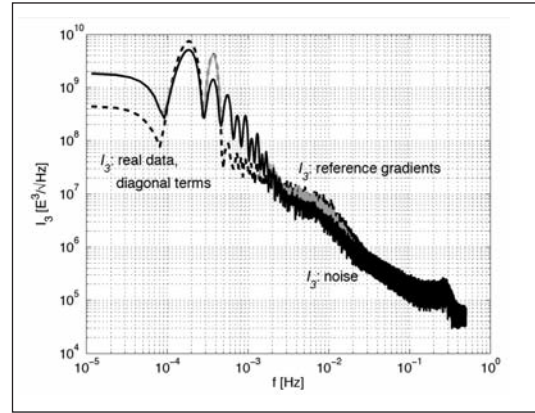


Figure 9: Invariant I_3 , 2. November 2009: real data, main diagonal GGs only (black dashed line); forward modeled reference invariants, all GGs (gray solid line); noise (black solid line).

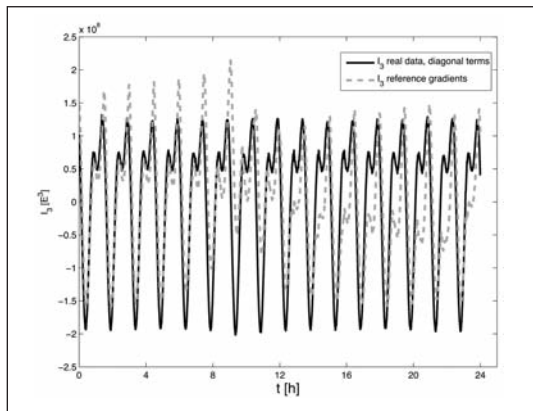


Figure 7: Invariant I_3 , 2. November 2009: real data, main diagonal GGs only (black line); forward modeled reference invariants, all GGs (gray dashed line).

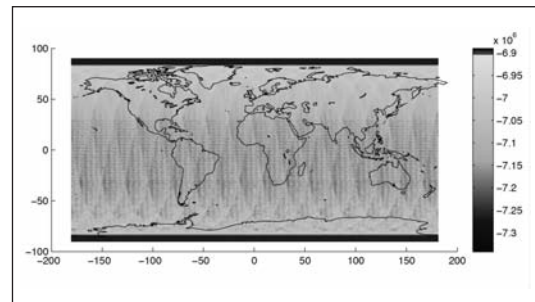


Figure 10: Global map of the Invariant I_2 from 02-Nov-2009 to 31-Dec-2009, in E2.

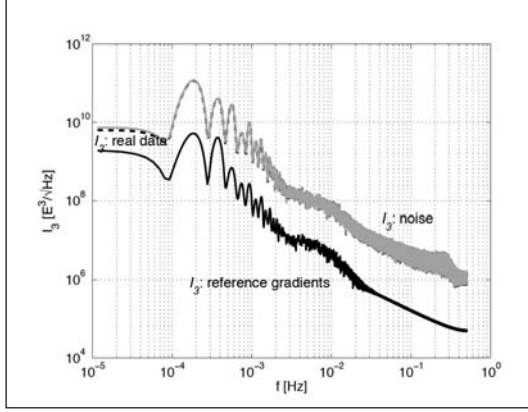


Figure 11: Invariant I_2 , GGs synthesis performance in terms of degree-error RMS values. Closed-loop simulation with initial linearization model OSU86F and additional synthesis of V_{12} and V_{23} with the trivial solution for the first iteration. The invariants solutions are relative to the V_{33} baseline accuracy.

tributions of V_{12} and V_{23} on invariants computation are small compared to the main diagonal components, the iterative process turned out to be insensitive towards the initial values for GGs synthesis. According to Figure 11, the elements can even be neglected in the first iteration without decisive influence on the convergence behavior and final results.

5. Stochastic model

Following the formalism in [11], temporal correlations of GGs can be modeled by means of an auto-regressive moving-average (ARMA) process. It is characterized by the filters \mathbf{F}_V subject to $\mathbf{D}(V_{ij}) = (\mathbf{F}_{V_{ij}}^T \mathbf{F}_{V_{ij}})^{-1}$ with $\mathbf{D}(V_{ij})$ the variance-covariance matrix of element V_{ij} . Here we make use of these filters in order to derive a filter for the invariants by error propagation.

According to Eq.(4b), the linearized invariant I_2 can be expressed by

$$I_2 = c_1 \delta V_{11} + c_2 \delta V_{12} + c_3 \delta V_{13} + c_4 \delta V_{22} + c_5 \delta V_{23} + c_6 \delta V_{33}. \quad (7)$$

The linear factors c_k , $k=1, \dots, 6$ are subject to the reference gradients U_{ij} , $i, j = 1, 2, 3$. Error propagation yields

$$\mathbf{D}(I_2) = \mathbf{J} \mathbf{D}(\mathbf{V}) \mathbf{J}^T. \quad (8)$$

Therein, \mathbf{J} denotes the matrix of linear factors (Jacobian matrix), $\mathbf{D}(\mathbf{V})$ the total GGs variance-covariance matrix, and $\mathbf{D}(I_2)$ the invariants variance-covariance matrix. Neglecting correlations between different types of GGs results in a block-diagonal structure of $\mathbf{D}(\mathbf{V})$. Consequently, $\mathbf{D}(I_2)$ simplifies to

$$\mathbf{D}(I_2) = \mathbf{J}_1 \mathbf{D}(V_{11}) \mathbf{J}_1^T + \dots + \mathbf{J}_6 \mathbf{D}(V_{33}) \mathbf{J}_6^T. \quad (9)$$

Inserting $\mathbf{D}(V_{ij}) = (\mathbf{F}_{V_{ij}}^T \mathbf{F}_{V_{ij}})^{-1}$ in Eq.(9) finally yields

$$\mathbf{D}(I_2) = \mathbf{J}_1 \mathbf{D}(V_{ij}) = (\mathbf{F}_{V_{ij}}^T \mathbf{F}_{V_{ij}})^{-1} \mathbf{F}_{V_{33}}^{-1} (\mathbf{J}_6^T \mathbf{F}_{V_{33}}^{-1})^T. \quad (10)$$

As a result, the invariants variance-covariance matrix is characterized by products between the (diagonal) matrices of linear factors and the inverse GGs filter matrices.

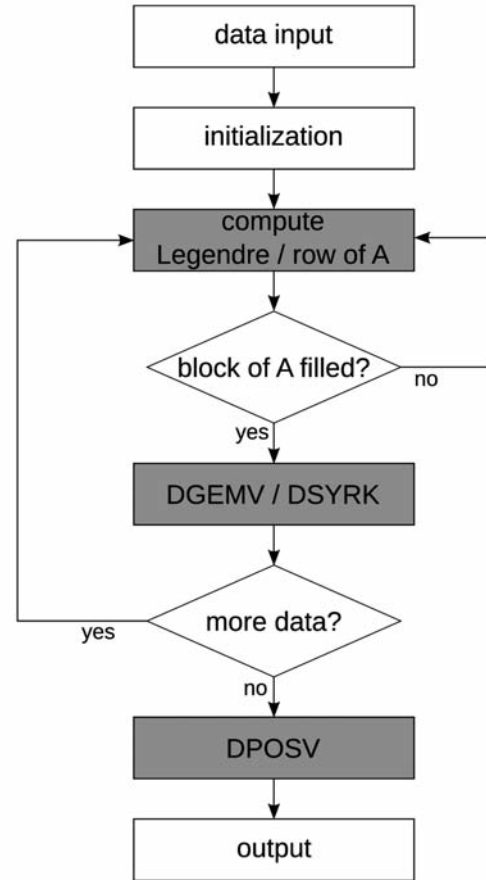


Figure 12: Implementation of normal equations system assembly and inversion on shard memory systems.

6. High Performance Computing

GOCE real data analysis requires the estimation of tens of thousands of unknown gravity field parameters from tens of millions of observations. The computational burden can only be tackled by a tailored parallel processing scheme. We implemented our analysis algorithms on high-performance computing platforms adopting OpenMP and MPI for parallelization. Here we present our parallelization strategies for the normal equations system inversion approach. A more comprehensive overview on least-squares solvers in the context of gravity field determination is provided in [2].

Figure 12 outlines our parallel processing scheme on shared memory systems. The design matrix is assembled block-wise (in order to reduce memory requirements) by the individual processors. Standard BLAS routines perform the necessary algebraic operations and sum up the block-wise normal equations systems. As all CPUs have access to all memory units of the system, data accessibility has not to be organized. After the assembling of the overall normal equations system, we solve it by inversion (Cholesky decomposition) using LAPACK routines.

On distributed memory systems, data accessibility has to be organized in detail, cf. Figure 13. CPU-specific data sets are inter-changed between the processors by block-cyclic distribution. PBLAS and ScaLAPACK routines allow for the assembly and inversion of the normal equations system.

Exemplary for the parallelization performance of our implementations, Table 1 summarizes achieved runtime results using up to 8~CPUs in parallel. Ranging from 88.8% to 93.8% of the total wall time, the NES computation is by far the most time-consuming part of the algorithm. With increasing number of CPUs, the NES inversion requires higher relative runtime costs. The computational effort for the design matrix assembly is less than 1%. The parallelization is performed successfully with very good speed-up results.

Table 1: Runtime results of normal equations system (NES) inversion, achieved with an SGI Altix 3700 system (shared-memory), 518400 observations, 40398 unknown parameters

CPUs	1	4	8
total runtime (h)	64.46	17.06	9.06
design matrix (%)	0.8	0.8	0.8
NES assembly (%)	93.8	92.1	88.8
NES inversion (%)	1.5	3.4	6.8
Speed-up	1	3.84	7.22

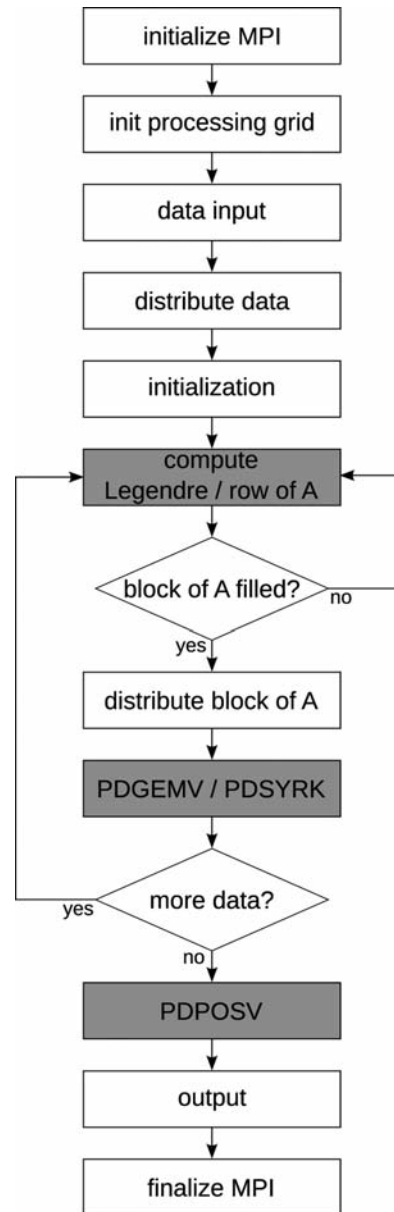


Figure 13. Implementation of normal equations system assembly and inversion on distributed memory systems.

7. Conclusions

We demonstrated the gravitational tensor invariants approach to be a viable alternative for GOCE gravity field recovery to more conventional analysis methods based on individual GGs. The alternative strategy is motivated by its independence of the gradiometer instrument orientation in space. Although rotation information in terms of angular velocities and accelerations is required to reduce the centrifugal and Euler effects, the orientation parameters themselves have not to be known.

The combination of linearization by means of perturbation theory, synthesis of unobserved GGs, error propagation for the modeling of the invariants variance-covariance information, and the parallelization of the analysis software prepare the approach for GOCE real data analysis.

Acknowledgements

This work was supported by the German Ministry of Education and Research (BMBF) in the framework of the GEOTECHNOLOGIEN research program under grant no. 03G0726G.

References

- [1] Baur O., Sneeuw N., Grafarend E.W., 2008, Methodology and use of tensor invariants for satellite gravity recovery, *J Geod* 82, 279--293, DOI~10.1007/s00190-007-0178-5
- [2] Baur O., 2009, Tailored least-squares solvers implementation for high-performance gravity field research, *Computers and Geosciences* 35, 548--556, DOI~10.1016/j.cageo.2008.09.004
- [3] ESA SP-1233, 1999, The four candidate Earth explorer core missions - gravity field and steady-state ocean circulation mission, European Space Agency Report SP-1233(1), Granada
- [4] Grafarend E.W., 1970, Die Genauigkeit eines Punktes im mehrdimensionalen Euklidischen Raum, Deutsche Geodätische Kommission, Series~C 153, Munich
- [5] Gurevic G.B., 1964, Foundations of the theory of algebraic invariants, P.~Noordhoff, Groningen
- [6] Korn G.A., Korn T.M., 2000, Mathematical handbook for scientists and engineers, Dover Publications, New York
- [7] Lemoine F.G., Kenyon S.C., Factor J.K., et al., 1998, The Development of the Joint NASA GSFC and NIMA Geopotential Model EGM96, NASA Goddard Space Flight Center, Greenbelt, 575pp
- [8] Rapp R.H., Cruz J.Y., 1986, Spherical harmonic expansions of the Earth's gravitational potential to degree 360 using 30' mean anomalies, Report~376, Department of Geodetic Sciences and Surveying, Ohio State University, Columbus
- [9] Rummel R., 1986, Satellite Gradiometry, in: Sünkel H. (Ed.) *Mathematical and Numerical Techniques in Physical Geodesy*, Lect Notes Earth Sci 7, Springer, Berlin Heidelberg New York, 317--363
- [10] Rummel R., Sanso F., van Gelderen M., et al., 1993, Spherical harmonic analysis of satellite gradiometry, Netherlands Geodetic Commission, New Series 39
- [11] Schuh W.-D., 1996, Tailored numerical solutions strategies for the global determination of the Earth's gravity field, *Mitteilungen der Universität Graz* 81
- [12] Siemes C., Schuh W.-D., Cai J., Sneeuw N. and Baur O. 2007, GOCE data processing: the numerical challenge of data gaps, GEOTECHNOLOGIEN Science Report Nr. 11 »Observation of the System Earth from Space«, 99-105

Stochastic model refinements for GOCE gradiometry data

Krasbutter I., Brockmann J.M., Kargoll B., Schuh W.-D.

Institute of Geodesy and Geoinformation, Department of Theoretical Geodesy, University of Bonn, Nussallee 17,
53115 Bonn, Germany, E-Mail: krasbutter@geod.uni-bonn.de

Abstract

In our approach to gravity field determination, the GOCE data are processed sequentially on a parallel computer system, iteratively via application of the method of preconditioned conjugate gradient multiple adjustment (PCGMA), and in situ via development of the functionals at the actual location and orientation of the gradiometer. GOCE gradiometry (SGG) data are auto-correlated in their three components V_{xx} , V_{yy} and V_{zz} so that one purpose of PCGMA is the adjustment of the unknown stochastic model of the gradiometer observations, described by decorrelation filters. A sequence of AutoRegressive-Moving Average (ARMA) filters is adjusted to the actual measurement noise to remove these correlations from the observations. This adjustment is refined iteratively, as it is embedded in the estimation of the gravity field parameters. In this contribution we show the effects of various filter complexities on the final gravity field solution and the corresponding error estimates based on two months of GOCE data.

1. Introduction

The Tuning Machine, as part of ESA's High-Level Processing Facility (HPF), was designed with the purpose of tuning the stochastic model of the gravity gradients observed by GOCE's gradiometer and to obtain an independent gravity field solution (cf. *Pail et al. 2006*, *Brockmann et al. 2010*, *Schuh et al. 2010*). Based on this gravity field model, the final solution of the so-called time-wise approach (cf. *Pail et al. 2006*, *Pail et al. 2010*) is com-

puted at TU Graz. The gravity field solution is determined by applying an iterative solver based on the method of preconditioned conjugate gradients (cf. *Schuh 1996*, *Boxhammer 2006*) and the corresponding covariance matrix by means of Monte-Carlo methods (cf. *Alkhatib 2007*).

In this paper we will demonstrate how the information content of the gravity gradient noise is effectively taken into account with the time-wise approach. In Sect. 2 we show the general characteristics of the real-data noise, and in Sect. 3 the effects of various approaches to modeling these characteristics by means of digital filters on the gravity field solution and its accuracies.

2. Characteristics of the gradiometer noise

To obtain a first impression of the gradiometer noise characteristics we determined the difference between mean- and GRS80-reduced measured gravity gradients (light gray curve) and mean- and GRS80-reduced gravity gradients computed from an a priori gravity field model (dark gray curve), see Fig. 1 This difference (black curve) serves as a first estimation of the unknown gradiometer noise (the three diagonal components V_{xx} , V_{yy} and V_{zz} show a very similar behavior, which is why only the V_{zz} component is depicted here). This noise estimate is seen to be of similar magnitude as the measured gravity field signal and to have low-frequency oscillations, indicating strong autocorrelatedness.

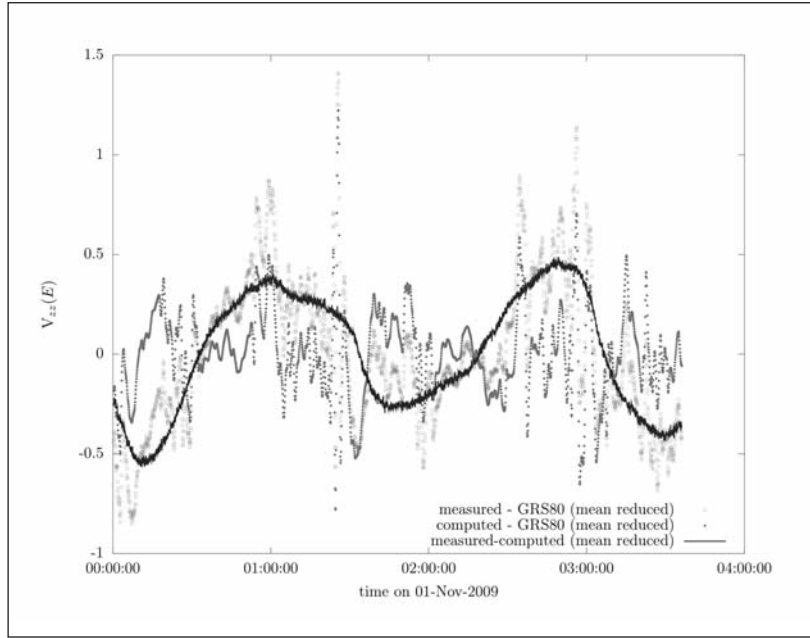


Figure 1: Reduced (mean and GRS80) measured gravity field gradients of GOCE for 3 hours and computed gravity field gradients from a gravity field model and the difference as a first estimation for the gradiometer

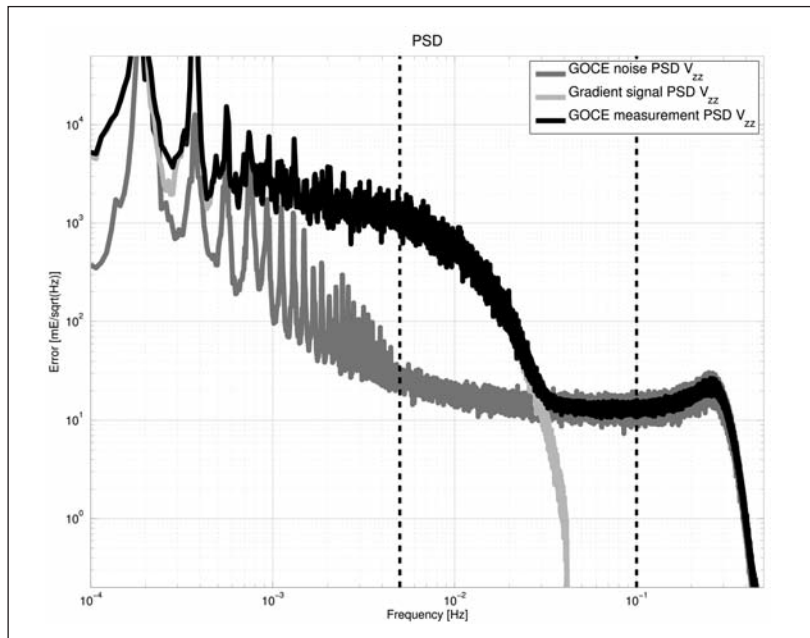


Figure 2: Power spectrum (PSD) of the gradiometer noise for the V_{zz} component, the gradient signal and the measured gravity gradients

These significant autocorrelations indicate that the noise is generated by a colored noise process, the details of which become more clearly visible after transforming the autocorrelation function of the noise time series into the spectral domain (see dark gray curve in Fig. 2). Within the measurement bandwidth (MBW, between 0.005 and 0.1 Hz), the power spectrum (PSD) is practically flat, i.e. white; between 0 and 0.005 Hz the spectrum is mainly characterized by an inverse proportional dependence (approx. $1/f$) and a large number of

sharp peaks. This reflects exactly the expected behavior, which was revealed by various case studies carried out before the satellite's launch (e.g. *Schuh et al. 2006*).

As the gravity field parameters are determined via a rigorous least-squares adjustment, this autocorrelation pattern must be taken into account by including the known (or an estimated approximation of the) data covariance matrix. However, due to the huge number of gradiometer data, this covariance matrix can-

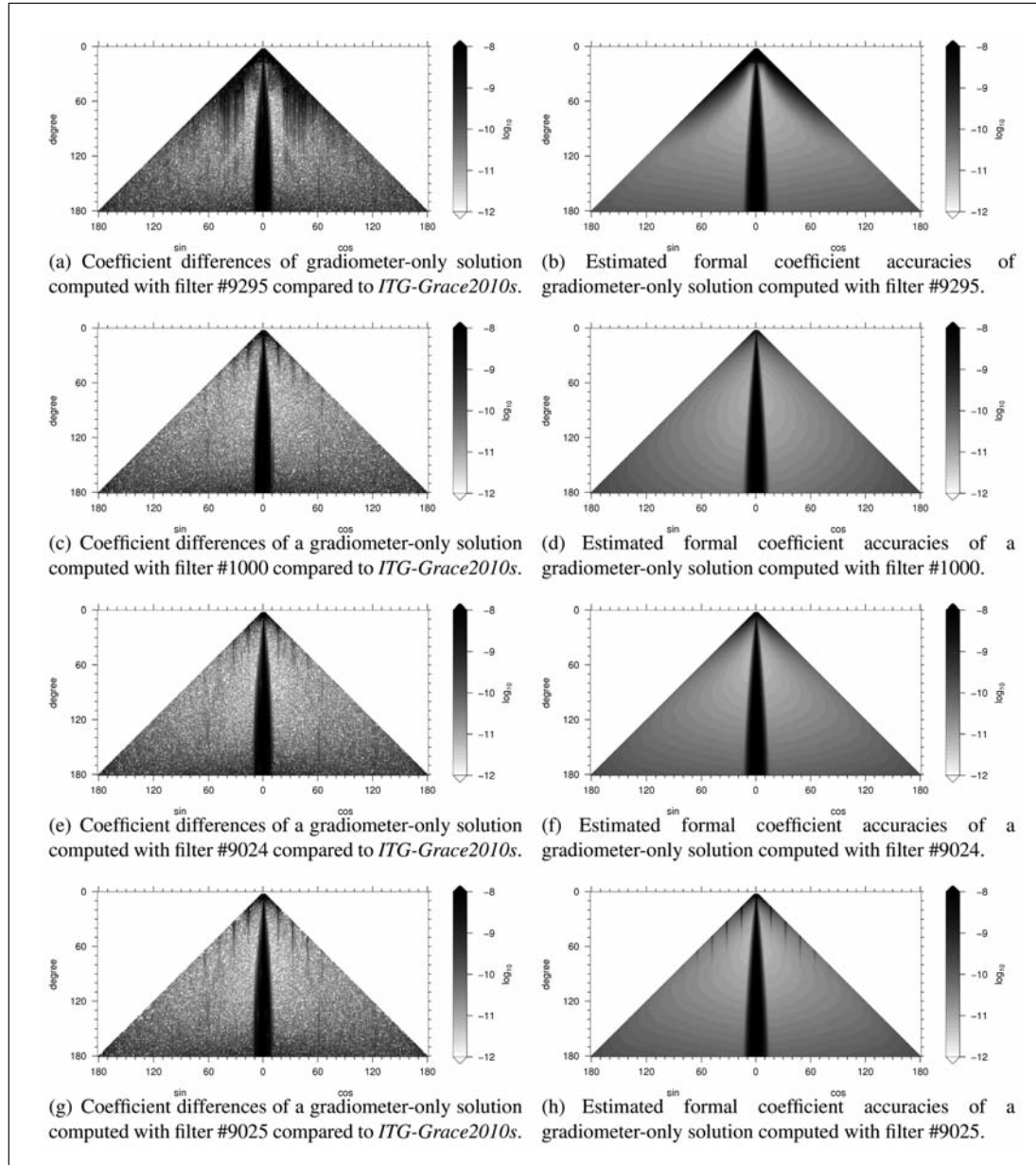


Figure 3: Coefficient statistics for all four presented gradiometer solutions with the four different filters. The shown statistics are: differences to the *ITG-Grace2010s* model (left column) and estimated formal coefficient standard deviations (right column)

not be stored in light of memory requirements of more than 20 PetaByte. An effective solution to this problem consists in a full decorrelation («whitening») of the gradiometer data before the adjustment is carried out. In the next section we show how such a decorrelation is performed through an application of digital filters (cf. *Schuh 1996, Siemes 2008 and Krasbutter 2009*).

3. Modeling the gradiometer noise

The colored noise characteristics of the gradiometer is taken into account by filtering the observations with a filter that has the inverse spectral characteristics with regard to the estimated noise characteristics as seen in the previous section. Such a filter acts as a decorrelation filter and can be modeled by means of cascades of ARMA processes (*Schuh 1995, Schuh 1996 and Siemes 2008*). As ARMA filters can be designed with an increasing num-

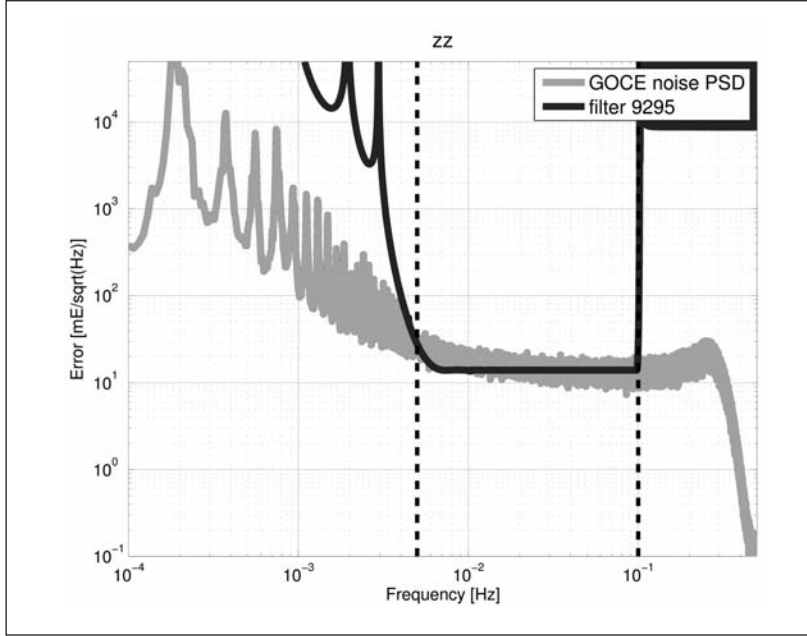


Figure 4: Noise power spectrum and inverse power spectrum of decorrelation filter # 9295 (MBW band-pass filter) w.r.t. the V_{zz} component (the other components show a similar behavior)

ber of free parameters to fit more and more details of the power spectrum the question arises how much the gravity field solution gains in accuracy when very detailed (and thus computationally more demanding as well as numerically more instable) ARMA filters are used in comparison to simpler filters. This question is investigated by fitting four types of ARMA filters to specific features of the spectrum.

3.1. Modeling of the MBW only

In the case that only the MBW is taken into account within the decorrelation process, a band-pass filter can be used (cf. Fig. 4), which cuts out the entire information outside the MBW. Gravity field determination with such a kind of filter is possible, but has certain disadvantages, as demonstrated in the following. A gradiometer-only gravity field solution computed with this filter is shown in terms of coefficient differences with respect to a GRACE-only model based on seven years of data and resolved up to degree and order (d/o) 180 ITG-Grace2010s, cf. *Mayer-Gürr et al. (2010)*.

Fig. 3 (a) shows that these differences are very large up to d/o 50 (the GRACE model is considered as a reference solution up to d/o 140, as GRACE is more sensitive to the lower degrees than GOCE gradiometry). In addition, large dif-

ferences occur for the sectorial coefficients from d/o 50 up to d/o 100. This behavior of the sectorial and near-sectorial coefficients is reflected by the estimated spherical harmonic coefficient accuracies shown in Fig. 3 (b). For d/o 80 up to 140, the differences to the GRACE model can be explained by the corresponding GOCE accuracies.

Thus, using a band-pass filter as shown in Fig. 4 produces a useful gradiometer-only gravity field and realistic estimates for the coefficient variances, but has the disadvantage that gradiometer information in the lower frequencies is ignored which affects the sectorial coefficients up to d/o 100.

3.2 Modeling the low-frequency part of the spectrum

As the band-pass filter of Sect. 3.1 was seen to produce systematic errors for the sectorial coefficients, it is advisable to also model the low-frequency noise characteristics. Such a filter should not completely filter out the low-frequency part of the power spectrum, but reflect its low accuracy when applied as a decorrelation filter in gravity field determination. The simplest filter of this kind is a differencing filter (#1000) as shown in Fig. 5.

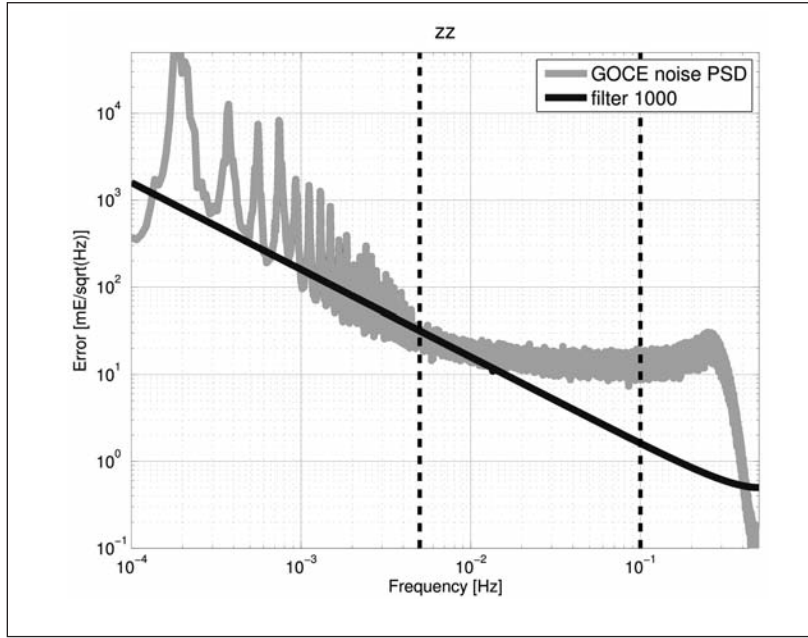


Figure 5: Noise power spectrum and inverse power spectrum of decorrelation filter # 1000 (differencing filter) w.r.t. the Vzz component (the other components show a similar behavior)

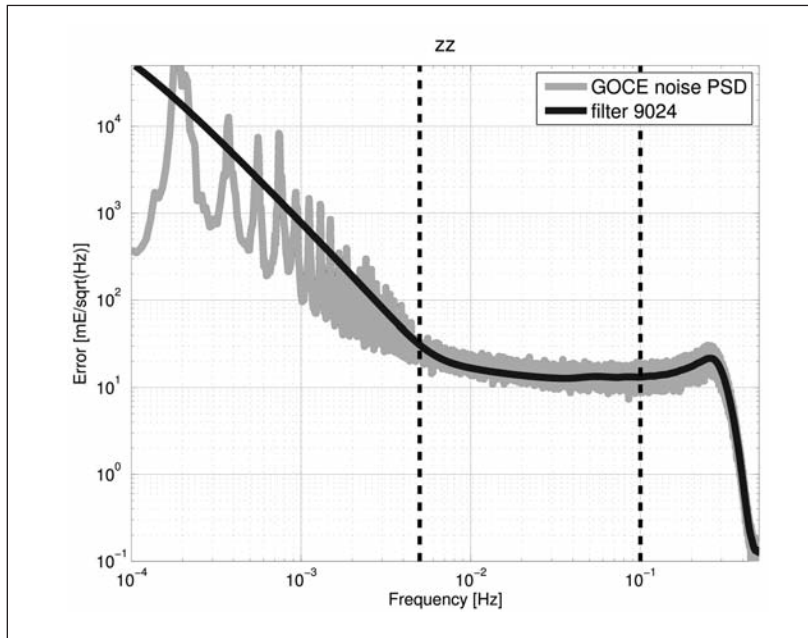


Figure 6: Noise power spectrum and inverse power spectrum of decorrelation filter # 9024 w.r.t. the Vzz component (the other components show a similar behavior)

A comparison of a gradiometer-only gravity field solution using this filter with a GRACE model is shown in Fig. 3 (c). It can be seen that the lower degree differences (up to d/o 80) are smaller than the corresponding degree differences based on the solution with a band-pass decorrelation filter (determined in Sect. 3.1). In addition, Fig. 3 (d) shows that the sectorial coefficients of d/o 20 and higher are determined more precisely in this case (compared to Fig. 3(b)) which is a desirable consequence of

having taken into account the low-frequency part of the power spectrum. However, as the differencing filter does not reflect the MBW as accurately as the band-pass filter, the variances of the higher degrees and orders cannot be estimated as realistically. To avoid the undesirable features of the band-pass and the differencing filter, both filter characteristics can be combined as demonstrated in the following.

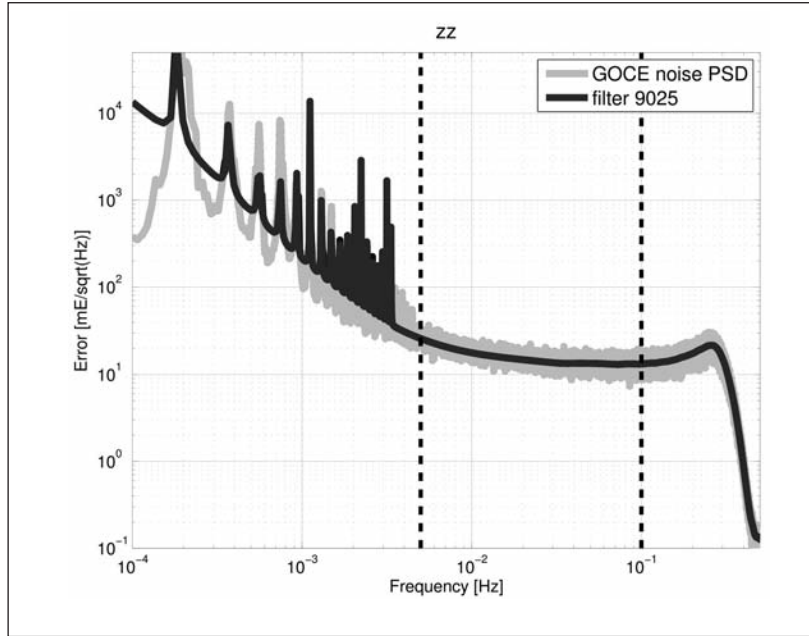


Figure 7: Noise power spectrum and inverse power spectrum of decorrelation filter # 9025 w.r.t. the V_{zz} component (the other components show a similar behavior)

3.3. Simple modeling of the complete spectrum

Combining the features of a band-pass and a differencing filter yields a simple filter model for the entire spectrum. Such a filter is represented by a sequence (cascade) of basic ARMA filters. Fig. 6 (filter # 9024) shows the spectral characteristics of a parsimonious cascade of ARMA filters, which nevertheless represents an apparently overall adequate fit to the noise characteristics, but ignores the sharp peaks in the low-frequency part of the spectrum.

The resulting gravity field solution (see Fig. 3 (e) and 3 (f)) combines the advantages of the band-pass filter solution and the difference filter solution: both the low-degree and the sectorial coefficients are determined accurately and the variances for the higher d/o coefficients are estimated more realistically than for the filter models used in Sect. 3.1 and 3.2.

3.4. Detailed modeling of the complete spectrum

Extending the ARMA filter cascade of the previous Sect. 3.3 to also take into account the sharp spectral peaks leads to a more complex decorrelation filter as shown in Fig. 7. These peaks are modeled by means of notch filters, represented by 20 additional individual AR - MA(2,2) filters.

Although such detailed modeling of the complete spectrum does not lead to a significant improvement of the solution (see Fig. 3 (g)), it evidently leads to far more realistic accuracy estimates (see Fig. 3 (h)). The error pattern with stripes occurring for degrees 16, 32,..., which is already clearly visible in the coefficient differences with respect to the ITG-Grace2010s solution (cf. Fig. 3 (g)), is now correctly mapped into the coefficients' covariance matrix (cf. Fig. 3 (h)).

4. Summary and conclusions

Much effort has been put into the refinement of the stochastic model of GOCE gradient measurements and matching digital decorrelation filters to obtain not only a realistic gravity field solution but also a corresponding realistic full covariance matrix. It must be stressed that the estimated spherical harmonic coefficients must be consistent with the corresponding accuracy estimates in order to provide meaningful GOCE-only gravity field information that can be used in a multitude of applications e.g. in geodesy, geophysics, and oceanography. Filter # 9024, which represents a simple decorrelation filter model for the entire gradiometer noise power spectrum (as described in Sect. 3.3), was applied for the computation of the

global gravity field model GO_CONS_GCF_2_TIM, which is based on the time-wise approach and constitutes one of the first GOCE-only gravity field models (Pail *et al* 2010).

Acknowledgments

This work was financially supported by the BMBF Geotechnologien program REAL-GOCE. GOCE data access was granted by ESA GOCE HPF main contract No. 18308/04/NL/MM. The computations were performed on the JUROPA supercomputer in Jülich. The computing time was granted by John von Neumann Institute for Computing (project HBN15).

References

Alkhatib, H. (2007) On Monte Carlo methods with applications to the current satellite gravity missions. Dissertation, <http://hss.ulb.uni-bonn.de/2007/1078/1078.htm>, Institute of Geodesy and Geoinformation, University of Bonn.

Boxhammer, C. (2006) Effiziente numerische Verfahren zur sphärischen harmonischen Analyse von Satellitendaten. Dissertation, Institute of Geodesy and Geoinformation, <http://hss.ulb.uni-bonn.de/2006/0799/0799.htm>, University of Bonn.

Brockmann, J.M., B. Kargoll, I. Krasbutter, W.-D. Schuh and M. Wermuth (2010) GOCE Data Analysis: From Calibrated Measurements to the Global Earth Gravity Field. Flechtner, F., T. Gruber, A. Güntner, M. Manda, M. Rothacher, T. Schöne and J. Wickert (eds.), System Earth via Geodetic-Geophysical Space Techniques, Advanced Technologies in Earth Sciences, Springer Berlin Heidelberg, 213-229.

Krasbutter, I. (2009) Dekorrelation und DatentüV der GOCE-Residuen. Diploma thesis, Universität Bonn.

Mayer-Gürr, T, E. Kurtenbach and A. Eicker (2010), ITG-GRACE2010. <http://www.igg.unibonn.de/apmg/index.php?id=itg-grace2010>, 2010.

Pail, R., B. Metzler, B. Lackner, T. Preimesberger, E. Höck, W.-D. Schuh, H. Alkathib, C. Boxhammer, C. Siemes and M. Wermuth (2006) GOCE gravity field analysis in the framework of HPF: operational software system and simulation results. In: 3. GOCE user workshop. ESA, Frascati.

Pail, R., H. Goiginger, R. Mayrhofer W.-D. Schuh, J.M. Brockmann, I. Krasbutter, E. Höck and T. Fecher (2010) Global gravity field model derived from orbit and gradiometry data applying the time-wise method. In: ESA Living Planet Symposium, ESA Living Planet Symposium. SP-686, Bergen.

Schuh, W.-D. (1996) Tailored Numerical Solution Strategies for the Global Determination of the Earth's Gravity Field, Vol. 81 Mitteilungen der geodätischen Institute der Technischen Universität Graz. TU Graz.

Schuh, W.-D., C. Boxhammer and C. Siemes (2006) Correlations, variances, covariances - from GOCE signals to GOCE products. In: 3. GOCE user workshop. ESA, Frascati.

Schuh, W.-D., J.M. Brockmann, B. Kargoll and I. Krasbutter (2010) Adaptive Optimization of GOCE Gravity Field Modeling. In: Münster, G., D. Wolf and M. Kremer (eds.), NIC Symposium 2010, Vol. 3 IAS Series. Jülich, Germany, 313-320.

Schuh, W.D. (1995) SST/SGG tailored numerical solution strategies. ESA-Project CIGAR III / Phase 2, WP 221, Final-Report, Part 2.

Siemes, C. (2008) Digital Filtering Algorithms for Decorrelation within Large Least Squares Problems. Dissertation, <http://hss.ulb.uni-bonn.de/2008/1374/1374.htm>, Institute of Geodesy and Geoinformation, University of Bonn.

GLObal gravity field determination with REgional refinements by the analysis of GOCE level-1b data (GLOREGOCE)

Shabanloui A., Schall J., Mayer-Gürr T., Eicker A., Kusche J., Kurtenbach E.

Astronomical, Physical and Mathematical Geodesy Group, Institute of Geodesy and Geoinformation, University of Bonn,
Nussallee 17, 53115 Bonn, Germany, E-Mail: shabanloui@geod.uni-bonn.de

1. Abstract

The Gravity Field and Steady-State Ocean Circulation Explorer (GOCE) is characterized by the fact that the GOCE satellite flies in an extremely low near polar orbit of 260 km altitude. The pure free fall motion is permanently maintained by a feedback system for compensating the surface forces acting on the GOCE. Based on high-low Satellite to Satellite Tracking (hl-SST) observations, orbit of GOCE can be estimated with an accuracy of 2-3 cm. The global and regional Earth's gravity field based on the short arc concept can be determined. In this paper, the GOCE precise orbit determination procedure is realized with an in-house developed software. Global Earth's gravity field and some regional refinements are introduced.

2. Introduction

GOCE, the first core explorer of the European Space Agency (ESA) Living Planet Program which was launched at 17 March 2009, is equipped with a gradiometer to measure the short wavelength of the Earth's gravity field (wavelength of 100-1500 km). In addition, GOCE flies a high precision, dual frequency GPS Lagrange receiver for precise orbit determination (POD) purpose and providing gravity field information for the long wavelengths (wavelength of 400-40000 km), which partially overlaps with the gradiometer sensitivity. The attitude of the satellite precisely is observed by star tracking camera. In addition, a drag-free control system compensates the re-

latively large atmospheric drag at the low altitude (about 260 km) of GOCE. The objective of GOCE is to model the mean Earth's gravity field with an accuracy of 1-2 cm and 1 mgal in terms of geoid and gravity anomalies at the wavelength of 100 km. In this paper, at first, precise orbit determination strategy has been introduced. Then, regional refinement strategies as complement to global gravity field recovery will be presented and applied to real GOCE data.

3. Precise Orbit Determination (POD)

Precise orbit determination of GOCE plays an important role in order to recover the Earth's gravity field based on hl-SST observations. Moreover, precise orbit determination is required for precise geo-locating the satellite gravity gradient (SGG) observations derived from gradiometer measurements and providing time series of point-wise precise satellite positions.

In this paper, the zero differenced estimation procedure has been applied to GOCE observations and the solution is denoted as Geometrical Precise Orbit Determination (GPOD). The geometrical POD solution is based on zero difference (un-differenced) hl-SST observations, final IGS GPS ephemerides at the interval of 15 minutes and GPS clocks from CODE at the interval of 30 sec. The final GPS ephemerides and clocks are fixed during the geometrical (point-wise) computation of the GOCE orbit. The orientation of GOCE can be derived from quaternion information which are observed by

star tracker camera. In addition, precise mass center position of GOCE can be determined based on quaternion values. The process of geometrical precise orbit determination is purely based on the tracking of hl-SST observations in combination with solutions of the GPS ephemerides and clocks and does not rely on forces acting on satellite (Shabanloui, 2008). In addition, it is possible to provide variance-covariance information between consecutive geometrically determined positions to improve kinematical velocities for use by gravity field retrieval methods e.g. energy balance method. The geometrical precise orbit determination solutions are point-wise and can be considered to be independent from a-priori force models for the GOCE trajectory. Therefore, they can be used for an independent contribution to the retrieval of the low to medium resolution part of the Earth's gravity field. It has to be noted that the geometrical solutions might contain data gaps since position estimates can be obtained only for those epochs for which a sufficient number of GPS satellites is in view.

It should be mentioned that the clock of the Lagrange GPS receiver on-board GOCE is a free running clock, so that its behavior includes occasional steering jumps of 20ms due to 50 Hz sampling rate. Therefore, the observation epoch is not steered to integer second. The jumps accumulate over time and can differ from integer seconds by as much as 0.5 sec (Visser et al. 2009). To handle hl-SST observations at non integer seconds, either the SST observation should be interpolate to integer seconds, or the GPS ephemerides and clock

solution should be interpolated to observed epochs. Because of the high velocity of GOCE, interpolation of SST observations to integer second seems to be dangerous. To avoid interpolation of SST observation in zero differenced estimation mode, it is recommended to interpolate the GPS ephemerides and clocks to the observation (real) second. When use is made of differences between observations from the GPS receiver on-board GOCE and high quality IGS ground stations, interpolation in the SST observation time is used for proper synchronization.

The geometrical point-wise of GOCE has been estimated based on an in-house developed GNSS data processing software package (Shabanloui, 2008). The estimated GPOD accuracy relies on the geometrical status of the GPS configuration, the number of tracked GPS satellites as well as on the GNSS measurements. The three-dimensional accuracy of 2-3 cm for the GOCE orbit is realized. Figures 1(a) and 1(b) show the point-wise absolute position differences between estimated GPOD of GOCE and geometrical PSO (Precise Science Orbit) solution based on hl-SST observations and corresponding carrier phase observation residuals for a short arc length of 30 minutes, respectively. It should be mentioned that the proposed geometrical precise orbit determination strategy can be used to estimated long arcs (e.g. 1 day) of the GOCE.

4. Short Arc Approach

The very low orbit altitude of GOCE and the observation concept of satellite gravity gradi-

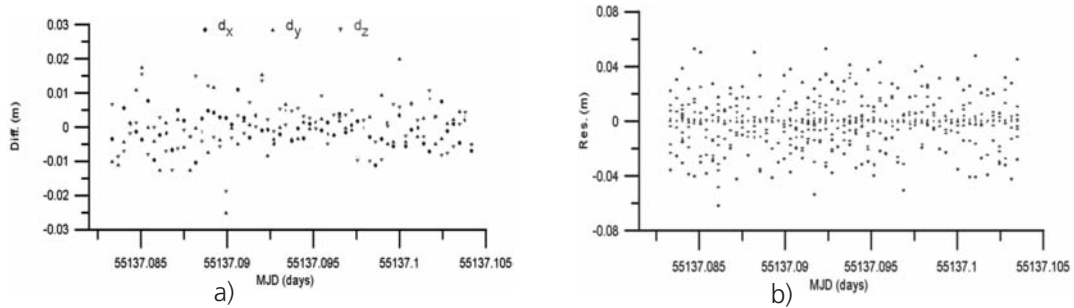


Figure 1: (a) Point-wise absolute position differences between estimated GPOD and PSO solution (b) SST carrier phase observation residuals.

metry which measures the second derivatives of the gravitational potential allows the determination of small gravity field details. The large number of parameters that is needed for the representation of such a high resolution gravity field has to be derived from an even larger number of correlated observations. Estimating the unknown gravity field parameters by a standard least squares adjustment results in very large equation systems, setting up of which would ask more storage than generally available. Also for runtime reasons it is reasonable to reduce the problem.

The analysis procedure applied here is dealing with short arcs of the satellite orbit. Thus the normal equations

$$\mathbf{N} = \sum_i \mathbf{A}_i^T \mathbf{P}_i \mathbf{A}_i \text{ and } \mathbf{n} = \sum_i \mathbf{A}_i^T \mathbf{P}_i \mathbf{l}_i \quad (1)$$

can be accumulated from the individual blocks \mathbf{A}_i , \mathbf{P}_i and \mathbf{l}_i of the design matrix, weight matrix and the observation vector given for each arc i , respectively. This procedure implies that the weight matrix is block diagonal and neighbouring arcs are independent. Variance covariance information per short arc is derived by estimating an empirical covariance function from the residuals to a highly expanded reference model. Since the gravity gradients are correlated over long periods of time the assumption of uncorrelated short arcs is not strictly valid. Therefore, further empirical parameters are introduced into the noise model. These additional parameters account for the long term error behaviour and should care for the independence of orbit arcs. For the time being, an unknown constant per arc and gradient tensor element is implemented.

The short arc approach provides numerous advantages: Firstly, discontinuities and gaps in the observation series can easily be dealt with by starting a new arc after each data gap. By arc-wise weighting of the observations the influence of outliers can be kept low, as explained in *Mayer-Gürr (2006)*. In addition, an analysis procedure based on short arcs can be applied for regional gravity field analysis as a method of refining global solutions, as applied in *Eicker et al. (2010)*. For the regional applica-

tions only satellite information covering the region of interest is used, which results in many discontinuous short arcs.

5. Regional Gravity Field Analysis

A spherical harmonic expansion is the classical way of representing the gravity field. The disadvantage is that spherical harmonics are basis functions with global support. The smoothness of the gravity field varies for different geographical areas. However spherical harmonics realise a global uniform resolution, which can be adapted neither to the local data density nor to the local data variability. Even if the series is expanded high enough to resolve local details, coefficients of high degree and order would be weakly determined and very noisy. By applying global regularisation detailed gravity information would finally get lost. Moreover a spherical harmonic model requires global, homogeneous distributed data or strong regularisation in case of data gaps such as GOCE polar regions. To overcome difficulties as mentioned above it makes sense to complement global gravity field recovery by regional refinement methods. For this purpose the observations are reduced by a global spherical harmonic model and the residuals are explained by alternative modelling techniques which can individually be adapted in resolution and regularisation. For the GOCE mission this aspect is of particular interest due to its strength in observing the short wavelength variations in the static gravity field. Many alternative gravity field representations based on space localising base functions has been proposed, examples are mascons (e.g. *Rowlands et al. 2010*), wavelets (e.g. *Panet et al. 2009*) and slepian functions (e.g. *Simons et al. 2006*). An overview of different regional modelling techniques applied to satellite gravitydata can be found in *Schmidt et al. (2006)*. In our approach we will use radial basis functions (RBFs), for a detailed description see *Eicker (2008)*.

The observation equation connecting RBFs to the gravity gradient tensor reads

$$\nabla \nabla V(\mathbf{x}) = \sum_i \alpha_i \nabla \nabla P(\mathbf{x}, \mathbf{x}_i) . \quad (2)$$

The function value at evaluation point is presented by a linear combination of RBFs $P(\mathbf{x}, \mathbf{x}_i)$ which are placed at nodal points \mathbf{x}_i and scaled by the base function coefficients α_i . The radial basis function

$$P(\mathbf{x}, \mathbf{x}_i) = \frac{GM}{R} \sum_{n=n_0}^N \left(\frac{R}{r}\right)^{n+1} k_n P_n(\mathbf{x}, \mathbf{x}_i) \quad (3)$$

can be expressed by a finite sum of Legendre polynomials $P_n(\mathbf{x}, \mathbf{x}_i)$ depending only on the spherical distance between evaluation and nodal point on the unit sphere. In this formula k_n controls the shape and smoothness of the function, $(R/r)^{n+1}$ is the continuation operator and the multiplication by GM/R ensures small, dimensionless values of the scaling coefficients. Fixing the truncation degree according to the expected signal content in the region under investigation there are still the number of RBFs and four more parameters per base function to be determined (shape, position, scale). The design of the radial basis functions is derived from the covariance function characterising the statistical properties of the gravity field. In practice the basis functions are always applied to model residual information to a given global reference field. Thus, in our approach the shape coefficients are chosen as the difference degree variances to the real gravity field which can be approximated by the formal errors of the reference solution. For degrees higher than the maximum degree provided by the reference field the difference degree variances become the degree variances themselves. The RBFs are located at the nodes of a globally defined, uniform grid with the number of global grid points corresponding to the number of unknown parameters of a spherical harmonic expansion with equal resolution.

The scaling coefficients are estimated in a regularised least squares adjustment. The normal equations are accumulated block by block, a Tikhonov regularisation matrix is added and the system is solved by a variance component estimation procedure, as described by *Koch and Kusche (2001)*.

6. Production of Gravity Field Models

In this section the applicability of the described approach is demonstrated. As a first step a global gravity field model based on a spherical harmonic expansion is determined using precise GOCE orbits only. This reference model is then refined by means of radial basis functions using very precise gravity gradiometry observations. All results that we will show here are derived from one month of GOCE data. A small test area which features rough gravity signal has been selected in the South Atlantic Ocean east of Patagonia.

6.1. Global Reference Solution

Precise orbit observations derived from satellite to satellite tracking in high-low mode are used as input data for the calculation of the global reference solution. The analysis procedure is based on the integral equation approach using short arcs of about 30 minutes. To avoid aliasing effects the same standard background models as for ITG-Grace2010 have been reduced (*Mayer-Gürr et al. 2010*). For a detailed description of the processing strategy readers are referred to *Mayer-Gürr (2006)*.

Figure 2 shows the difference degree variances to ITG-Grace2010s and the formal errors for an unconstrained and a constrained SST solution. In the variance view the influence of the polar data gap becomes clearly visible. The unregularised SST solution up to the safely determined degree 100 provides the basis for further local refinements.

6.2. Regional Refinement Procedure

For the regional refinement procedure only satellite observations covering the test area are of interest. As input data the three main diagonal elements of the gravity gradient tensor are used. They are reduced by observations calculated from the global reference solution and by the standard de-aliasing models as mentioned above. For the design of the local basis functions the formal errors of the SST solution are used up to degree $n=100$. Above the signal content is approximated by the degree variances of EGM2008 up to degree $n=220$. The nodal points as locations for the basis func-

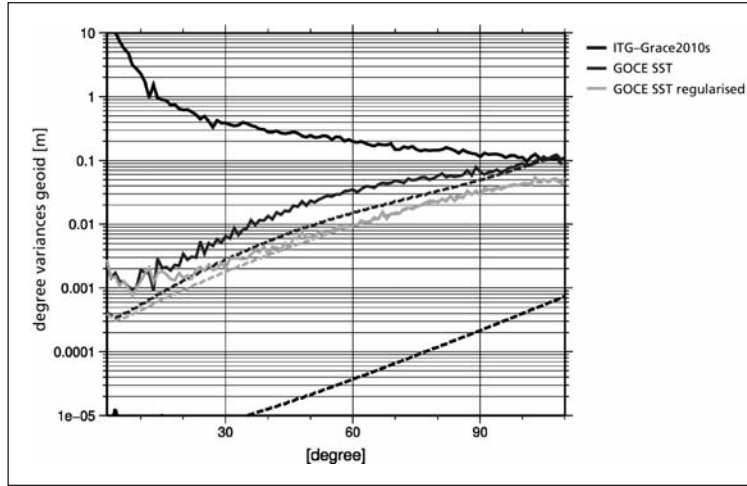


Figure 2: Difference degree variances to ITG-Grace2010s.

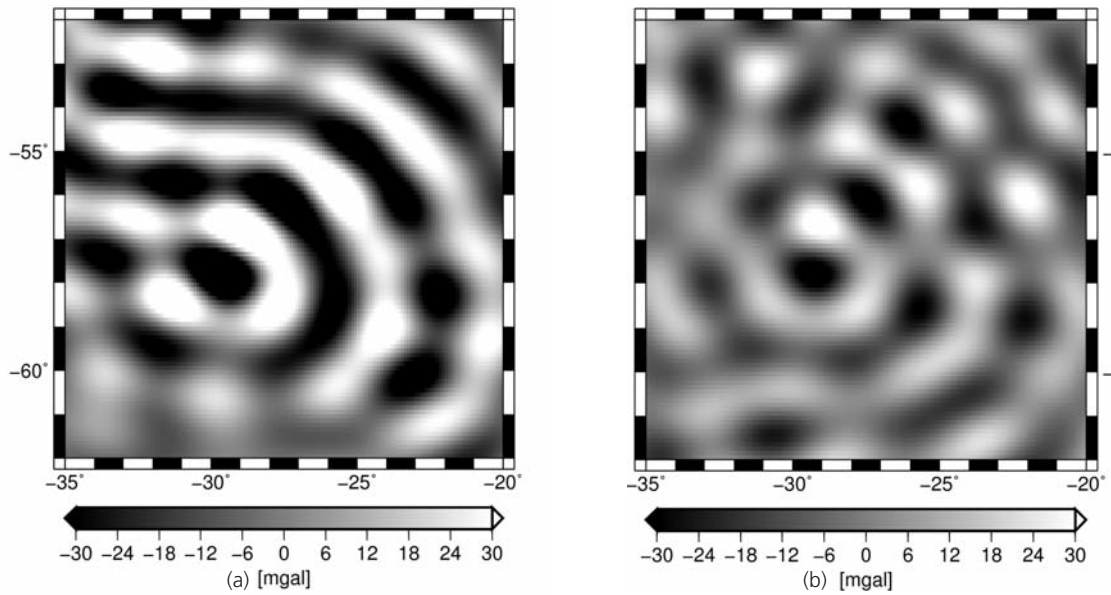


Figure 3: Differences to ITG-Grace2010c expressed in gravity anomalies
(a) Difference between ITG-Grace2010s (d/o 180) and ITG-Grace2010c (d/o 220), rms = 23mga,
(b) Difference between regionally refined GOCE SST solution and ITG-Grace2010c (d/o 220), rms=12mgal.

tions are generated on a grid by a uniform subdivision of an icosahedron resulting in a triangular grid with 59292 global grid points. This corresponds to a resolution slightly higher than a spherical harmonic degree of $n=220$. When the global grid is cut to the test area, an additional stripe of 3° is considered to prevent the interior solution from modelling errors.

This setting is then applied to calculate a regional gravity field model from one month of GOCE gradiometer data as refinement to the global SST reference solution. The results are shown in Figure 3(b) as differences to the global model ITG-Grace2010c. This combination

model includes terrestrial data sets and serves as pseudo-real comparison due to the superior accuracy of the terrestrial information in the higher frequencies. To illustrate the improvements achieved by GOCE, in Figure 3(a) differences for the GRACE-only model ITG-Grace2010s compared to the combination model are plotted. The reduced RMS value for the GOCE solution demonstrates the applicability of the approach described above.

7. Conclusions and Outlook

Gravity field recovery procedures have been presented and applied to the analysis of real

GOCE observations. It can be concluded that the use of short arcs is adequate for global and regional gravity field determination from GOCE. To evaluate the influence of the regional refinement procedure with more detail, a comparison of a regionally refined model to a global GOCE SGG solution will be necessary. This will be carried out in the future. Despite the results already achieved there still remains potential for further improvements. For example further effort should be made for an appropriate modelling of the observation errors. So far long wavelength correlations have been taken into account by estimating a bias per arc and gradient tensor component. It has to be investigated if there is any better description for the long term error behaviour of the gravity gradients. Another advancement is possible with regard to the regional refinement approach. So far the nodal points of local basis functions has been selected such that they build a regular nodal point pattern without considering the specific gravity field features. First investigations have already been made to estimate the positions of the basis function nodal points jointly with their scaling coefficients. Finally, the gravity models presented above have been calculated from a relatively small amount of observation data, i.e. one month GOCE data. An improvement in accuracy will be achieved when dealing with a longer observation period, not only due to the additional data but also because of a better global coverage.

Acknowledgements

The financial support by BMBF (Bundesministerium für Bildung und Forschung) within the frame of the Geotechnologien-Programm and providing GOCE data by ESA (European Space Agency) are gratefully acknowledged.

References

EICKER, A. (2008): Gravity field refinements by radial basis functions from in-situ satellite data. Ph.D. thesis, University of Bonn, Bonn, Germany.
EICKER, A., T. MAYER-GÜRR, K.-H. ILK and E. KURTENBACH (2010): Regionally refined gravi-

ty field models from in-situ satellite data. FLECHTNER, F., T. GRUBER, A. GÜNTNER, M. MANDEA, M. ROTHACHER, T. SCHOENE and J. WICKERT (Eds.), *System Earth via Geodetic-Geophysical Space Techniques*, Springer. ISBN (Print) 978-3-642-10227-1, DOI: 10.1007/978-3-642-10228-8, pp 41 - 58, 2010.

KOCH, K.R. and J. KUSCHE (2001): Regularization of geopotential determination from satellite data by variance components. *Journal of Geodesy*, 76(5):641–652.

MAYER-GÜRR, T. (2006): *Gravitationsfeldbestimmung aus der Analyse kurzer Bahnbögen am Beispiel der Satellitenmissionen CHAMP und GRACE*. Ph.D. thesis, University of Bonn, Bonn, Germany.

MAYER-GÜRR, T., E. KURTENBACH and A. EICKER. (2010): ITG-Grace2010 gravity field model, 2010. <http://www.igg.uni-bonn.de/apmg/index.php?id=itg-grace2010>.

PANET, I., Y. KUROISHI and M. HOLSCHNEIDER (2009): Wavelet modeling of the gravity field by domain decomposition methods: an example over Japan. *Geophysical Journal International*, submitted.

ROWLANDS, D.D., S.B. LUTHCKE, J.J. MCCARTHY, S.M. KLOSKO, D.S. CHINN, F.G. LEMOINE, J.-P. BOY and T.J. SABAKA (2010): Global mass flux solutions from GRACE: A comparison of parameter estimation strategies - Mass concentrations versus Stokes coefficients. *Journal of Geophysical Research*, 115, B01403.

SCHMIDT, M., M. FENGLER, T. MAYER-GÜRR, A. EICKER, J. KUSCHE, L. SANCHEZ and S.-C. HAN (2006): Regional gravity modeling in terms of spherical base functions. *Journal of Geodesy*, 81:17–38.

SHABANLOUI, A. (2008): A new approach for a kinematic-dynamic determination of Low satellite orbits based on GNSS observations. Ph.D. thesis, University of Bonn, Bonn, Germany.

SIMONS, F.J., F.A. DAHLEN and M.A. WIECZOREK (2006): Spatiospectral concentration on the sphere. *SIAM Review*, 48:504–536.

VISSER, P.N.A.M., J. VAN DEN IJSSEL, T. VAN HELLEPUTTE, H. BOCK, A. JÄGGI, G. BEUTLER, D. SVEHLA, U. HUGENTOBLE and M. HEINZE (2009): Orbit determination for the GOCE satellite. *Advances in Space Research*, 43:760–768.

Modelling topographic effects in GOCE gravity gradients

Grombein T., Seitz K., Heck B.

Geodetic Institute, Karlsruhe Institute of Technology (KIT), Englerstraße 7, D-76128 Karlsruhe, Germany,

E-Mail: thomas.grombein@kit.edu

1. Introduction

The basic observables of the satellite gravity gradiometry mission GOCE (Gravity Field and Steady-State Ocean Circulation Explorer) are the second-order derivatives of the Earth's gravitational potential V (components of the symmetric Marussi tensor M). These gravity gradients can be defined in a local north oriented frame (LNOF) whose x-axis is pointing North, y-axis towards West and z-axis upwards in geocentric radial direction:

$$\mathbf{M} = \vec{\nabla} (\vec{\nabla} V) = \begin{bmatrix} V_{11} & V_{12} & V_{13} \\ V_{12} & V_{22} & V_{23} \\ V_{13} & V_{23} & V_{33} \end{bmatrix} = \begin{bmatrix} V_{xx} & V_{xy} & V_{xz} \\ V_{xy} & V_{yy} & V_{yz} \\ V_{xz} & V_{yz} & V_{zz} \end{bmatrix}.$$

Gravity gradients observed by GOCE contain significant high- and mid-frequency components resulting from the attraction of the topographic (and isostatic) masses of the Earth. The existence of these signal components with short-wavelength affects the further processing of GOCE observation data, e.g. in the framework of regional and global gravity field modelling or the combination with terrestrial gravity anomalies. In all of these applications the harmonic downward continuation of the observed gradients from satellite height to mean sea level (MSL) can be seen as an ill-conditioned process. In order to mitigate the instability of downward continuation, it is recommended to smooth the gradients by applying topographic and isostatic reductions (*Wild-Pfeiffer, 2007, 2008*). In work package (WP) 150 of the REAL GOCE project the focus is laid on the efficient numerical modelling and calculation of topographic and isostatic effects in the observed GOCE gravity gradients.

In this paper we will concentrate on modelling topographic effects. In the first part we describe how to model them and discuss the input data and different modelling parameters. To quantify the influence of these parameters several numerical tests have been performed, which are presented and analyzed in the second part. Based on these results we try to figure out the »best fitting« modelling parameters for an efficient calculation of topographic effects in the context of the GOCE satellite mission.

2. Modelling topographic effects

The modelling of topographic effects in gravity gradients as observed by GOCE is based on the numerical evaluation of functionals of Newton's integral extending over the domain of the topographic masses which include the masses of the continents as well as the oceanic masses. In order to evaluate these kinds of volume integrals, the geometry of the topographic boundary surface and the density function inside the topographic masses must be known. Due to the fact that the topography is only known at discrete points (represented by a digital terrain model (DTM) with a specific grid resolution) it is not possible to evaluate Newton's integral directly over the entire domain. Practical numerical computations rely on a discretization and approximation of the problem. The topographic masses are usually decomposed into regular elementary bodies, where their density is assumed to be constant. Newton's integral is then evaluated for each particular body and the total effect is calculated by summation. For the decomposition,

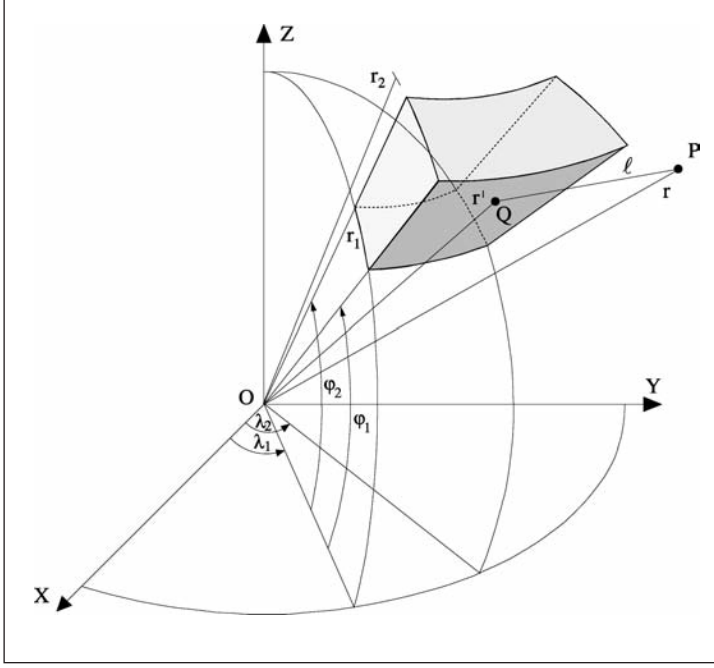


Figure 1: Geometry of a tesseroïd (Kuhn, 2000)

various geometric elementary bodies such as tesseroïds, prisms or point-masses can be used. Tesseroïds are bodies bounded by three pairs of surfaces: A pair of concentric spheres ($r_1 = \text{const}$, $r_2 = \text{const}$), a pair of meridional planes ($\lambda_1 = \text{const}$, $\lambda_2 = \text{const}$) and a pair of coaxial circular cones defined by the parallels $\varphi_1 = \text{const}$, $\varphi_2 = \text{const}$ (Fig. 1, cf. Heck and Seitz, 2007). Tesseroïds are well suited for the decomposition if the topography of the Earth is represented by a DTM which is usually given in geographical coordinates. Based on Newton's integral the effect of a tesseroïd on gravity gradients can be determined by optimized, non-singular tesseroïd formulas (cf. Grombein et al., 2010a):

$$V_{ij} = G\rho \int_{\lambda_1}^{\lambda_2} \int_{\varphi_1}^{\varphi_2} \int_{r_1}^{r_2} \left(\frac{3\Delta x_i \Delta x_j}{\ell^5} - \frac{\delta_{ij}}{\ell^3} \right) r'^2 \cos \varphi' dr' d\varphi' d\lambda'$$

$$i, j \in \{1, 2, 3\}$$

$$\Delta x_1 = r' \cos \varphi \sin \varphi' - \sin \varphi \cos \varphi' \cos (\lambda' - \lambda)$$

$$\Delta x_2 = -r' \cos \varphi' \sin (\lambda' - \lambda)$$

$$\Delta x_3 = r' \cos \varphi - r.$$

In these formulas G denotes Newton's gravitational constant and ρ the constant density value of the tesseroïd. The Euclidean distance between the computation point $P(r, \varphi, \lambda)$ and the running integration point $Q(r', \varphi', \lambda')$ is denoted by ℓ . Since the respective volume integrals for tesseroïds cannot be solved analy-

tically, numerical methods have to be applied, which will be described below.

3. Input data and modelling parameters

In Fig. 2 an overview of the required input data and the parameters for the modelling of topographic effects is given. The most important input data is global information about topography and density. As mentioned above, precise models of Earth's topography are available through global high-resolution DTMs. Compared to this high-resolution topography information, global density models only exist in a very low resolution, like the Crust2.0 model of seismic velocities and density (Bassin et al., 2000; Tsoulis, 2004). Therefore, regarding density, assumptions for the modelling of topographic effects have to be made. If there is no further information, topographic masses respectively the particular tesseroïds are usually modelled with a standard density value of $\rho = 2670 \text{ kg/m}^3$, which represents an average of rock density at the Earth's surface. Since this is only a very rough approximation, it is better to use at least combined topography/bathymetry models such as SRTM30_PLUS (Becker et al., 2009), allowing to model the ocean masses with a corresponding density value, additionally. Another class of DTMs, which will be used in our research, are global topographic databases



Figure 2: Input data and modelling parameters for the calculation of topographic effects

like DTM2006.0 (Pavlis *et al.*, 2007), which was developed for compiling the Earth Gravitation Model EGM2008, or the former JGP95E (Lemoine *et al.*, 1998). Beside topographic heights and bathymetric depths these DTMs also contain further details about ice thickness and lake depths. Each grid element is classified by six terrain types: (1) Dry Land Below MSL, (2) Lake, (3) Oceanic Ice Shelf, (4) Ocean, (5) Grounded Glacier, (6) Dry Land Above MSL.

A common way to take different density values of terrain types into account is the concept of rock-equivalent heights (Kuhn and Seitz, 2005; Rummel *et al.*, 1988). Based on the principle of mass balance the DTM heights of different terrain types are converted into rock-equivalent heights with respect to a constant reference density (e.g. $\rho = 2670 \text{ kg/m}^3$). Corresponding formulas for a spherical approximation are explicitly given in Kuhn and Seitz (2005). The use of this method allows a simple modelling of different terrain types with only one density value which also means that for each grid element the effect of only one tesseroïd has to be calculated. The disadvantage of this approach is that the geometry of the mass distribution changes if the actual mass-density is strongly different from the adopted constant density value (Tsoulis and Kuhn, 2007). To avoid this effect a rigorous, separate modelling of different terrain types in a vertical arrangement is necessary. As a consequence, the computation

time for the whole calculation process is increasing. Within our developed Rock-Water-Ice method (RWI method) the database of the $5' \times 5'$ DTM2006.0 is used to compile a three layer model, where each grid element consists of a rock, water and ice proportion in vertical direction. Consequently, for each grid element the topographic masses are modelled by three tesseroïds with different heights of the respective top surface (h_R , h_W , h_I) in relation to MSL and consistent thickness (t_R , t_W , t_I) and density values ($\rho_R = 2760 \text{ kg/m}^3$, $\rho_W = 1000 \text{ kg/m}^3$, $\rho_I = 920 \text{ kg/m}^3$), see Fig. 3.

Beside the topographic and density information which define the geometry and mass of the particular tesseroïds, their spatial arrangement has to be fixed. Even though the used tesseroïd formulas are given in a spherical manner, these bodies can be set up on different reference surfaces approximating MSL. We can either arrange them on a spherical earth of constant mean radius or, in a more realistic composition, on the surface of an ellipsoid of revolution. Through the different arrangement of the topography the distance between an arbitrary computation point and the tesseroïd bodies changes and therefore affects the impact on the gravity gradients.

When the tesseroïds are defined in size and fixed in space, we have to constitute, how to evaluate the volume integrals of the tesseroïd

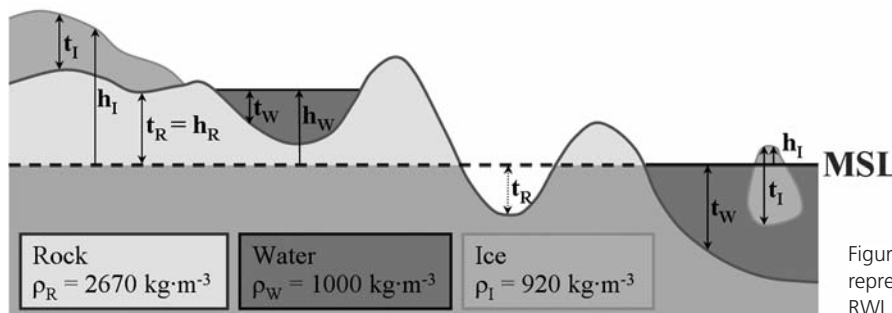


Figure 3: Schematic representation of the RWI method

formulas. As mentioned above, there is no analytical solution due to occurring elliptical integrals. Therefore, another modelling parameter is the calculation method used for solving these volume integrals numerically with a specific approximation quality. A second-order approximation has been developed at the Geodetic Institute Karlsruhe and proposed by *Heck and Seitz (2007)*. This approach is based on a Taylor series expansion of the integral kernel and subsequent term-wise integration. It can be seen as an extension of MacMillan's approximation for the prism formulas (*MacMillan, 1930*). While *Heck and Seitz (2007)* originally consider the effect on the potential and on gravity, in *Wild-Pfeiffer (2007, 2008)* this approach is extended on gravity gradients. As an alternative to Taylor series expansions, Gauss-Legendre cubature (3D) has been investigated by *Wild-Pfeiffer (2007, 2008)*. Depending on the number of used nodes Gauss-Legendre cubature (3D) reaches a higher approximation quality than Taylor series expansion, but on the other hand more computation time is required. Since the effect of distant masses on functionals of the gravitational potential diminishes, for remote bodies a tesseroïd can also be approximated by a point-mass, which concentrates the whole mass of the tesseroïd to its geometric centre. For a more detailed description of the mentioned calculation procedures as well as the explicit numerical calculation formulas related to the presented optimized tesseroïd formulas see *Grombein et al. (2010a)*. It should be mentioned that the accuracy which is achievable with a specific calculation method also depends on the DTM resolution and thus on the level of decomposition of the topographic masses.

4. Numerical Investigations

In order to quantify the impact of the discussed parameters, several numerical tests have been performed, where topographic effects in gravity gradients were calculated on a grid in the satellite height of GOCE. The computation points are located on a GOCE-like circular orbit with a geocentric radius $r = R + h$. The mean

earth radius is $R = 6378.137$ km and $h = 254.9$ km is the adopted altitude of GOCE. For the analysis differences between any two options were performed, where only one modelling parameter was varied in order to avoid interfering effects. The differences in the gravity gradients are plotted for the V_{zz} component and are described by statistical parameters for all components. In order to find an efficient method of calculation by analyzing the modelling parameters, it is necessary to obtain a good balance between achievable accuracy and required computation time. In our application the accuracy of the topographic effects should be adjusted with the measuring accuracy of the GOCE gravity gradients (1-2 mE). Therefore, an adequate level of accuracy (LOA) seems to be $\pm 10^{-2}$ mE. Remind that the absolute topographic effects in gravity gradients observed in the satellite height of GOCE are in the range of about ± 8 E (*Wild-Pfeiffer 2007, 2008*).

Digital Terrain Model

Calculations with the 5' x 5' DTM2006.0 as well as with the 5' x 5' JGP95E have been performed. The differences in the gravity gradients are in the range of -964 to 1319 mE (Tab. 1) and therefore far beyond the defined LOA. As can be seen in Fig. 4 the maximum and minimum differences are located in Antarctica and the northern part of Greenland, i.e. in regions with large ice masses. On the one hand, this discrepancy might be explained with a mass displacement and melting of the ice masses within the long time period between the creation of the DTM2006.0 and the JGP95E. On the other hand, when comparing both DTMs it becomes apparent that in these regions much more high-resolution input data were included in the DTM2006.0. Since the DTM2006.0 was generally generated by actual data and especially by much more high-resolution sources this DTM will be preferred. However, this comparison clearly illustrates that the differences induced by different DTMs can cause very large effects, and thus raises the question which DTM reflects best the »real« topography of the Earth.

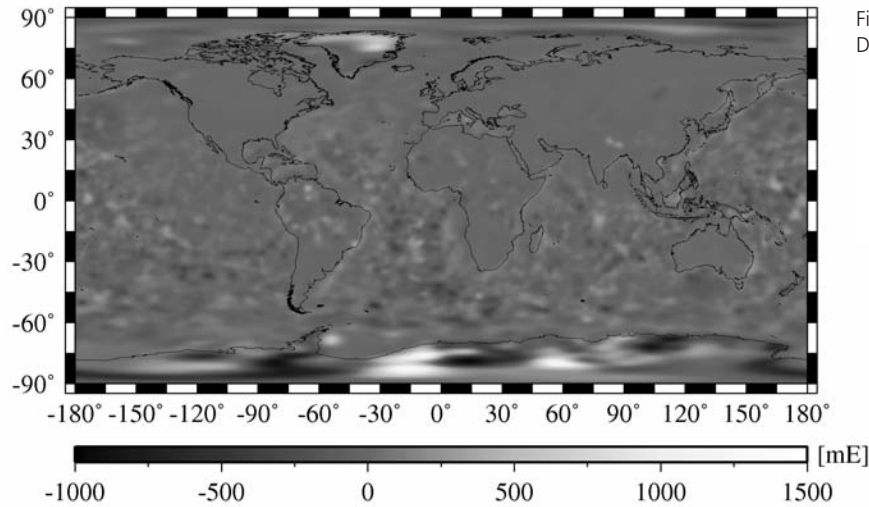


Figure 4: V_{zz} differences:
Digital Terrain Model

Table 1: Statistics: Digital Terrain Model in [mE]

	V_{xx}	V_{xy}	V_{xz}	V_{yy}	V_{yz}	V_{zz}
min	-528.724	-347.615	-542.222	-956.719	-945.074	-964.381
max	567.424	327.154	649.586	686.143	981.729	1319.323
mean	2.047	0.000	-2.568	4.421	0.000	-6.467
rms	70.083	42.868	82.321	87.804	105.659	130.788

Density

The discussed density concepts of rock-equivalent heights and the RWI method are compared based on the information of the DTM2006.0 database. Tab. 2 describes the statistics of the differences: The minimum is reached in the V_{zz} component and has a value of -19 mE; the maximum can be found in the V_{yz} component and amounts to 24 mE. The illustration in Fig. 5 shows that the differences can be classified according to the three areas: rock, water and ice. In the case of the continental rock areas the differences are zero due to the fact that in both approaches the modelling is the same. Although the density contrast between rock and ice is the most extreme, the differences for the ice areas are also relatively small. The largest differences can be registered in the case of water areas, especially at the sites of deep ocean trenches or mid-ocean ridges, like the Mid-Atlantic ridge. Therefore, the mass displacement in the concept of rock-equivalent heights is not only influenced by large density contrasts between the constant

and actual density value, but also by the magnitude of the condensed height itself. Since the differences show that the resulting effects also exceed the defined LOA, it is proposed to use the more realistic but also more time consuming RWI method.

Mass arrangement

To investigate the impact of the mass arrangement, tesseroids have been set up on a spherical earth of constant radius $R = 6378.137$ km as well as on the surface of an ellipsoid of revolution (GRS80; Moritz, 1980). In both cases the GOCE orbit is still assumed circular. The differences in the modelled topographic effects between the spherical and ellipsoidal arrangement of the topography are in a range of -268 to 336 mE (see Tab 3.). The minimum value is reached in the V_{xz} component, the maximum in the V_{zz} component. In general, the differences are minimum near the equator and increase towards the polar regions (see Fig. 6). This trend clearly illustrates that the differences originate from the earth flattening which effects

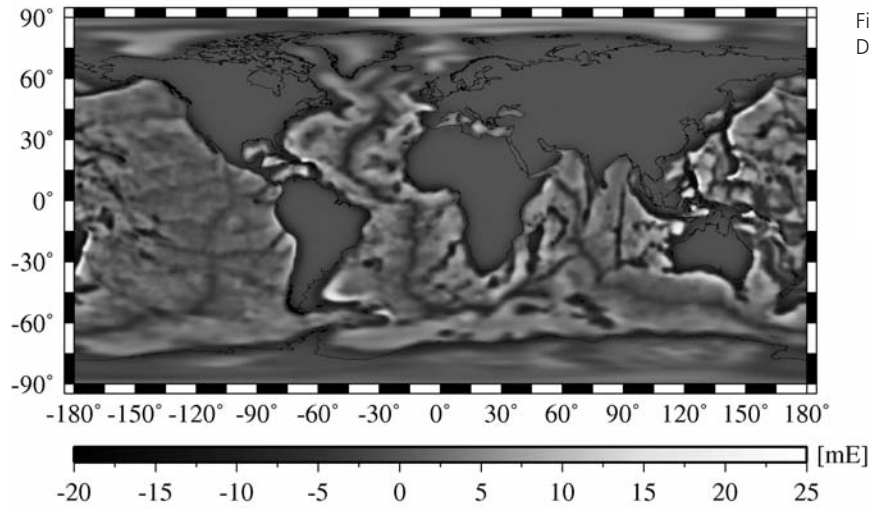


Figure 5: V_{zz} differences:
Density

Table 2: Statistics: Density in [mE]

	V_{xx}	V_{xy}	V_{xz}	V_{yy}	V_{yz}	V_{zz}
min	-17.262	-9.497	-18.694	-16.105	-16.144	-18.919
max	13.813	7.322	17.406	16.660	24.419	21.296
mean	0.054	0.000	-0.072	-0.016	0.000	-0.038
rms	2.132	1.111	2.451	2.040	2.360	3.472

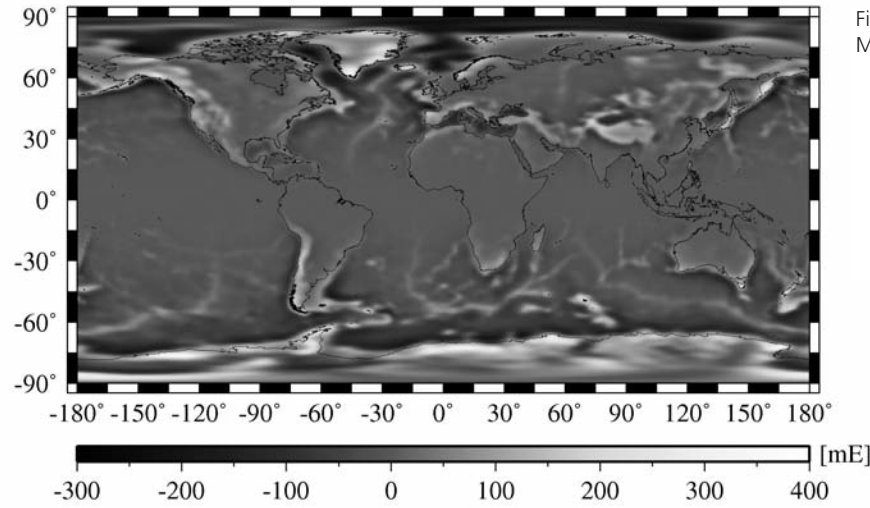


Figure 6: V_{zz} differences:
Mass arrangement

Table 3: Statistics: Mass arrangement in [mE]

	V_{xx}	V_{xy}	V_{xz}	V_{yy}	V_{yz}	V_{zz}
min	-235.192	-91.489	-268.123	-216.036	-220.136	-258.573
max	186.915	104.707	276.636	227.854	226.204	336.387
mean	0.253	0.000	5.873	0.778	0.000	-1.031
rms	38.451	17.880	43.943	33.740	37.084	60.551

a mass displacement particularly in the polar regions. In many applications spherical approximation yields sufficient results, but in this study the differences reach an order of magnitude above the defined LOA. The ellipticity of the reference surface cannot be neglected and should be considered when modelling topographic effects in gravity gradients for a satellite-mission like GOCE (cf. *Grombein et al., 2010b*).

Calculation method

Finally, the use of different calculation methods for the solution of the tesseroïd formulas has to be investigated. Previous investigations (*Grombein et al., 2010a*) have already theoretically shown that the Gauss-Legendre cubature (3D) with 27 nodes in combination with a DTM resolution of 5' x 5' will guarantee the defined LOA, if the computation point P is situated in satellite height. In the numerical tests performed in the present study with the use of the 5' x 5' DTM2006.0 it was found that calcu-

lations with Taylor series expansions and Gauss-Legendre cubature (3D) with 8 as well as with 27 nodes provide the same results within the defined LOA. The differences between the use of Taylor series expansions and the much faster point-mass approximation are shown in Fig. 7 and are described by the statistics in Tab. 4. It can be realized that the differences are strongly correlated with the topography. The minimum values (about -0.7 mE) are reached over large mountain ranges such as the Andes or the Himalaya. The maximum values (about 0.8 mE) can be found at the continental boundaries. Since the differences are an order of magnitude above the defined LOA, the Taylor series expansion cannot be replaced by the point-mass approximation.

To reduce the computation time it seems beneficial to use a combination of the Taylor series expansion and the point-mass approximation. A common approach for a combination is to divide the total integration area into a near

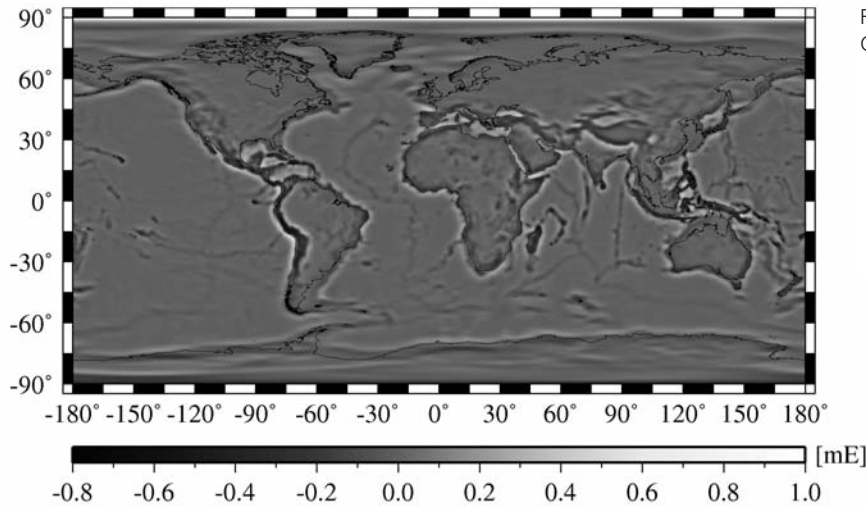


Figure 7: V_{zz} differences: Calculation method

Table 4: Statistics: Calculation method in [mE]

	V_{xx}	V_{xy}	V_{xz}	V_{yy}	V_{yz}	V_{zz}
min	-0.413	-0.323	-0.474	-0.424	-0.536	-0.739
max	0.475	0.270	0.652	0.542	0.476	0.824
mean	0.000	0.000	-0.009	-0.003	0.000	0.003
rms	0.054	0.022	0.063	0.053	0.041	0.093

and far zone with respect to the spherical distance from the computation point. The near zone of the computation point is then modelled with the more accurate but slower Taylor series expansion, while the diminishing influence of the remote masses of the far zone are modelled with the much faster point-mass approximation. To apply such an approach a value for the spherical distance Ψ_c which defines the boundary between the near and far zone has to be fixed. In Fig. 8 the maximum (absolute) difference that occurs in an arbitrary computation point between the results of the Taylor series expansion and the combined approach is plotted in relation to spherical distance values in a logarithmic scale. The resulting curve shows that the differences increase almost exponentially when the spherical distance is decreasing. In order to guarantee the LOA the spherical distance should not be smaller than $\Psi_c = 11^\circ$.

5. Conclusions and Outlook

In this paper the modelling process of topographic effects in gravity gradients was described and the handling of several modelling parameters was discussed. With the help of numerical tests the impact of these parameters on gravity gradients could be quantified. In the context of the GOCE satellite mission and relating to the measuring accuracy of the obser-

ved gradients suitable modelling parameters have been proposed to get an efficient calculation method regarding computation time and accuracy.

As input data the global topographic database of the 5' x 5' DTM2006.0 is used for the description of the topographic surface as well as for providing information about the density, which is modelled with the RWI method. According to the DTM resolution the topographic masses are decomposed into tesserooids which are arranged on an ellipsoidal reference surface. For the numerical solution of the tesseroid formulas the Taylor series expansion is used in the near zone of the computation point whereas in the far zone (beginning at a spherical distance of $\Psi_c = 11^\circ$) a point-mass approximation is applied.

In the next step, the selected parameters will be used to model topographic effects in real GOCE observations of gravity gradients as well as to determine the isostatic signal components that were not discussed in this paper. Furthermore, the degree of smoothing of the gradients after applying the combined topographic-isostatic reductions will be investigated and compared to other possible smoothing approaches.

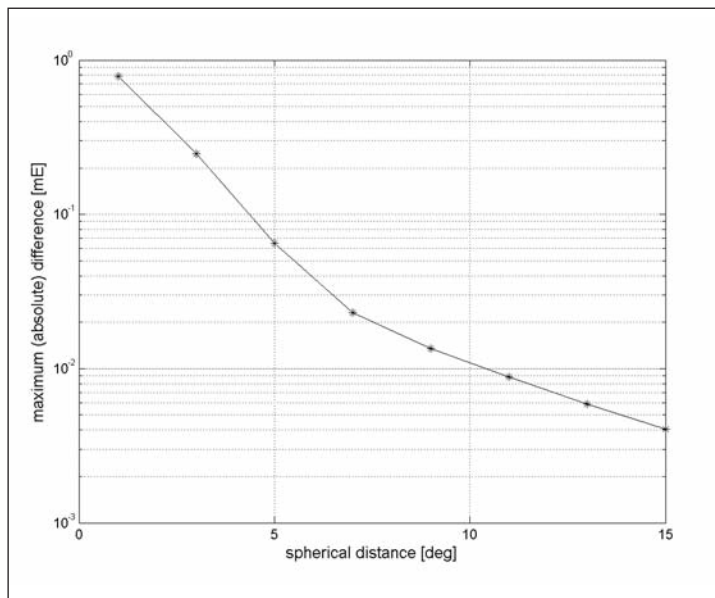


Figure 8: Defining the near and far zone

Acknowledgements

The authors would like to thank N.K. Pavlis for providing the Global Digital Terrain Model DTM2006.0. The Bundesministerium für Bildung und Forschung (BMBF, German Federal Ministry of Education and Research) is acknowledged for the financial support of this research within the REAL GOCE project of the GEOTECHNOLOGIEN Programme.

References

- Bassin C., Laske G., Masters G. (2000): The current limits of resolution for surface wave tomography in North America. *EOS Trans AGU* 81 (48), F897.
- Becker J.J., Sandwell D.T., Smith W.H.F., Braud J., Binder B., Depner J., Fabre D., Factor J., Ingalls S., Kim S.-H., Ladner R., Marks K., Nelson S., Pharaoh A., Trimmer R., von Rosenberg J., Wallace G., Weatherall P. (2009): Global Bathymetry and Elevation Data at 30 Arc Seconds Resolution: SRTM30_PLUS. *Marine Geodesy*, 32(4):355-371.
- Grombein T., Seitz K., Heck B. (2010a): Untersuchungen zur effizienten Berechnung topographischer Effekte auf den Gradiententensor am Fallbeispiel der Satellitengradiometriemission GOCE. KIT Scientific Reports 7547, Schriftenreihe des Studiengangs Geodäsie und Geoinformatik, No. 2010/1, KIT Scientific Publishing, Karlsruhe.
- Grombein T., Seitz K., Heck B. (2010b): Spherical and ellipsoidal arrangement of the topography and its impact on gravity gradients in the GOCE mission. Presented at the General Assembly of the European Geosciences Union, Vienna, Austria, 2-7 May 2010.
- Heck B., Seitz K. (2007): A comparison of the tesseroid, prism and point-mass approaches for mass reductions in gravity field modelling. *JGeod*, 81(2):121–136, DOI: 10.1007/s00190-006-0094-0.
- Kuhn M. (2000): Geoidbestimmung unter Verwendung verschiedener Dichtehypothesen. Deutsche Geodätische Kommission, C520, München.
- Kuhn M., Seitz K. (2005): Comparison of Newton's integral in the space and frequency domains. In: Sansò F. (ed.): *A Window on the Future of Geodesy*. IAG Symposia Vol. 128, Springer, 386-391.
- Lemoine F.G., Kenyon S.C., Factor J.K., Trimmer R.G., Pavlis N.K., Chinn D.S., Cox C.M., Klosko S.M., Luthcke S.B., Torrence M.H., Wang Y.M., Williamson R.G., Pavlis E.C., Rapp R.H., Olson T.R. (1998): The Development of the Joint NASA GSFC and the National Imagery and Mapping Agency (NIMA) Geopotential Model EGM96. NASA Goddard Space Flight Center, Greenbelt, Maryland, USA.
- MacMillan W.D. (1930): *Theoretical Mechanics, Vol 2: the Theory of the potential*. McGraw-Hill, New York (reprinted by Dover Publications, New York, 1958).
- Moritz, H. (1980): Geodetic reference system 1980. *Bulletin Géodésique*, 54:395–405.
- Pavlis N.K., Factor J.K., Holmes S.A. (2007): Terrain-related gravimetric quantities computed for the next EGM. In: Kiliçoglu A., Forsberg R. (eds.): *Gravity Field of the Earth, Proceedings of the 1st International Symposium of the IGFS, Istanbul, Turkey*, 318-323.
- Rummel R., Rapp H.R., Sünkel H., Tscherning C.C. (1988): Comparison of global topographic/isostatic models to the Earth's observed gravity field, Report No. 388, Department of Geodeic Science and Surveying, The Ohio State University, Columbus, 33 pp.
- Tsoulis D. (2004): Spherical harmonic analysis of the CRUST 2.0 global crustal model. *JGeod*, 78 (1-2):7-11, DOI: 10.1007/s00190-003-0360-3.

Tsoulis D., Kuhn M. (2007): Recent developments in synthetic Earth gravity models in view of the availability of digital terrain and crustal databases of global coverage and increased resolution. In: Kiliçoglu A., Forsberg R. (eds.): Gravity Field of the Earth, Proceedings of the 1st International Symposium of the IGFS, Istanbul, Turkey, 354–359.

Wild-Pfeiffer F. (2007): Auswirkungen topographisch-isostatischer Massen auf die Satellitengradiometrie. Deutsche Geodätische Kommission, C604, München.

Wild-Pfeiffer, F. (2008): A comparison of different mass elements for use in gravity gradiometry. *JGeod*, 82(10):637-653, DOI: 10.1007/s00190-008-0219-8.

Quality Assessment of GOCE Gradients

Brieden P. (1), Müller J. (1, 2)

(1) Institut für Erdmessung, Leibniz Universität Hannover, Schneiderberg 50, 30167 Hannover, Germany

(2) Centre for Quantum Engineering and Space-Time Research (QUEST), Welfengarten 1, 30167 Hannover, Germany

Abstract

The first ESA Earth Explorer Core Mission GOCE (Gravity Field and Steady-State Ocean Circulation Explorer) entered the operational measurement phase in September 2009. Before gravity field processing, the quality of the GOCE gradients in the measurement bandwidth (5-100 mHz), MBW, has to be assessed. Here, two procedures have been developed in Hanover, the mutual comparison and analysis of observed gradients in satellite track cross-overs and the application of terrestrial gravity data which are upward continued and transformed into reference gradients for the GOCE gradiometer measurements.

First the gravity gradients are filtered, where the longer wavelength signals below the MBW are replaced by global geopotential model (GPM) information. The filtered time series is used as input signal for both validation methods.¹

1. Pre-Processing

The GOCE gravity gradients result from a combination of differential mode accelerations along and inertial angular rates about the three gradiometer axis on board the GOCE satellite. Because of accelerometer drift as a natural and expected behavior of the accelerometers, gravity gradients are affected by drift, too. This leads to inaccuracies in the gravity gradients over long periods.

The GOCE gradiometer has been designed such

that the error characteristics of the gravity gradients are optimized in the so-called measurement bandwidth (MBW). The MBW of the GOCE gradiometer is between 5 and 100 millihertz (mHz). It is the spectral domain where validation is primarily required.

1.1. The idea

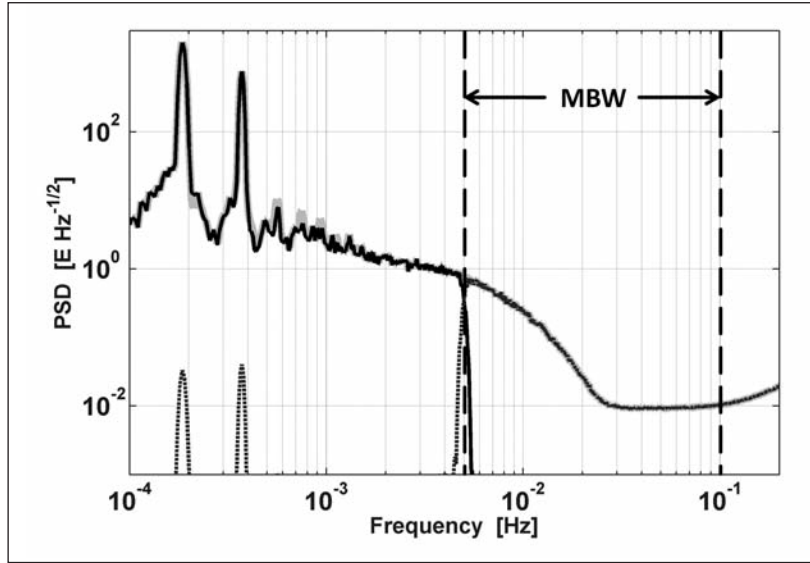
For both validation methods, which are presented in this paper, full signal information is needed, so a simple high-pass filtering of the time series is not sufficient. The goal is to get the signal with the highest possible quality (for validation of the gradiometer data), both at low frequencies (for reduction purposes only) and in the MBW. The idea is to combine short-wavelength signal information from GOCE measurements with long wavelength signal input on the basis of a global geopotential model (GPM). The resulting, combined signal is used as input for the validation methods.

1.2. Filtering

In the analysis, a FIR (finite impulse response) filter with a cut-off frequency of 5 mHz is used to high pass filter the time series of the GOCE gradients and low pass filter a gradients' time series computed on the basis of a GPM in GOCE altitude and attitude. Filtering is performed separately for the time series of all tensor components. The GPM that is used in the following analysis is the ITG-Grace2010s [5] up to degree and order 180.

¹ REMARK

A similar paper has been presented at the ESA Living Planet Symposium under the title »TWO METHODS FOR QUALITY ASSESSMENT OF GOCE GRADIENTS« [1]. It obtained the publication number GEOTECH-1396 of the German Ministry of Education and Research (BMBF) R&D-Programme GEOTECHNOLOGIEN. The present paper has been modified and data of another period (November 2009) was investigated.



Power Spectral Density (PSD) of the GOCE gravity gradient tensor component V_{yy} (gray), its high pass filtered part (dotted gray) and the low pass filtered part of the ITG-Grace2010s (black)

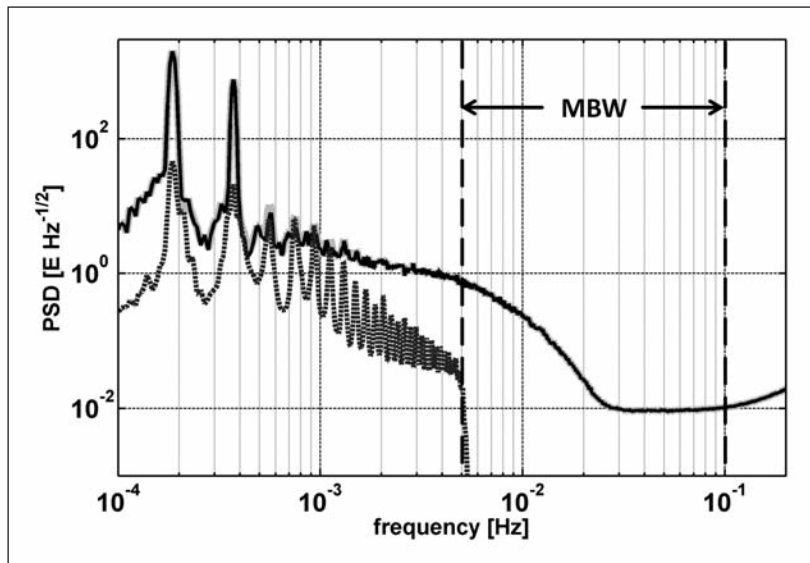


Figure 2: Power spectral density of the original GOCE gradient V_{yy} time series (gray), the filter result (black) and the differences (dotted gray)

Figure 1 shows the power spectral density (PSD) of the GOCE gravity gradient component V_{yy} in gray, its high pass filtered part (dotted gray) and the low pass filtered part of the ITG-Grace2010s in black.

In order to achieve the best possible quality as assessment, the resulting combined filtered GOCE signal has also been low pass filtered to remove possible errors above 50 mHz. This upper cut-off frequency corresponds to a spherical harmonic degree of about 270, where no significant gravity signal is expected as there the signal level is below the noise level.

The resulting gradient PSD after filtering is illu-

strated in Figure 2, where the PSD of the GOCE measurements (gray), the filtered signal (black) and the differences between these two (dotted gray) are shown. The differences in the MBW are very small, about four orders of magnitude below the signal power. It is obvious that GOCE also has good signal quality below the MBW down to 1.5 mHz.

The resulting time series of the gravity gradients, consisting of long-wavelength information from ITG-Grace2010s and short-wavelength information from GOCE measurements (black PSD in Figure 2), is used as input for our validation analysis. The data period is one month: November 2009.

2. Reference Gradient Approach

The idea of the reference gradient approach is based on regional gravity field data over well surveyed areas, that is upward continued to gradients at satellite altitude, serving as reference gradients for the GOCE data. These reference gradients in the GOCE observation frame can then be used for evaluating the quality of the measured gradients.

2.1. The reference gradient method

The reference gradient approach is based on regional gravity data in terms of global geopotential models (GPM), terrestrial gravity anomalies and residual terrain models (RTM). The terrestrial data (Δg_G), a combination of terrestrial gravity anomalies, airborne gravimetry and satellite altimetry, is reduced from long-wavelength (Δg_M) and short-wavelength (Δg_{RTM}) contributions (remove-restore-technique):

$$\Delta g^r = \Delta g_G - \Delta g_M - \Delta g_{RTM}. \quad (1)$$

The resulting residual gravity anomalies Δg^r (Eq. 1) are upward continued into GOCE altitude, transformed to residual 'disturbing gradients' T_{ij} and restored to full tensor components V_{ij}^{ref} , as it is shown in Figure 3. These computed, so called, reference gradients V_{ij}^{ref} and the GOCE gradiometer measurements V_{ij}^G are compared; the differences ΔV_{ij}^{RG} are further analyzed.

A detailed explanation of the procedure of reference gradient determination and the reference gradient approach can be found in [2], [6] and [7].

2.2. Analysis of the gradient differences

The current regional evaluation area is central Europe. Hence, only satellite tracks that cross this area and are at least 200 seconds long are evaluated. The differences of each tensor component are reduced by a mean value. Ideally the mean value is zero; in practice, offsets remain indicating a constant difference between the filtered GOCE gradients and the computed reference gradients. The remaining constant differences might be caused by the filtering of the data or some inconsistent choice of datum parameters. Future work will focus on possible reasons for those constant differences.

2.3. Reference gradient results

Figure 4 shows the mean-reduced gray-coded differences ΔV_{yy} within the evaluation area. In the given data set, a mean value of -132 mE has been reduced. The differences in ΔV_{xx} and ΔV_{yy} have a magnitude of about 11 to 15 mE. The differences in ΔV_{zz} are slightly worse with a magnitude of about 25 mE.

The residual differences are to be analysed along each track (Figure 4). The analysis is carried out in the frequency domain to identify relevant frequencies in the differences. Figure 5 shows the power spectral densities (PSD) of the differences along each track within the evaluation area. Each of the black, grey and white curves specifies the PSD of one track. The average of all PSDs is given by the thick gray line. The requirements of the GOCE tensor trace is pictured in dotted black. Obviously, almost all results meet the requirements. Some of the PSD curves show single spectral signals

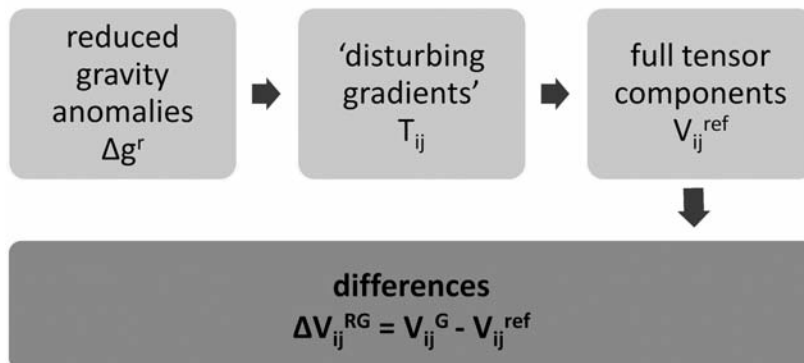


Figure 3: Computation steps from terrestrial gravity data to gradient differences of GOCE measurements

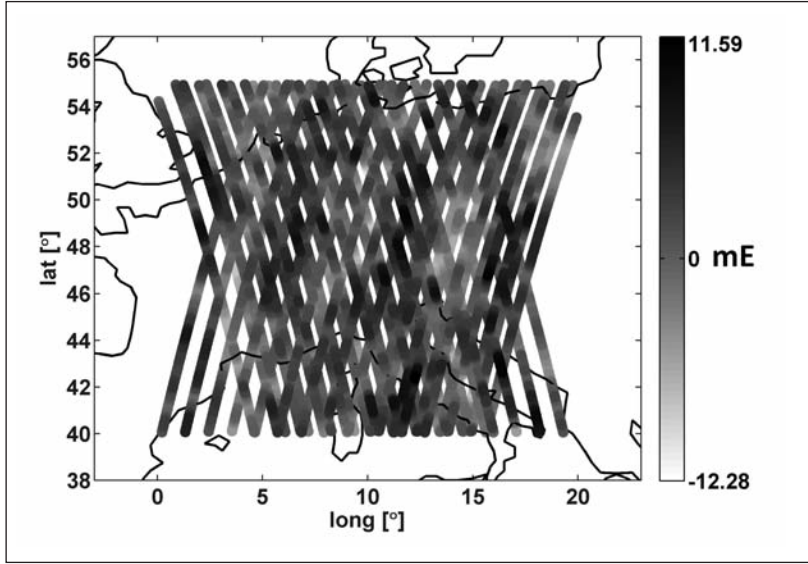


Figure 4: Residual differences ΔV_{yy} [mE], mean value of -132 mE is reduced

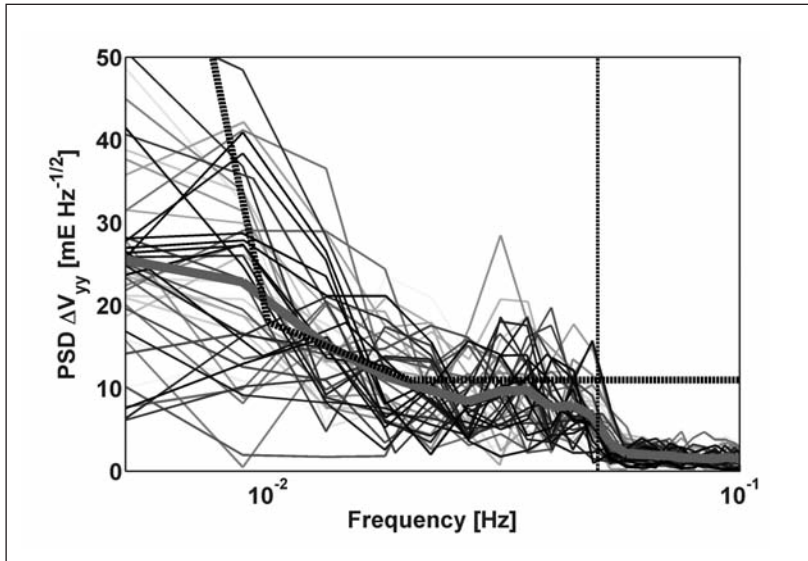


Figure 5: PSD of each track within the evaluation area (black to white), the averaged PSD (wide gray line) and the requirement of the GOCE trace (dotted black)

above the requirements, but one has to have in mind, that each PSD is computed on the basis of very short time-series of only 200 s. The effect of the second filtering at 50 mHz that is described in chapter 1.2 is also visible in the PSD of the differences in Figure 5. The cut-off frequency of 50 mHz is indicated by the vertical dotted black line.

It is a very good result having achieved a noise performance of 10 (higher frequencies) to 25 mE/√Hz (lower frequencies) for V_{yy} . The performance of V_{zz} is slightly larger, up to about 35 mE/√Hz.

3. Cross-Over Approach

The cross-over (XO) approach is a relative validation method, i.e., a procedure using GOCE data only. XO analysis allows checking the gravity gradients at the accuracy level expected for GOCE.

3.1. The XO method

The idea of the XO approach is to use the geographical correlation between two GOCE tracks crossing each other over the same point on earth, in which the gradiometer should measure the same gravity gradients.

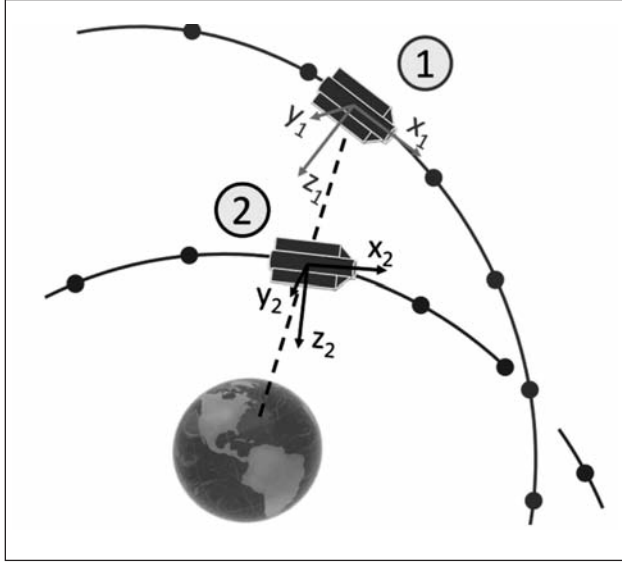


Figure 6: Principle of the XO approach – different attitude and altitude of the GOCE gradiometer in two orbits crossing each other over the same point on earth

What has to be considered are differences in attitude and altitude between the two satellite and gradiometer positions (Figure 6). These differences have to be reduced for the XO analysis. The reduction of attitude and altitude effects is performed by using the global geopotential model ITG-Grace2010s [5]. Reference values for the measured gradients in the XO are computed in the gradiometer reference frame (GRF) for both gradiometer positions. The resulting accuracy of those gradients is obviously not high enough, since the GPM is less accurate in the MBW than the GOCE measurements. The idea of the XO approach is that the difference of reference gradients in the two gradiometer positions is the same as the difference of real GOCE measurements. Based on this assumption, the differences between the real measurements are reduced by using the differences between the reference values:

$$\Delta V_{ij}^{XO} = V_{ij,G}^1 - V_{ij,G}^2 - \left(V_{ij,GPM}^1 - V_{ij,GPM}^2 \right). \quad (2)$$

The residual gradient differences ΔV_{ij}^{XO} that should be zero in the ideal case are then further analyzed, where $V_{ij,G}^1$ and $V_{ij,G}^2$ are the measured GOCE gradients in the two satellite positions (see Figure 6) and $V_{ij,GPM}^{1,2}$ are the corresponding tensor components that are computed from the ITG-Grace2010s.

A detailed description of the procedure of

cross-over analysis and its application for validating GOCE gravity gradients is given in [2], [3], [4] and [6].

3.2. XO results

Based on about one month of GOCE data from November 2009, the XO approach produces a set of residual differences ΔV_{ij}^{XO} according to Eq. (2). Even an ideal reduction of the GPM part provided, the differences are not always reduced to zero because GOCE data might contain some anomalies that are to be detected with this validation approach. To get a first impression, a threshold of maximum allowed difference in the XO is selected. The statistics in Table 1 points out, how much percentage of the differences in the cross-over points are below the selected threshold and thus are good XOs. Table 1 gives an overview for the main diagonal components of the gravity gradient tensor.

Obviously for a given threshold of only 11 mE, more than 97 % of the differences in all cross over points are below this limit for the XX and YY tensor component, which is a very good result. Despite a higher threshold, the ZZ component shows a slightly less accurate behaviour. Taking a threshold of 20 mE for ZZ, the percentage of differences exceeding it is reduced to about 1 %.

Table 1: Percentage of good XOs that are below a given threshold depending on the tensor component

tensor component	threshold [mE]	percentage of good XOs
XX	11	99.3 %
YY	11	97.5 %
ZZ	15	94.8 %

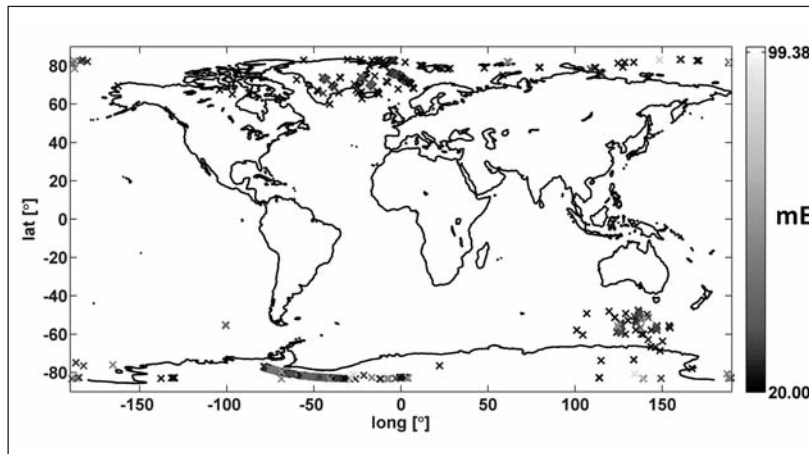


Figure 7: Gray-coded XO-differences [mE] of tensor component V_{yy} that exceed a threshold of 20 mE, data base: November 2009

For gravity field processing the highly accurate main diagonal components of the gravity gradient tensor are used. The XO results show that more than 97 % (V_{xx} and V_{yy}) of the main diagonal components achieve the expected quality level.

The differences of tensor component V_{yy} that exceed a threshold of 20 mE are shown in Figure 7. It gives the geographical distribution of the gray-coded differences that almost exclusively can be found near the poles. That is not astonishing, as most of the XO's occur in high latitudes. The XO approach also allows to identify individual inaccurate measurements along orbit parts. Moreover, accumulations of differences in certain areas like south of Australia are detected.

As Figure 7 also shows, almost all the threshold-exceeding differences have values close to the threshold and only very few of them have bigger amplitudes. Nevertheless some

scattered larger differences appear which will be subject to future investigations.

The results reflect the good suitability of the XO approach to validate the GOCE data at the level of some mE. The XO approach underlines the good data quality of the GOCE gravity gradients.

4. Conclusions and Outlook

The inaccuracies in the longer wavelengths in the GOCE gravity gradients are improved with long wavelength information from the ITG-Grace2010s. The GOCE gravity gradients are filtered first. Here, a finite impulse response filter (FIR) is applied. In the future, the determination of a best cut-off frequency will be investigated. The resulting filtered time series is used as input for both Hanover validation methods.

On the basis of about one month (Nov. 2009)

of GOCE data, the results of the reference gradient approach show residual differences between the measured and the reference gradients at about 10 to 15 mE for the XX and YY tensor components. The differences for the ZZ component are slightly larger up to about 25 mE. The differences in the spectral domain show a noise performance up to about 25 mE/ $\sqrt{\text{Hz}}$ (XX, YY) to 35 mE/ $\sqrt{\text{Hz}}$ (ZZ) for the main diagonal components in the measurement bandwidth.

The results of the cross-over (XO) approach give a similar picture: more than 99 % of the residual differences in the cross-over points are smaller than 15 mE for the XX and YY components. The percentage of differences in ZZ exceeding 15 mE is 95 %, but ZZ is also at the level of 99 % for a threshold of 20 mE.

In summary, on the basis of about one month of GOCE data, both approaches have proved their suitability to validate GOCE data. The noise performance of the tensor component V_{zz} is slightly worse compared to the other main diagonal components. The two validation methods underline the very good quality of the GOCE gravity gradients.

Acknowledgement

The project REAL GOCE is part of the R&D Programme GEOTECHNOLOGIEN. GEOTECHNOLOGIEN is funded by the German Ministry of Education and Research (BMBF) and the German Research Foundation (DFG), Grant (03G0726C) of project REAL GOCE.

References

- [1] Brieden, P., Müller, J. (2010): Two Methods for Quality Assessment of GOCE Gradients, ESA Living Planet Symposium, Conference proceedings, ESA SP-686, Bergen (Norway), 2010.
- [2] Jarecki, F., Wolf, K.I., Denker, H., Müller, J. (2006): Quality assessment of GOCE gradients. In: Flury, J. et al. (eds.), *Observation of the Earth System from Space*, Springer, New York, pp. 271–285.

- [3] Jarecki, F. (2010): Kreuzungspunktdifferenzen zur relativen Validierung satellitengradiometrischer Messungen, *Wissenschaftliche Arbeiten der Fachrichtung Geodäsie und Geoinformatik der Leibniz Universität Hannover*, ISSN 0174-1454, Nr. 286, 2010.

- [4] Jarecki, F., Müller, J. (2009): Robust trend estimates from GOCE SGG satellite track cross-over differences. In: Sideris, M. (ed.), *Observing Our Changing Earth. IAG Symposia 133*, Springer, New York, pp. 363–370.

- [5] Mayer-Gürr, T., Kurtenbach, E., Eicker, A. (2010): The static solution ITG-Grace2010s. Available at: <http://www.igg.uni-bonn.de/apmg/index.php?id=itg-grace2010>.

- [6] Müller, J., Jarecki, F., Wolf, K.I., Brieden, P. (2010): Quality Evaluation of GOCE Gradients. In: Flechtner, F.M., (eds.), *System Earth via Geodetic-Geophysical Space Techniques*, Springer, New York, pp. 265-276.

- [7] Wolf, K.I. (2007): Kombination globaler Potentialmodelle mit terrestrischen Schweredaten für die Bestimmung der zweiten Ableitungen des Gravitationspotentials in Satellitenbahnhöhe, Ph.D. thesis, Deutsche Geodätische Kommission, Reihe C Nr. 603, www.dgk.badw.de, identical with: *Wissenschaftliche Arbeiten der Fachrichtung Geodäsie und Geoinformatik der Leibniz Universität Hannover*, ISSN 0174-1454, Nr. 264, Hannover 2007.

Inferring the mean dynamic topography by using GOCE geoid information in ocean state estimations

Siegismund F., Köhl A. und Stammer D.

University of Hamburg, Institute for Marine Research

Introduction

The Dynamic Topography of the ocean is an important dynamic variable since it determines via its gradient the large scale surface circulation on a time scale of a few days and longer and, in combination with the density field, also the deep circulation. Since direct current meter data is sparse, assimilation of the (time) Mean Dynamic Topography (MDT) is expected to have large impact on ocean state estimation. *Stammer et al. (2007)* worked out an assimilation of MDTs based on former geoid models (EGM96 and GGM01) and found, that, given the provided errors on the geoid and the Mean Sea Surface (MSS) from satellite altimetry, the ocean state estimate is hardly impacted by the MDT. From sensitivity experiments, with artificially reduced error estimates on the MDT, they found, however, significant changes in the modeled MDT and the ocean circulation, with reasonable changes in the control terms in most regions. Today, geoid models with strongly reduced error estimates are available, and thus have an enhanced potential to impact ocean state estimation. We present here a number of sensitivity experiments covering a two years period (1992-1993) to test the sensitivity of ocean state estimation to assimilation of MDT and the influence of co-variance information in the geoid error. We then discuss first results from an ongoing 'realistic' 7-years (1993-1999) optimization using the first available combined GOCE-GRACE geoid solution (GOCO01s) and a recent MSS (MSS_CNES_CLS_10, see <http://www.aviso.oceanobs.m/en/data/tools/citation/index.html>) to calculate the MDT.

Methodology

The GECCO (German part of Estimating the Circulation and Climate of the Ocean) model is based on the Massachusetts Institute of Technology general circulation model (MITgcm; *Marshall et al. [1997]*), which is a numerical implementation of the primitive equations formulated on z-levels on a spherical coordinate system.

The set-up we use for the optimizations here, is basically identical to the 50-yr run (1952-2001) of the GECCO model [*Köhl and Stammer, 2008*], also the initial ocean state is taken from this model synthesis. The syntheses use the adjoint method to bring the model into consistency with available hydrographic and satellite data as well as prior estimates of surface fluxes. The estimation of the control parameters was changed from a direct estimation of the fluxes every 10 days to the estimation of daily atmospheric state variables, which include surface air temperature, humidity, precipitation and the 10 m wind. The prior of the atmospheric state derives as in the previous estimate from the National Centers for Environmental Prediction (NCEP).

These control fields are then adjusted by the method to yield model states that are dynamically consistent with the model physics and the assimilated data within given error limits. We refer to *Wunsch [1996]* for a general introduction of the methodology. As before, the set of assimilated data includes altimeter data, AMSR/E SST, Argo temperature and salinity profiles. The assimilation of MDT consists of a spa-

tial MDT map as constraint of the modeled topography, and, since the geoid error is provided as spherical harmonic (SH) coefficients, the MDT cost function contribution is evaluated in spectral space.

The MSS model is transformed to SH coefficients, truncated at degree and order (d/o) of the geoid and transformed back to physical space. This methodology ensures, that the MSS contains the same spatial resolution as the geoid. The difference between MSS and geoid is computed and the resulting MDT is filtered using a Gaussian filter, with a filter scale just long enough to smooth out small scale noise.

Sensitivity experiments

The sensitivity experiments span the period 1993-1994. The MDT is computed from the difference of the CLS01 MSS and the ITG-GRACE03s geoid. A spatial smoothing with a 2° Gaussian filter is performed to smooth out small scale noise. The MDT error estimate consists of the error in the geoid, provided with the geoid, the error in altimetry (4 cm white noise for each single observation), and the impact of the representation error of the hydrodynamic model due to limited spatial resolution (estimated from one half of the R.M.S. signal in Sea Level Anomaly from satellite alti-

metry). Two experiments are performed, where MDT is assimilated together with the standard constraints, which includes most available observed ocean data. One experiment uses full co-variance information (GECCO-COV), while the second uses only the error variances (GECCO-VAR). Further two experiments only assimilate MDT data using the full error co-variance matrix (GECCO-MDT-COV) or only the variances (GECCO-MDT-VAR). As reference, a fifth optimization run was performed with the standard data assimilated, but without MDT (GECCO-REF). For comparison, the leftmost, black bars indicate the costs for the free run (iteration 0), which includes no corrections to the control variables.

Figure 1 shows the most important components of the cost function, which is the error weighted sum of squares of the model data differences, after 38 iterations. For comparison, the leftmost, black bars indicate the costs for the free run (iteration 0), which includes no corrections to the control variables. The comparison of MDT residual maps from different experiments is displayed in Fig. 2. From Figs. 1 and 2 we conclude, that

1. the MDT residuals are highly affected by MDT assimilation,
2. the optimization wins by assimilation of MDT with smaller costs in all important constraints compared to standard data assimilation,

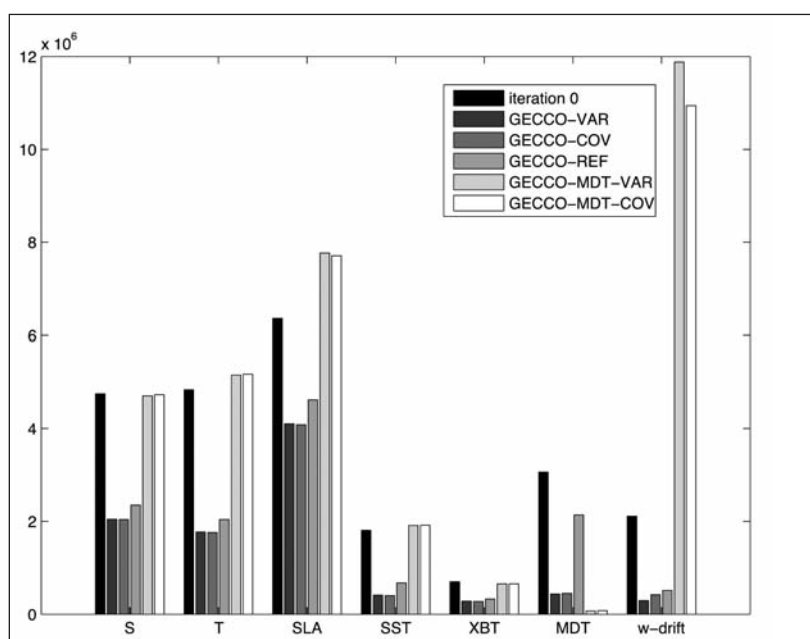


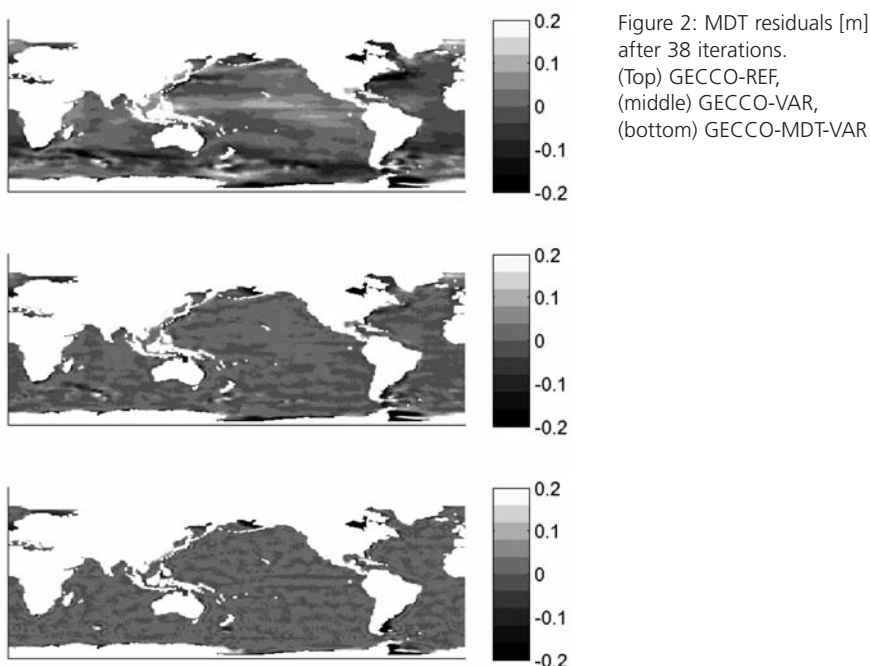
Figure 1: Cost functions of the sensitivity experiments after 38 iterations: most important contributions

3. co-variance information has no significant impact on the costs averaged over all length scales,
4. the dynamic model is able to reproduce assimilated MDT very closely, but with increasing costs on other constraints.

From the experiments we conclude, that the MDT constraint adds new information to the optimization process, and that this information is consistent with the other data sets assimilated, at least in a global sense. To what extent this statement holds for specific regions has to be further investigated. Co-variance information has local effects on the MDT residuals (not shown), especially in the ACC, but the tendency is not clear. Both, patches of increasing as well as decreasing residuals, in the order of a few cm, are present. The close reproduction of the assimilated MDT in the MDT-only experiments does indicate, that the MDT is essentially consistent with the dynamics of the ocean model. The higher residuals regarding other data sets not assimilated does not indicate inconsistency of the MDT, but rather indicates, that the model system is under-determined, meaning, that a number of ocean states is dynamically consistent with essentially the same MDT.

Ocean State Estimation Experiment

For the ocean state estimation experiments we targeted on reproducing the MDT together with other parameters of the ocean state as realistic as possible. The assimilation period is therefore prolonged to 7 years, from 1993 to 1999, identical to the reference period of the MSS (CLS2010) applied for calculating the MDT. The geoid applied is the first available combined GRACE-GOCE solution (GOCO01s). The error on the MDT includes all components we already considered in the sensitivity experiments, and, in addition, the mapping error of the MSS is estimated. But since high resolution geoid information is taken into account when estimating the MSS (see <http://www.aviso.oceanobs.com/en/data/products/auxiliary-products/mss/mss-description/index.html> for more information), we estimate only the mapping error of the MDT. To do so, we simulate altimeter observations by subsampling a high resolution modeled MDT (from the POP model, see *Maltrud and McClean, 2005*) along the ground tracks of the JASON and EnviSat altimeters. By interpolating the 'observed' data to the GECCO model grid and comparing it with the original MDT, we get an error estimate for the MDT mapping, that is then projected to spherical harmonic functions.



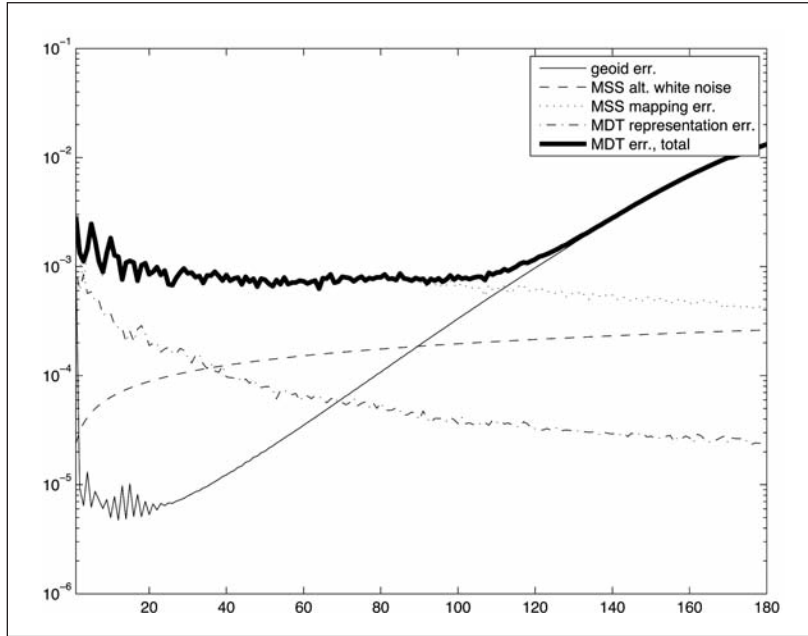


Figure 3: Square root of degree variance [m] for the components of the MDT error estimate.

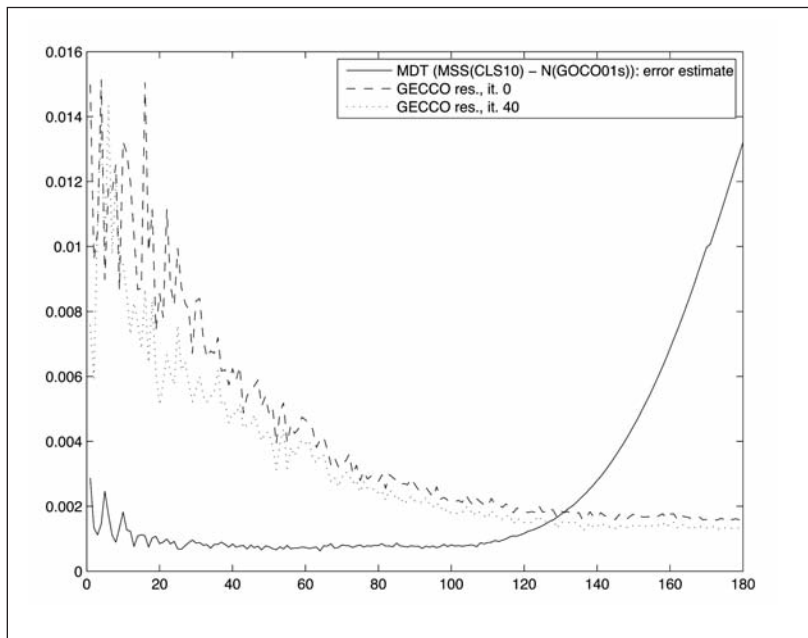


Figure 4: Square root of degree variance [m] in MDT residuals, compared to prior error estimate.

The MDT error contributions are displayed in Fig. 3. While the representation error has some impact on very long scales, the altimeter white noise error is negligible everywhere. The main contribution comes from the MSS mapping error, which dominates the MDT error up to approximately d/o 100, then the geoid error takes over.

Results from the optimization after 40 iterations are displayed in Fig. 4. From the spectral

representation of the MDT residuals (Fig. 4) we see, that the residuals, despite for degrees 3-9, are reduced through the optimization for all length scales. But for degrees lower approximately 100, the residuals are still much larger than the estimates errors, and though convergence in the cost function is not reached yet (not shown), it is foreseeable, that also the final residuals will remain above those estimates. The reasons might be too small error estimates in the MDT or model errors not accounted for.

Conclusions

Assimilation of MDT has significant effect on ocean state estimation, also if most available ocean data, including especially Sea Level Anomaly data from altimetry, ARGO and other ocean data is also assimilated. The additional assimilation of MDT further improves the model state towards the other assimilated data sets, and strongly reduces the residuals in the MDT, indicating, that the MDT puts additional information to the optimization process, which is essentially consistent with the other data streams and the dynamics of the ocean model. The error in MDT is dominated by the mapping error of the MSS up to about degree 100, meaning that in low resolution circulation models (1° in our case) this error determines the influence the MDT can have on the optimized solution, while, when based on the newest available satellite data, the error in the geoid plays only a marginal role.

Acknowledgements

This work was supported by the German Ministry of Science and Education (BMBF) geotechnology program, theme 2: »Survey of System Earth from Space«. MSS_CNES_CLS_10 was produced by CLS Space Oceanography Division and distributed by Aviso, with support from Cnes (<http://www.aviso.oceanobs.com/>).

References

Köhl, A., and D. Stammer, 2008, Decadal Sea Level Changes in the 50-Year GECCO-2 Ocean Synthesis, *J. Clim.*, 21, 1876-1890

Maltrud, M.E. and J.L. McClean, 2005, An eddy resolving global $1/10$ degree ocean simulation. *Ocean Modelling*, 8, 31-54.

Marshall, J., A. Adcroft, C. Hill, L. Perelman, and C. Heisey, 1997, A finite-volume, incompressible Navier Stokes model for studies of the ocean on parallel computers, *J. Geophysical Res.*, 102 (C3), 5753-5766.

Stammer, D., A. Köhl, and C. Wunsch, 2007, Impact of accurate geoid fields on estimates of the ocean circulation, *J. Atmos. Ocean. Tech.*, 24, 1464-1478

Wunsch, C., 1996, *The ocean Circulation Inverse Problem*, Cambridge University Press, 458 pp.

Validation of GOCE products by terrestrial data sets in Germany

Voigt C. (1), Rülke A. (2), Denker H. (1), Ihde J. (2), Liebsch G. (2)

(1) Institut für Erdmessung (IfE), Leibniz Universität Hannover, Schneiderberg 50, D-30167 Hannover, Germany;

E-mail: voigt@ife.uni-hannover.de; Phone: ++49 511 762-5787

(2) Bundesamt für Kartographie und Geodäsie, Karl-Rothe-Straße 10-14, D-04105 Leipzig, Germany;

E-mail: axel.ruelke@bkg.bund.de; Phone: ++49 341 5634-388

1. Abstract and Introduction

Within the framework of the REAL GOCE project, one of the main objectives is the validation of the GOCE products. In this contribution, the focus is on the regional validation of the GOCE products by independent terrestrial data sets in Europe and particularly in Germany, including terrestrial gravity anomalies, height anomalies from the high-resolution gravimetric quasigeoid models EGG2008 and GCG05, and astrogeodetic vertical deflections. Differences between the terrestrial data sets and the available GOCE geopotential models, with envisaged accuracies of 1 mgal for gravity and 1-2 cm for geoid heights, both at a resolution of 100 km, are computed and analyzed. The progress with respect to the GRACE models and the impact on regional gravity field modelling is outlined.

2. Data Sets

The first GOCE global geopotential models (GGM) are based on an observation period of approx. two months (begin of November 2009 to January 11, 2010) using different approaches: the direct approach (up to degree and order (d/o) 240; *Bruinsma et al., 2010*), the space-wise approach (d/o 210; *Migliaccio et al., 2010*), and the time-wise approach (d/o 224; *Pail et al., 2010*). In addition, the GOCO01S model (d/o 224; GOCO consortium, 2010) combines 7 years of GRACE observations (August 2002 to August 2009) and two months of

GOCE data (November and December 2009). The impact of the GOCE models is outlined with respect to the GRACE model ITG-Grace2010s (d/o 180; *Mayer-Gürr et al., 2010*) and the ultra-high degree model EGM2008 (d/o 2190; *Pavlis et al., 2008*) based on GRACE and terrestrial data.

For the evaluation of the GGMs, extensive terrestrial data sets are available for Europe and particularly for Germany; for details see *Ihde et al. (2010)*. Approx. 5.3 million terrestrial gravity anomalies exist for Europe and were combined with EGM2008 to derive the European Gravimetric Quasigeoid 2008 (EGG2008; *Denker et al., 2009*). As a second high resolution quasigeoid model, the German Combined Quasigeoid 2005 (GCG05; *Liebsch et al., 2006*) is employed; it is based on 400,000 gravity anomalies (accuracy 0.1 - 1.0 mgal) and 900 GPS/levelling points as well as the EIGEN-CG01C global model (*Reigber et al., 2006*). The spatial resolution is 1' x 1' for EGG2008 and 1' x 1.5' for GCG05, respectively; the accuracy of the height anomalies is roughly 2 - 3 cm in Germany. Within the GOCE GRAND II project, a completely independent data set of approx. 300 astrogeodetic vertical deflections was determined with an accuracy of 0.1" and a spacing of 2.5 to 5 km along a North-South and a West-East profile, both having a length of 500 km.

3. Evaluation of the GOCE geopotential models by regional terrestrial data sets

In the evaluation process, the different spectral content of the GGM and terrestrial data has to be taken into account by filtering out the high-frequency signals not included in the GGM. For the comparisons between the GGM data and the terrestrial gravity anomalies as well as the EGG2008 height anomalies, a Gaussian filter with filter widths (and corresponding resolutions) from 100 to 200 km was applied to both the GGM and terrestrial data. The differences were computed within 5' x 5' grids, derived from the finer grids by averaging. Table 1 shows the standard deviations of the differences between terrestrial gravity anomalies as well as EGG2008 height anomalies and corresponding GGM values in connection with different Gaussian filter widths. The largest differences occur between the terrestrial data sets and the GRACE model ITG-Grace2010s. At a filter width of 100 km, the differences are about two times larger than those of the best fitting GOCE model, the direct solution (2.6 mgal and 7.4 cm). However, the differences of the GOCE models are between 2 (direct approach) and 3 (space-wise approach) times larger than the EGM2008 differences. For increasing filter widths up to 200 km, the differences between terrestrial and GGM data become smaller. Nevertheless, the aspired GOCE accuracy level of 1 mgal and 1-2 cm (at 100 km resolution) is almost reached for lower resolutions of about 200 km (direct approach: 1.1 mgal and 2.2 cm,

respectively). Figure 1 shows the differences between the terrestrial and various GGM gravity anomalies after Gaussian filtering with a filter width of 100 km. A considerable improvement of the GOCE based models with respect to the GRACE models is evident.

In addition, the GCG05 height anomalies were used for the evaluation of the GOCE GGMs in connection with different filtering approaches.

Table 1: Standard deviations of the differences between 928,790 terrestrial gravity anomalies and EGG2008 height anomalies and corresponding values from various geopotential models after Gaussian filtering with the specified filter widths.

Geopotential Model	Filter width [km]	Std.dev. [mgal]	Std.dev. [m]
Direct approach	100	2.57	0.074
Space-wise approach	100	3.86	0.118
Time-wise approach	100	3.55	0.108
GOCO01S	100	3.49	0.104
ITG-Grace2010s	100	5.18	0.172
EGM2008	100	1.45	0.036
Direct approach	120	1.82	0.054
Space-wise approach	120	2.61	0.082
Time-wise approach	120	2.42	0.075
GOCO01S	120	2.36	0.071
ITG-Grace2010s	120	3.63	0.122
EGM2008	120	1.34	0.031
Direct approach	150	1.37	0.037
Space-wise approach	150	1.63	0.049
Time-wise approach	150	1.56	0.046
GOCO01S	150	1.52	0.042
ITG-Grace2010s	150	2.15	0.070
EGM2008	150	1.23	0.025
Direct approach	200	1.12	0.022
Space-wise approach	200	1.14	0.025
Time-wise approach	200	1.14	0.026
GOCO01S	200	1.12	0.022
ITG-Grace2010s	200	1.21	0.027
EGM2008	200	1.09	0.016

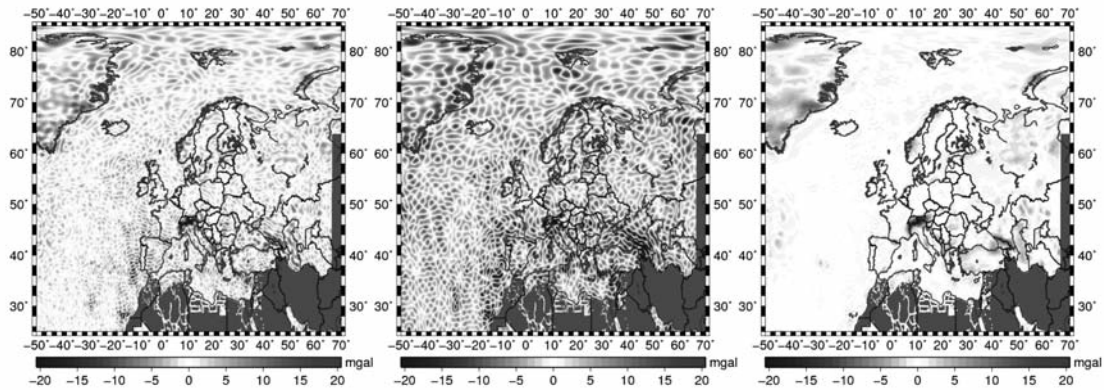


Figure 1: Differences between terrestrial gravity anomalies and corresponding values from the GOCE direct approach (left), ITG-Grace2010s (center) and EGM2008 (right) after Gaussian filtering with a filter width of 100 km.

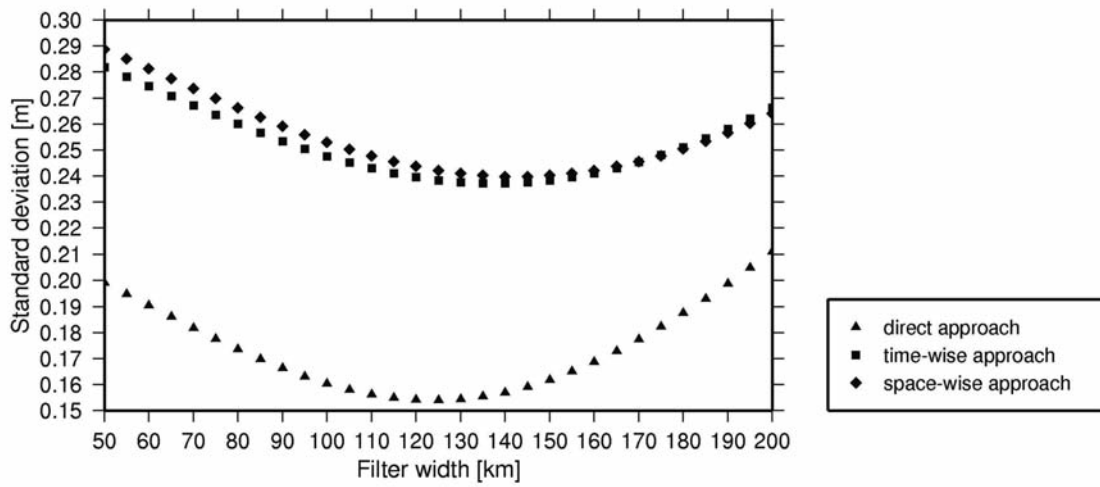


Figure 2: Standard deviations of the differences between the Gaussian filtered GCG05 height anomalies and corresponding values from the three GOCE models in connection with different filter widths.

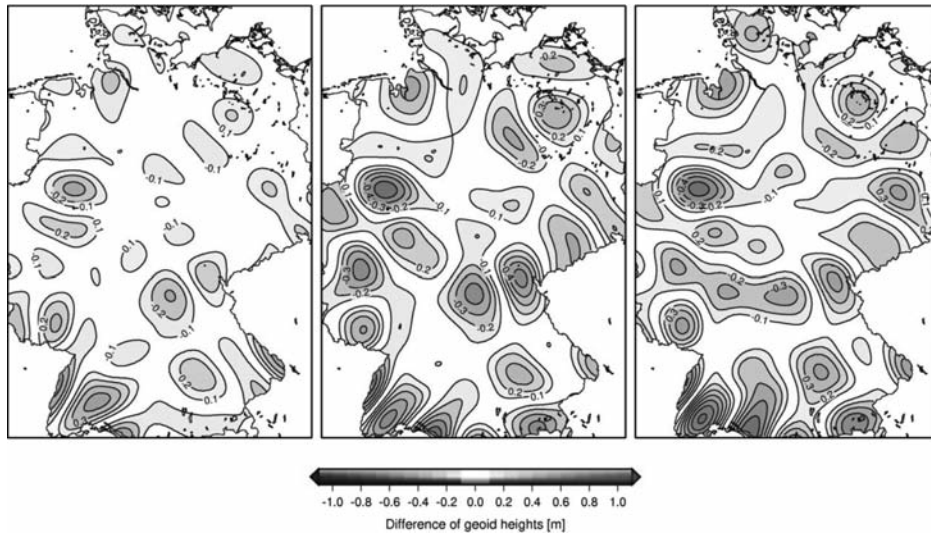


Figure 3: Differences between Gaussian filtered GCG05 height anomalies with a filter width of 125 km and height anomalies from the GOCE direct approach (left), the time-wise approach (center) and the space-wise approach (right).

In a first step, the Gaussian filtering is applied to the GCG05 only. Figure 2 shows the standard deviations of the differences between the filtered GCG05 height anomalies and the GOCE GGMs with regard to different filter widths. Again, the direct approach gives the best agreement, while higher differences are found for the time-wise and space-wise approaches. The minimum values occur at filter widths of approx. 125 km, 135 km and 140 km for the direct, the time-wise and the space-wise approach, respectively, showing that also the higher degrees of the GOCE models contain significant signals. Table 2 provides the

mean and the standard deviation of the differences between the GCG05 and various GGM height anomalies after different filtering procedures: 1. no filtering applied, 2. Gaussian filter with 125 km width applied for GCG05 only, and 3. the Gaussian filter (125 km width) applied for both data sets. It is evident, that all three GOCE models provide significantly more information than the GRACE model ITG-Grace 2010s, but the EGM2008 results are still superior within this study area. Figure 3 shows the spatial patterns of the differences between GCG05 and the three GOCE solutions after Gaussian filtering (filter width 125 km).

Table 2: Statistics of the differences between GCG05 and various GGM height anomalies after different Gaussian filtering approaches with a filter width of 125 km.

Geopotential Model	Truncation	No filter applied		Regional model filtered		Both models filtered	
		Mean	Standard deviation	Mean	Standard deviation	Mean	Standard deviation
		[m]	[m]	[m]	[m]	[m]	[m]
Direct approach	240	0.331	0.226	0.329	0.154	0.328	0.121
Space-wise approach	210	0.334	0.310	0.332	0.242	0.328	0.194
Time-wise approach	224	0.334	0.303	0.332	0.238	0.329	0.187
ITG-GRACE2010s	180	0.348	0.372	0.370	0.309	0.344	0.259
EGM2008	2190	0.321	0.034	0.319	0.168	0.312	0.026

Table 3: RMS-differences ["] between the North-South and East-West astrogeodetic vertical deflection components ξ and η and corresponding values from various GGM with regard to a maximum degree along the North-South (155 stations) and the West-East profile (128 stations) after a multistage filtering process.

Geopotential Model	Truncation	North-South Profile		West-East Profile	
		RMS $\Delta\xi$	RMS $\Delta\eta$	RMS $\Delta\xi$	RMS $\Delta\eta$
Direct approach	180	0.53	0.55	0.33	0.22
Space-wise approach	180	0.51	0.68	0.34	0.39
Time-wise approach	180	0.52	0.62	0.36	0.34
GOCO01S	180	0.50	0.60	0.35	0.28
ITG-Grace2010s	180	0.91	0.88	1.11	0.56
EGM2008	180	0.48	0.48	0.34	0.21
Direct approach	210	0.62	0.66	0.33	0.28
Space-wise approach	210	0.96	0.98	0.56	0.56
Time-wise approach	210	0.68	0.81	0.50	0.60
GOCO01S	210	0.63	0.79	0.47	0.59
EGM2008	210	0.48	0.48	0.34	0.21
Direct approach	224	0.56	0.63	0.36	0.29
Time-wise approach	224	0.65	1.19	0.80	0.78
GOCO01S	224	0.60	1.21	0.78	0.72
EGM2008	224	0.48	0.48	0.34	0.21
Direct approach	240	0.58	0.65	0.41	0.33
EGM2008	240	0.48	0.48	0.34	0.21

For the evaluation of the GOCE models with astrogeodetic vertical deflections, a stepwise procedure was used in order to account for the different spectral content. In a first step, vertical deflections were computed from the GGMs for the astrogeodetic stations. The maximum degree of the spherical harmonic expansions was varied from 100, 150, 180, 210, 224 to 240; the omitted signal between these maximum degrees and degree 2190 was modelled by EGM2008 (cf. *Gruber, 2009*). As vertical deflections are strongly correlated with the local topography, the high-frequencies beyond degree 2190 are modelled by Residual Terrain Model (RTM) effects (*Forsberg, 1984*) with a reference topography of 5' x 5' resolution and a Gaussian filtering with a filter width of 20 km. In Table 3, the RMS differences between

the filtered astrogeodetic vertical deflections and corresponding values from the geopotential models, truncated at degrees 180, 210, 224 and 240, are shown. Up to d/o 150, no significant differences show up between the various geopotential models. Up to d/o 180, the RMS differences between the astrogeodetic vertical deflections and the GRACE model ITG-Grace2010s are significantly increasing in contrast to all models including GOCE data. Hence, a considerable improvement within the spectral range between d/o 150 and 180 is evident when utilizing the GOCE GGMs; the RMS differences are at the level of the combined solution EGM2008. Beyond degree 180, the RMS differences of all GOCE models are increasing steadily up to the maximum degree of 210 (space-wise solution) and 224 (time-wise

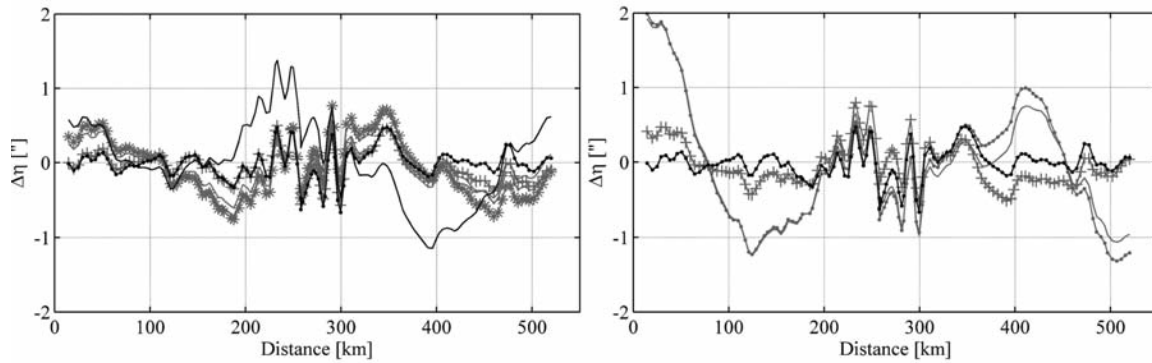


Figure 4: Differences between the East-West astrogeodetic vertical deflection components and corresponding values from the GOCE direct approach (grey, +), the space-wise approach (grey, *), the time-wise approach (grey, -), GOCO01S (grey, ---), ITG-Grace2010s (black, ---) and EGM2008 (black, -) up to a maximum degree of 180 (left) and 224 (right) along the West-East profile after a multistage filtering process.

solution, GOCO01S), respectively; the space-wise solution shows the greatest increase. Merely, the direct solution nearly remains at the accuracy level of the EGM2008 even up to the maximum degree 240. In Fig. 4, the differences between the filtered astrogeodetic East-West vertical deflection components η and corresponding values from various GGM, truncated at degree 180 (left) and 224 (right), are shown along the West-east profile exemplarily.

4. Combination of GOCE and terrestrial gravity anomalies

First high-resolution combined quasigeoid solutions for Europe were computed from the existing terrestrial gravity anomalies and the GOCE geopotential models using the spectral combination method in connection with the remove-restore procedure. As at present only formal errors exist for the GOCE models, different weighting schemes were tested. The evaluation of the combined solutions by various national GPS/levelling data sets in Europe showed small improvements for some but not all cases. Mostly the GOCE direct solution performed best, revealing improvements at the few millimetre level (e.g., in France and Russia).

5. Conclusions

The new GOCE geopotential models include significantly more high frequency information than any GRACE model. In the comparisons of the GOCE models with terrestrial gravity

anomalies and EGG2008 height anomalies, the GOCE direct approach shows the best performance with RMS differences of 2.6 mgal and 7 cm, respectively (at a resolution of 100 km). The comparisons with the GCG05 height anomalies confirm the better performance of the GOCE direct solution. Regarding the vertical deflections, the GOCE models are superior to the GRACE models within the spectral range between d/o 150 and 180; for higher degrees up to 240, the quality of the GOCE models degrades with respect to EGM2008, except the direct approach. However, it should also be noted the better performance of the GOCE direct approach may be due to the included a priori information from the combined geopotential model EIGEN-51C (*Bruinsma et al. 2010*). With regard to the high-resolution combination solutions of terrestrial gravity anomalies and the GOCE geopotential, the weighting may be problematic at present, as only formal errors exist for the GOCE models. The evaluation of the combined solutions with GPS/levelling data show small improvements in some but not all areas. Further improvements are expected from refined GOCE models based on more extensive input data covering a longer observation period.

Acknowledgements

The project REAL GOCE is part of the R&D-Programme GEOTECHNOLOGIEN. GEOTECHNOLOGIEN is funded by the German Ministry of Education and Research (BMBF) and the

German Research Foundation (DFG), Grant (03G0726C) of project REAL GOCE.

References

Bruinsma, S.L., Marty, J.C., Balmino, G., Biancale, R., Förste, C., Abrikosov, O., Neumayer, H. (2010). GOCE Gravity Field Recovery by Means of the Direct Numerical Method. Presented at the ESA Living Planet Symposium, 28 June – 2 July 2010, Bergen, Norway. See also: earth.esa.int/GOCE.

Denker, H., Barriot, J.-P., Barzaghi, R., Fairhead, D., Forsberg, R., Ihde, J., Kenyeres, A., Marti, U., Sarrailh, M., Tziavos, I.N. (2009). The Development of the European Gravimetric Geoid Model EGG07. In: Sideris, M. (Ed.), *Observing Our Changing Earth*.

Forsberg, R. (1984). *A Study of Terrain Reductions, Density Anomalies and Geophysical Inversion Methods in Gravity Field Modelling*. Report No. 355, Department of Geodetic Science and Surveying, The Ohio State University, Columbus, Ohio.

GOCE consortium (2010). The satellite-only global gravity field model GOCO01S derived from GOCE and GRACE. http://portal.tugraz.at/portal/page/portal/TU_Graz/Einrichtungen/Institute/Homepages/i5080/forschung/GOCO/.

Gruber, T. (2009). Evaluation of the EGM2008 gravity field by means of GPS-levelling and sea surface topography solutions; External evaluation reports of EGM08, *Newton's Bulletin*, Nr. 4, pp. 3-17, Bureau Gravimétrique International (BGI) / International Geoid Service (IGeS), ISSN 1810-8555.

Ihde, J., Wilmes H., Müller, J., Denker, H., Voigt, C., Hosse, M. (2010). Validation of Satellite Gravity Field Models by Regional Terrestrial Data Sets. In: *System Earth via Geodetic-Geophysical Space Techniques (Advanced Technologies in Earth Sciences)*.

Liebsch, G., Schirmer, U., Ihde, J., Denker, H., Müller, J. (2006). Quasigeoidbestimmung für Deutschland. *DVW-Schriftenreihe* 49, 127-146.

Mayer-Gürr, T., Kurtenbach, E., Eicker, A. (2010). ITG-Grace2010. <http://www.igg.uni-bonn.de/apmg/index.php?id=itg-grace2010>.

Migliaccio, F., Reguzzoni, M., Sanso, F., Tschering, C.C., Veicherts, M. (2010). GOCE data analysis: the space-wise approach and the first space-wise gravity field model. *Proceedings of the ESA Living Planet Symposium*, 28 June – 2 July 2010, Bergen, Norway. See also: earth.esa.int/GOCE.

Pail, R., Goiginger, H., Mayrhofer, R., Schuh, W.-D., Brockmann, J.M., Krasbutter, I., Hoeck, E., Fecher, T. (2010). GOCE gravity field model derived from orbit and gradiometry data applying the time-wise method. *Proceedings of the ESA Living Planet Symposium*, 28 June – 2 July 2010, Bergen, Norway. See also: earth.esa.int/GOCE.

Pavlis, N.K., Holmes, S.A., Kenyon, S.C., Factor, J.K. (2008). An Earth Gravitational Model to Degree 2160: EGM2008. *EGU General Assembly*, Vienna, Austria, April 13-18.

Reigber, C., Schwintzer, P., Stubenvoll, R., Schmidt, R., Flechtner, F., Meyer, U., König, R., Neumayer, H., Förste, C., Barthelmes, F., Zhu, S.Y., Balmino, G., Biancale, R., Lemoine, J.-M., Meixner, H., Raimondo, J.C. (2006). A High Resolution Global Gravity Field Model Combining CHAMP and GRACE Satellite Mission and Surface Data: EIGEN-CG01C. *Scientific Technical Report STR06/07*, GeoForschungsZentrum Potsdam.

High-resolution global gravity fields by combining GOCE, GRACE and terrestrial data

First results from the REAL GOCE project

Shako R. (1), Förste C. (1), Abrikosov O. (1), Bruinsma S. (2), Dahle C. (1), Flechtner F. (1), Neumayer H. (1) and Marty J. C. (2)

(1) Helmholtz-Zentrum Potsdam Deutsches GeoForschungsZentrum – GFZ, Telegrafenberg, 14473 Potsdam, Germany

(2) CNES/Groupe de Recherches de Geodesie Spatiale, 18, avenue Edouard Belin, F-31401 Toulouse, France

Abstract / Introduction

The main goal of the REAL-GOCE WP320 is the computation of a high-resolution gravity field model up to degree and order 720 or higher in terms of spherical harmonics with a global coverage and an outstanding quality. Compared to the recently available combined gravity field models like EIGEN-5C (Förste *et al.* 2008), EIGEN-51C (Bruinsma *et al.* 2010), EGM 2008 (Pavlis *et al.* 2008) or GGM03C (Tapley *et al.* 2007), such a combined model including GOCE data should benefit from the accuracy of the new GOCE satellite gradiometry data in the medium wavelength components (i.e. spatial resolution between about 70 and 100 km) of the Earth's gravity field.

Since July 2010 a first cycle (i.e. about two months) of GOCE gradiometry data is available. Additionally, the first GOCE-only global gravity field models were published by ESA. One of these first GOCE-only models has been computed by GFZ Potsdam and GRGS Toulouse within ESA's GOCE High Level Processing Facility (GOCE-HPF) by using the so-called direct approach. This model is called GO_CONS_GCF_2_DIR (Bruinsma *et al.* 2010; Pail *et al.* 2010) and its data has been used by GFZ within the REAL-GOCE WP320 to compute a preliminary GRACE/GOCE combined satellite-only model. This is an important milestone for the further computation of a combined model including terrestrial data.

Basic Strategy

Based on the experience with the GRACE and CHAMP missions, GFZ Potsdam processes all present-day satellite data which are suitable for gravity field determination, i.e., GPS high-low SST from GRACE and GOCE, KBR low-low SST data from the GRACE twin satellites, gradiometry measurements from GOCE and SLR data from the LAGEOS satellites. These data are the basis for the computation of global mean satellite-only gravity field models like EIGEN-5S (Förste *et al.* 2008) and the further combination with terrestrial and altimetry gravity data to obtain high resolution combined gravity field models.

The basic workflow of combining the contributions of the different data sets as applied at GFZ is shown in figure 1. The left hand side on this figure concerns the processing steps for the terrestrial and altimetry gravity data. The right hand side shows, in which sequence the normal equations are generated from the GOCE gradiometer and SST measurements. These normal equations are later on combined with GRACE based and complete surface data normal equations. The final step is their combination with the outcome of a block diagonal solution which gives the high resolution gravity model up to d/o 720 or higher.

It should be noted that due to the huge size of one single complete normal equation system of a maximum degree/order of 360 (that means

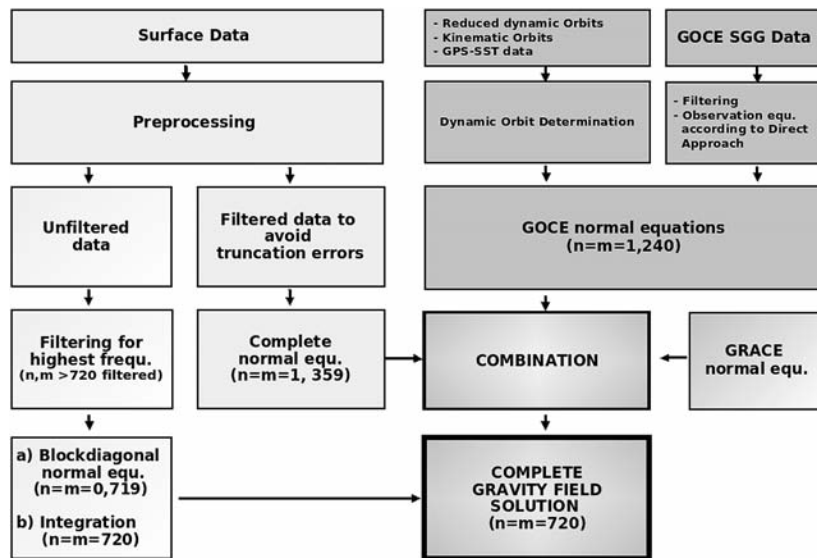


Figure 1: Basic workflow of the generation of combined gravity field models within WP320

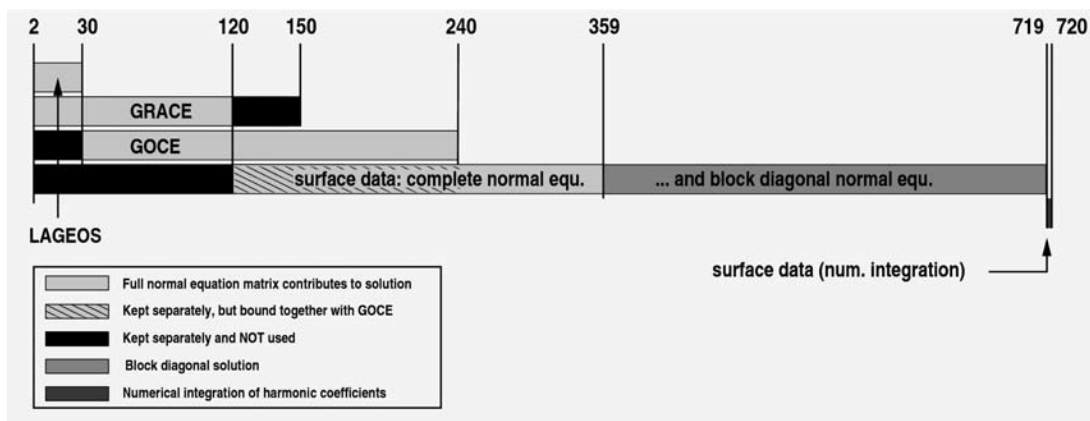


Figure 2: Combination Scheme of the planned high resolution combination model

more than 128 GB for 1 individual normal equation), a gravity field model of maximum d/o higher than 360 can only be composed by use of block diagonal techniques. A block diagonal solution is identical with a complete solution if the following preconditions are met by all data:

- one data type only with global coverage (no data gaps!),
- equidistant and equator-symmetric data grid,
- equator-symmetric weighting,
- uniform weight for each degree of latitude.

The most recent outcome of the activities within WP320 concerning combined gravity field models including terrestrial data is EIGEN-51C (Bruinsma et al. 2010). This global gravity field

model consists of six years of CHAMP and GRACE data, which were processed in accordance to the GFZ release 4 GRACE processing standards (Flechtner 2007). EIGEN-51C is a solution where for the first time for GFZ a combined gravity field model has been computed from the inversion of a full normal equations matrix till d/o 359.

Combination Scheme

Figure 2 shows a typical scheme as applied at GFZ how the individual contributions from the different data sources were distributed on different degree ranges during the combination for a high resolution combination model. It should be noted that this figure illustrates the combination scheme as presently planned at

WP320; one or the other detail may change during the final processing.

The basic idea of such a combination scheme is to restrict the contributions of the individual data sets on such spectral ranges where they are known to perform best. This can be achieved by separation of unknowns when combining the normal equations, for instance the spherical harmonics of the surface data up to d/o 120 are set up as additional and individual unknowns which are kept separate and thrown away after the adjustment. With this method, the surface data do not contribute to the solution below degree 120. In a similar way the GOCE and GRACE contributions are combined.

Surface data sets

Figure 3 shows the global distribution of the surface data sets which are currently available for the computation of the combined gravity field models at GFZ. This data sets were used for instance for the generation of EIGEN-5C (Förste et al. 2008)

The surface data sets as indicated in fig. 3 have the following specifications:

1. Geoid undulations, 2'x2' resolution, (T. Schöne and S. Esselborn, GFZ, 2005, personal communication and Stammer et al., 2002)
2. Gravity anomalies North Atlantic/Mediterranean, 15'x15' resolution, (H. Denker, IfE

Hannover, 2007, personal communication),

3. Gravity anomalies in Europe & North Africa, 15'x15' resolution (in Russia only 30'x30'), H. Denker, IfE Hannover, 2007, personal communication.
4. Arctic Gravity Project ArcGP, 5'x5' resolution, Forsberg, Kenyon 2004 & 2006.
5. NAFA Gravity anomalies in North America, 2'x2' resolution, M. Véronneau 2003, National Ressources Canada, pers. communication.
6. Gravity anomalies in China, 30'x30' resolution (J.Y. Chen, pers. comm., 2003) and Gravity anomalies in Australia, point data, resolution better than 5'x5' (A. Murray, Geosciences Australia, 2001),
7. LDO (Bell et al., 1999) and AWI (Studinger 1988) gravity anomalies, point data, resolution better than 5'x5',
8. NGA (formerly NIMA) terrestrial gravity anomalies, 30'x30' resolution.
9. NGA altimetric gravity anomalies for coastal and shallow water areas, 30'x30' resolution.
10. New Zealand: NGA terrestrial gravity anomalies, 30'x30' resolution.

In addition to this individual data sets we also use the DNSC08 global gravity anomaly grid (Anderson and Knudsen 2009) which has a resolution of 2' x 2'. For the continents this data set is composed from the terrestrial data as used for EGM2008. This DNSC08 data set is suitable to substitute the low resolution NGA and China data.

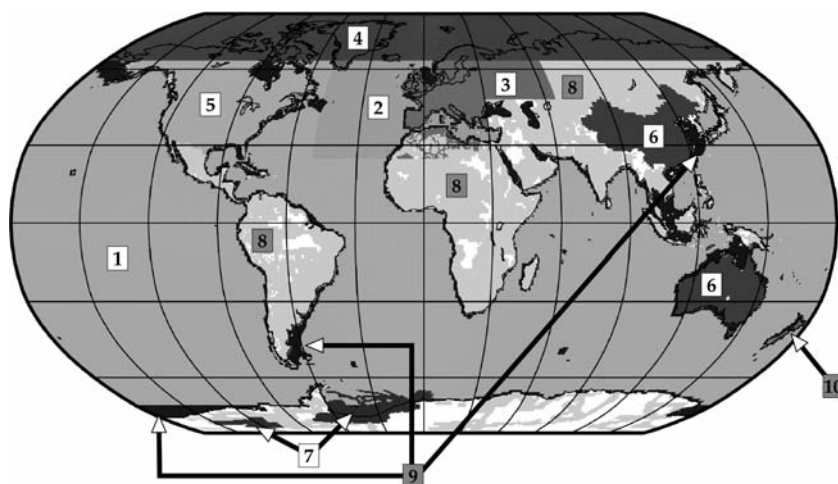


Figure 3: Overview of the surface data sets presently used at GFZ Potsdam, see text above for further details.

First results

Three groups within the GOCE-HPF have generated the first GOCE gravity models by using the first available GOCE SGG and SST measurement data. These three models have been published by ESA in July 2010. One of these solutions is GO_CONS_GCF_2_DIR, a joint GFZ-GRGS model computed by the so-called Direct Approach (Abrikosov and Schwintzer 2004). This solution comprises the first two available months of GOCE SGG and SST data and is complete up to d/o 240. For overcoming the polar gaps in the GOCE data for the computation of GO_CONS_GCF_2_DIR, the so-called polar cap regularization has been applied (Metzler and Pail 2005) which means filling the polar gaps by external gravity pre-information. For this filling we used the EIGEN-51C model up to d/o 240.

The GOCE gradiometry data as included in the GO_CONS_GCF_2_DIR model were used within the REAL GOCE WP320 to compute for the first time for GFZ a GRACE/GOCE combination model. For this purpose the GOCE SGG data as used for GO_CONS_GCF_2 (including the mentioned spherical cap regularization) have been combined with seven years of GRACE data from the GFZ release 4 processing. The result of this combination is the preliminary

gravity field model EIGEN-6Sp05, which was calculated in late August 2010 and which is complete up to d/o 240.

Figure 4 shows the difference degree amplitudes of EIGEN-6Sp05 and CONS_GCF_2_DIR w.r.t. to EGM2008. Furthermore, the differences of EIGEN-51C and GOCO01S w.r.t. EGM 2008 are also given. GOCO01S is the first GOCE-GRACE combination model and has been released recently by the GOCO consortium (http://portal.tugraz.at/portal/page/portal/TU_Graz/Einrichtungen/Institute/Homepages/i5080/forschung/GOCO/). The GOCO01S model is online available at the ICGEM data base at GFZ (<http://icgem.gfz-potsdam.de>).

From degree 2 up to 110 the GRACE-containing models (EIGEN-51C, GOCO01S and EIGEN-6Sp05) are very close together. One can expect that these three models are of similar quality within this degree range. This is confirmed by GOCE orbit adjustment tests by the authors as given in table 1. These orbit tests were carried out by using different gravity field models up to d/o 120. Table 1 contains the mean values of the RMS values of the orbit fit residual of 60 GOCE dynamics orbit computations. The length of each orbit was 1.25 days. As observations GOCE kinematic orbit positions were used. For

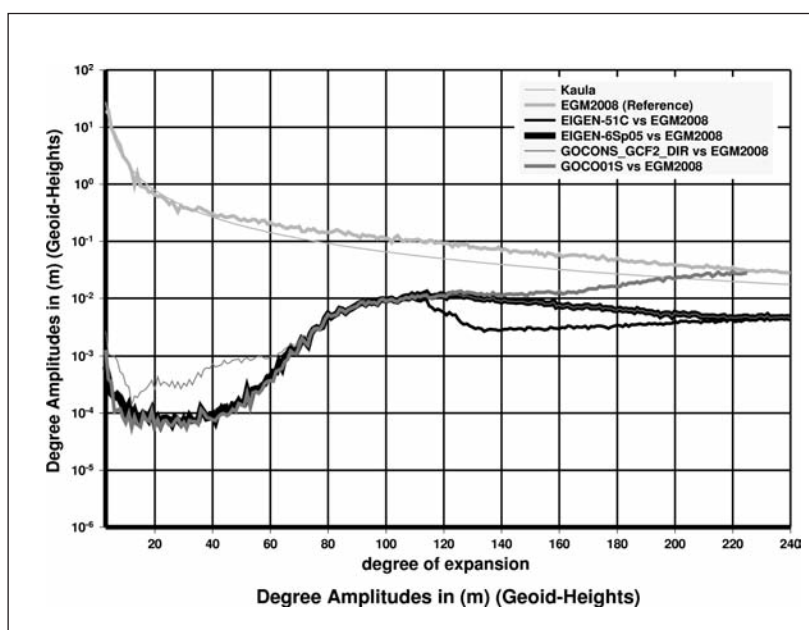


Figure 4: Degree Amplitudes (Geoid Heights). Differences of EIGEN-51C, EIGEN-6Sp05, CONS_GCF_2_DIR and GOCO01S against EGM 2008. Beyond degree 80, the curve for EIGEN-6Sp05 (black, broad) is identical with that for CONS_GCF_2_DIR (grey, slight)

EIGEN-51C, GOCE001S and EIGEN-6Sp05 about the same RMS numbers were reached. For GO_CONS_GCF_2_DIR a significant larger value was obtained which means that this model has a worse performance in the long wavelength degree range compared to EIGEN-51C, GOCE001S and EIGEN-6Sp05. This is not a surprise, since the GO_CONS_GCF_2_DIR contains only 2 months of SST data which dominating the long wavelengths.

For the higher degrees beyond 110 one can see that the difference between GOCO01S on the one side and EIGEN-6Sp05 and GO_CONS_GCF_2_DIR on the other side becomes larger with increasing degrees. EIGEN-6Sp05 and GO_CONS_GCF_2_DIR get closer to EIGEN-51C with increasing degree. This is an effect of the polar cap regularization applied in EIGEN-6Sp05 and GO_CONS_GCF_2_DIR which constrains the shortest wavelengths to the a-priori model EIGEN-51C.

Figure 5 finally shows the global distribution of the geoid height differences between EIGEN-6Sp05 and EGM2008. In this plot EGM2008

has been truncated at d/o 240. The patterns of the significant differences for instance over South America, Antarctica, Africa and Central Asia coincide with the gaps in the terrestrial as depicted in figure 2. It is known that EGM2008 contains these gaps in the terrestrial data as well. Thus one can conclude that the differences in figure 5 must be interpreted as significant improvements over EGM2008 realized by GOCE.

Conclusion

In WP320 a first GOCE/GRACE combination model has been successfully computed. This is an important milestone on the way to a combined model including data of these satellites and terrestrial data.

Acknowledgements

The German Federal Ministry for Education and Research (BMBF) supports the REAL GOCE project within the GEOTECHNOLOGIEN research and development programme under the grant ID 03G0726H.

References

Abrikosov O., Schwintzer P. (2004): Recovery of the Earth's Gravity Field from GOCE Satellite Gravity Gradiometry: a Case Study, Proc. Second International GOCE User Workshop »GOCE, The Geoid and Oceanography«, ESA-

Table 1: GOCE orbit fit residuals [cm], obtained from a dynamic orbit computations of 60 orbits of an arc length of 1.25 days for different used gravity field models which where used up to d/o 120

Gravity field model	/	max. d/o	120 x 120
EIGEN-51C			3.2
GOCO01S			3.3
EIGEN-6Sp05			3.2
GO_CONS_GCF_2_DIR			3.9

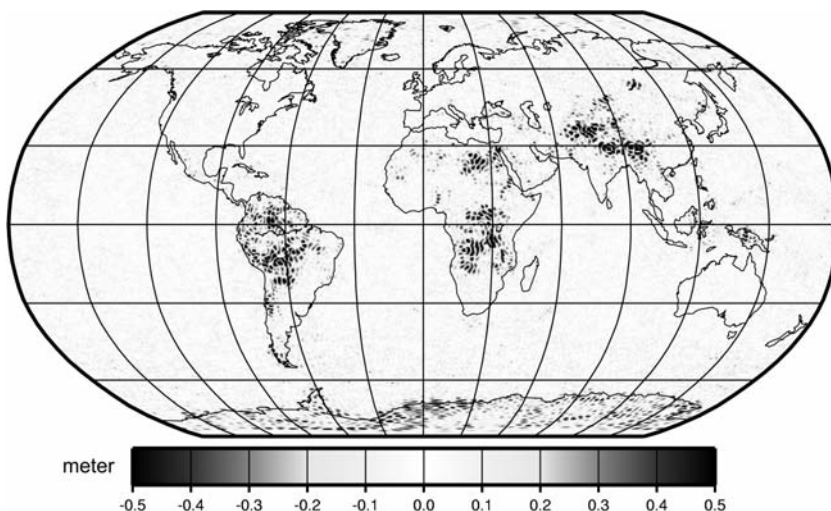


Figure 5: Global distribution of the geoid height differences between EIGEN-6Sp05 and EGM2008 (max d/o 240)

- ESRIN, Frascati, Italy, 8-10 March 2004 (ESA SP-569, June 2004)
- Andersen O. B. and Knudsen P. (2009): DNSC08 mean sea surface and mean dynamic topography models, *Journal of Geophysical Research*, Vol. 114, c11001 12 pp., 2009, doi:10.1029/2008JC005179
- Bell, R.E., Childers, V.A., Arko, R.A. (1999) Airborne and precise positioning for geologic applications. *J Geophys Res* 104 (B7): 15281-18292
- Bruinsma S.L. (2), Marty J.C. (2), Balmino G.(2), Biancale R.(2), Förste C.(1), Abrikosov O.(1) and Neumayer H.(1) (2010), GOCE Gravity Field Recovery by Means of the Direct Numerical Method, presented at the ESA Living Planet Symposium 2010, Bergen, June 27 - July 2 2010, Bergen, Norway
- Förste C., Flechtner F., Schmidt R., König R., et al. (2007a): Global Mean Gravity Field Models from Combination of Satellite Mission and Altimetry/ Gravimetry Surface Data, *Proceedings of the 3rd GOCE User Workshop*, ISBN 92-9092-938-3, ISSN 1609-042X, ESA 2007.
- Förste C., Flechtner F., Schmidt R., Stubenvoll R. et al. (2007b): EIGENGL05C – A new global combined high-resolution GRACE-based gravity field model of the GFZ/GRGS co-operation, *EGU 2008, Geophysical Research Abstracts*, Vol. 10, EGU2008-A-03426, 2008, SRef-ID: 1607-7962/gra/EGU2008-A-03426
- Flechtner F (2007) GFZ Level-2 Processing Standards Document for Product Release 0004. Rev. 1.0, GRACE project documentation 327-743
- Gruber T. (2000): Hochauflösende Schwerefeldbestimmung aus Kombination von terrestrischen Messungen und Satellitendaten über Kugelfunktionen, *Scientific Technical Report STR00/16*, Potsdam, 2000.
- Metzler B., Pail R. (2005): GOCE data processing: The spherical cap regularization approach, *Stud Geophys Geod*, 49:441-462, doi:10.1007/s11200-005-0021-5
- Pail R., Bruinsma S., Migliaccio F., Förste C., et al.: First GOCE gravity field models derived by three different approaches, submitted to *Journal of Geodesy*, Sept 2010.
- Pavlis N.K., Holmes S.A., Kenyon S.C., Factor J.K. (2008): An Earth Gravitational Model to Degree 2160: EGM2008, presented at the 2008 General Assembly of the European Geosciences Union, Vienna, Austria, April 13-18, 2008
- Reigber C., Schwintzer P., Stubenvoll R., et al. (2001): A high resolution global gravity field model combining CHAMP and GRACE satellite mission and surface data: EIGEN-CG01C, *Scientific Technical Report STR06/07*, Potsdam, 2006.
- Shako R., Förste C., Abrikosov O., Kusche J. (2010): GOCE and Its Use for a High-Resolution Global Gravity Combination Model. In: F. Flechtner et al (eds) *System Earth via Geodetic-Geophysical Space Techniques*, Springer, ISBN 978-3-642-10227-1, 231 – 242. doi: 978-3-642-10228-8.
- Stammer, D., Wunsch, C., Giering, R., Eckert, C., Heinbach, P., Marotzke, J., Adcroft, A., Hill, C.N., Marshall, J. (2002) Global ocean circulation during 1992-1997 estimation from ocean observations and a general circulation model. *Journal of Geophysical Research* 107 (C9): 3118, doi: 10.1029/2001JC000888
- Studinger, M. (1998): Interpretation and Analyse von Potentialfeldern im Wedellmeer, Antarktis: der Zerfall des Superkontinents Gondwana, *Rep Polar Res* 276, Alfred Wegener Institut, Bremerhaven
- B. Tapley, J. Ries, S. Bettadpur, D. Chambers, M. Cheng, F. Condi, S. Poole, (2007): *Eos Trans. AGU* 88(52), Fall Meet. Suppl., Abstract G42A-03, 2007

Constraints for Future Missions

Doll B., Sand R.

SpaceTech GmbH, Seelbachstr. 13, 88090 Immenstaad

1. Introduction

We discuss constraints for satellite gravity missions from a standpoint of current feasibility and cost driving aspects. Examples for constraints are the number of satellites, the kind of satellite orbits and the type of the link between the satellites. The merits and drawbacks of different satellite orbits and the impact of using a laser link between the satellites are analysed. Three proposed Future Missions are studied in more detail.

of the satellites a Doppler shift of the frequency is introduced. Together with the current small bandwidth of photodetectors and phase-meters of 20 MHz this results in a constraint for the satellites orbits.

The one way Doppler shift is given by

$$\Delta f = v/\lambda \quad (1)$$

λ =wavelength (1064 nm)

v =relative velocity between two satellites [m/s]

The current phase-meters have a bandwidth of 20 MHz.

2. Discussion of Constraints

2.1. Relative velocity between satellites

It is very attractive to use an optical link between two satellites to measure the distance changes between the satellites caused by the varying gravity field. The reason for this is the higher measurement accuracy compared to a microwave link. Nevertheless the small wavelength ($\lambda=1064$ nm) of the optical link also has a drawback. Because of the relative movement

$$\Delta f < 20 \text{ MHz} \quad (2)$$

Using equation (1) and (2) the maximum relative velocity is 10 m/s.

2.2. Air drag compensation

The meaning of air drag compensation is the continuous cancellation of external non-gravitational forces on the spacecraft, which contains an inertial sensor. The sensor contains a freely floating proof mass, shielded from aerodynamic drag and solar pressure, so that it follows

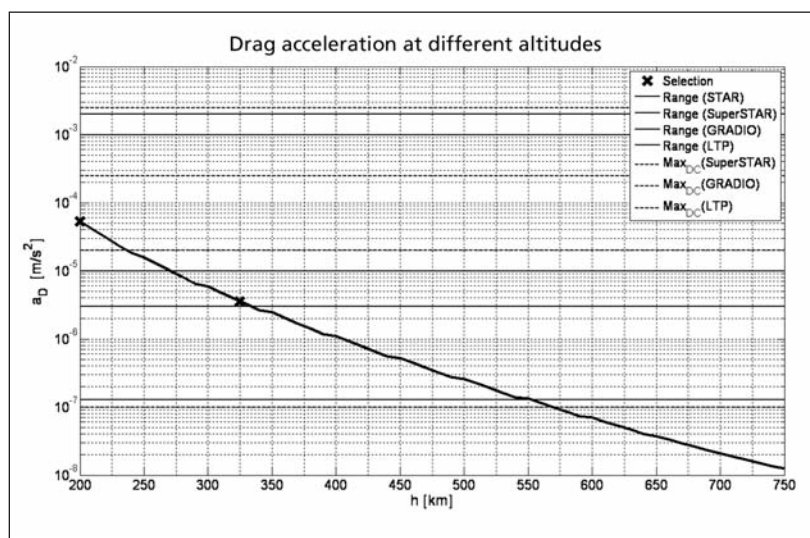


Figure 1 : Drag acceleration at different altitudes

a purely gravitational orbit. The force needed to keep the proof mass at its centre is used to command the propulsion system to make the satellite follow the proof mass.

On the other hand the drag compensation only needs to counteract the drag but does not need to control the drag to a drag free movement of the satellite. This eases the control effort. However, also the cumulated thrust of the different thrusters should not exceed the maximum measurement range of the accelerometer. Thus the drag will be counteracted constantly but it will not be controlled to zero at each time. However the measurement sensitivity is worse when the nonconservative forces are not completely removed.

Air Drag compensation is not mandatory for Orbit heights $h > 350$ km.

2.3. Transponder system

The transponder is the preferred solution:

Assuming that a mission is focusing on $n < 200$ harmonics measurements, the gravity signal is optimised for around 200km S/C distance (like GRACE)

From a laser ranging instrument point of view there are two principle concepts:

- With a laser retro reflector the distance between the satellites is limited. A SST distance of 200 km could not be realized with the available laser power and the possible aperture diameters.

An active transponder system (slightly more complex system) uses also a laser on the second spacecraft. This laser is phaselocked to the received laser beam. Large Spacecraft to Spacecraft distances (200 km) can be realized. Based on above findings a laser transponder system has been selected allowing to adjust the S/C distance according to the best science signal (< 250 km).

2.4. Yaw/Pitch angle

A pendulum orbit is acceptable if the across track angle is limited to max 30° . S/C design optimisation criteria in such a case are all con-

sidered resolvable without significant cost impact

- Compact configuration with minimum average cross section and no significant air drag induced moments (external shape optimisation)
- More fuel consumption, more dynamic AOCS (and fine pointing) controller
- More variations of solar aspect angles (issues on thermal stability, star-tracker blinding etc.)

2.5. Location of accelerometer relative to the centre of mass of the S/C

The principle of Satellite-to-Satellite-Tracking is to measure the velocity variations between two test masses on different satellites. The orbit of the test masses should be influenced only by the earth's gravity field. In reality there are also non-gravitational forces like air-drag and solar pressure acting on the test masses. To separate the nongravitational forces from the pure geodetic motion the test masses are located inside an accelerometer. The accelerometer measures the disturbances and the nongravitational forces can then be subtracted from the SST measurement to restore the pure gravitational motion.

The location of the accelerometer is preferable identical with the position of the centre of mass of the satellite. It turns out that this is difficult to achieve. In addition the position of the centre of mass is not constant due to changes of the mass of the satellite, thermal influences or moving parts. That means there is a decentering of the accelerometer and the centre of mass and the satellite rotates about an axis which is decentered to the centre of mass. The outcome of this is the accelerometer measures also fictitious (pseudo) forces.

CoM=centre of mass

r =CoM offset [mm]

ω =angular velocity

The acceleration induced by the CoM offset is given by:

$$a_{cc} = \frac{d^2}{dt^2} r - \left(\frac{d}{dt} \omega \right) \times r - 2\omega \times \left(\frac{d}{dt} r \right) - \omega \times (\omega \times r)$$

The introduction of the pseudo forces seems to have no relevant impact and therefore there is no need to avoid the decentering (<10 mm) of the centre of mass and the accelerometer. That also means that a mass trim system is not mandatory.

Summary of discussed constraints

Table 1

Constraints	Pendulum Orbit	Satellite distance	Orbit height	Satellite Design	Science improvements	Higher Order gravitational perturbations due to the earth
Relative velocity $\Delta v < 10$ m/s	The maximum across track distance is limited				Small across track distance is a limiting factor	The impact of higher order perturbations has to be clarified
Retroreflector		<40 km				
Transponder		<250 km Transponder is the preferred solution				
Air Drag compensation			For $h=350$ km No Air drag compensation is necessary			
yaw/pitch angle α				If $\alpha > 30$ degree More complex satellite design		
No mass trim						

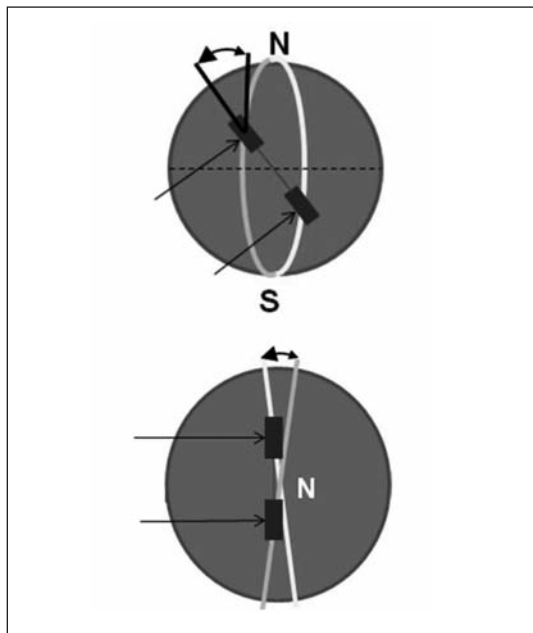


Figure 2: sketch of a pendulum configuration. The two satellites are moving with constant inter-satellite distance, but on two orbital planes slightly rotated relative to each other.

3. Proposed satellite gravity missions mission

Three satellite gravity missions were proposed considering science improvements and constraints which are discussed in chapter 3. In this chapter we analyse the relative velocity of the satellites and the Euler angles.

3.1 Pendulum orbit.

The relative velocity between the 2 satellites and the Euler angle are two crucial constraints for satellite gravity missions using a laser link. The results are given in fig.2 and fig. 3.

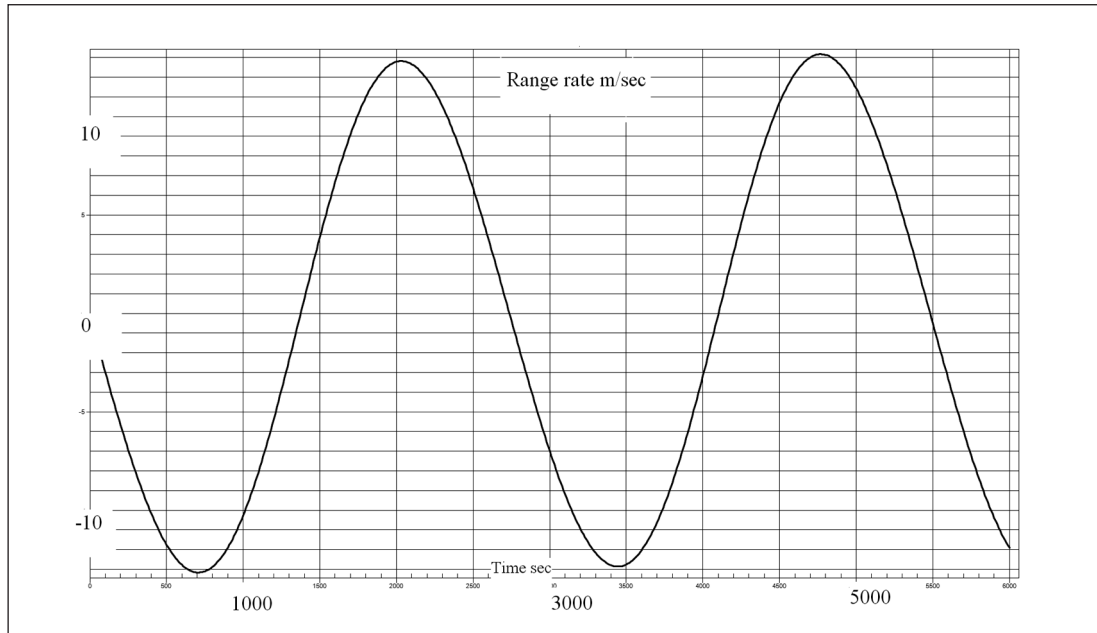


Figure 3: Range rate [m/sec]

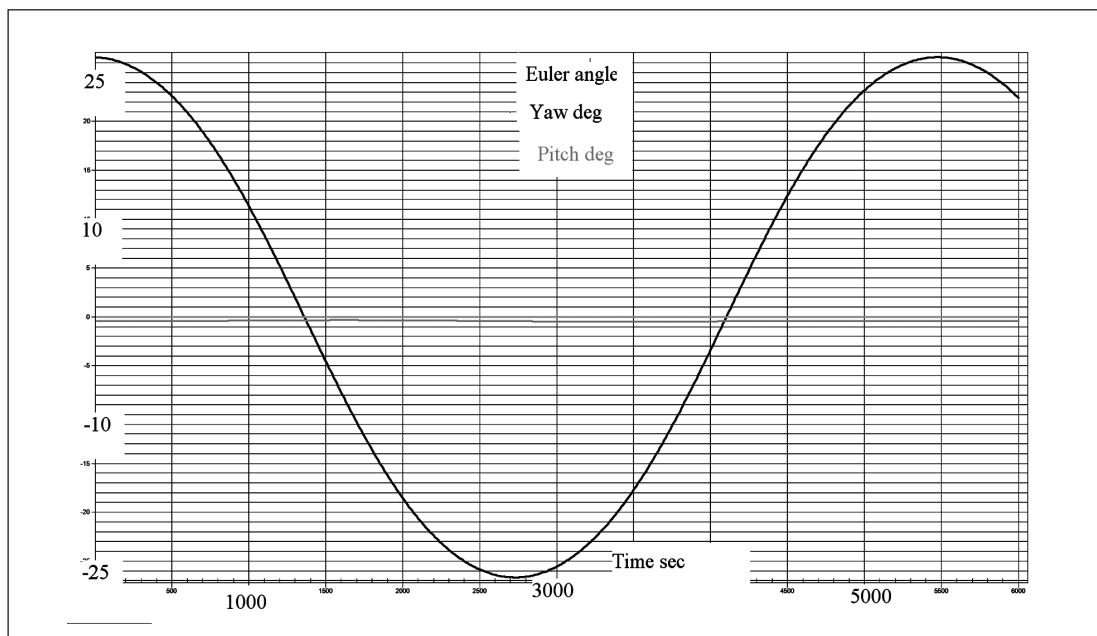


Figure 4: Euler angles [deg]

3.2. Cartwheel Orbit

Cartwheel orbits perform 2:1 relative elliptical motion about their center of mass. There is one relative revolution per orbit about the Earth. Cartwheel Orbits have the advantage of providing both radial and along track information.

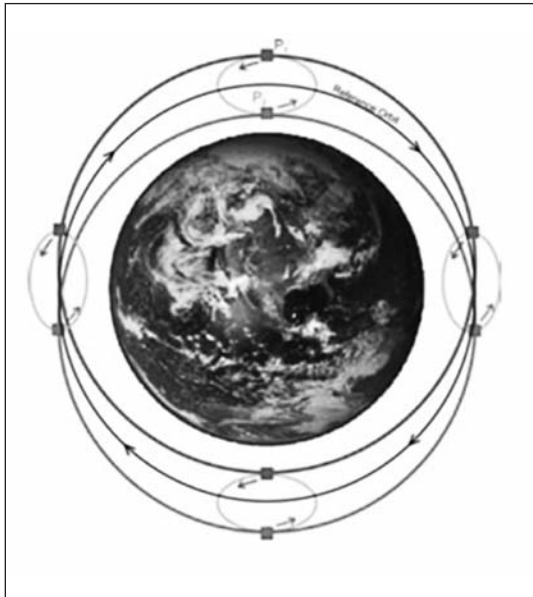


Figure 5: Sketch of a cartwheel orbit

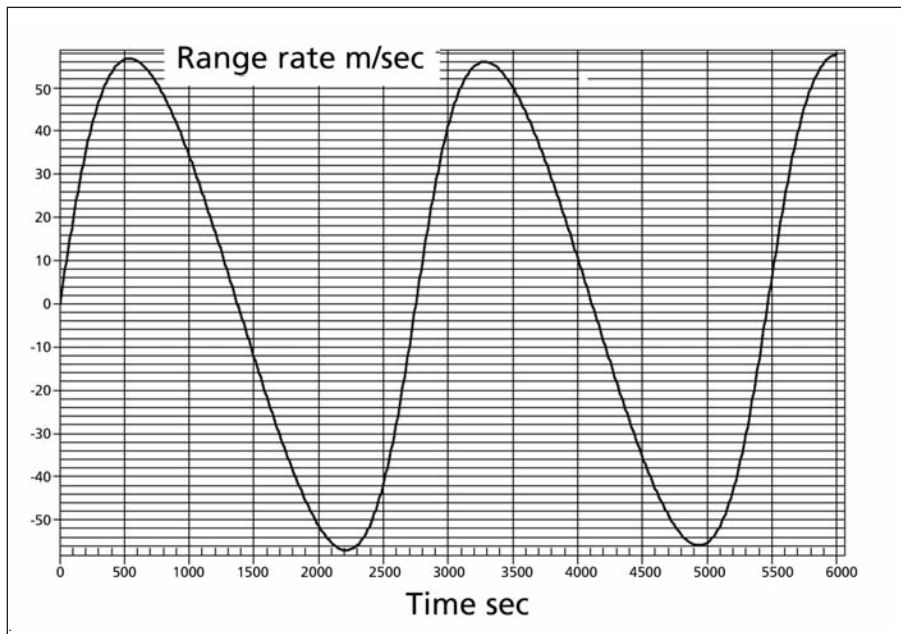


Figure 6: Range rate [m/sec]

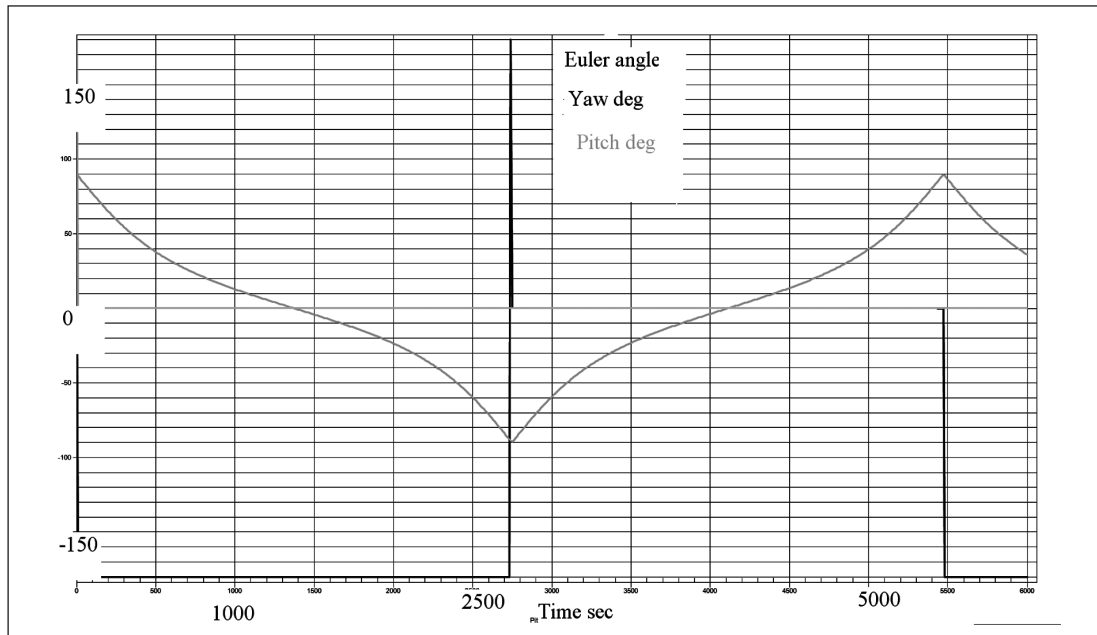


Figure 7: Euler angles [deg]

3.3. Helix



Figure 8: Example of a Helix orbit. Shown are orbits of TerraSAR-X and TanDEM-X

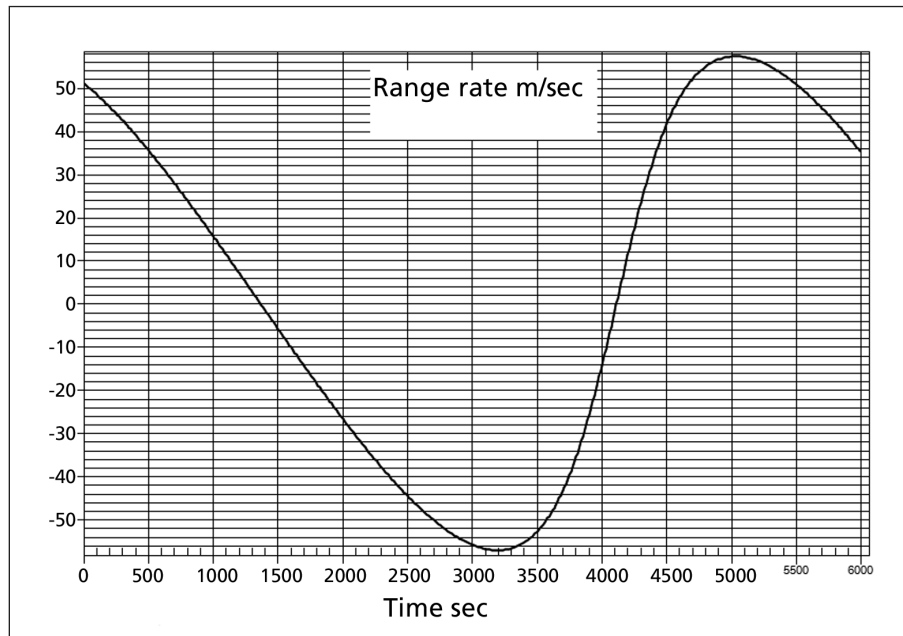


Figure 9: Range rate [m/sec]

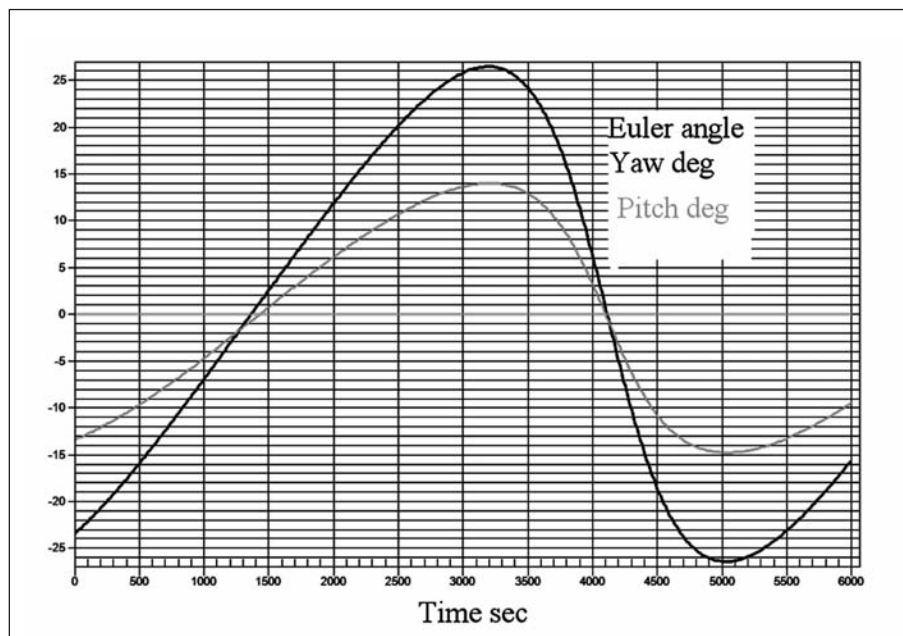


Figure 10: Euler angles [deg]

The summary of the results are given in table 2.

Mission Option	Relative velocity m/s	Distance between Satellites km	Euler angles deg
Pendulum conservative	+/- 13.2 m/s	95 km – 106 km Along track: 95km Cross track +/- 47.5 km	<25
Cartwheel	+/- 57 m/s	50 km – 120 km Along track: +/- 100 km Radial: +/- 50 km	<100
Helix	+/- 50 m/s	99 km – 104 km Along track: 99 km Cross track: +/- 43 km	<25

Conclusion:

The mission called Pendulum conservative meets the requirements concerning the Range rate and the Euler angles. The two other proposed missions pose a challenge. The feasibility of these missions has to be further studied.

Acknowledgements

The project FE III »Satellitenmissionen – Zukunfts - konzepte für Schwerfeldsatellitenmissionen« is part of the R&D-Programme GEOTECHNOLOGIEN. GEOTECHNOLOGIEN is funded by the German Ministry of Education and Research (BMBF) and the German Research Foundation (DFG), Grant (03G0729G) of project Future Gravity Mission.

Quick-look gravity field analysis of formation scenarios selection

Reubelt T., Sneeuw N., Iran-Pour S.

Geodätisches Institut, Universität Stuttgart, Geschwister-Scholl-Straße 24D, 70174 Stuttgart

1. Introduction

The development of an advanced future gravity field mission for time variable gravity field recovery is a difficult task. A lot of options exist to improve the performance, accuracy and sensitivity compared to GRACE. Besides technological progress in satellite system and metrology as for instance the application of laser and advanced drag-free and orbit control systems also a variety of geodetic parameters exist which can be tuned in order to improve the mission. These geodetic parameters include for instance the selection of the orbit height, the satellite distance, the inclination, the repeat mode, the sensor type, the formation and a possible multi-satellite/formation mission. Especially the last two options – advanced formations and multi-formation mission – are regarded as the key instruments to improve the main weaknesses of GRACE, which are i) North-South striations caused by anisotropy of the measurements and ii) aliasing due to temporal undersampling of time-variable signals. By means of advanced formations, which are able to detect signals different from the along-track-direction a higher isotropy is reached and striations might be reduced or avoided. Aliasing might be reduced by multi-formation missions, which enlarge the temporal/spatial sampling.

In order to identify suitable missions from the huge variety of options a huge amount gravity simulations have to be performed. However, a time-consuming full-scale gravity retrieval is the only possibility to take all effects, especially the severe aliasing into account. In order to reduce the search space for the full-scale simu-

lations dramatically, quick-look tools have been developed. They enable a sensitivity analysis by means of error propagation. The influence of the following parameters can be investigated: orbit height, satellite distance, inclination, duration, sensor type and combinations, measurement noise (as PSD (power spectral density)). By means of a new quick-look-tool additionally the sensitivity of advanced formations as pendulum, cartwheel, LISA-type, trailing cartwheel and helix (trailing LISA) can be estimated. However, quick-look tools are not capable of investigating aliasing effects, since they are based purely on error propagation. Despite of this, quick-look tools are regarded as a useful tool for the sensitivity analysis of future mission options.

In this paper the sensitivity of the six basic formations, including the standard inline formation and the five advanced formations, is investigated. However, from technological side of view, constraints on some formation parameters as maximum range-rate or maximum variation of the yaw/pitch angle exist, which seems to be problematic for all five advanced missions. Therefore a set of advanced formations is additionally investigated, which fulfils the mission constraints.

2. Quick-look-tools

Under the assumption of a circular nominal orbit with constant inclination ($r = r_0$, $I = I_0$) a fast and efficient block-diagonal error propagation (order wise with even/odd degree separation) from the observational and stochastic model to gravity field errors can be performed

with the original semi-analytic quick look tool (QLT). It is based on *Sneeuw (2001)* and described here briefly. The lumped coefficient representation of a gravitational signal $f(t)$ along the orbit reads

$$f(r, u, I, \Lambda) = \sum_m \sum_k A_{mk}^f(r, I) e^{i\psi_{mk}(t-t_0)}$$

$$A_{mk}^f(r, I) = \sum_l \underbrace{\frac{GM}{R} \left(\frac{R}{r}\right)^{l+1} \bar{F}_{lmk}(I) K_{lm}}_{H_{lmk}^f(r, I)}$$

with the inclination function $\bar{F}_{lmk}(I)$, the frequency $\psi_{mk} = k\dot{u} + m\dot{\Lambda}$ and the complex SH coefficients K_{lm} . For a nominal orbit the transfer coefficient $H_{lmk}^f(r, I)$ and the lumped coefficient $A_{mk}^f(r, I)$ become constant and the normal equation gets a orderwise blockdiagonal structure. The transfer coefficient $H_{lmk}^\rho(r, I)$ of the low-low-SST for an inline-formation (leader-follower) is derived as $H_{lmk}^\rho \approx 2i \sin(\eta \beta_{mk}) H_{lmk}^{\Delta x}$ with $\sin \eta = 0.5 \rho_0 / r$. In our case, we are not interested in the solution for the SH coefficients but in their accuracy (variance-covariance matrix $\mathbf{Q}_{\hat{x}}$), which can be estimated by means of blockwise variance-covariance propagation $\mathbf{Q}_{\hat{x}} = (\sum_i \mathbf{A}_i^T \mathbf{Q}_{yi}^{-1} \mathbf{A}_i)^{-1}$ from the variance-covariance matrix \mathbf{Q}_{yi} of the observations. The design matrix \mathbf{A} is composed by the transfer coefficients H_{lmk} and the variance-covariance matrix \mathbf{Q}_{yi} of the corresponding block can easily be derived as a diagonal matrix from the PSD of the functional f . Here the psd-value belonging to the frequency $\psi_{mk} = k\dot{u} + m\dot{\Lambda}$ of the lumped coefficient A_{mk}^f has to be inserted. From the

estimated variance-covariance matrix the error measures used for visualisation are derived. With the semi-analytic QLT the influence of the parameters (i) measurement type, (ii) measurement noise (as PSD), (iii) orbit height, (iv) inclination, (v) mission period, (vi) intersatellite distance can be studied. The estimated formal errors are represented as (i) degree-RMS, (ii) triangle plots, (iii) geoid errors per latitude and (iv) covariance functions (at the equator).

The influence of two basic mission parameters, the intersatellite distance ρ and the orbit height h is studied in Figure 1 for a future standard mission (polar and circular orbit, time span of $T = 15$ days, PSD of future laser and accelerometer). As visible, the best geodetic sensitivity is reached for a large intersatellite distance and a low orbit height. However, a low orbit height is problematic due to a higher air drag (high energy and propulsion consumption) and a large satellite distance faces problems with the laser technology (pointing, signal strength, noise). Thus, an orbit height of $h = 350$ km and a satellite distance of $\rho = 100$ km seem to be a good compromise between geodetic sensitivity and technological feasibility.

However, a constant transfer-coefficient for other formations than the standard inline formation could not be derived so far, thus another strategy was used for the formal error simulation of the advanced formations. This formation-QLT can be regarded as some kind

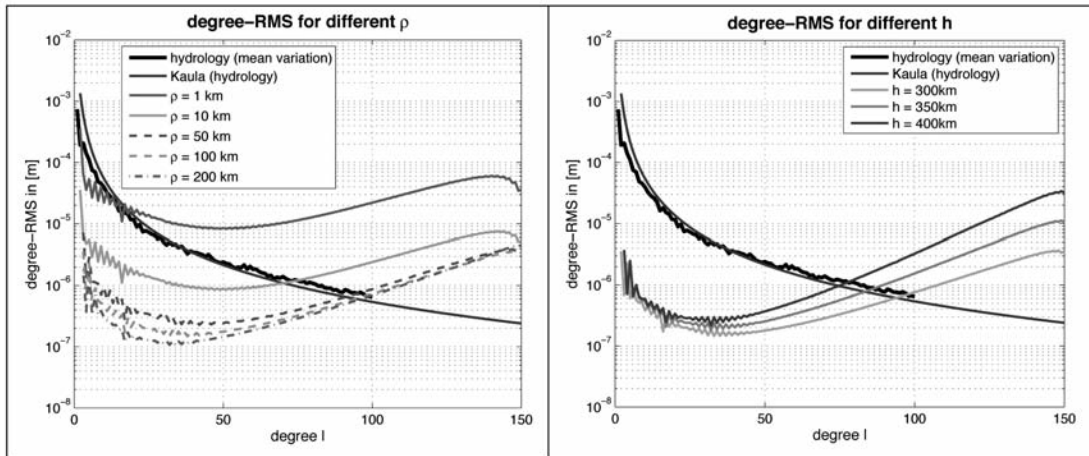


Figure 1: Impact of different intersatellite distance and orbit height on the accuracy of the gravity field recovery.

of pseudo-QLT, i.e. in between QLT and full scale simulation. It is based on the formulation of the equation for range-accelerations:

$$\ddot{\rho}(t) - \frac{1}{\rho(t)} \left((\Delta \dot{\mathbf{x}}_i(t))^2 - \dot{\rho}^2(t) \right) = \mathbf{e}_i^T (\text{grad} V(\mathbf{X}_2(t)) - \text{grad} V(\mathbf{X}_1(t)))$$

The designmatrix is composed from the right hand side of this equation. The needed positions of the two satellites $\mathbf{X}_2(t)$, $\mathbf{X}_1(t)$ are computed by (i) computation of circular (β/α)-repeat orbits ($I = I_0$, $r = r_0$) for the center $(\mathbf{X}_2 + \mathbf{X}_1)/2$ of both satellites and (ii) computation of the relative movement of the two satellites by means of the homogeneous solution of the Hill-equations (e.g. *Sharifi et al., 2007*):

$$x(t) = -2A \sin(nt + \alpha) - \frac{3}{2} n t z_{\text{off}} + x_{\text{off}}$$

$$y(t) = B \cos(nt + \beta)$$

$$z(t) = A \cos(nt + \alpha) + z_{\text{off}}$$

with the initial conditions

$$A = \frac{1}{n} \sqrt{\dot{z}_0^2 + (2\dot{x}_0 + 3nz_0)^2} \quad \tan \alpha = \frac{\dot{z}_0}{2\dot{x}_0 + 3nz_0} \quad x_{\text{off}} = x_0 - \frac{2}{n} \dot{z}_0$$

$$B = \frac{1}{n} \sqrt{\dot{y}_0^2 + (ny_0)^2} \quad \tan \beta = \frac{\dot{y}_0}{ny_0} \quad z_{\text{off}} = \frac{2}{n} (\dot{x}_0 + 2nz_0)$$

The following initial elements have to be chosen for the formations (start point at t_0 is over the equator):

- inline (leader-follower, GRACE-like): $x_0 = \rho$
- Pendulum: $x_0 = \rho_x$, $y_0 = \rho_y$ (along-track distance ρ_x , maximum cross-track-distance over equator ρ_y)
- Cartwheel: $z_0 = \rho_r$, $\dot{x}_0 = -2n\rho_r$ (maximum radial distance: ρ_r (maximum along track-distance $\rho_x = 2\rho_r$))
- LISA: $y_0 = -\sqrt{3}\rho/2$, $z_0 = \rho/2$, $\dot{x}_0 = -n\rho$, (constant satellite distance ρ)
- trailing Cartwheel: $x_0 = \rho_{x\text{-offset}}$, $z_0 = \rho_r$, $\dot{x}_0 = -2\rho_r$ (Cartwheel with shift $\rho_{x\text{-offset}}$ in along-track direction)
- Helix: $x_0 = \rho_{x\text{-offset}}$, $y_0 = -\sqrt{3}\rho/2$, $z_0 = \rho/2$, $\dot{x}_0 = -n\rho$ (trailing LISA with shift $\rho_{x\text{-offset}}$ in along-track direction)

The angular velocity of the reference orbit is n , here also secular effects caused by J_2 on the angular velocity are considered (). In contrast to the semi-analytic QLT the formation QLT is slower since analysis for a complete repeat orbit is performed. Furthermore the formation QLT so far works only for white noise of range accelerations. In the following sections the

sensitivity of the advanced formations is investigated.

3. Formation analysis

It is expected that the advanced formations will lead to a higher sensitivity and isotropy compared to the standard inline-formation since signal components apart from the along-track direction are measured. The six formations are investigated using the following parameters: orbit height $h = 334$ km (corresponding to $\beta/\alpha = 503/32$ repeat mode), inclination $I = 90^\circ$, average satellite distance $\rho_{\text{avg}} = 100$ km, time interval $T = 30$ d, range acceleration white noise of 10^{-10} [m/s²/sqrt(Hz)] corresponding to an average combined laser/accelerometer noise level. Figure 2 shows the resulting formations in the Hill-system as well as the range, the range-rates and the yaw-/pitch-angles. As visible, the pendulum adds cross-track information over equatorial regions while the cartwheel is sensitive for radial information. The LISA-formation is a combination of both and thus gathers additionally both, cross-track and radial information. In general, the feasibility of cartwheel- and LISA-formations is regarded as problematic due to the rotating yaw-/pitch-angle (360° per revolution). Thus LISA- and cartwheel-formations with an along-track shift are also regarded (named as helix, trailing cartwheel), where the maximum yaw-/pitch-angle can be controlled to stay between certain limits. Of course the main measurement-direction now is again along-track, which will probably lead to reduced sensitivity and isotropy compared to the non-trailing formations.

The results for the six formations are displayed in Figures 3-5 in terms of triangle plots, covariance functions, degree-RMS and geoid-errors per latitude. As the figures show, the advanced formations of pendulum, cartwheel and LISA lead to a significant improvement in sensitivity and isotropy compared to the inline-formation with a similar performance for all three cases. As shown by the degree-RMS, the improvement is almost one order of magnitude. The geoid error is reduced mainly over regions of lower latitude since the cross-track and radial

components are largest over the equator, while over the poles the measurements of the advanced formations still contain mainly along-track information. The advanced formations show a high isotropy, as the covariance functions show and thus might be able to reduce the striping effects well known from GOCE (LISA here has even a stronger pronunciation of East-West structures). The higher isotropy is depicted also in the triangle plots of Figure 3 where the accuracy of higher orders is improved compared to the inline case. The adapted trailing formations of helix and trailing cartwheel show a significant improvement compared to the inline case, although it is not as pronounced as for the other three non-trailing formations. Especially the helix shows a good performance which is only slightly worse than for the cartwheel if degree-RMS and geoid-errors are concerned. The trailing cartwheel still leads to an improvement of a factor of three compared to the inline-case. However the stronger impact of the along-track component in the trailing formations is clearly visible in the covariance functions and triangle plots with a lower isotropy indicated North-South structures and a lower accuracy of higher orders compared to the non-trailing formations. Taking into account that cartwheels and LISA formations (and thus also their trailing variants) are unstable due to the perigee drift caused by the Earth flattening a pendulum seems to be a very promising option for a future formation.

3.1. Mission constraints

Although the advanced missions seem to be of great benefit for geodesy, their technical feasibility is regarded as critical. From the technological side, two crucial constraints for the formation design exist up to now:

- 1) the maximum range-rate has to be kept within ± 10 m/s. This is a constraint from the laser link in order to keep the Doppler effect sufficiently small
- 2) the line-of-sight angle between the two satellites is allowed to change only within $\pm 30^\circ$ in yaw-/pitch-direction around the

mean axis in order to guarantee spacecraft- or beamsteering-pointing.

As it can be seen in Figure 2, neither the advanced non-trailing formations nor the trailing formations fulfil these mission constraints (critical parameters are shaded dark grey, less critical bright grey). Within a pendulum, the maximum range-rate and yaw angle can be controlled by reducing the cross-track component and or the average satellite distance in general. For the cartwheel, the pitch-angle can only be kept within the limits if it is regarded within the space-fixed system. Then, it stays within $\pm 20^\circ$, but this option might afford cylindrical satellites with a similar drag coefficient in every possible air-drag direction. But then still the cartwheel shows a strong dynamical range such that the intersatellite-distance has to be reduced significantly (this is also important for the reduction of the differential air-drag of both satellites). The LISA-formations seems to be perfect regarding the range-rate since it has almost no dynamical range. However, the yaw- or pitch-angles can not be kept both within the limits, neither in the Hill-system nor in the space-fixed system. Thus this formation doesn't seem feasible at the moment. The two trailing formations can be trimmed within the limits by downscaling the shown formations to a shorter intersatellite-distance.

3.2. Realistic formations

In this chapter the formations adapted to the mission constraints are investigated. In case of the cartwheel, the trailing cartwheel and the helix the intersatellite is scaled down significantly to average values of approximately 15 km such that the constraints are met. In case of the pendulum different options exist to keep the formation within the mission constraints, e.g. (i) by applying the maximum yaw angle of 30° and downscaling the average range to a value < 100 km such that the range-rate limits are met, or (ii) selecting a maximum yaw angle $< 30^\circ$ such that an average range of 100 km can be hold and the range-rate can be kept within the limits. Here the more promising case (ii) with the larger satellite-distance is

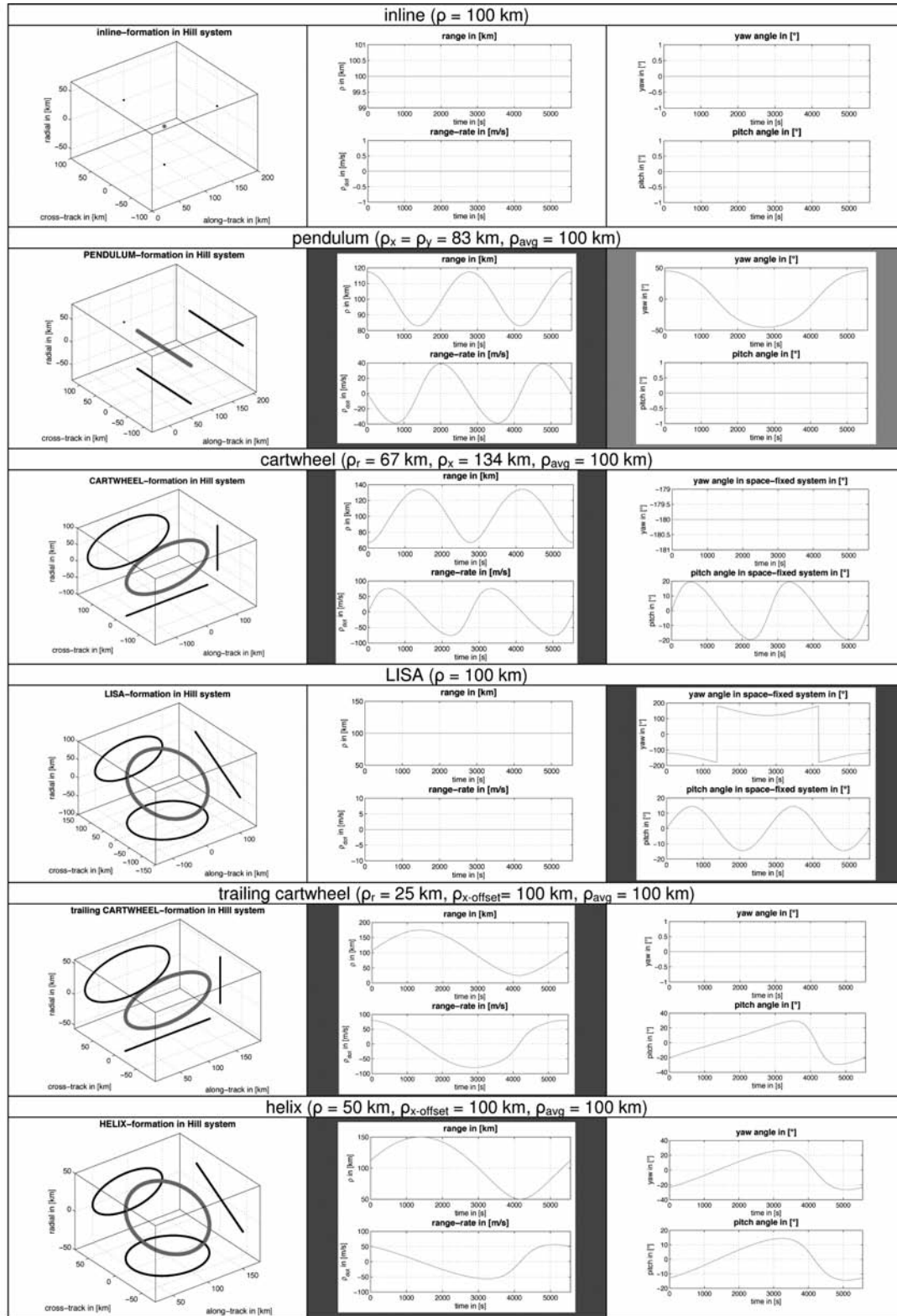


Figure 2: representation of the 6 basic formations with an average intersatellite distance of 100 km; left: relative movement of satellite 2 in the Hill-system; middle: range and range-rate; right: yaw and pitch angle. Critical values concerning the mission constraints are colored dark grey, less critical are light grey.

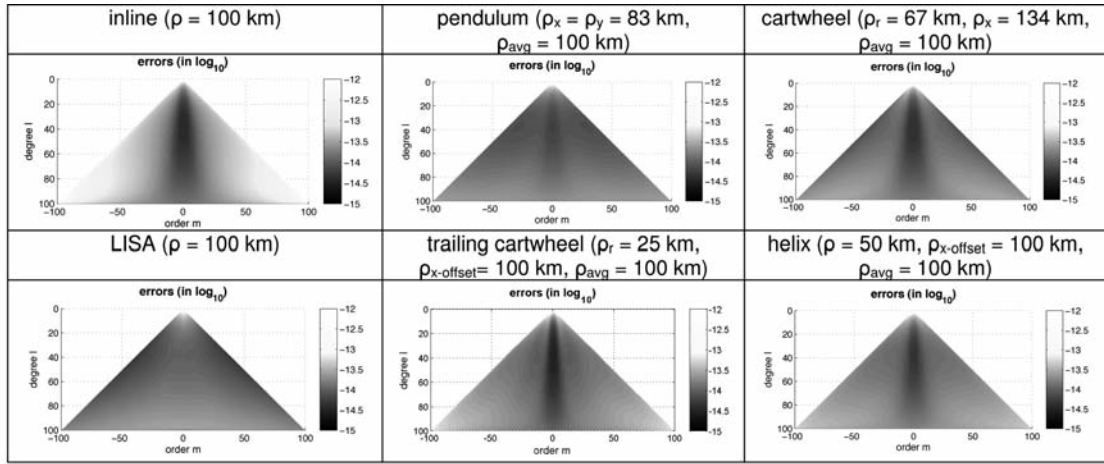


Figure 3: formal errors of the six basic formations.

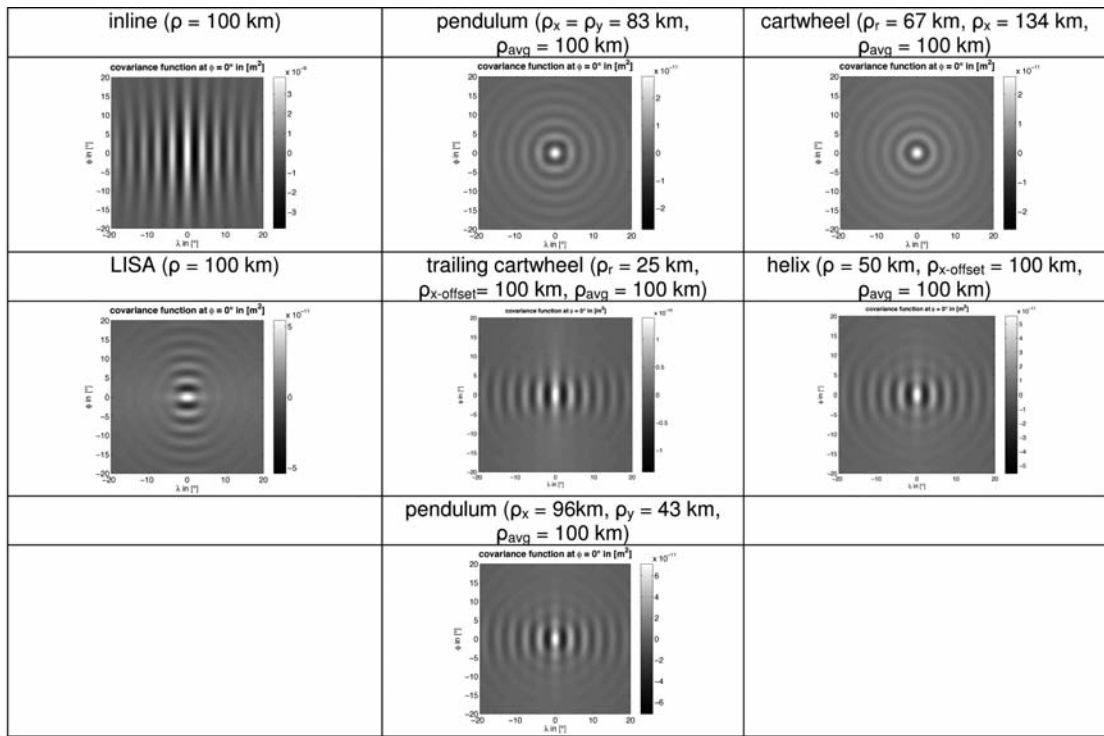


Figure 4: covariance functions of the six basic formations as well as of a pendulum adapted to the mission constraints.

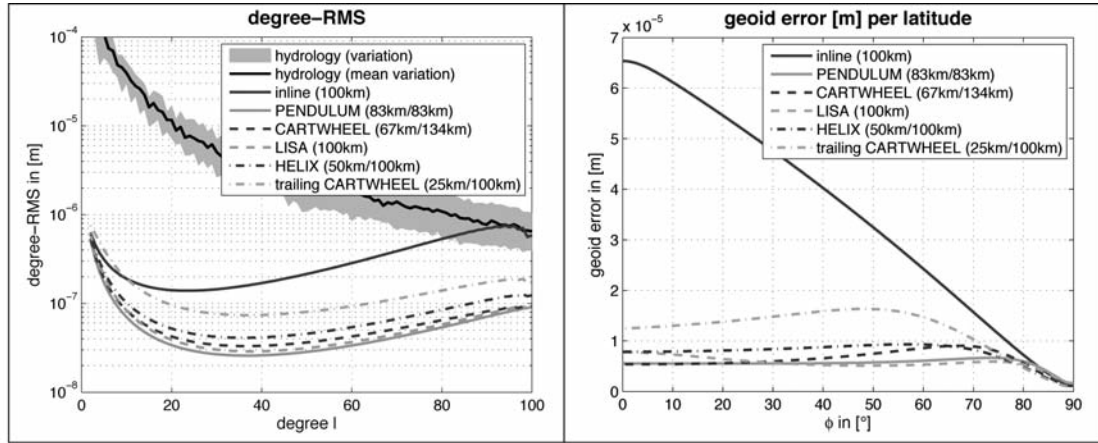


Figure 5: degree-RMS and geoid errors per latitude for the six basic formations.

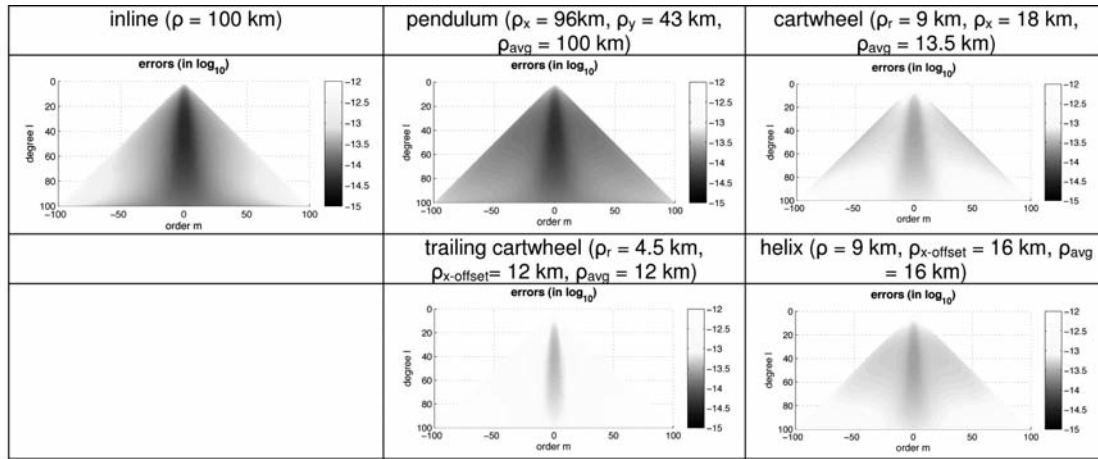


Figure 6: formal errors of the basic formations adapted to the mission constraints.

chosen due to the strong dependence of the sensitivity on the satellite distance shown in Figure 1. Of course such a pendulum leads to less isotropy than by application of a larger yaw-angle, as shown in the covariance functions of Figure 4, where now North-South structures are more pronounced.

The results for the more realistic formations concerning the mission constraints are shown in Figures 6 and 7 in terms of triangle plots, degree-RMS and geoid errors per latitude (the covariance functions are not shown, their shape corresponds to those of the »wanted« formations in Figure 4). As it can be seen the best results are obtained with the »realistic« pendulum. The improvement of this pendulum still is approximately a factor of 4 in terms of

degree-RMS compared to the inline case. Due to the higher isotropy compared to the inline-case an improvement of the higher order coefficients and the geoid errors in regions of lower latitude is reached. The other „realistic“ formations of the cartwheel, the helix and especially the trailing cartwheel perform even worse as the inline formation, which is caused by the loss of sensitivity due to a significant shorter intersatellite distance.

4. Results and outlook

The quick-look tools has proven to be a fast and efficient tool for the investigation of the influence of basic mission parameters and of the formation type on the sensitivity of a future

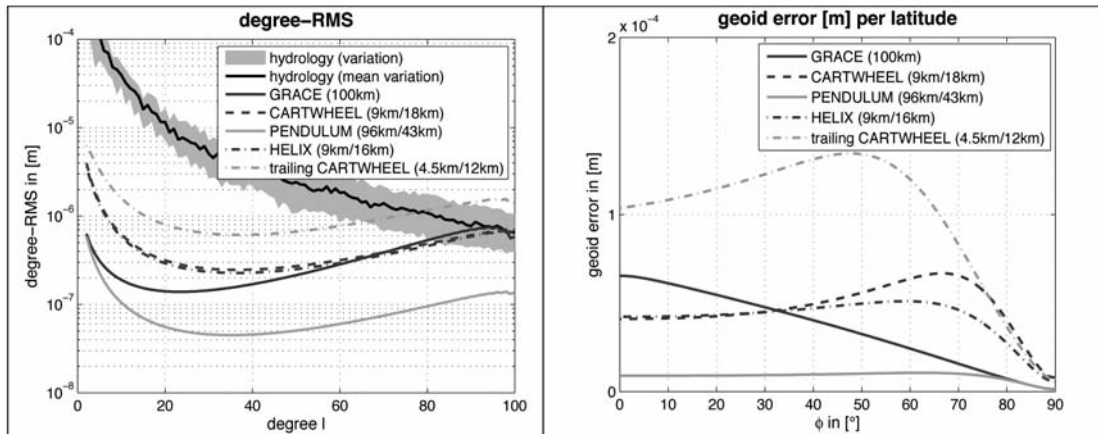


Figure 7: degree-RMS and geoid-errors per latitude of the basic formations adapted to the mission constraints.

mission. However, further improvements of the formation quick-look tool are desirable, e.g. the application of coloured noise (as PSD) instead of white noise of the derivation of transfer-coefficients for the advanced formations.

Advanced formations as pendulum, cartwheel or helix are able to improve the sensitivity and especially the isotropy significantly compared to the inline-case so that striping patterns known from GRACE can be avoided. However, the advanced formations make great demands on satellite technology/control systems and metrology which will make their realisation difficult. Even worse, due to restrictions on range rate and yaw/pitch angles coming from the laser and beamsteering-/satellite-pointing the advanced formations in their wanted design are not feasible at the present state of technology. By means of tuning parameters most of the suggested formations can be tailored to the given mission constraints. However, under these constraints, the »realistic« pendulum proposed seems to be the only formation which is able to improve sensitivity compared to the standard inline-case.

Under the current mission constraints and II-SST sensor noise assumptions pendulum formations seem to be the most promising option. However, with advancements in technology also the other formations might become interesting options.

Acknowledgements

This work was supported by the German Ministry of Education and Research (BMBF) in the framework of the GEOTECHNOLOGIEN research program under grant no. 03G0729A.

References

- Sharifi MA, Sneeuw N, Keller W (2007) Gravity recovery capability of four generic satellite formations. In: Kiliçoglu A and R Forsberg (Eds.) Gravity field of the Earth. General Command of Mapping, ISSN 1300-5790, Special Issue 18, pp 211-216. 1st Int. Symp. of the International Gravity Field Service, 28.8.-1.9.2006, Istanbul, Turkey
- Sneeuw N (2001) A Semi-Analytical Approach to Gravity Field Analysis from Satellite Observations, DGK, Reihe C, Dissertationen, Heft Nr. 527, Verlag der Bayerischen Akademie der Wissenschaften, München.

The mission option OPTIMA – novelties and benefit

Brieden P. (1), Müller J. (1,2), Flury J. (1,2), Heinzel G. (2,3)

(1) Institut für Erdmessung, Leibniz Universität Hannover, Schneiderberg 50, 30167 Hannover, Germany

(2) Centre for Quantum Engineering and Space-Time Research (QUEST), Welfengarten 1, 30167 Hannover, Germany

(3) Max-Planck-Institut für Gravitationsphysik (Albert-Einstein-Institut), Leibniz Universität Hannover, Callinstraße 38, 30167 Hannover, Germany

Abstract

The mission option OPTIMA (*OPTical Interferometry for global MAss change detection from space*) is one out of a variety of mission concepts which are investigated in the Future Gravity Missions project in detail. OPTIMA is based on experiences and observation concepts of GRACE and GOCE, that are combined and improved by innovative laser system components. More precisely two spacecraft in GRACE-like constellation for determining the long wavelengths of the gravity field are complemented by a gradiometer for the precise determination of medium and short wavelengths. Novelty here is that both the distance measurement between the satellites and the observation of the gradiometer test masses is based on optical techniques. The satellites will carry GNSS antennas that are mounted on the zenith side for spacecraft positioning and on the nadir side for GNSS reflectometry. GNSS reflectometry provides the opportunity to obtain a further functional of the gravity field at the same position and time besides gradients and range rates.

Considering the noise behavior of the new instrumentation, the benefit of the OPTIMA concept in terms of RMS error per degree is compared to an »older« GRACE mission scenario. OPTIMA will allow monthly gravity field determination with much increased accuracy over all spherical harmonic degrees up to $l = 250$.

1. Introduction

The missions CHAMP, GRACE and GOCE form a very successful series of satellites observing the gravity field of the earth. CHAMP (CHALLENGING Minisatellite Payload), the pioneer in space borne gravimetry, was launched in 2000. GRACE (Gravity Recovery and Climate Experiment), the twin satellites, in particular aiming for the time variable gravity field were launched in 2002, and GOCE (Gravity Field and Steady State Ocean Circulation Explorer) carrying a highly sensitive gravity gradiometer, was launched in March 2009. GRACE and GOCE are still operational, but the lifetime of the last of them is expected to end in 2015. For most users of gravity field products, such as from hydrology, solid-earth physics and oceanography, it is of high relevance to have long continuous time series, which extend over several years, and reaches a higher spatio-temporal resolution. For continuing global gravity field measurements after 2015, it is necessary to now designing the concept for a future gravity field satellite mission.

The BMBF Geotechnologien project *Future Gravity Field Satellite Missions (FGM)*, has the ambitious goal to design the next generation gravity field satellite mission for the period after the missions GRACE and GOCE [11]. The aim of this project is to develop feasible mission scenarios that will not only be able to meet the geo-scientific requirements, but will also be realistic from the perspective of technology readiness, system engineering and cost efficiency. Thus the project FGM is broken

down into three modules: Geodesy, Metrology and System [13]. A variety of project partners from different disciplines work together to prepare various options for mid- and long-term future missions. There, the technical feasibility as well as the scientific utility will be elaborated in collaboration with industrial partners.

As a very important work package (WP) of FGM, WP 140 (»Sensor analysis and error budgeting«) serves as interface between the technology and science communities and as interface between the FGM research bundle and related activities in the Hanover cluster of excellence QUEST (Quantum Engineering and Space-Time Research), where, e.g. developments in laser inter-satellite links, quantum gravimetry or high-precision clock measurements are developed [1],[3],[13].

In collaboration with several partners from QUEST Task Group 7, in particular the Albert Einstein Institute (AEI) in Hanover, and the FGM-group, the mission option **OPTIMA** (*OPTical Interferometry for global MAss change detection from space*) has been defined. OPTIMA was originally submitted as proposal to Deutsches Zentrum für Luft- und Raumfahrt (DLR), but did not succeed to get additional

financial support. It is further investigated in FGM because of its expected high performance for earth system research.

2. Mission design

The OPTIMA mission design is essentially based on expertise from the gravity satellite missions GRACE and GOCE. Approved technology components that have already been used in the previous gravity field missions will be combined and improved by innovative laser-based system components. What is to be measured by the satellite mission OPTIMA, are temporal mass changes in the earth's gravity field. Because of the complex space time structure of gravity field variations, the concept of an unidirectional measurement as in GRACE is not optimal to achieve a substantial increase in accuracy and resolution. The sensor technology of GOCE on the other hand is limited inherently by the noise level and sensor drifts [2].

A series of new technologies that can improve the accuracy of gravity measurements significantly were developed for the fundamental physics missions LISA and LISA Pathfinder at the Albert-Einstein-Institute (AEI) in Hannover. AEI is also working on new techniques for use

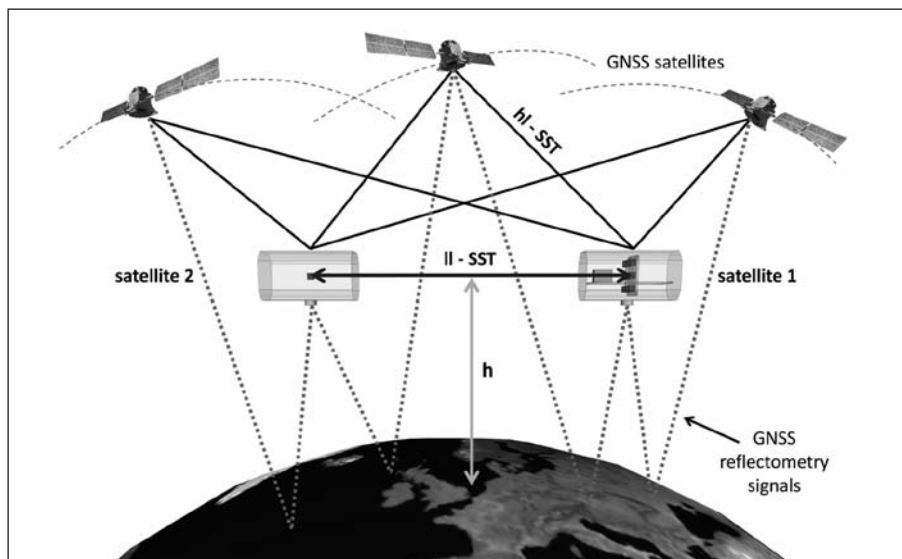


Figure 1: OPTIMA mission design - Two satellites with low-low satellite-to-satellite tracking (SST) mode via laser interferometry, positioning via GNSS in high-low SST mode and GNSS reflectometry via additional GNSS antennas on the nadir side of the satellites, augmented by optical gradiometry in one of the satellites

in future satellite missions. The related knowledge and expertise in developing space-qualified optical ranging systems greatly helps to design dedicated laser systems for OPTIMA and makes AEI to an important partner in the FGM project.

The satellite mission OPTIMA will consist of two satellite bodies following each other in a GRACE-like configuration, see Figure 1. The orbit altitude h over ground is about 250-350 km. From a geodetic point of view the spacecraft should be at a very low orbit to capture fine structures of the earth's gravity field. The counter-argument for a low orbit is the necessity of drag compensation below an altitude of about 350 km. The scheduled inter satellite distance should be between 100 and 200 km. Due to possible restrictions by the laser power, the choice of the optimal distance is still under investigation. One should have in mind that the sensitivity increases with larger satellite spacing, which is an advantage from a geodetic point of view.

The payload of OPTIMA includes three main instruments that provide complementary measurements of the gravity field. OPTIMA combines measurements of three independent functionals of the gravity field simultaneously in the same position. The major sensors are:

- an *optical gravity gradiometer* to observe the medium and short wavelengths of the gravity field;
- a *laser interferometer* to observe the longer wavelength parts by using low-low satellite to satellite tracking;
- highly accurate position information from *GNSS antennas* in high-low satellite to satellite tracking mode;
- GNSS antenna on the nadir side of the platform for *GNSS reflectometry* observations, in order to determine the altimetric distance to the sea surface. The joint processing of GNSS reflectometry with the other gravity functionals will offer unique new insight into earth system science. Details will be investigated in a later phase of FGM;

- a *drag-free system* in case of selecting an orbit altitude below 350 km;
- a configuration of *star sensors*;
- corresponding precise *attitude control system*;
- further auxiliary instrumentation (magnetic torquers, heaters, etc.) still to be defined in detail.

3. Instrumentation

OPTIMA consists of two satellites with different instruments on board. Satellite 1 is equipped with an optical gravity gradiometer that is described more precisely in chapter 3.1. For the observation of the inter satellite range and fluctuations, a laser interferometer is used that is discussed in chapter 3.2. The integrated mission concept and first simulation results are presented in chapter 4.

3.1. Gradiometer

The optical gravity gradiometer of OPTIMA is a constellation of test masses on one satellite platform. The differential motion of the test masses is detected by a laser interferometer very precisely. This configuration allows the determination of gravity gradients that reflect the spatio-temporal structure of the gravitational field of the earth. The accuracy of the novel gradiometer is estimated as

$$\delta_{\text{gradiometer}}(f) = 1.67 \cdot 10^{-2} \left(1 + \frac{0.0005}{f} \right)^2 \frac{mE}{\sqrt{Hz}} ,$$

where the distance between two accelerometer test masses is assumed with 0.5 meters. This is an improvement of a factor 500 compared to GOCE. A similar laser-based sensor is realized for LISA Pathfinder [5],[6],[7] for the first time. The number of measured gradients and the sensitivity of the system depend on the number and spatial arrangement of the test masses. The optimal configuration that enables highest sensitivity and scientific gain is still under investigation [2]. In particular, various constellations of the test masses will be tested, which allow to measure third derivatives of the gravitational potential of the earth for the first time. From these, a further increase of sensitivity

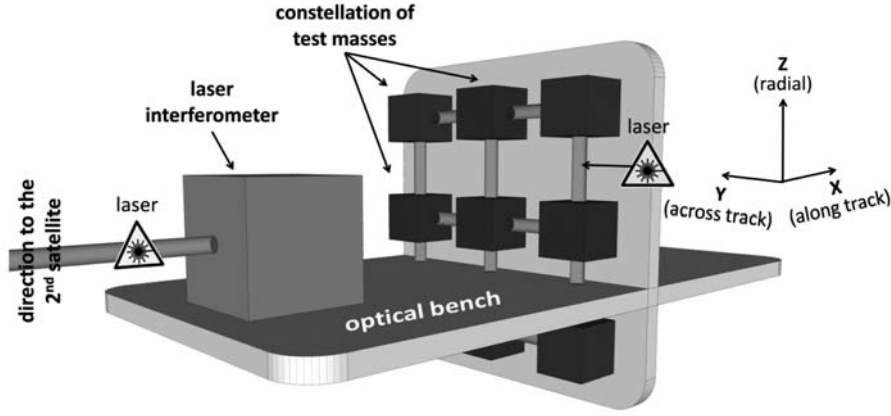


Figure 2:
Constellation of
test masses and
laser interferome-
ter on the same
optical bench in
satellite 1

ty and resolution is expected, and possible errors due to the rotation of the satellite will be eliminated automatically [9],[10].

A possible constellation of nine test masses is illustrated in Figure 2. Here an arrangement was chosen, in which the test masses are placed in a 3 x 3 matrix structure perpendicular to the flight direction. The relative position (acceleration) and orientation of the test masses is observed very precisely using the above mentioned optical system.

Besides the very precise determination of range variations between the satellites via laser interferometry, optical gradiometry allows the very accurate determination of angular velocities and angular accelerations acting on the test masses. If angular accelerations are known very precisely from test mass monitoring, the separation of inertial and gravity contributions is easily possible. This offers a complete altered satellite design, where the gradiometer has not necessarily to be placed in the center of mass of the satellite. Further discussion on this subject will be dealt with in the paper of [8], in the present status report.

3.2. Laser interferometer

The inter-satellite distance and the distance changes will be observed by a laser interferometer. The parts of the interferometer that are placed in satellite 1 are mounted on the same optical bench as the gradiometer. The common optical bench (Figure 2) provides a stiff structure ensuring the stability of the relative

position of all relevant sensors to each other.

The knowledge of AEI obtained during LISA and LISA Pathfinder studies is used for accuracy assessment of the laser interferometer [5],[6],[7]. The accuracy level for inter satellite ranging will be

$$\delta(f) = \sqrt{\left(50 \cdot 10^{-9} \frac{m}{\sqrt{Hz}}\right)^2 + \frac{100 \text{ Hz}}{f} \cdot \left(355 \cdot 10^{-12} \left(\frac{L}{100 \text{ km}}\right) \frac{m}{\sqrt{Hz}}\right)^2}$$

which includes frequency noise and a white background noise comprising also other noise sources to be analyzed in more detail. This noise level is more than 3 orders of magnitude relaxed compared to the LISA requirements. Dominant noise sources are expected to be the laser frequency noise and the coupling of spacecraft alignment jitter into the length measurement. Laser frequency noise requires an active stabilization, which has already been demonstrated in laboratories several times, and which is being converted now into space-qualified versions. Coupling of alignment jitter is a common nuisance in precision interferometers and several techniques are available and under investigation for its mitigation, such as the measurement, calibration and subtraction [4] and, of course the reduction of the jitter in the first place with either a beam steering mechanism or by improving the pointing of the spacecraft as a whole, with the latter solution being the preferred one.

4. Preliminary results and benefits for gravity field determination

Against the background of technologies that

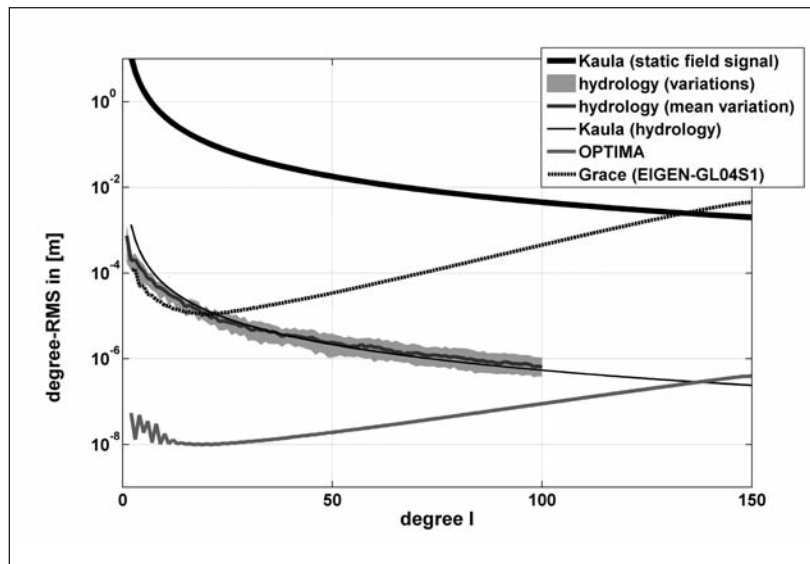


Figure 3: Degree-RMS of OPTIMA confronted with a degree-RMS of GRACE and a hydrology model, representing earth system signals to be observed

still exist and that will be further investigated in the next years, we assume the accuracies of the main gravity measuring instruments as mentioned in chapters 3.1 and 3.2. These accuracies for the laser interferometer and the gradiometer measurements are used as input for the Quick Look Tool [12]. This tool allows error propagation of frequency-dependent instrument accuracies to gravity field quantities. The input noise of the SST-measurement is a combination of the power spectral density (PSD) of the laser interferometer and the accelerometer PSD, where the common mode noise level of the gradiometer (chapter 3.1) is taken here. In the Quick Look Tool, some simplifications are adopted as that of a circular orbit. In addition to the sensor PSDs, further input quantities are:

- altitude over surface: 250 km,
- inclination of the orbit: 90°,
- satellite separation: 100 km.

The resulting error distribution in terms of RMS error per degree of OPTIMA mission is illustrated in Figure 3. Compared to GRACE, the error will be reduced by up to 4 orders of magnitude. Figure 3 also shows that OPTIMA can detect hydrological effects in a wide frequency spectrum. OPTIMA will therefore significantly contribute to a better understanding of the earth system.

5. Conclusions and outlook

OPTIMA combines proven concepts of the previous gravity missions GRACE and GOCE aided with novel optical technology developed for LISA. This innovative concept allows gravity field determination with about up to four orders of magnitude improvement compared to present knowledge. The performance of OPTIMA is greatly increased compared to recent gravity missions by applying optical sensor technology and extending the frequency range for gravity field recovery.

OPTIMA is a mission with long-term perspective as space-qualified versions of the laser components are already to be tested on board of precursor satellite missions in the next years. In future work, detailed analysis of the system components, the system integration, the satellite environment and the gravity field retrieval (added by GNSS reflectometry) will be carried out within the FGM project. This includes feasibility studies to identify possible limiting factors. Also different orbits for the two satellites will be investigated, and different formations, like pendulum orbits, which might lead to a further improved sensitivity of OPTIMA.

Acknowledgement

We are grateful to Tilo Reubelt from the Geodetic Institute (GIS) in Stuttgart, who has computed the RMS error per degree from the given noise scenarios with the help of the 'Quick-Look-Tool'.

The project Future Missions is part of the R&D Programme GEOTECHNOLOGIEN. GEOTECHNOLOGIEN is funded by the German Ministry of Education and Research (BMBF) and the German Research Foundation (DFG), Grant (03G0729C) of project Future Missions.

References

- [1] Cluster of Excellence QUEST, Centre for Quantum Engineering and Space-Time Research, Interim Report, Leibniz Universität Hannover, 2010.
- [2] Cluster of Excellence QUEST, Centre for Quantum Engineering and Space-Time Research, Task Group 7: OPTical Interferometry for global MASS change detection from space (OPTIMA). J. Müller, K. Danzmann, J. Flury, G. Heinzel, D. Bindel, N. Sneeuw, E. Rasel, E. Stephan, O. Romberg, T. Gruber, J. Kusche, S. Schön, W. Ertmer, proposal for call of DLR, 2009.
- [3] Cluster of Excellence QUEST, Centre for Quantum Engineering and Space-Time Research. Webpage <<http://www.questhannover.de/>>, retrieved 27 September 2010.
- [4] Guzman Cervantes, F; Steier, F; Wanner, G; Heinzel, G; Danzmann, K: Subtraction of test mass angular noise in the LISA technology package interferometer; APPLIED PHYSICS B-LASERS AND OPTICS, Volume 90, Issue 3-4, page 395-400, 2008.
- [5] Heinzel, G; Braxmaier, C; Schilling, R; Rudiger, A; Robertson, D; Plate, MT; Wand, V; Arai, K; Johann, U; Danzmann, K: Interferometry for the LISA technology package (LTP) aboard SMART-2; CLASSICAL AND QUANTUM GRAVITY, Volume 20, Issue 10, page S153-S161, 2003, ISSN 0264-9381.
- [6] Heinzel, G; Wand, V; Garcia, A; Jennrich, OP; Braxmaier, C; Robertson, D; Middleton, K; Hoyland, D; Rudiger, A; Schilling, R; Johann, U; Danzmann, K: The LTP interferometer and phasemeter; CLASSICAL AND QUANTUM GRAVITY, Volume 21, Issue 5, page S581-S587, 2004, ISSN 0264-9381.
- [7] Heinzel, G; Braxmaier, C; Caldwell, M; Danzmann, K; Draaisma, F; Garcia, A; Hough, J; Jennrich, O; Johann, U; Killow, C; Middleton, K; te Plate, M; Robertson, D; Rudiger, A; Schilling, R; Steier, F; Wand, V; Ward, H: Successful testing of the LISA Technology Package (LTP) interferometer engineering model; CLASSICAL AND QUANTUM GRAVITY, Volume 22, Issue 10, page S149-S154, 2005.
- [8] Hirth, M; Fichter, W: Test Masses and Accelerometers for Future Gravity Missions. GEOTECHNOLOGIEN science report, SR17, 2010.
- [9] Ilk, KH: Zukünftige Möglichkeiten der globalen hochauflösenden Schwerfeldbestimmung, in: Satellitengeodäsie, ed. by M. Schneider, VCH Verlagsgesellschaft, Weinheim, S. 213-256, 1990.
- [10] Müller, J: Die Satellitengradiometriemission GOCE - Theorie, technische Realisierung und wissenschaftlicher Nutzen. Habilitation, DGK, Reihe C, Heft 541, Verlag der Bayerischen Akademie der Wissenschaften, 2001.
- [11] Projektträger Jülich: Erfassung des Systems Erde aus dem Weltraum. Webpage <<http://www.fz-juelich.de/ptj/geotechnologien/fernerkundung>>, retrieved 15 September 2010.
- [12] Sneeuw, N: A semi-analytical approach to gravity field analysis from satellite observations. DGK, Reihe C, Heft 527, Verlag der Bayerischen Akademie der Wissenschaften, ISBN (Print) 3 7696-9566-6, 2000.
- [13] Sneeuw, N; Fichter, W; Müller, J: Future Gravity Field Satellite Missions. Joint Proposal to the BMBF/DFG Research and Development Program GEOTECHNOLOGIEN, 2008.

Optimized Gravity Field Determination from Future Satellite Missions

Elsaka B. and Kusche J.

Astronomical, Physical & Mathematical Geodesy, Institute for Geodesy und Geoinformation, University of Bonn

Abstract

Various concepts for future satellite-gravimetric missions are investigated within the German joint research project »Concepts for future gravity field satellite missions«, funded by the German Geotechnologies program »Observation of the Earth system from space« of the German Federal Ministry of Education and Research (BMBF). One of the project goals is to define and assess different scenarios of satellite formation flight (SFF) configurations by implementing full-scale simulations. To this end, we create simulated measurements for these satellite configurations, compute and assess closed-loop results and finally optimize the mean and time-varying gravity field determination in terms of spatio-temporal resolution and error isotropy. Our full-scale simulations are performed using the software system GROOPS (*Gravity field Recovery Object-Oriented Programming System*) developed in the Group of Astronomical, Physical and Mathematical Geodesy at the Institute of Geodesy and Geoinformation (APMG-IGG) at Bonn University. Our results are used in the joint project for developing concepts and designs required for the next generation (i.e. after CHAMP, GRACE and GOCE) of future satellite gravity missions.

1. Introduction

The unprecedented accuracy achieved by the current space-based gravity missions opened a new opportunity in satellite geodesy for improving the understanding of the Earth's system from space. However, some shortcomings still hamper these successful missions. One of

these shortcomings is the weakness of the gravitational signal because of the orbital geometry of the satellite configuration. This weakness appears clearly in the monthly gravity field solutions of the GRACE mission ('stripes' in the meridional direction). Pursuing our goals involves dealing with four tasks of the work-package WP110 as a part of the co-ordinated research project »Concepts for future gravity field satellite missions« funded by the Geotechnologies programs »Observation of the Earth system from space« of the German Federal Ministry of Education and Research (BMBF). These four tasks are briefly summarized as follow:

1. Definition and implementation of stable satellite formation configurations (WP111).
2. Development of optimized In-situ gravity field determination methods for satellite formation configurations (WP112).
3. Gravity field determination based on simulated formation flight scenarios (WP113).
4. Optimization of computational algorithms and optimization of satellite configurations (WP114).

In this paper, we discuss only the first task (WP111) obtained in the period from 01-01-2010 to 31-07-2010, concerning the definition of mission scenarios of different satellite formation flight (SFF) configurations and their stability when flying in pseudo-real gravity field. First, we will define a set of selected orbital geometries that enables satellite observations in different various directions (e.g. along-, radial- and cross-track), assuming the satellites are equipped with an inter-satellite precision ranging system (microwave or laser). Secondly, we will imple-

ment a full-scale simulation of these observations and the gravity recovery, to assess potential improvements in the spatial and temporal resolution of the gravity solution in presence of aliasing effects. After that, for the pendulum formation, the separation angle will be adjusted to fulfil the mission constraints that were agreed upon and published during this project at the beginning of the year 2010. This document (Sand 2010) states the requirements that should be taken into consideration when establishing a future mission, e.g. for the orbital altitude (for air drag compensation), for the relative velocity between the satellites (e.g. $\Delta v \leq 10 \text{ m/s}$ should limit the cross-track distance change) and yaw/pitch angle of the satellite (e.g. $\alpha < 30^\circ$ should limit the cross track angle). In the following sections, the orbital characteristics of different SFF types will be defined. Furthermore, the six proposed satellite mission scenarios will be described. They include three scenarios having two satellites in out-of-plane pendulum, east-west radial cartwheel and out-of-plane radial (called 'LISA configuration' in this study), one mission scenario of GRACE-pendulum (include three satellites) and two mission scenarios consisting of four satellites including 'multi-GRACE' ΔM and 'multi-GRACE' $\Delta \Omega$ mission scenarios. After that, some results are dis-

cussed and finally the summary is outlined.

2. Geometrical orbit characteristics

Generic SFF types are commonly characterized by approximately circular and approximately polar orbits for a better coverage of the Earth. Here, all orbits have been defined using the Keplerian elements: the semi-major axis (a), the eccentricity (e), the inclination (i), RAAN (Ω), the argument of perigee (ω) and the mean anomaly (M). Small eccentricities (of 0.001, 0.005 and 0.01) for an approximately circular orbit have been selected in this paper, whereas no attempt has been made to control the long-term evolution of the orbit (as e.g. with frozen orbits). Orbital inclination of 89.5° and altitude of 400 km have been chosen for all SFF types. It should be mentioned that the last two mentioned orbital parameters have been selected to stay away from too short repeat periods of the satellites in order to provide a homogeneous ground coverage. The above mentioned elements create a repeat period of 759 satellite revolutions in 49 nodal days, i.e. no repeat of the satellite revolutions during one month takes place (the shorter the repeat period, the more insufficient coverage results). Further details can be found in *Elsaka (2010)*.

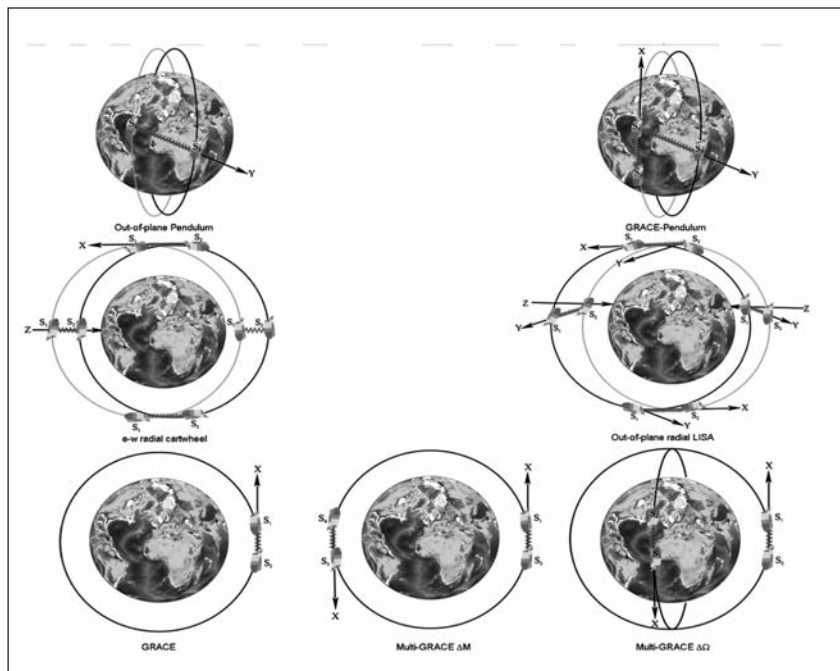


Fig. 1 Satellite formation flight configurations: the axes X, Y, Z are for along-track, cross-track and radial directions.

3. Mission scenarios of satellite formation flights

Fig. 1 shows the proposed six SFF mission scenarios as mentioned in section 1. In Fig.1, axis X stands for along-track, Y stands for the cross-track and Z stands for the radial direction. The out-of-plane pendulum collects inter-satellite measurements in cross-track direction above the equator of the Earth. The GRACE-pendulum collects satellite observations in two different Line-of-Sight directions: along- and cross-track, and the east-west radial cartwheel collects information in both along-track and radial directions. The inter-satellite measurements in along-track direction take place over the poles while those in radial direction take place over the equator. This means that the satellite baseline when carrying out the radial measurements, is perpendicular to the meridian direction (north-south), and therefore, we refer to this formation as east-west radial cartwheel. Adding a cross-track component to the last formation, the so-called out-of-plane radial LISA is obtained.

Other solutions for improving the spatial-temporal resolution of the current satellite missions without deteriorating accuracy are also

investigated here: the so-called multi-GRACE constellations. This means that a second GRACE-type formation will be added to a GRACE-type one in order to form a four-satellite GRACE constellation. Fig. 1 shows also two suggestions for the multi-GRACE type: one of them (multi-GRACE ΔM) improves the temporal resolution without sacrificing in the spatial one and the other one (multi-GRACE $\Delta \Omega$) improves the spatial sampling without losing on the temporal resolution. One should note that in our simulations, one month of simulated data was used for all two-satellite and three-satellite configurations, but in case of multi-GRACE constellations, only 12 days of simulated observations were used.

Fig. 2 shows the evaluation of the inter-satellite distance for each of the above mentioned formations. The GRACE ranges stand for the two SST links of both the multi-GRACE ΔM and $\Delta \Omega$ constellations. One can easily observe that all configurations fly in stable formation except the out-of-plane LISA one, whose inter-satellite range changes with time (a fact that can easily be explained from linear perturbation theory).

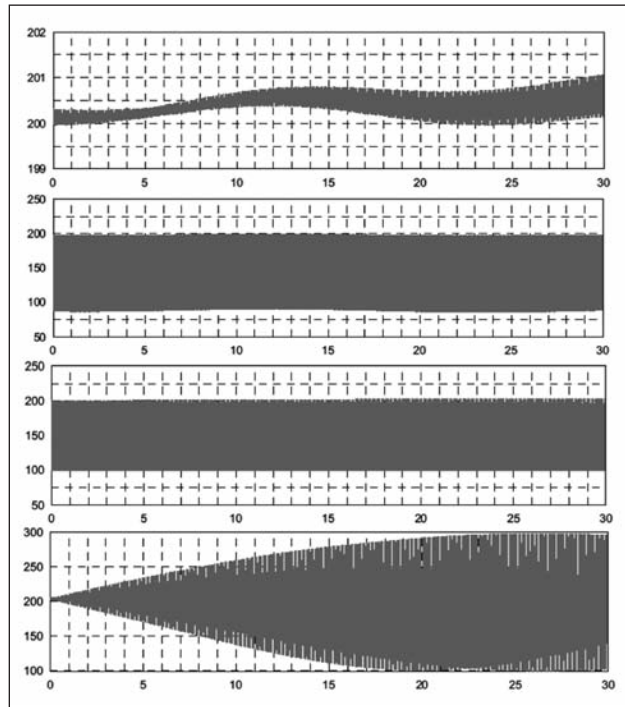


Fig. 2 Inter-satellite distances [in km] of the different SFF types (given in the vertical axis) versus time span of 30 days (given in horizontal axis): from top to bottom, GRACE, pendulum, radial cartwheel and out-of-plane radial LISA.

4. Assessment of gravity recovery results of the SFF mission scenarios

The objective of implementing full-scale simulations of measurements for different SFF scenarios is to assess and finally optimize the gravity field retrieval, especially for the time-varying field. Fig. 3 visualizes such an assessment in terms of the geoid errors between the ITG-GRACE03s (Mayer-Gürr et al. 2007) as a reference gravity model and the gravity solutions determined from the investigated SFF types, here caused by ocean tidal aliasing errors. The simulated aliasing errors of the ocean tides have been considered as the difference between the two oceanic tidal models FES2004 (Letellier et al. 2004) and EOT08a (Savcenko and Bosch 2008). One observes that gravity solutions determined by all SFF types are less affected by the tidal aliasing compared to the GRACE solution (we don't co-estimate tidal harmonics here). Improvements by the radial and out-of-plane formations as well as by the multi-GRACE $\Delta\Omega$ configuration can easily be seen in the oceans, especially in the north Atlantic, the Pacific and the Caribbean regions. Interesting is that the information contained in the satellite observables of each SFF can be recog-

nized in the behaviour of the geoid errors. For instance, as both satellites of the GRACE formation fly in along track direction, one finds strong error behaviour in north-south (or meridional) direction (as with the real GRACE mission). For the radial cartwheel, the error structure is aligned in vertical direction and since the out-of-plane radial LISA has an additional cross track component, the error behaviour appears as diagonal structure. The combination of the north-south GRACE error behaviour and the east-west pendulum one yields the most homogeneous and isotropic error structure for the GRACE-pendulum. Also the north-south GRACE error structure has been reduced with the multi-GRACE $\Delta\Omega$. The multi-GRACE ΔM has aggravated the aliasing errors since the weakness of its observations in many regions of the Earth (see Elsaka 2010).

One can conclude from this preliminary assessment of a selection of different satellite configurations that one can significantly reduce (w.r.t. a GRACE-type formation) and mitigate the ocean tidal aliasing errors. This result has already significantly contributed to the goals of our project.

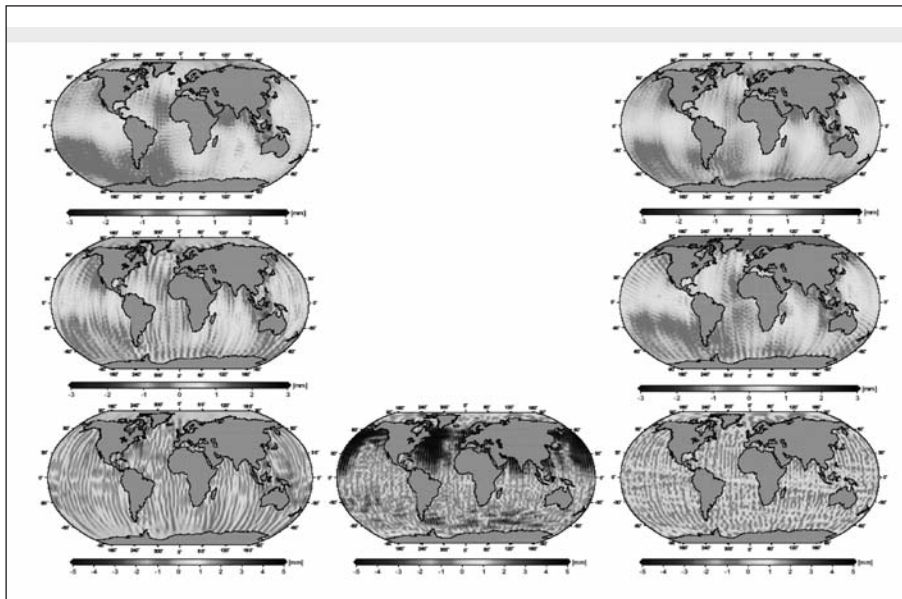


Fig. 3. Geoid heights differences between the ITG-GRACE03s and the gravity solutions as determined from all SFF types: pendulum (top-left), GRACE-pendulum (top-right), radial cartwheel (middle-left), out-of-plane radial LISA (middle-right), GRACE (bottom-left), multi-GRACE ΔM (bottom-middle) and multi-GRACE $\Delta\Omega$ (bottom-right).

5. Adjustment of the cross-track separation of the pendulum formation

As the cross-track distance between the two satellites of a pendulum formation increases, the relative velocity between them increases as well. As mentioned, it has been agreed upon in our project that the inter-satellite velocity will limit the cross-track distance and hence should Δv not exceed ± 10 m/s. For keeping pendulum within this limit, we adjusted the out-of-plane cross-track distance by minimizing the separation angle ($\Delta\Omega$) between the two satellites. Fig. 4 shows the difference of the previously investigated pendulum formation with higher relative velocity and the same formation after the separation angle has been reduced from 1.5° to 0.45° . One observes that the cross-track separation angle of 1.5° yields inter-satellite velocity of approx. ± 125 m/s while the angle of 0.45° yields inter-satellite one of approx. ± 8 m/s.

It should also be noted here that the corresponding inter-satellite distance for the pendulum formation with separation angle 1.5° ranges from 90 to 200 km while the one for separation 0.45° ranges from 200 to 212 km. The latter inter-satellite separation is still capable for detecting the time-varying gravity field with sufficient spatial resolution.

6. Summary

The results obtained within this study demonstrate clearly that optimizing the satellite formation flights is important when one designs a future gravity mission. The results show the benefit of incorporating additional information into the along-track observable like adding radial and cross-track components. The GRACE formation, albeit technologically the simplest one, is found sub-optimal in terms of the gravity solution (of course, this is a result that many others discovered already). The incorporation of other information provides significant improvements in terms of the error levels and more isotropic distribution of the errors. Strongest improvements have been found for the cross-track configurations like pendulum and GRACE-pendulum and for the radial configurations like radial cartwheel and out-of-plane radial LISA. Yet, improved gravity solutions are to be expected from the along-track configuration by merging two collinear GRACE SFF types as simulated here with the multi-GRACE $\Delta\Omega$ constellation. At the end, we recommend in this paper the pendulum SFF type as a future candidate mission after adjusting the cross-track separation. This adjustment has been carried out by reducing the cross-track separation angle from 1.5° to 0.45° . The last

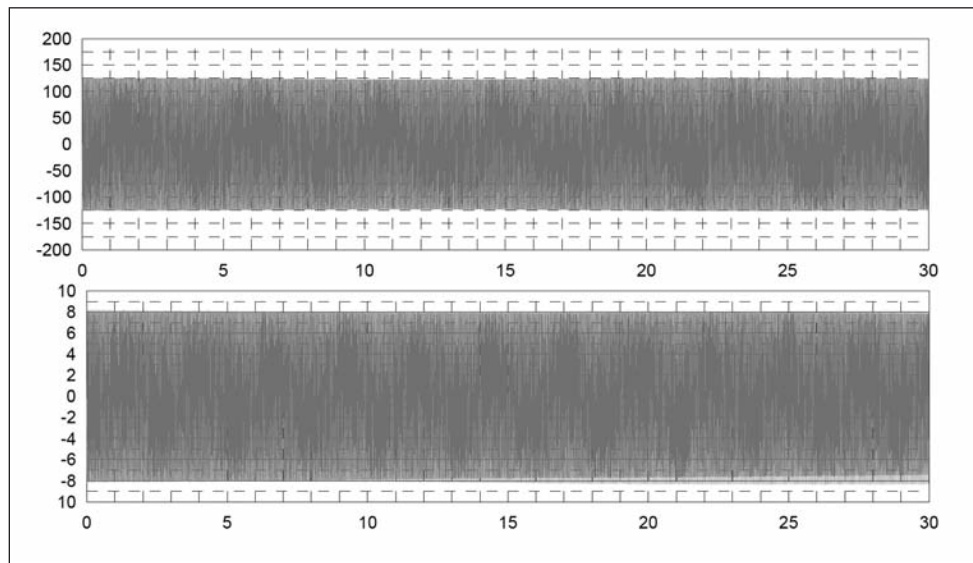


Figure 4. Inter-satellite velocities [given in vertical axis in m/s] of the pendulum formation with separation angle 1.5° (top) and 0.45° (bottom) versus time span of 30 days (given in horizontal axis).

separation angle yields an inter-satellite velocity of $\pm 8\text{m/s}$.

Acknowledgement

The financial support of the German Federal Ministry for Education and Research (BMBF) under the project »BMBF-Geotechnologien concepts for future gravity field satellite missions« is gratefully acknowledged.

Literature

Elsaka, B. (2010): Simulated Satellite Formation Flights for Detecting the Temporal Variations of the Earth's Gravity Field. PhD thesis, University of Bonn, Germany.

Letellier, T., Lyard, F. and Lefebvre, F. (2004): The new global tidal solution: FES2004. Presented at: Ocean Surface Topography Since Team Meeting, St. Petersburg, Florida, Nov. 4-6.

Mayer-Gürr, T., Eicker, A. and Ilk, K.H. (2007): ITG-Grace03 Gravity Field Model. <http://www.geod.uni-bonn.de/itg-grace03.html>.

Sand, R (2010): Constraints for Future Missions. Technical Doc.No.FGM_STI_TN2_000_V1, SpaceTech GmbH, 2-Jan-2010.

Savcenko, R. and Bosch, W. (2008): EOT08a – empirical ocean tide model from multi-mission satellite altimetry. Report No. 81. Deutsches Geodätisches Forschungsinstitut (DGFI), München, Germany.

Numerical Simulations of new Gravity Mission Concepts

Raimondo J. C., Neumayer K. H. and Flechtner F.

Helmholtz Centre Potsdam, GFZ German Research Centre For Geosciences, D-14473 Potsdam, Germany

Introduction

With the successful GRACE mission scientists have demonstrated that precise measurements of the Earth's changing gravity field can effectively monitor changes in the planet's climate and weather. In order to pursue this task of studying geophysical phenomena involving significant mass redistribution in the Atmosphere (global and small scale circulation), in the Hydrosphere (sea-level changes, ocean dynamics, major river basins, continental reservoirs), in the Cryosphere (mass balance of polar ice sheets, mountain glaciers melting) and in the Lithosphere (post glacial rebound, tectonic subduction) new gravity missions are planned which should determine the static and time variable gravity field with unprecedented temporal and spatial sampling.

In order to assess the performance of the potential various mission scenarios in a realistic manner numerical simulations in the presence of measurements and background models (ocean tides, static and time variable gravity field) errors are needed. In a first step here, we limit our investigations to single pair of satellite formations and consider only the measurement error for satellite-to-satellite tracking (SST) and the error of the GPS measurements between the GPS satellites and in the Low Earth Orbit (LEO) orbiting satellite formations.

At this stage we do not take into account other measurement and background model errors. Naturally the background models errors are very important since they are a major source of aliasing in the solution, in particular the errors in the ocean tides models can be quite critical. We plan to include these background model errors in the near future.

Simulation Scenarios

In this study we investigate the simulation of four formations of single pair of satellites: the GRACE case as reference, as well as the pendulum, the cartwheel, and the helix formation types. The four scenarios are treated as drag-free that means that the satellites should be equipped with a compensation mechanism to take care of all non-conservative forces (air-drag, solar radiation pressure, Earth albedo and Earth infra-red radiation, etc...), in the GRACE test case we also ignored all the non-conservative forces.

The three (in blue) scenarios considered here have been proposed in *Reference 1*, and for comparison purpose we included also the GRACE test case (in red) in the simulations. The four formations of satellite pairs have accordingly the following differential mean keplerian elements:

GRACE:

$h=458\text{km}$, $\Delta a=\Delta e=\Delta i=\Delta \omega=\Delta \Omega=0$, $\Delta M=1.9^\circ$

PENDULUM:

$h=350\text{km}$, $\Delta a=\Delta e=\Delta i=\Delta \omega=0$, $\Delta \Omega=0.4058^\circ$, $\Delta M=0.8115^\circ$

CARTWHEEL:

$h=350\text{km}$, $i=90^\circ$, $e=3.69\text{e-}03$, $M1=\omega1=0^\circ$

$\Delta a=\Delta e=\Delta i=\Delta \Omega=0$, $\Delta \omega=\Delta M=180^\circ$

HELIX:

$h=350\text{km}$, $i=90^\circ$, $e=1.858\text{e-}03$, $\omega1=0.4258^\circ$, $M1=0^\circ$

$\Delta a=\Delta e=\Delta i=0$, $\Delta \Omega=0.3687^\circ$, $\Delta \omega=180.8516^\circ$, $\Delta M=180^\circ$

where:

a = semi-major axis

e = eccentricity

i = inclination

ω = argument of perigeum

Ω = right ascension of the ascending node

M = mean anomaly

M1 and ω_1 refer to values for satellite 1. These keplerian mean elements have to be converted into osculating elements to provide the initial orbital elements of the simulation process.

The measurement error for the SST range-rate was set to 15 nm/s which is a feasible figure for nowadays technology and it represents about a factor 7 improvement compared to the GRACE mission (100 nm/s).

We limited the gravity field recovery to degree and order 90.

Simulation Process

The simulation creates four weeks of data batches, each one having the length of one day. The simulated data comprehend GPS code/ phase measurements, simulated surface forces accelerations time series (zeros for the drag-free scenarios) as well as SST range-rate tracking data.

The simulation is achieved in two steps.

In a first step, both satellites are sequentially integrated over the complete four weeks with dedicated models for the surface forces accelerations (if not drag-free). A modus switch of the orbit integrator does not only yield two orbit files of 28 days length but also »measured« numerical surface forces accelerations simulated from the models. From the orbit files, initial elements are created for midnight on every day and the simulated acceleration data are chopped into pieces of one day length.

In a second step, those initial states and acceleration data are fed into 28 individual jobs of one day length that simulate GPS and K-band range-rate data. For the surface forces accelerations, the models are switched off and replaced by the oneday accelerometer data batches created in the first step.

The recovery is also achieved in two steps.

First, the one-day data batches of simulated GPS, SST tracking data are fed into 28 adjustment jobs where arc-specific parameters, like accelerometer calibration factors, empirical K-

band parameters, daily initial satellite positions and velocities as well as GPS phase ambiguities are recovered, but where the gravity field is kept fixed. If convergence has been achieved, one run is started with the gravity field coefficients added to the list of solve-for parameters creating design equation files.

Secondly, day-wise normal equations for every observation type are computed from the design equations. Those normal equations are added up over the whole 28 days, the resulting equation is then solved and yields the adjusted gravity field. The simulations have been carried out with the GFZ EPOS chain of programs. It takes about 11 hours computing time to perform a four-week gravity field recovery up to degree and order 90. The epoch taken for the simulations is March 1 2004 00:00:00 GPS time.

The models used:

- Precession: IAU2000A
- Nutation: IAU2000A
- Siderial time: IAU2000A
- Earth Orientation Parameters (EOP): EOP00C4
- EOP tidal corrections: IAU2000A
- Nutational EOP corrections
- UT1 zonal tidal corrections: IAU2000A
- Geopotential: EIGEN-5C up to 150x150
- Lunar potential: Ferrari 77 up to 4x4
- Planetary ephemerides: JPL DE-405
- Atmospheric pressure (gravity): AOD1B
- Earth tides: Wahr model (IERS Conventions 2000)
- Ocean tides: FES2004 up to 80x80
- Atmospheric tides (Bode & Biancale 2003)
- Polar tide model from Desai

The simulated measurements used:

- SST: K-band range-rate
- GPS to LEO satellites (code and phase)

The measurements errors used:

- 15 nm/s white noise for SST range-rate
- 30 cm for GPS code
- 3 mm for GPS phase

The above errors on the GPS code and GPS phase measurements represent an absolute error of about 5 mm (value derives from comparison

with the kinematic orbit) which is rather too optimistic, more realistic would be to consider an absolute orbit error of about 2cm, this should be taken into account in future simulations.

Results of the Simulations:

Below are some quality assessment plots for the GRACE reference case and three proposed scenarios, namely the plot of the geoid height differences between the initial gravity field and the recovered gravity field (spatial domain), the plot of the degree variance (spectral domain) as well as the plots of the coefficients differences between initial and recovered gravity field (true errors) together with the coefficients formal errors of the solution.

Table 1 gives a summary of the performance of the studied mission scenarios. The three pro-

posed scenarios show all an improvement in terms of geoid height differences weighted mean and weighted RMS compared to the GRACE case. The cartwheel outperforms the GRACE case by a factor about 2.5 in term of weighted RMS, whereas the pendulum and the helix cases surpass the GRACE case by a factor around 8 in term of weighted mean. However we have to keep in mind that the simulations were conducted with rather optimistic errors assumptions and it will be very interesting to see how these different scenarios behave in the presence of more realistic measurements errors and above all when introducing background models errors.

GRACE Formation

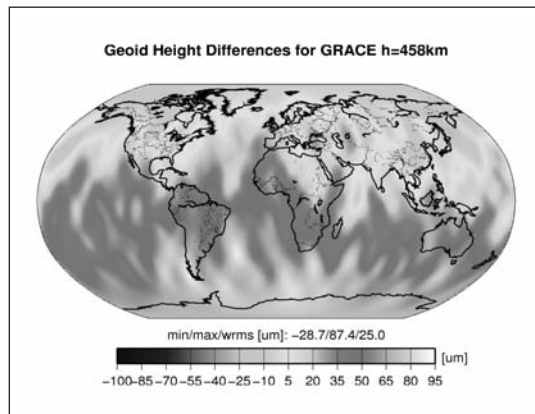


Figure 1: Geoid height differences (μm) for GRACE

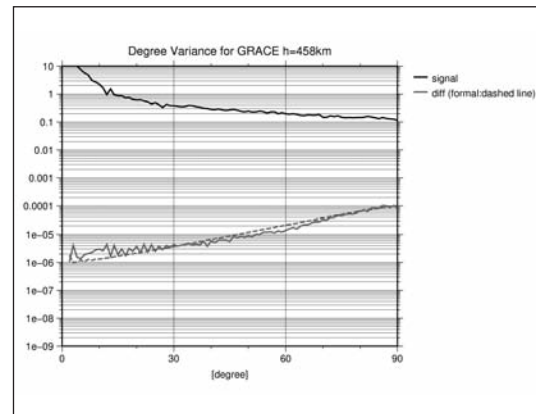


Figure 2: Degree variance for GRACE

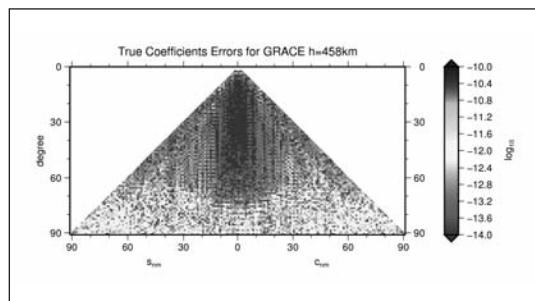


Figure 3: True coefficients errors for GRACE

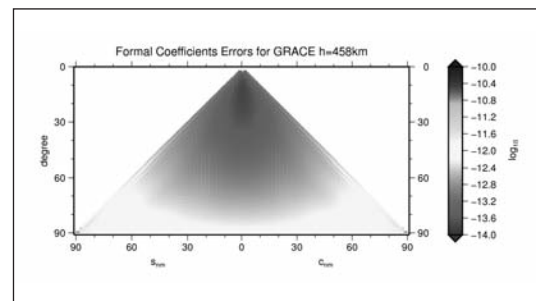


Figure 4: Formal coefficients error for GRACE

Pendulum Formation

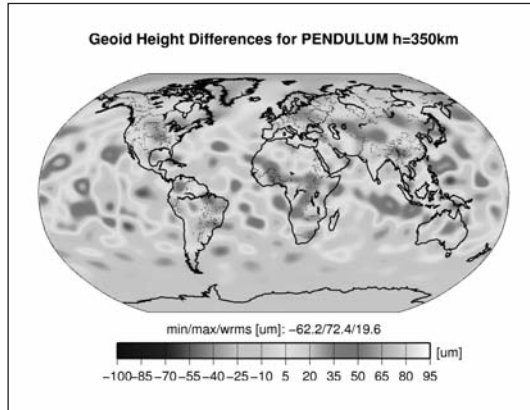


Figure 5: Geoid height differences (μm) for pendulum formation

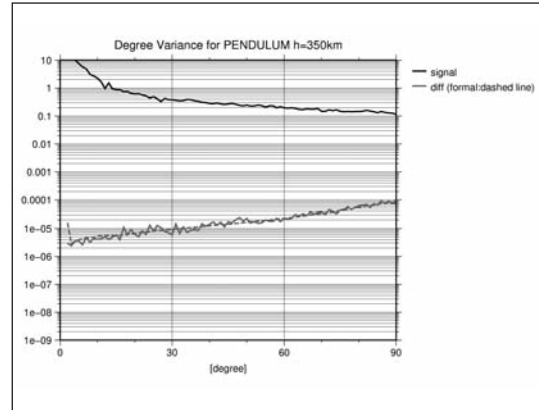


Figure 6: Degree variance for pendulum formation

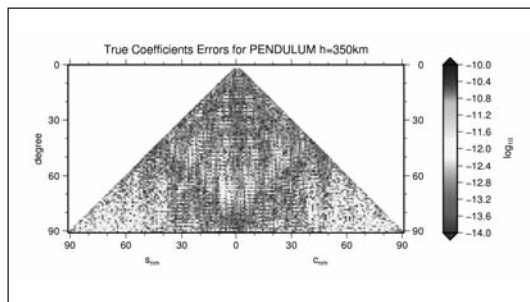


Figure 7: True coefficients errors for pendulum formation

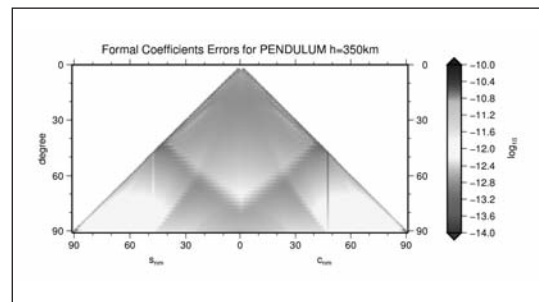


Figure 8: Formal coefficients errors for pendulum formation

Cartwheel Formation

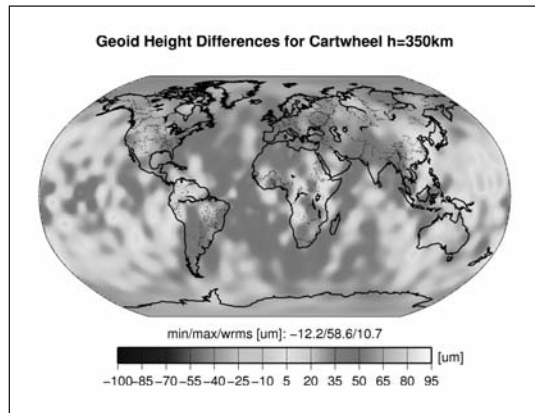


Figure 9: Geoid height differences (μm) for cartwheel formation

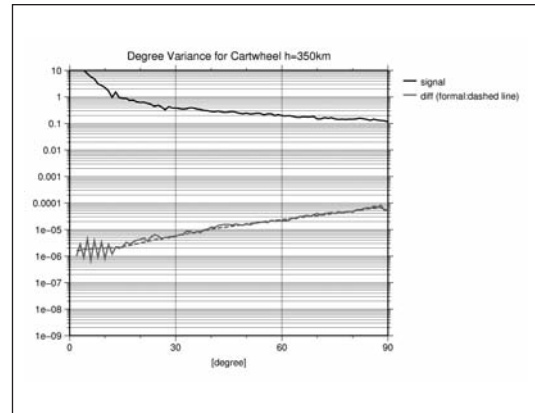


Figure 10: Degree variance for cartwheel formation

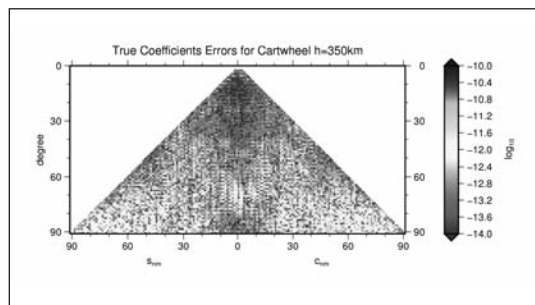


Figure 11: True coefficients errors for cartwheel formation

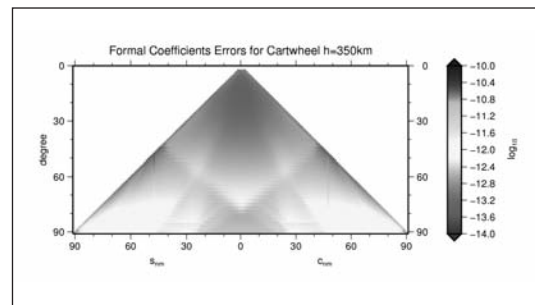


Figure 12: Formal coefficients errors for cartwheel formation

Helix Formation

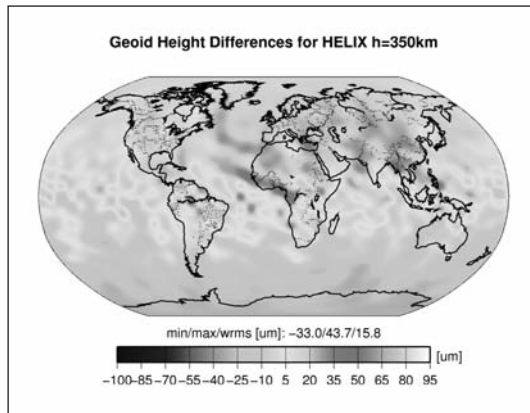


Figure 13: Geoid height differences (μm) for helix formation

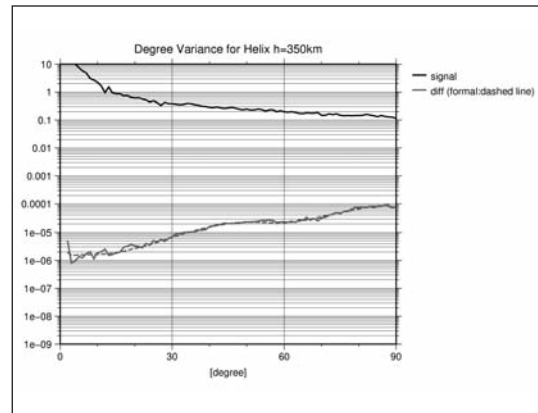


Figure 14: Degree variance for helix formation

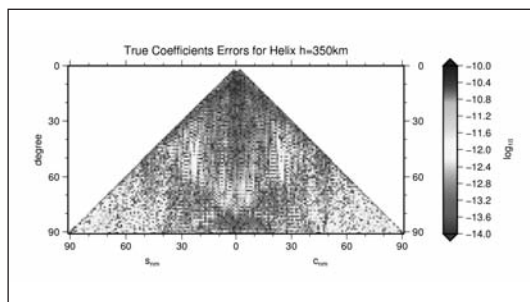


Figure 15: True coefficients errors for helix formation

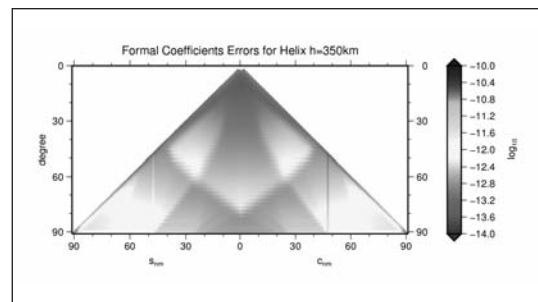


Figure 16: Formal coefficients errors for helix formation

Table 1: Geoid height differences (μm) statistics

Formation	Minimum	Maximum	Weighted Mean	Weighted RMS
GRACE	-28.7	87.4	31.3	25
PENDULUM	-62.2	72.4	4.1	19.6
CARTWHEEL	-12.2	58.6	26.1	10.7
HELIX	-33	43.7	3.8	15.8

Further plans

- include more sophisticated measurement noise (colored noise)
- take into account more realistic orbit errors for the LEO satellites
- consider background models errors (ocean tides, time variable and static gravity field) errors
- optimize the simulation process computation time

Acknowledgement

This work was done under grant 03G0729B of the BMBF Geotechnologien program.

References

1. Reubelt, T., Auswahl von Basic-Missionsszenarien, Technical Note 8, GIS Stuttgart, 2010

Inertial Sensing for Future Gravity Missions

Hirth M. (1), Brandt N. (2), Fichter W. (1)

(1) iFR, Institut für Flugmechanik und Flugregelung, Universität Stuttgart, Pfaffenwaldring 7a, 70569 Stuttgart

(2) Astrium GmbH, 88039 Friedrichshafen

Introduction

The application of accelerometers for gravity missions is assessed within a system framework. Several questions concerning the accelerometer impact on the science performance are discussed. Is the accelerometer noise performance balanced with the performance of the SST-link metrology? Is its measurement range compatible with the system properties? How accurate must the sensor be placed with respect to the spacecraft center of mass? And finally, would it be possible to use the accelerometer test mass center of mass as reference point for the measurements rather than the spacecraft center of mass?

Baseline and Motivation

For an initial estimation of the mission performance top-level assumptions for the single instrument noise power spectral densities (PSD) were available. The total interferometer noise n_{IFO} is based on the predictions for the instrument currently developed at the Albert Einstein Institute, Hannover (AEI):

$$n_{IFO} = \sqrt{\left(50 \frac{nm}{\sqrt{Hz}}\right)^2 + \left(\frac{100Hz}{f}\right) \cdot \left[\left(\frac{\lambda}{1064nm}\right) \cdot \left(\frac{L}{200km}\right) \cdot 712 \frac{pm}{\sqrt{Hz}}\right]^2}$$

It contains mainly a frequency noise dependent term and a white noise assumption for remaining effects like thermal stability, coupling with spacecraft motion, etc. Concerning the accelerometer, the noise shape prediction for the e.motion mission was provided (n_A) which represents the performance of a modified GRADIO sensor from ONERA (aiming for equal sensitivity on all axes).

$$n_A = 5 \cdot 10^{-11} \sqrt{1 + \left(\frac{0.005Hz}{f}\right) + \left(\frac{f}{0.081Hz}\right)^4} \cdot \frac{1}{1 + \left(\frac{f}{0.5Hz}\right)^2} \frac{m}{s^2 \sqrt{Hz}}$$

In this case no information was available whether only instrument noise or total noise is covered. An initial performance estimate was computed using the quick-look tool from the Geodetic Institute of the University of Stuttgart (GIS). The selected baseline mission parameters are shown in Table 1.

Table 1: Baseline parameters for QLT

Parameter	Value
Orbit Height	325 km
Inclination	Polar ($\approx 90^\circ$)
Satellite Separation	200 km
Measurement Period	30 days

The sensor noise shapes are converted to a common range-rate level [1] and used as input for the QLT. The overall PSD and the resulting RMS error in the spherical harmonic degrees are shown in Figure 1a and 1b, respectively. While the PSDs look balanced over the measurement bandwidth (≈ 0.2 mHz to 40mHz), i.e. larger accelerometer contribution at low frequencies and larger interferometer (IFO) contribution at high frequencies, the situation is different regarding the geodetic errors.

Here the accelerometer errors exceed those of the IFO up to degrees about $L=160$. Concerning the time varying gravity field (represented by the hydrology signal in the plot below), the performance is totally driven by the accelerometer. Assuming a $SNR=1$ as limit for the maxi-

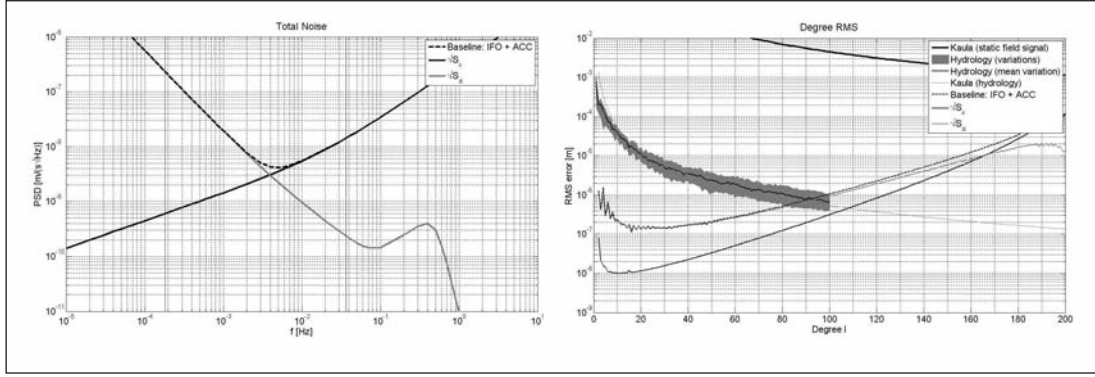


Figure 1: a) PSD of single instrument noise and total on range-rate level. b) Resulting RMS errors

imum resolvable degree, the overall resolution is constraint to $L_{\max} = 90$ while the limit from solely interferometer noise would be close to $L = 110$. Assuming that external couplings are not included in the accelerometer noise, the situation would be even worse.

This result motivated a further investigation of external and internal noise sources of the non-gravitational acceleration measurement to identify the main drivers for the overall science performance.

Measurement Model

For the analysis the main measurement equations were evolved. First, the acceleration at the test mass center of mass is given by:

$$\mathbf{a} = (\mathbf{U} - \ddot{\boldsymbol{\omega}} - \tilde{\boldsymbol{\omega}}^2) \mathbf{r}_A - \mathbf{d} + \mathbf{b}$$

Apart from non-gravitational forces acting on the spacecraft (\mathbf{d}), this includes direct forces on the test mass ('DC bias' \mathbf{b}) and couplings of gravity gradient (\mathbf{U}) and rotational dynamics ($\boldsymbol{\omega}$ - terms) of the spacecraft with the offset \mathbf{r}_A from its center of mass. Using this equation, the total DC accelerations will be estimated later on. This budget delivers insight into the question whether drag compensation is needed and how accurate the sensor has to be placed with respect to the spacecraft CoM to ensure operation in the accelerometer measurement range.

At this point another question arises: If the ac -

celeration measurement is related to the spacecraft center of mass, the terms in parentheses are treated as errors and consequently have to be subtracted to obtain the non-gravitational acceleration at the reference point (SC CoM). Referencing the measurement with respect to the accelerometer test mass CoM would generally avoid this problem as the mentioned terms would directly be part of the desired quantity, i.e. accelerations disturbing the gravitational free fall at the reference point. In this case only the bias on the test mass remains as error concerning the science output. Another advantage would be that the knowledge of the rather unstable and uncertain position of the spacecraft center of mass would not be required with high accuracy. It only has to be ensured that the coupling terms do not exceed the budget. Concerning the SST measurement, the interferometer reference consequently would have to be related to the test mass CoM as well. This seems to pose no problem as the mapping of both sensors mounted on a common bench would benefit from the good relative position stability.

Considering the desired final acceleration measurement along the SST reference direction, additional terms have to be accounted for:

$$\mathbf{a}_M = \Phi(\mathbf{K}_S \mathbf{K}_{CC} \mathbf{a} + \mathbf{n}_A)$$

This includes - apart from instrument noise - cross-coupling errors \mathbf{K}_{CC} due to non-orthogonality of the sensor axes, scale factor errors \mathbf{K}_S due to knowledge of the voltage-force conver-

sion and misalignment Φ of the sensor axes due to spacecraft pointing errors. For the analysis, the impact of individual external noise sources is derived by first-order approximation of the possible fluctuations as shown below (cross-couplings are neglected and fluctuations of the bias are part of the internal noise \mathbf{n}_A):

$$\delta \mathbf{a}_M = \sqrt{\sum \left(\frac{\partial \mathbf{a}_M}{\partial \Phi_i} \delta \Phi_i \right)^2 + \sum \left(\frac{\partial \mathbf{a}_M}{\partial K_{S,j}} \delta K_{S,j} \right)^2 + \sum \left(\frac{\partial \mathbf{a}_M}{\partial \dot{\omega}_i} \delta \dot{\omega}_i \right)^2 + \sum \left(\frac{\partial \mathbf{a}_M}{\partial \omega_i} \delta \omega_i \right)^2 + \sum \left(\frac{\partial \mathbf{a}_M}{\partial r_{A,i}} \delta r_{A,i} \right)^2 + (\Phi \mathbf{n}_A)_i^2}$$

DC Budget

First an analysis of the DC ranges was carried out. Different to the baseline scenario in Table 1 the pendulum configuration described in [2] was chosen to include the 'increased dynamics' due to additional yaw dynamics of the satellite. Concerning external forces, the aerodynamic drag was computed from an MSIS atmosphere model assuming maximum solar activity. Solar radiation pressure was estimated from standard equations, assuming the sun incident on x and y faces to maximize the contributions. Satellite surface areas and properties are taken from GRACE [3]. For the couplings due to the CoM offset, the gravity gradient magnitude was estimated from a first-order model (central gravity field). In addition to the orbital pitch rate, the maximum values for the angular velocity and acceleration due

to the sinusoidal pendulum motion (although not appearing simultaneously and not being real DC) are taken into account for worst case considerations. Bias contributions are represented by the gold wire damping (modeled according to the results in [4]), stray voltages on the electrodes, and thermal effects like radiation pressure and radiometer effect. Table 2 gives an overview of the results. Considering the DC bias only the significant contributions (thermal effects) are shown. Results are kept parametric concerning the offset from the SC CoM.

The contribution of the bias is negligible in the overall budget. It is as expected driven by the atmospheric drag acceleration on the satellite. The effect of external coupling depends linearly on the center of mass offset. However, keeping it below a level of 0.1m, results in contri-

Table 2: DC budget for pendulum configuration ($\rho_x = 57\text{km}$ and $\rho_y = 33\text{km}$)

DC Acceleration [m/s ²]	x	y	z
Radiometer Effect	$1.07 \cdot 10^{-11}$	$1.07 \cdot 10^{-11}$	$4.26 \cdot 10^{-11}$
Radiation Pressure	$7.93 \cdot 10^{-12}$	$7.93 \cdot 10^{-12}$	$3.17 \cdot 10^{-11}$
Gravity Gradient Coupling	$-1.32 \cdot 10^{-6} r_{Ax}$	$-1.32 \cdot 10^{-6} r_{Ay}$	$2.65 \cdot 10^{-6} r_{Az}$
Angular Velocity Coupling	$1.89 \cdot 10^{-6} r_{Ax}$	$1.43 \cdot 10^{-6} r_{Ay}$	$2.19 \cdot 10^{-6} r_{Az}$
Angular Acc. Coupling	$-8.65 \cdot 10^{-7} r_{Ax}$	$-8.65 \cdot 10^{-7} r_{Ay}$	≈ 0
Solar Radiation Pressure	$-3.24 \cdot 10^{-8}$	$\pm 2.48 \cdot 10^{-8}$	≈ 0
Aerodynamic Drag	$-6.36 \cdot 10^{-6}$	$\pm 4.87 \cdot 10^{-6}$	≈ 0
Total Bias	$1.86 \cdot 10^{-11}$	$1.07 \cdot 10^{-11}$	$7.44 \cdot 10^{-11}$
Total Coupling	$-3.00 \cdot 10^{-7} r_{Ax}$	$-9.72 \cdot 10^{-7} r_{Ax}$	$4.83 \cdot 10^{-6} r_{Az}$
Total External	$-6.39 \cdot 10^{-6}$	$\pm 4.90 \cdot 10^{-6}$	≈ 0
Total	$-(6.39 + 0.3 \cdot r_{Ax}) \cdot 10^{-6}$	$(\pm 4.90 - 0.97 \cdot r_{Ay}) \cdot 10^{-6}$	$4.83 \cdot 10^{-6} r_{Az}$

butions at least one order of magnitude smaller than by atmospheric drag. Even more as the main contributors -gravity gradient and angular velocity partially cancel each other. Concluding, from a DC point of view and assuming a dynamic range of the sensor of some 10^{-6} m/s^2 , a resolution below 10^{-11} m/s^2 seems possible without special effort. Otherwise only a moderate level of drag compensation by thrusters or adaptation of the dynamic range (better ADC resolution) would be required. These results would also generally allow for a referencing to the test mass CoM, whilst the 'free' spacecraft CoM motion remains in the mentioned range.

Noise Budget

The noise budget is subdivided into two main parts: internal instrument noise and external noise which is affected by the closed-loop control of the spacecraft and sensor placement.

Internal noise sources can be classified into capacitive sensing noise, actuation noise, readout noise and noise on direct forces acting on the test mass ('bias stability'). The latter contains contributions from noise which is dependent on mechanical and electrical effects like gold wire damping and fluctuation of stray voltages on the electrodes. Another source are the effects that relate to thermal stability, i.e. temperature, temperature difference and pressure fluctuation. To model the closed-loop

behavior of the accelerometer with all relevant devices, the scheme from the GRADIO sensor shown in Figure 2 was converted into a simplified loop model for one translational axis (Figure 3). It mainly consists of the test mass dynamics including electrostatic stiffness, gains for the different devices and a PID controller and the noise sources for the different devices and effects.

Noise shapes and controller gains were derived starting from 'best guess' assumptions and available information and iteratively tuned such that they fit to results for GRADIO (shown in Figure 4) while keeping the involved parameters (environment, TM dimensions and gaps, controller bandwidth, etc.) in the expected range. Figure 5 shows the results from the parametric model that are in very good agreement with the ONERA noise prediction. The only significant difference shows up in the modeling of thermal effects. ONERA assumes a quite conservative $1/f^3$ -law while we have chosen a typical $1/f^2$ law for the temperature/temperature difference stability affecting the radiation pressure and radiometer effects. Additionally, our model shows an influence of the pressure fluctuation (radiometer effect) that flattens the shape to $1/f$ above 1mHz, however, this is not dominating.

The impact of this divergent modeling assumption is negligible concerning science performance as it only affects the very lower end of

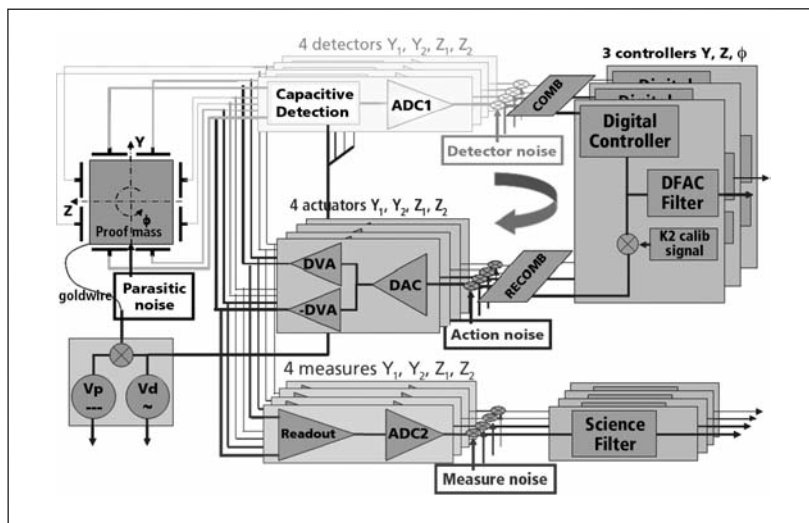


Figure 2: ONERA scheme of GRADIO [5]

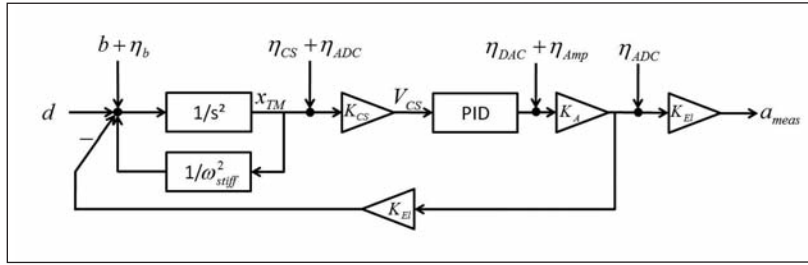


Figure 3: Simplified loop model

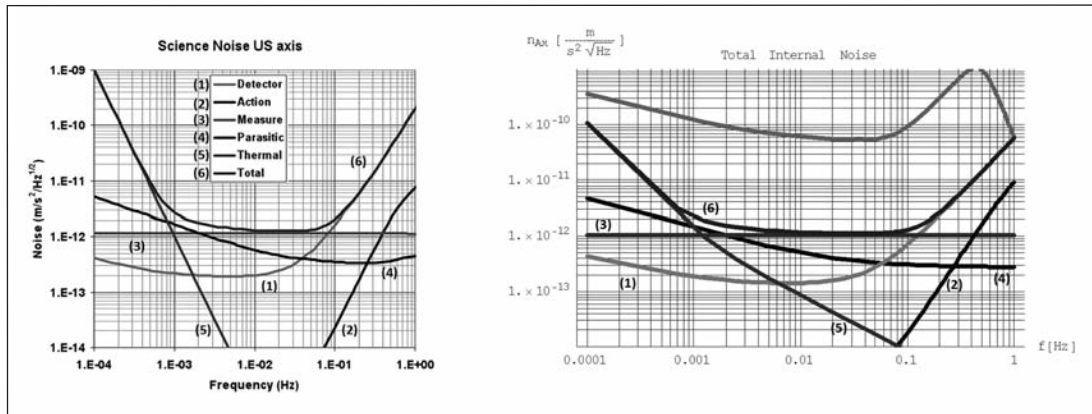


Figure 4: a) GRADIO noise [5], b) Results from parametric model

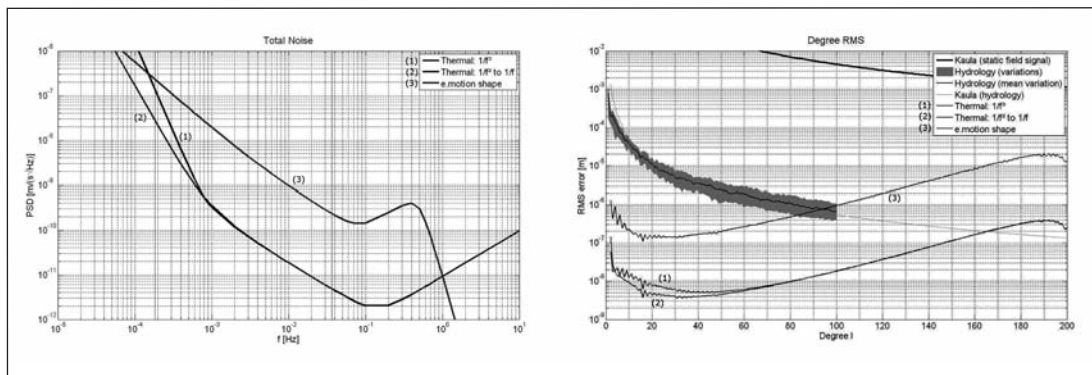


Figure 5: Total internal noise for different thermal stability assumptions. a) PSD level, b) Resulting RMS errors; both plots include initial baseline shape

the MBW. This is shown in Figure 5. The same plots also show the initial assumption for the overall accelerometer noise. Compared to that, the instrument noise seems to be totally negligible which further motivates a focus on the errors due to coupling of external noise and its mitigation by spacecraft control and sensor placement.

External noise sources to be modeled are stability of the scale factor (although not 'really

external'), fluctuations of the distance between spacecraft CoM - test mass COM, and couplings with the angular dynamics of the spacecraft.

The initial guess for the first contribution is a moderate white noise level $10^{-7}/\sqrt{\text{Hz}}$. For the second contribution, only expansion due to the thermal stability of a ZERODUR bench is taken into account. The dynamics contribution is again related to closed-loop performance

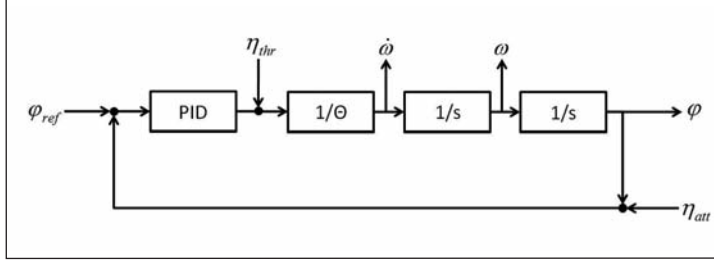


Figure 6: SISO loop for attitude control

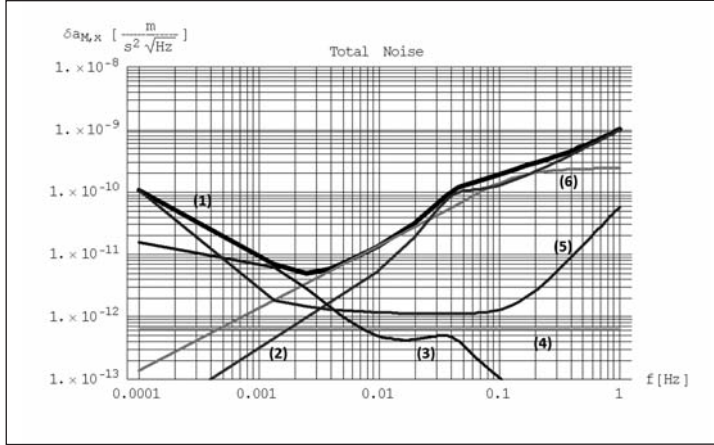


Figure 7: Total accelerometer noise (0.05 Hz controller BW, 10mm offset from SC CoM);
(1) Total noise,
(2) Coupling with angular acceleration noise,
(3) Coupling with pointing noise,
(4) Coupling with scale factor fluctuations,
(5) Internal noise,
(6) Coupling with angular velocity noise

and a simple SISO loop model (Figure 6) for attitude control has been set up. It is assumed that main noise sources arise from the thruster actuation and attitude readout. The noise shape for the thrusters is adapted from the FEEPs for LISA Pathfinder with an upscaled thrust and noise level to fit the gravity mission needs. Concerning the readout noise, usage of differential wavefront sensing from the interferometer signals is assumed for two axes (yaw, pitch). The noise shape is adapted from the LISA DWS performance, again with an upscaled high-frequency level (50 nrad/ $\sqrt{\text{Hz}}$). For the third axis, a white noise level of 50 $\mu\text{rad}/\sqrt{\text{Hz}}$ is assumed, representing the performance of an 'off-the-shelf' star tracker.

As a starting point, PID controllers with different bandwidths were investigated. Figure 7 shows the result for the total noise of the accelerometer measurement and 0.05 Hz controller bandwidth. The CoM offset is assumed to be 10mm on all axes.

First, the internal noise generally remains far below the external contributions except for

very low frequencies $< 1\text{mHz}$. The same is true for the impact of the thermal stability of the reference point, which is orders of magnitudes below other contributors (not shown) and seems negligible under the current assumptions. The influence of pointing noise is most crucial concerning the science performance as it mainly affects the lower region of the measurement bandwidth. The mid- and upper part of the MBW are significantly driven by couplings from angular velocity and acceleration noise, thus only effecting the errors on higher harmonic degrees. The impact of scale factor stability coupling does not play an important role in the current budget. However, more effort has to be put in the modeling here to finally confirm this result.

At this point, the idea of referencing the measurement to the test mass CoM comes up again. Using it as reference, the noise induced by angular velocity and angular acceleration couplings would no longer have to be treated as error but would simply be part of the desired measurement.

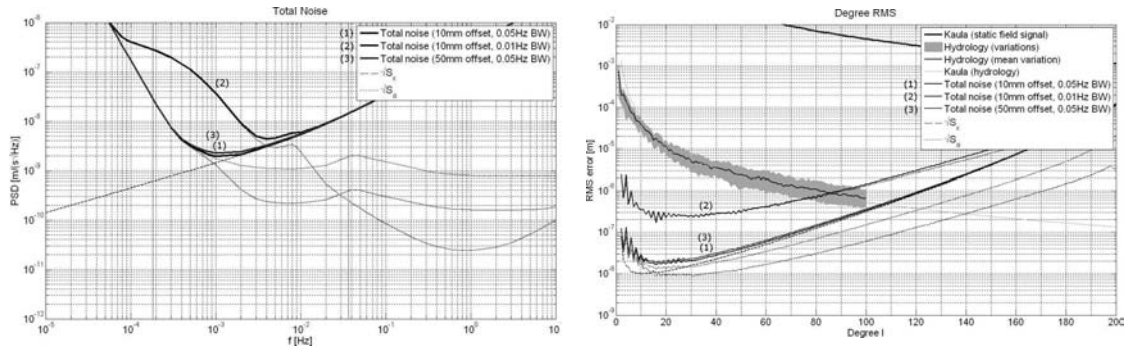


Figure 8: Mission performance for different controller bandwidths and accelerometer displacement w.r.t. SC CoM
a) PSD level, b) Resulting RMS errors; both plots include baseline shape

Figure 8 finally shows the science performance regarding the total noise of the baseline SST mission including accelerometer and interferometer performance. The reason for the switch-back to evaluation the GRACE-like baseline mission (though with pendulum related accelerometer budget) rather than the pendulum configuration for is simply that the quick-look tool currently cannot handle colored noise in other configurations. However this is no real restriction, as the relative behavior between different noise shapes is likely to be the same. For 0.05 Hz controller bandwidth and 10mm CoM offset the time-varying field resolution would be augmented to $L_{\max} = 110$ while the laser would become the limiting instrument in this case (resolution due to accelerometer alone around $L = 140$). Thus the sensor positioning offset with respect to the spacecraft center of mass could even be increased to 50mm before inducing a significant contribution to the overall performance.

Figure 8 shows another important feature: The dependency of the science performance on the attitude control bandwidth. While for (a relatively high) 0.05 Hz bandwidth above statements hold, the situation is remarkably different when reducing the bandwidth to 0.01 Hz. In this case a 10mm offset leads back to a total domination of accelerometer noise, mainly induced by the larger pointing noise coupling. Improvement towards balanced behavior would then require accurate positioning of the accelerometer with respect to the spacecraft CoM again.

Note that generally another factor of $\sqrt{2}$ would have to be added to the accelerometer noise PSD to account for uncorrelated noise of the sensors on the distinct spacecraft, which was neglected in the analysis above.

Conclusions

An initial performance estimation for the accelerometer within an SST mission was carried out. Expected DC forces do not significantly limit the performance of the accelerometer. A moderate drag-compensation to $< 10^{-6} \text{ m/s}^2$ seems sufficient. Alternatively the sensor dynamic range might be adapted by improved ADC resolution. Considering the sum of individual noise sources, the internal accelerometer noise seems to be negligible. A balanced behavior of the two main sensors must be ensured by appropriate control design and accelerometer placement. As the limitation for accelerometer placement is highly dependent on the attitude control bandwidth, the feasibility of high bandwidth control and assumptions for the involved noise models have to be confirmed. Switching the reference point from spacecraft to test mass center of mass seems to be a useful option. It reduces the need to accurately determine external coupling parameters like angular velocities, accelerations and spacecraft center of mass knowledge as it would turn related error terms into desired measurements of non-gravitational forces.

Acknowledgements

The project »Zukunftskonzepte für Schwerefeldsatellitenmissionen« is part of the R&D-Programme GEOTECHNOLOGIEN. GEOTECHNOLOGIEN is funded by the German Ministry of Education and Research (BMBF) and the German Research Foundation (DFG), Grant 03G0729A of project »Zukunftskonzepte für Schwerefeldsatellitenmissionen«. We are grateful for this support and we would like to thank all project partners for the pleasant collaboration.

References

- [1] M. Hirth, Impact of basic parameters on the scientific measurement, FGM-IFR-TN6-332, Issue 1, Project Documentation
- [2] T. Reubelt, Auswahl von Basic-Missionsszenarien, FGM-GIS-TN8-000, Issue 2, Project Documentation
- [3] GRACE 327-720 Issue 4.5, Product Specification Document, available on NASA/JPL website
- [4] E. Willemenot, B. Foulon, On-ground investigation of space accelerometer noise with an electrostatic torsion pendulum, Rev. Sci. Instrum. 71 (302). 2000
- [5] B. Christophe, J-P. Marque, B. Foulon, Accelerometers for the ESA GOCE Mission: one year of in-orbit results, ONERA, presentation available on ESA website

Laser interferometry for future satellite gravimetry missions

Sheard B., Dehne M., Mahrdrdt C., Gerberding O., Müller V., Heinzel G. and Danzmann K.

Albert Einstein Institute Hannover and Centre for Quantum Engineering and Space-Time Research (QUEST),
Callinstraße 38, 30167 Hannover, Germany

Abstract

This report presents an overview of the status of the ongoing research and development of laser interferometry for future satellite gravimetry missions at the Albert-Einstein-Institute in Hannover, Germany.

ging in a GRACE like configuration using a laser interferometer, although laser interferometer could conceivably be applied to gradiometry by using an optical readout of test masses (based on the technology developed for LISA Pathfinder [REF3]).

Introduction

Laser interferometry has been suggested as a way to improve the ranging performance of future gravity field missions based on satellite-to-satellite tracking. There is much overlap with the developments on laser interferometry for monitoring inter-satellite distance fluctuations for the future space-based gravitational wave detector, Laser Interferometer Space Antenna (LISA). For further information about LISA see e.g. [REF1] and [REF2]. We have initially focused our analysis on inter-satellite ran-

Interferometer and system design aspects

For an inter-satellite ranging configuration like GRACE one of the major limiting noise sources is laser frequency noise due to the large inter-satellite distance (few hundred kilometres). Frequency noise couples into the inter-satellite range measurement according to the following relationship:

$$x_v(f) = \left(\frac{\lambda L}{c} \right) v(f)$$

where L is the spacecraft separation, c is the speed of light, λ is the operating wavelength (here assumed to be 1064 nm) and $v(f)$ is the amplitude spectral density of the laser frequency fluctuations. Thus the coupling of laser frequency noise scales linearly with the inter-spacecraft distance. The performance characteristics of a space qualified frequency stabilisation system are not yet known, however estimates from laboratory level experiments can be made. Figure 1 shows the differential laser frequency noise for two lasers each stabilised to a reference cavity in a separate vacuum chamber measured at the AEI and also a simplified performance model with margin.

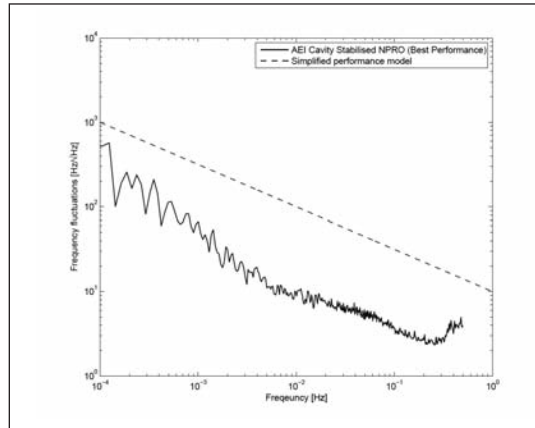


Figure 1: Differential laser frequency noise for two lasers each stabilised to a reference cavity in a separate vacuum chamber and a simplified performance model with margin [REF4].

Another significant consideration for inter-satellite interferometry is the Doppler shift due to

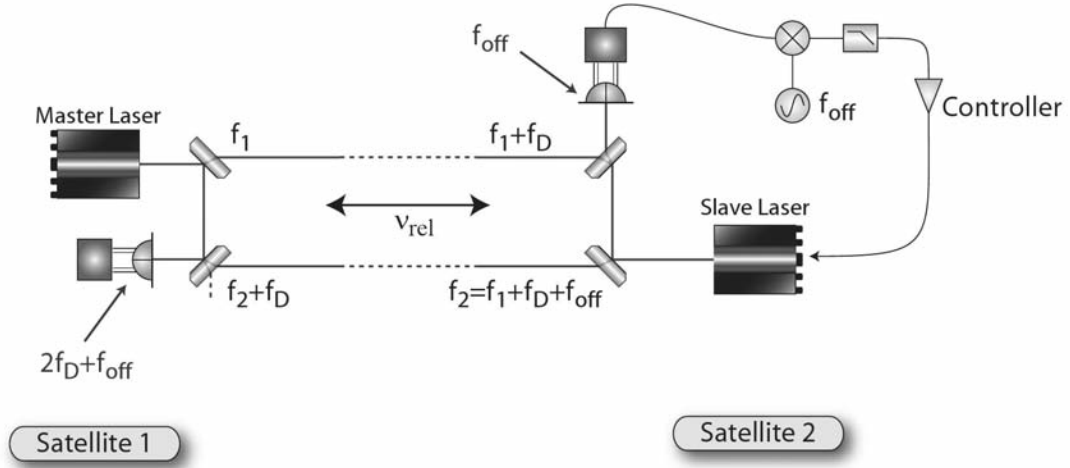


Figure 2: Offset phase locking in the presence of Doppler shifts. The transmit and receive paths are separated for clarity only. In reality the transmit and receive paths are collinear.

the relative velocity along the line-of-sight between the satellites. Figure 2 shows the frequencies measured by the photodetectors on each spacecraft in the presence of Doppler shifts due to the relative velocity along the line-of-sight. The one-way Doppler shift is given by

$$f_D = \frac{-v_{rel}}{\lambda}$$

where v_{rel} is the relative velocity along the line of sight and λ is the wavelength (1064 nm for the NPRO Nd:YAG lasers that will be used in LISA Pathfinder and LISA). The Doppler shift is larger for laser based interferometric ranging than that of a microwave ranging system, due to the smaller wavelength used. The measured beatnotes on both photodetectors must be within the phasemeter limits, which leads to the following constraints on the frequency offset used in the transponder and Doppler shifts:

$$f_{min} \leq f_{off} + 2f_D \leq f_{max}$$

$$f_{min} \leq f_{off} \leq f_{max}$$

where f_{min} and f_{max} is the minimum and maximum frequency respectively that the phasemeter can measure. Thus the phase measurement bandwidth places a constraint on the allowable relative spacecraft velocity along the line-of-sight and therefore is an important consideration when designing orbits of future satellite-to-satellite ranging systems, e.g. pendulum orbits. The current photodetectors and phase-

meter prototypes for LISA have a bandwidth from 1 MHz to 20 MHz.

If a fixed offset with the optimal value of 10.5 MHz were used the allowable one-way Doppler shift is ± 4.75 MHz (which is equivalent to a relative line-of-sight velocity of ± 5 m/s for 1064 nm). The time evolution of the heterodyne frequency on each photodetector for this case is shown in figure 3. If it possible to roughly predict the Doppler shift (which is dominated by a sinusoidal component for a pendulum configuration) in real-time on-board each spacecraft, then by regularly adjusting the transponder offset frequency the tolerable relative velocity can be doubled to ± 10 m/s (as shown in figure 4). Development of a phase-meter prototype with twice the LISA bandwidth has begun at the Albert Einstein Institute Hannover, which would allow ± 10 m/s without an offset adjustment or ± 20 m/s with an offset adjustment.

Although not presented here a detailed analysis of the optical link power budget with imperfect beam pointing with currently available laser powers has been carried out, allowing sizing of the transmitted beam and receiving aperture parameters. Strategies for link acquisition are also currently under investigation.

Polarising components

A key component of proposed interferometer

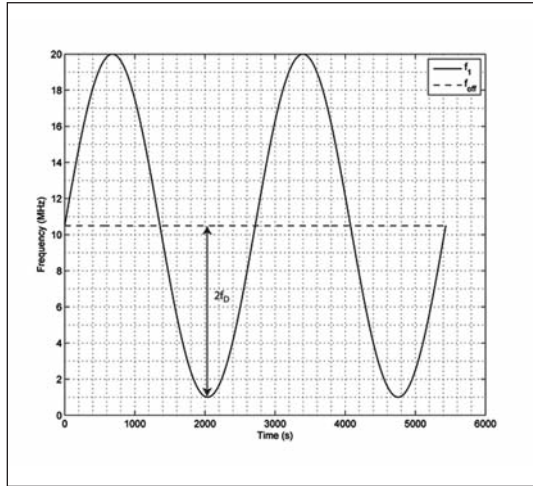


Figure 3: Heterodyne frequencies for constant offset

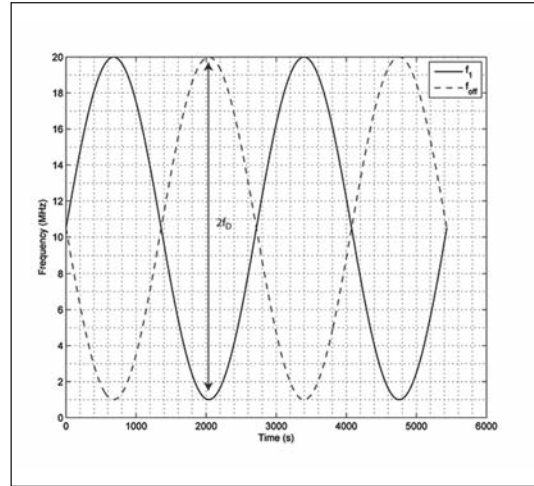


Figure 4: Heterodyne frequencies with variable offset

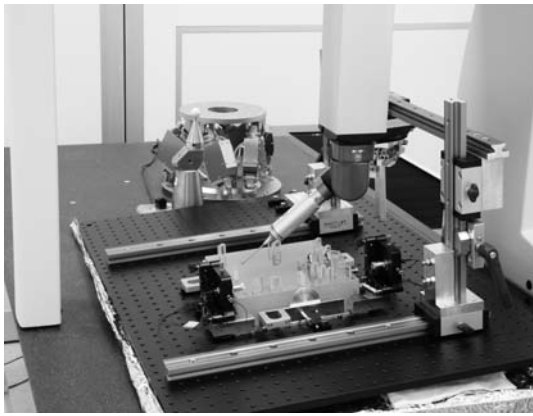


Figure 5: To place the components onto the optical bench a coordinate measuring machine in combination with an alignment tool was used.

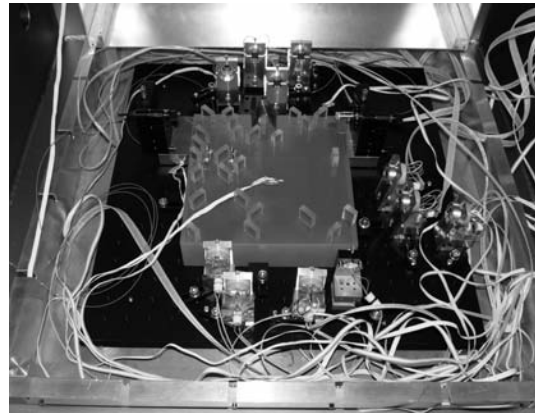


Figure 6: Implementation of the quasi-monolithic optical bench in the measurement environment.

designs are polarising optics. In order to investigate the influence of polarising components on interferometer sensitivity, an optical bench containing four different interferometers has been designed [REF5]. Two interferometers measure the position fluctuations of the same mirror (acting as test mass), but only one includes polarising optics. The remaining two interferometers are used for reducing noise, such as an active frequency stabilisation.

The hydroxide-catalysis bonding technique [REF6] was used to build the optical bench on an ultra-stable glass-ceramic baseplate made of Clearceram to compare polarising and non-polarising optics. For aligning the position of each optical component onto the optical bench a coordinate measuring machine in combination with an alignment tool was

used. With the alignment setup depicted in figure 5 we achieved a positioning accuracy of the order of 10 μm .

In order to reduce coupling of acoustic and thermal effects into the phase readout the measurement was conducted in a vacuum chamber. For a further reduction of thermal noise, the optical bench was additionally enclosed by a thermal shield. Tests performed using the quasi-monolithic optical bench demonstrated a length stability orders of magnitude below the required stability for a straw-man design of future geodesy missions. The obtained noise performance is shown in figure 7.

That pre-experiment has validated that heterodyne interferometry using polarising optics is possible and that even picometre stability is

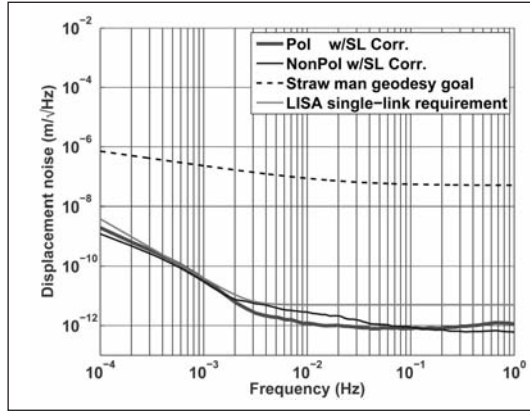


Figure 7: Noise performance of the polarising and non-polarising interferometer. A normalised stray-light correction is implemented in data post-processing. For comparison the LISA single-link requirement and a straw-man geodesy mission sensitivity goal are also shown.

achievable. Different stabilisations such as an amplitude stabilisation (DC laser intensity) and a stabilisation of the laser frequency are not yet implemented, so that we are confident that we are able to improve the sensitivity of the setup. Further breadboards to verify other interferometer concepts are under development.

Interferometer Simulations

All inter-satellite interferometers require analysis of propagation of non-Gaussian beams as from a practical point of view the received beam has to be clipped at the receiving aperture. The propagation of the non-Gaussian beam and the calculation of the interferometer signals have to be done by computer simulations. A software tool based on decomposition into Hermite-Gauss modes is under development and is currently under-going verification and validation.

Appropriate simulation tools to aid the design of the interferometer setup are needed because the conditions under which the final instrument will take data are not completely reproducible in laboratory experiments, for example effects related to the large spacecraft separation of approximately 200 km. Also the coupling of rotations of the satellites into the length measurement can be estimated and different interferometer topologies can be tested to optimise the layout and minimise the coupling.

The laser beam transmitted by the far spacecraft has to be clipped at the receiving telescope as it is not practical to build telescopes large enough to collect all of the light at the receiving telescope. Furthermore, large receiving apertures correspond to small receiving field-of-view as the heterodyne efficiency is inversely proportional to the receiving aperture radius. In practice one always has to clip the incoming light field at the receiving aperture and change its characteristic to a non-Gaussian field distribution. In order to simulate the propagation of non-Gaussian beams, numerical simulations have to be used since only few simple examples are analytically solvable.

Despite methods based on integration of diffraction integrals that are numerically challenging, the non-Gaussian light beam can be approximated by a set of higher order Hermite-Gauss modes which comprise a complete orthonormal set of functions. To approximate the non-Gaussian field distribution by Hermite-Gaussian modes, a unique amplitude for each mode is calculated via a two dimensional integral over the aperture plane [REF7]. To reconstruct the approximated field the modes are summed up weighted by the computed amplitudes. The calculation of the amplitudes and reconstruction of the field for signal calculation are the parts of highest computational cost. The propagation of the complete set can then be done by simple transformations of a complex parameter. Figure 8 shows the intensity distribution of an approximated top-hat beam up to order $N=25$ of considered Hermite-Gauss modes. The approximation considerably gains in accuracy if higher order mode components are included.

Since only a finite number of modes can be considered in the approximation, systematic errors in the calculated interferometer signals may occur.

Tests carried out for verification contain estimation of the error in the reconstructed field compared to the original distribution, comparison of propagated light fields generated by the mode expansion method and numerical integration. Also interferometer signals for appro-

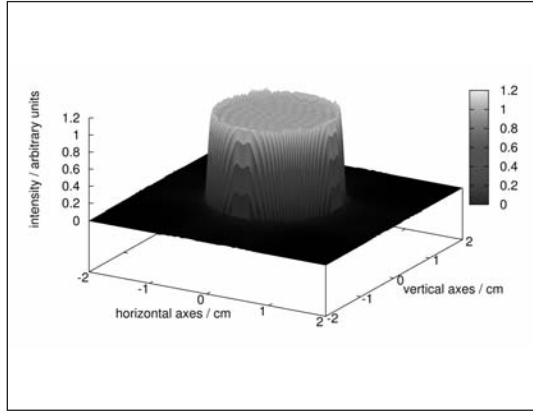


Figure 8: Intensity distribution of an approximated top-hat beam. The order of the highest included mode is 25.

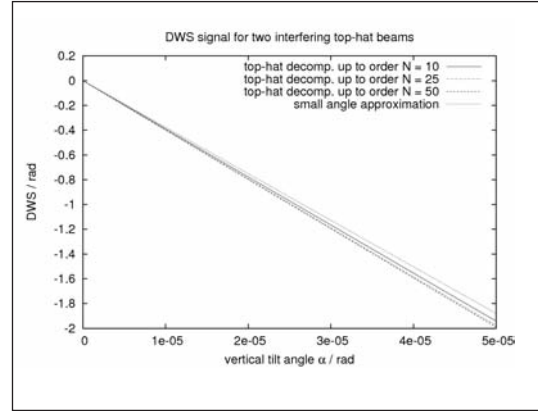


Figure 9: DWS signal for two interfering top-hat beams, comparing different orders of approximation and an approximate analytical result.

ximated fields were calculated and compared to known analytical results. Figure 9 shows the calculated differential wavefront sensing (DWS) signal for two interfering top-hat beams. The signal is shown for three different orders of approximation with the highest mode number being 10, 25 and 50 respectively and an approximate analytical result. The behaviour for small tilts is in good agreement with an approximate analytic result.

Future work will include optimisation of the algorithms for decomposition into Hermite-Gauss modes and the signal calculation by parallelisation and faster algorithms. Also simulation of interferometric setups for future geodesy missions will start.

Phasemeter

The readout of an inter-satellite interferometer is performed by a phasemeter, which measures the phase of the heterodyne beatnote between the incoming and local laser beam using a photodetector. The phasemeter consists mainly of an analogue front-end with anti-aliasing filters, analogue to digital converters and a FPGA, which contains the digital phasemeter core.

Relative satellite movements introduce Doppler shifts on the order of several MHz. The bandwidth of the phasemeter therefore constrains the relative inter-satellite velocity and possible orbit configurations. To address this problem, a phasemeter with a clock speed of 100MHz

and a resulting bandwidth of 1 to 40 MHz was designed and tested, potentially doubling the allowable spacecraft relative velocity for a laser link compared to the previous designs. First results show that the phase-measurement performance is already better than that required for future geodesy missions.

After this proof of principle, a more detailed design of the analogue and digital components of the phasemeter needs to be carried out. Since the core of the phasemeter consists of a digital phase-locked-loop a linear digital model was created and verified by loop simulations. This model allows designing the phasemeter architecture for various noise influences, the required performance and minimal resources. Further investigations have to deal with nonlinear behaviours of the phasemeter and effects like cycle slipping. These studies will partly be performed by simulations and analytical methods. A signal generator, creating electrical input signals based on orbit and noise models, is under design, will be built and used to determine the actual phasemeter performance under realistic conditions.

An inter-satellite interferometer also allows measuring the alignment of the two satellites with very high precision. This technique is called differential-wavefront-sensing and is performed by a relative phase measurement of segments of a quadrant photodiode [REF9]. In future missions it will be used to measure the misalignment with very high precision and control the satellite attitude or beam steering

mechanism. The generation of this signal is also performed in the phasemeter. One potential readout scheme has already been designed and tested successfully in our prototype. Further investigations have to deal with offsets and noise sources in the analogue front-end of the phasemeter. A model for this readout is already included in our detailed digital model. The phasemeter performs also the offset phase locking of the local laser to the received one. This control loop needs to be designed and tested. Analogue counterparts of this are already designed and in use.

Since the phasemeter is working at a clock speed of 100MHz, downsampling of the data has to be performed to a reasonable readout frequency, for example 10Hz. To reduce aliasing, a suitable filter has to be designed and tested. One possible filter design is used in the prototype and further designs are available, but remain to be validated. The connection of a microcontroller to the FPGA allows reducing the amount of filtering in the FPGA, to perform complicated DSP algorithms and include a higher level programming for intelligent operations. One possible candidate for this was evaluated and a new prototype including microcontroller is in development.

Another research field is the acquisition of the link between two satellites, which is a very complex and interesting problem. The phasemeters main task during this is the detection and acquisition of the beatnote signal between the local and remote lasers. Since the local laser frequency is controlled by the pha-

semeter, an intelligent algorithm needs to be designed to scan the degrees of freedom until lock is acquired. The microcontroller will allow developing an algorithm combining the different hardware levels. Such an algorithm can then be tried by applying electrical input signals similar to real mission conditions. The use of optical signals in different interferometer configurations will then be used to test the combination of the abilities mentioned before.

Orbit Simulator

An Orbit Simulation Toolkit (OSTK) for evaluating orbits and constellations for future gravity missions has been developed and tested. Models for Earth's static gravity field like the Earth Gravitational Model EGM08 are usually provided as coefficients of a spherical harmonic expansion. Various models have been implemented in OSTK to facilitate comparison between them. The time-variable components of the gravitational field can be expressed as time-dependent corrections of the spherical harmonic coefficients. The major contributions caused due to ocean tides (models: FES2004 & EOT 08a), atmospheric tides (Bode and Biancale) and solid Earth tides (IERS model) can be taken into account in the computations. Furthermore, the gravitational attraction due to other celestial bodies like Sun, Moon, Venus and Jupiter is non-negligible for precise orbit simulations. In OSTK planetary ephemeris data from JPL DE-405 catalogue is used to consider these perturbations.

Proper modeling of non-gravitational forces like drag and direct solar radiation pressure is sophisticated due to the dependency on environmental parameters as well as the satellites' attitude and surface properties. Presently simplified force models with fixed satellite attitude are used in the simulations. The atmosphere density is estimated using the empirical model NRLMSISE-00, which takes also the geomagnetic and solar activity into account. However, future development focuses on the implementation of 3D satellite models to allow an attitude dependent consideration of drag and solar radiation pressure.

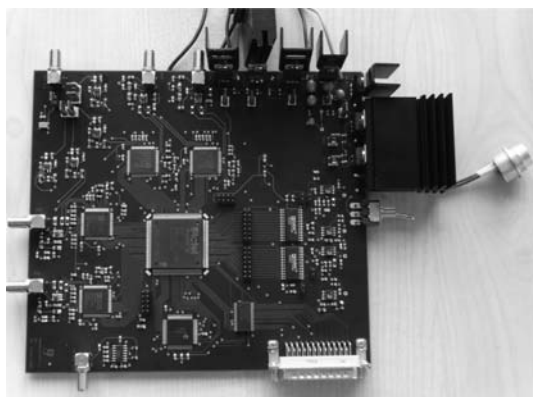


Figure 10: Phasemeter prototype

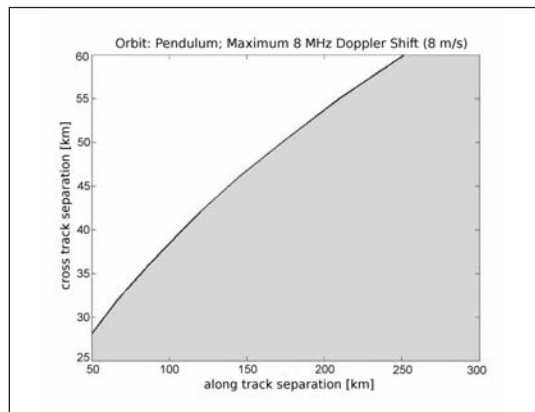


Figure 11: The grey area indicates orbits with Doppler shifts smaller 8 MHz

The orbit propagation itself is computed numerically by Runge-Kutta methods or an Adams-Bashforth-Moulton multistep procedure, though rough orbit estimations can be provided by Keplerian solutions.

The OSTK was used to simulate a satellite pair in pendulum orbit constellations with different cross-track separations, where the relative line-of-sight velocity served as a constraint. In figure 11 different pendulum orbit constellations at 480 km height and relative line-of-sight velocities of less than 8 m/s are shown as shaded area. Another future application can be found in the simulation of interferometer blinding periods by the Sun. Actual simulation results for a GRACE like constellation are being used to compare different approaches for processing GRACE Level-1b data [REF8]. Figure 12 shows the graphical user interface, which is used to configure and control the simulation scenarios as well as to provide visual feedback.

Acknowledgements

The Future Gravity Field Satellite Missions project is part of the R&D-Programme GEOTECHNOLOGIEN. This work was supported by the German Research Foundation (DFG) within the Cluster of Excellence QUEST (Centre for Quantum Engineering and Space-Time Research).

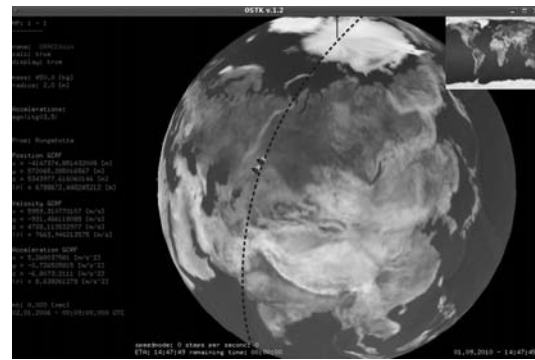


Figure 12: Screenshot of the graphical user interface of the OSTK

References

- [REF1] K. Danzmann and A. Rüdiger, LISA technology—concept, status, prospects, Classical and Quantum Gravity 20, S1 (2003)
- [REF2] D. A. Shaddock, Space-based gravitational wave detection with LISA, Classical and Quantum Gravity 25, 114012 (2008)
- [REF3] P. McNamara, et al., LISA Pathfinder, Classical and Quantum Gravity 25, 114034 (2008).
- [REF4] M. Troebs, Private Communication, 2007.
- [REF5] M. Dehne et al., Laser interferometer for spaceborne mapping of Earth's gravity field, Journal of Physics: Conference Series 154, 012023 (2009)
- [REF6] E. J. Elliffe et al., Hydroxide-catalysis bonding for stable optical systems for space, Classical and Quantum Gravity 22, S257-S267 (2005)
- [REF7] Y. Liu and B. Lü, Truncated Hermite–Gauss series expansion and its application, Optik 117, 437–442 (2006)
- [REF8] M. Naemi et al., Comparing Different Approaches for Processing GRACE Level-1 Data, EGU Gen. Ass., Vienna, Austria, 2010-05-02/0
- [REF9] E. Morrison, et al., Automatic alignment of optical interferometers, Applied Optics 33, 5041-5049 (2004)

New concepts for high precision laser based space metrology

Klein V., Bedrich S.

Kayser-Threde GmbH, München

Introduction

With GRACE in routine operation, multi-spacecraft (S/C) constellations have proven to be a valuable tool for high precision determination of the terrestrial geopotential.

Based on state-of-the-art microwave technology, GRACE is continuously measuring the distance between the two identical spacecraft with an accuracy of some micrometers. However in the light of future GRACE-like missions, an increased accuracy for these distance measurements will be one of the driving operational requirements.

This can e.g. be realized by using electromagnetic radiation with short wavelength: laser light. Laser based distance measurements in space are based on a heritage which is summarized by the exemplary missions below:

EARTH:

- LITE (STS-64), 1994
- GLAS (Icesat), 2009

MOON:

- Lunar laser altimeter (Apollo 15, 16, 17), 1971-1972
- LOLA (LRO), 2009

MARS:

- MOLA (MGS), 1996

MERCURY:

- BELA (BepiColombo), 2013

FUTURE:

- LISA (extreme long range relative distance measurements).

Over the last 5 years, a number of studies have been funded by the European Space Agency; specifically devoted to the determination of **H**igh **A**ccuracy **A**bsolute **L**ong **D**istance **M**easurements (**HAALDM**) between individual spacecraft.

Originally, this theoretical work was supposed to assist multi-spacecraft configurations such as DARWIN or XEUS, where complex and huge optical instruments were intended to be realized as independent spacecraft; floating in a fixed formation.

Unfortunately, these missions had been cancelled, but the remaining laser technology is still available, originally foreseen to monitor the distance and orientation between these modules relative to each other.

These new measurement concepts operate on ultra-short (femtosecond) laser pulses, are based on low power optical fibre configurations and can be realized as compact devices. These lasers are mainly based on Yb:fibre, Er:fibre, Cr:LiSAF, Cr:fosterite or Ti:sapphire gain media.

The implementation of this generation of pulsed lasers is currently regarded as a supplement for existing space borne microwave based technology; however with the potential of exclusive use for future missions.

This new laser technology enables flexible accommodation within the spacecraft, since these laser systems can be mounted at suitable locations and their optical signals can easily be transferred by optical fibres. One of the main advantages is the fact that the measurement can be performed within or in immediate vicinity of the S/C mass centre; at least currently not achievable for microwave systems.

The accuracy of this absolute distance measurement technique has been demonstrated to be better than 50 nm. The repetition frequency of these lasers is relatively high: 100 MHz can be regarded as a standard value, but frequencies up to some 2 GHz are possible with special on-chip technologies.

Figure 1 below is illustrating the basics of such a femtosecond based measurement technique. The laser is feeding its continuous chain of equally separated narrow pulses into one or more optical heads (terminals) which are acting as a combined transmitter / receiver unit. A miniaturized collimating optics inside the terminal is transforming the fibre output into a parallel beam.

Since the laser signal is emitted as a continuous sequence of periodical (equally spaced)

pulses, this version of a HAALDM system is subdivided into independent procedures for (i) fine and (ii) coarse resolution distance measurements.

Fine resolution

During this measurement period, the femtosecond laser is operated in its continuous mode. The intensity of the laser pulses is partially split into the internal reference path, directed onto an internal reference corner cube and then onto an interferometer detector (Michelson arrangement). The corner cube can be moved and positioned with high precision along this optical axis. The other part of the pulse intensities is again fed onto a miniaturized steering optics (MEMS device) and emitted through the

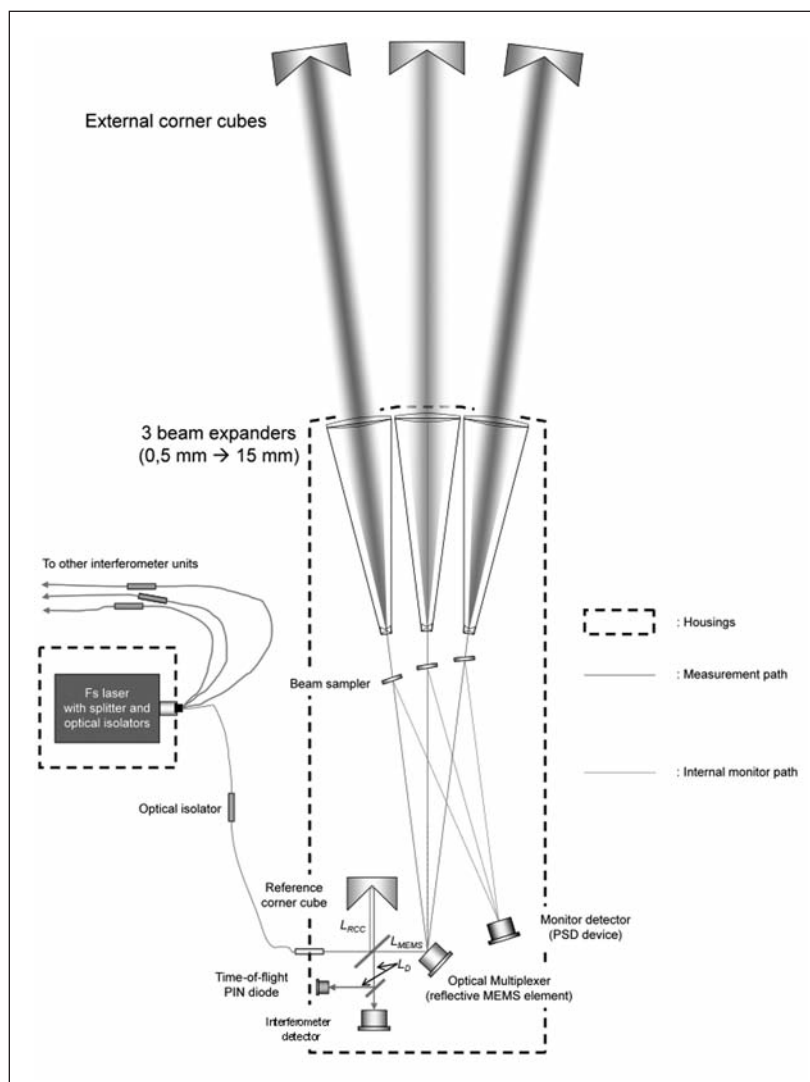


Figure 1: Block diagram of a multichannel **H**igh **A**ccuracy **A**bsolute **L**ong **D**istance **M**easurement (HAALDM) device

transceiver optics onto the remote retro reflector at the opposite spacecraft.

The emitted laser light is expanded in order to reduce its divergence angle and to increase the strength of the optical return signal, reflected by the corner cubes of the opposite spacecraft(s). This transceiver system is sharing the same components for transmitting and receiving the optical signals and is thus saving valuable mass and volume.

As shown above, the modular design of these fibre based compact laser systems allows flexible operation. The geometric steering of the laser pulses into the different measurement directions depends on the actual spatial distribution of the participating spacecraft. It may be necessary that additional pointing optics need to be accommodated in order to cover the required angular range(s).

It should be pointed out that either a single measurement direction or a number of independent directions can be realized; being served by the laser in a rapid closed loop sequence. A setup as depicted in figure 1 comprises three independent measurement directions.

The return signal is fed into the analyzing section, where it is superimposed with the outgoing pulse train onto the interferometer detector. By adjusting the length of the reference arm (from the internal corner cube to the detector) it is possible to co-align the outgoing sequence of laser pulses with the sequence of back scattered pulses. Interferometric and phase analysis of the resulting electric signal finally yields the high resolved distance information (accuracy around 50 nm) within a range of ambiguity, which is determined by the pulse repetition frequency of the laser. An assumed value of 100 MHz is corresponding to an ambiguity range of 1,5 m.

Coarse resolution

In order to obtain useable absolute distance information, the above cited ambiguity range needs to be eliminated. This is accomplished by the emission of a single laser pulse at the beginning of each measurement sequence. For this coarse measurement a high speed electro-

optic switch (pulse picker) behind the femtosecond laser is activated.

Part of the single laser pulse intensity is split into the internal reference path and is detected by the time-of-flight PIN diode. The other part of the pulse intensity is directed onto the MEMS device, where it is diverted into the transmitting optic(s) of the system. A high precision monitor detector is controlling the absolute angular positioning accuracy of the MEMS device.

After being reflected by the external corner cube, the returned laser pulse is recorded by the transceiver optics and also fed onto the time-of-flight PIN diode. A high precision clock determines the duration between transmission and reception of the laser pulse:

$$s = 0,5 \cdot c \cdot t$$

The absolute distance can be determined to an accuracy of some 10 micrometers (time-of-flight). This measurement is eliminating the 1,5 m ambiguity range of the fine resolution procedure as described above. Summarizing the results of the fine and coarse measurement finally yields the highly resolved absolute distance between both spacecraft.

Relative velocities

The above described interferometric analysis of the detector signal can also be used to determine the relative velocity between the participating spacecraft. Based on the »carrier frequency« f_0 of the laser light

$$f_0 = \frac{c}{\lambda}$$

the frequency of the return signal will be shifted in frequency due to the Doppler effect, in case that both spacecraft have a Line-of Sight (LOS) speed component relative to each other:

$$\Delta f = \frac{f_0}{c} \cdot v$$

For velocities $\neq 0$, the electric signal of the interferometer detector will show an AC component with the above given frequency Δf .

A subsequent Fourier analysis of this periodic signal yields the relative velocity v between both spacecraft. Assuming the femtosecond laser is

based on Er:fibre gain material ($\lambda = 1,56 \mu\text{m}$), f_0 is 1,923E14 Hz. A relative velocity of 0,1 m/s is thus generating a beat signal of 128,2 kHz which can easily be quantified via Fourier algorithms. This technique is well proven by numerous heterodyne Doppler lidar systems for atmospheric investigations.

Figure 2 below is representing a scenario, which is currently under investigation within the current study work. This setup could be used to introduce multi-axis laser based distance measurements:

Three identical GRACE-like spacecraft are travelling on two orbits (height: 350 km) with slightly different inclination. During their orbits, S/C 1 and S/C 3 (nominal constant distance: 96 km) are performing yaw oscillations relative to S/C 2 with a maximum cross distance of 43 km. The maximum horizontal yaw angle for S/C 2 (as observed from S/C 1 and S/C 3) will be $41,4^\circ$ and the maximum distance between S/C 2 and S/C 1 or S/C 3, respectively will be 64 km.

By these means, the distance measurements will be expanded perpendicular to the nominal flight track of S/C 1 and S/C 3; generating an increased coverage for the analysis of the terrestrial geopotential.

In order to perform meaningful distance mea-

surements, the line of sight between the optical transmitters and the opposite corner cubes needs to be established for extended periods of time.

For small yaw angles (e.g. $<\pm 5^\circ$) this can be achieved by the implementation of cylinder optics, concentrating the energy of the emitted laser light within a horizontal plane. The control of the measurement direction itself needs to be performed by high precision compact steering optics.

Larger yaw angles cannot be covered by this approach. Gimbal devices as e.g. in use for optical communication between satellites or ground stations are not suitable due to mass constraints and the creation of unwanted momentum around the yaw axis. In fact it appears necessary that the whole spacecraft is performing the required oscillating yaw manoeuvres in order to maintain the optical link between the corresponding spacecraft.

From the current point of view it appears beneficial to combine both options, meaning to use the thrusters of the spacecraft for coarse positioning and the compact internal steering optics of the laser system for fine positioning.

Absolute velocity between the spacecraft

For the above scenario it is possible to combi-

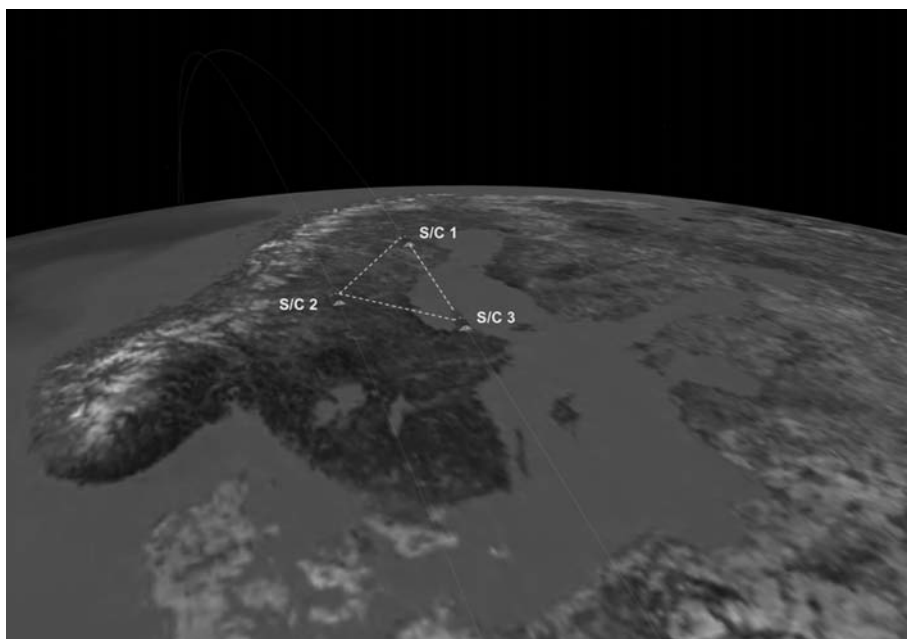


Figure 2:
Three-spacecraft
scenario in pen-
dulum configu-
ration

ne the yaw angle information with the relative LOS velocity information and by basic geometric considerations relative velocities can be transferred into absolute speed information: During increasing yaw angles, the distance between S/C 2 and the other S/C is increasing, resulting in a corresponding absolute velocity and vice versa.

Summary

Theoretical work, laboratory investigations and state-of-the-art laser technology - specifically carried out for space borne high accuracy distance measurements - have reached a level so that femtosecond based metrology can be regarded as a suitable candidate for GRACE-like multi spacecraft missions for future investigations of the terrestrial geopotential. Based on Interferometric analysis of the signals, it appears feasible to combine high resolution absolute distance measurement with the determination of relative LOS velocities between the different spacecraft in general and absolute velocities for specific S/C constellations.

Acknowledgements

The project »Satellitenmissionen – Zukunftskonzepte für Schwerefeldmissionen« is part of the R&D-Programme GEOTECHNOLOGIEN. GEOTECHNOLOGIEN is funded by the German Ministry of Education and Research (BMBF) and the German Research Foundation (DFG), Grant 03G0729E,PT-J, Falk.

High Accuracy Long Distance Measurement with Frequency Combs

Lezius M., Steinmetz T., Holzwarth R.

Menlo Systems GmbH, Am Klopferspitz 19, 82152 Planegg, Contact: m.lezius@menlosystems.com

1. Introduction

The ability to determine absolute distance to an object is one of the most basic measurements of remote sensing. High precision ranging finds important application in future tight formation flying satellite missions, where rapid High Accuracy Absolute Long Distance Measurements (HAALDM) are critical for maintaining the relative pointing and position of the individual satellites, or movable parts therein. Frequency comb lasers [1] have the potential to revolutionize long distance absolute measurements in space by allowing a sub-micrometer accuracy of distances up to, and possibly beyond 10000 km. Comb lasers are pulsed (ultra-fast) mode-locked lasers with a precisely controlled repetition rate and phase of the pulses. Stabilizing the output of a femtosecond laser provides a spectrum of well-defined frequencies, originally used as a ruler in frequency space and to measure differences between optical frequencies. The periodic pulse train of a femtosecond laser generates a »comb« of eq -

ually spaced modes that can be stabilized by a phase-locked loop to a precision radio-frequency reference oscillator (e.g. an atomic clock) to achieve the same timing stability in the optical domain. This optical frequency synthesizer can be used to measure or synthesize not only almost any optical frequency but also to provide a multitude of well-stabilized frequencies for multi-wavelength interferometry and to link the time-of-flight domain of long-distance measurement with the interferometric regime of sub-wavelength accuracy. The basic concept is to use this incredibly regular pulse structure to measure a distance in units of the pulse separation length. Because units of length and time are fixed to each other by the definition of the vacuum speed of light, every timing measurement can be immediately translated into length with the same precision. Because the phase of every pulse is well controlled, one can measure a distance with sub-wavelength accuracy, even for pulses emitted from the laser at different times. In practical terms

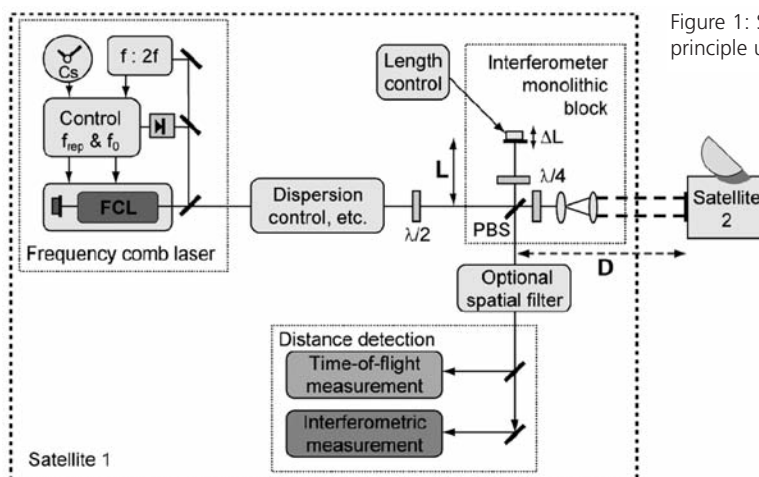


Figure 1: Schematic overview of the HAALDM principle using a frequency comb laser (FCL).

this is achieved by comparing the position and the phase of pulses from the comb laser with those reflected from an object (such as another satellite) in a Michelson-type setup. A generalized scheme of such a technique is shown in Figure 1. Several approaches have been suggested for Michelson-type long distance measurements based on comb lasers and here we have compared their projected performance and suitability for a typical near earth surveying mission. based on a formation flight scenario with up to 500 km distance. Apart from the Michelson itself there would be two major technical components in such a system, namely the comb laser unit itself and the detection unit. The careful selection of these components will be crucial for system performance in outer space.

2. Frequency comb laser source

Regarding the comb laser itself, the most commonly used systems employ Ti:sapphire, Cr:forsterite, Cr:LiSAF, Er:fibre or Yb:fiber gain media. However, there are several examples of other comb sources, most notably Cr:LiSAF and Cr:forsterite, and there are even more potential candidates of laser materials from which frequency combs can be generated. For a comparison of femtosecond comb generators with respect to future space missions, a list of parameters is given below:

- Power efficiency (diode pumped systems)
- Uncritical alignment and robustness (few-element, integrated configuration)
- Possibly all-waveguide configuration
- Compactness (small size and weight, including the pump set-up)
- Low noise operation
- Power scalability (boost amplification)
- Space environment compatible, radiation hardness
- Lifetime of critical elements, e.g. pump diodes, gain materials, actuators ...

A very general comparison of all-solid-state femtosecond sources on a reduced set of criteria, leaving out the aspect of radiation hardness and mission specific aspects which are to be discussed elsewhere, shows that Cr:LiSAF and

erbium as well as ytterbium lasers are particularly promising. The electrical-to-optical efficiency is particularly important for space applications because of limitations in power consumption and heat dissipation. The electrical-to-optical efficiency should be particularly good for directly diode-pumped systems with a low quantum defect, which gives Cr:LiSAF, Er:fibre and Yb:fibre lasers an advantage over Ti:sapphire, Cr:forsterite and Cr:YAG lasers. Also, the pump diode lifetime in the 940-980 nm range is much longer than in the 660-690 nm range. From the engineering point of view, fiber laser oscillators are superior to free space optics oscillators, because of their mechanical stability and optical guidance properties. It appears also obvious that the Ti:sapphire laser, a commonly used laboratory »work horse« for optical frequency combs, is unlikely to be a candidate for space missions, mainly because of the pump wavelength requirement of 532 nm (or 514 nm). Also, the critical alignment makes Kerr-lens mode-locking less attractive than Soliton-SESAM mode-locking. Of the all-solid state bulk lasers, Cr:LiSAF looks more promising

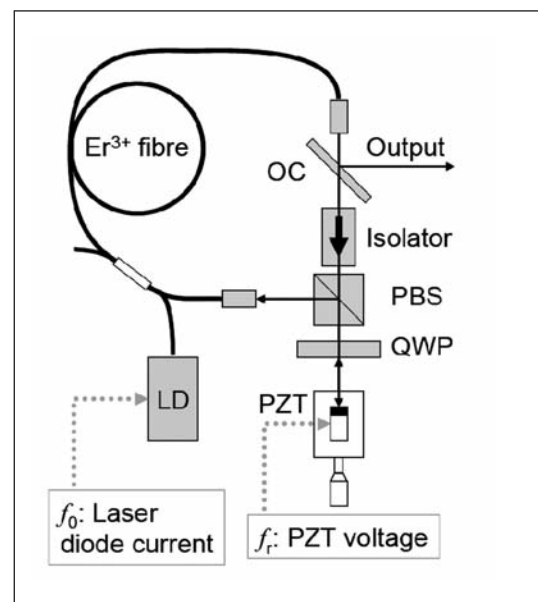


Figure 2: Stabilization of the offset-frequency f_0 and the repetition rate f_t in a standard fiber laser with a free-space section. The cavity length is tuned with a piezo transducer (PZT) and translation stage for coarse adjustment and locking of the repetition rate, while the laser diode (LD) pump power is used for locking of the offset frequency. (OC is the output coupler, PBS a polarizing beam splitter and QWP a quarter-wave plate)

because of direct diode pumping. A portable battery-powered version of this comb generator has already been demonstrated by Menlo Systems. With respect to all-waveguide confined lasers the technical readiness of Er:fiber is presently slightly more advanced than Yb:fiber. We expect, however, that Yb:fiber comb lasers will be developed substantially over the upcoming years, and that they will be finally more attractive to remote space applications because of better efficiency and radiation hardness. A generalized set-up of a typical fiber comb laser is shown in Figure 2.

3. Distance detection scheme

The other choice, that has to be made, is the method for detection of the pulse position beyond the interferometer. For accuracies down to the 10 μm level, it is sufficient to use fast photodetectors and timing detection via electronic mixers for a Time Of Flight measurement (TOF) [2,3]. For sub-wavelength accuracy in the nanometer range we have singled out spectral interferometry (SI) [4,5] (for schematics see also Figure 3) as the preferred method over the alternative method of temporal SHG-interferometric autocorrelation (IA) [6,7]. A direct comparison on various technical specifications between these three different approaches is given in table 1. A further approach based on comb-locked multi-wavelength interferometry has been suggested recently [8], and is based on

the MSTAR technique [9]. Compared to SI, however, the use of stabilized selected wavelengths makes such approaches always inferior to the use of the full comb bandwidth. The advantages of SI over IA include fast single-shot detection, no pulse-overlap required, relaxed dispersion requirements, and a much bigger tolerance for movement during distance measurement on the order of km/s. A possible issue with spectral interferometry is the use of a spectrometer. Because the position is measured using interference fringes in the spectral domain, the accuracy of the spectrometer frequency axis influences the precision of the measurement. However, this only plays a role at the highest precisions ($< 1/10\text{th}$ of the laser wavelength). The required spectrometer accuracy needed in that case (better than a few times 10^{-4}) is still quite feasible. One could for this purpose include in-flight calibration of the spectrometer with the comb laser itself.

Using spectral interferometry, the detector (such as a CCD camera or photodiode array) will record an oscillatory pattern as a function of the frequency components present in the comb pulses:

$$I(\omega) = |E_1|^2 + |E_2|^2 + 2|E_1||E_2|\cos(\omega\tau + \Delta\varphi_{CE} + \Delta\varphi_{noise}) \quad (1)$$

The phase in Eqn. 1 consists of three parts. The distance information is encoded in the first term, $\omega\tau$, where ω is the optical (angular) fre-

Table 1: Comparison of various specifications for FCL based distance measurements

Parameter	Time of Flight	Interference Correlation
Distance range (km)	1,00E+003	1,00E+006
Accuracy (fractional)	1,00E-007	1,00E-014
Maximum relative velocity (m/s)	10	10
Detection technique	Heterodyne	Frequency Doubling
Operating wavelength (nm)	1030 or 1555	1030 or 1555
Operating frequency (Mhz)	100	100
Sampling rate (Hz)	10	1
Technology	absolute	relative
Angular detection	possible	possible
Angular sensitivity (μRad)	10	10
Beam divergence (μRad)	10	10
Transmitter dimension (mm)	50	50
Detector type	2x Si-Pin APD	1x Si-PIN APD or PM
Detector sensitivity (J)	1,00E-012	1,00E-012
Detector sampling	per pulse	per pulse
Metrology/reference points	Fixed to COM	Fixed to COM
Estimated noise (nm/Hz ^{-1/2})	1000 – 10000	100 – 500
Wall Plug Efficiency	TBD	TBD

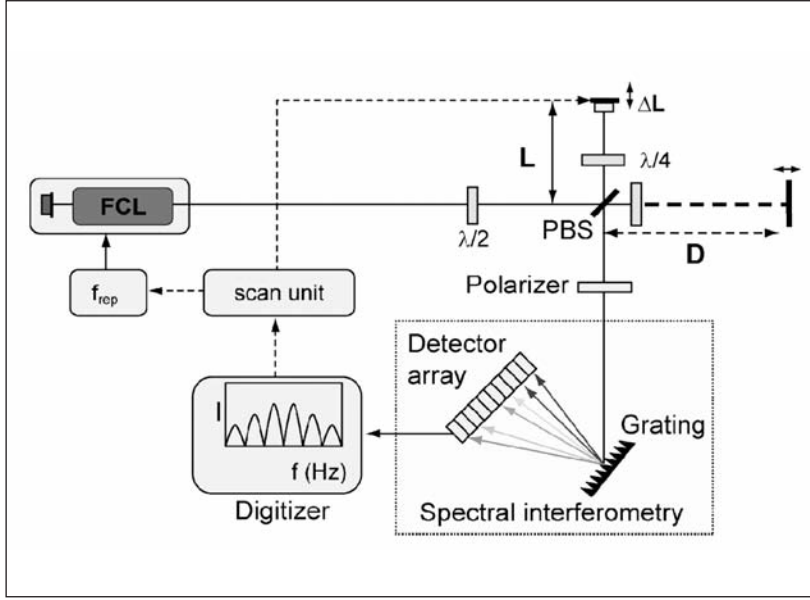


Figure 3: Spectral interferometry length measurement scheme.

quency, and t is the time delay between the arrival of the pulses. The delay can be written as $t=2(D-L)/c$, if the time is taken modulo the repetition time of the comb laser. The second term accounts for the carrier-envelope phase shift between the pulses that interfere, while the third term represents the noise on the phase of the pulses. The delay dependent phase term can be rewritten:

$$\varphi(\omega) = \omega \left[\frac{2(D-L)}{c} \right]_{\text{mod}(1/f_{\text{rep}})} \quad (2)$$

It means that the distance can be obtained by determining the slope of the phase as a function of the optical frequency. In Figure 4 the principle for a distance measurement is demonstrated by means of a simulation. Part (A) shows the raw data in the form of the recorded spectral fringes. The first step involves Fourier-transformation (FFT) of the interferogram to the time domain, as shown in part (B) of Figure 4. The time-domain representation has two sidebands of which only one is shown in here, and a central component at $t=0$. If the spectrum is smooth enough compared to the oscillation period of the spectral fringes, then the sidebands are well separated from the central peak. This condition is essential for a proper reconstruction of the phase evolution as a function of the frequency. One practical consequence of this measurement scheme is that

the pulses do not need to overlap, and that the interference pattern can be obtained instantaneously without scanning the reference arm or f_{rep} of the comb laser. Variations in the repetition rate have therefore far less consequences for spectral interferometry than for temporal interferometry because CCD and diode array detectors can capture the whole interferogram at once. It merely results in a different reading for the position for each measurement. After analysis of the distance from the pattern, the results can be averaged, so that the long-term stability of frequency comb lasers can still be exploited fully.

An interesting approach has been recently suggested by Coddington and coworkers [5]. They measured the spectral interference by use of two coherent frequency combs with slightly detuned repetition rate. In this way they continuously scan one comb over the other and achieve some nanometer level of precision with an ambiguity range of 1.5 m within 60 ms, at low light levels and with high immunity to spurious reflections. It is suggested that the ambiguity range could be easily extended to 30 km, by use of a smaller frequency difference. If another factor 10 in the ambiguity range could be achieved, remains to be determined. An ambiguity range of 500 km would make the system very well adapted to formation

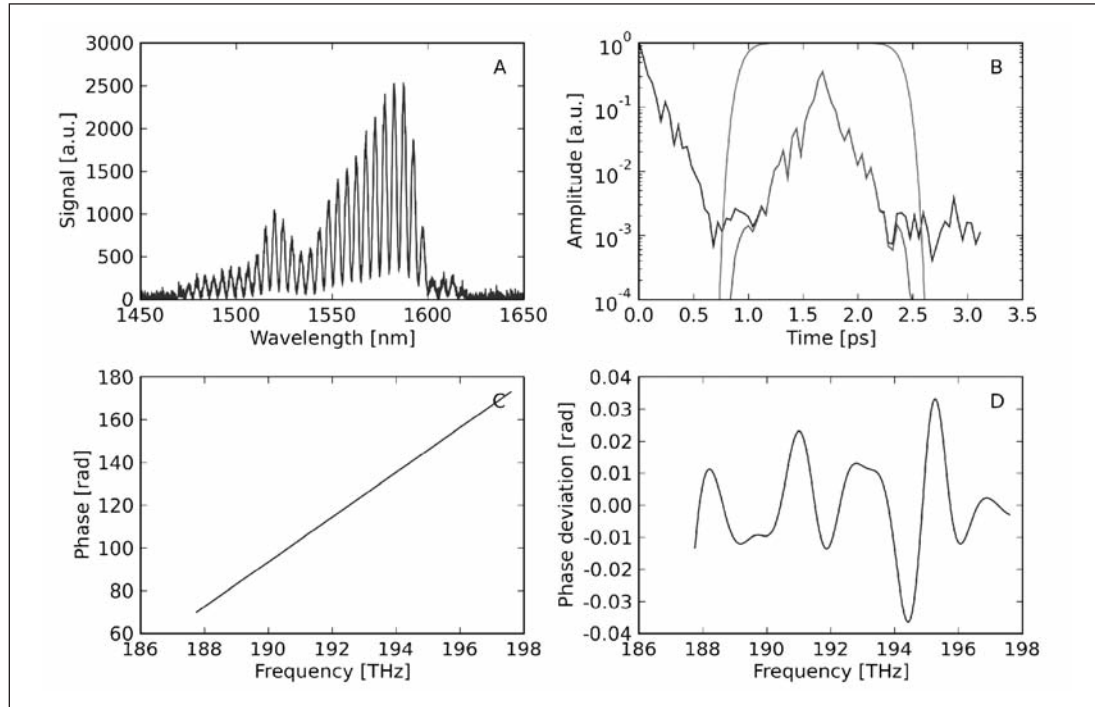


Figure 4: (A) Simulated spectral interferogram, together with (B) the time-domain analysis (FFT from panel A), and (C) the reconstructed phase from which the pulse distance is extracted (Eqn. 2), and (D) the deviation of the phase from a linear fit.

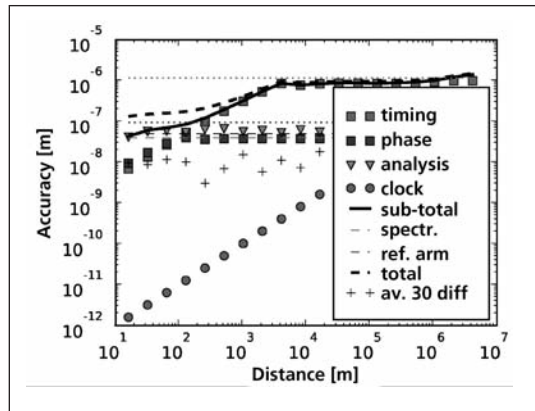


Figure 5: An example of the full analysis of the single (individual) measurement accuracy of HAALDM with a RF-stabilized fibre comb (see text for an explanation of the symbols and lines).

flight applications. In addition, the time resolved signal of the dual comb method allows for measurements between multiple reference planes in a single beam path. This host of features is presumably unavailable in any other single system discussed so far.

As a main result we have recently developed a software in order to be able to fully simulate SI

based distance measurements, taking into account the properties of any selected laser system and various other effects. Here we show the result of a HAALDM system based on an Er-fibre comb. The total analysis can be quite complicated, as can be seen from an example of the full analysis in Figure 5. The individual uncertainty components are: 'timing': uncertainty due to pulse timing noise; 'phase': likewise due to pulse phase noise; 'analysis': accuracy due to the evaluation of the interferogram; 'clock': frequency reference induced; 'sub-total': sum of the effects mentioned above; 'spectr.': induced uncertainty due to spectrometer calibration; 'ref. arm': uncertainty of the reference arm in the Michelson interferometer; 'total': all components combined; '+': distance error from the interferogram analysis when 30 measurements are averaged. Furthermore, two dotted lines are visible that indicate the maximum expected error based on single pulse timing deviations (upper dotted line), and phase fluctuations of the pulses (lower dotted line). As a major result of our analysis we find a step-wise increase in the total error indica-

ting the critical distance where the contrast of the interferogram is no longer sufficient (due to accumulated timing and phase noise) to perform a proper analysis. This timing and phase noise ultimately stems from timing jitter of the comb itself, and depends on accuracy of the RF clock that locks the comb laser repetition rate. In our study we have assumed a typical RF clock precision of 10^{-13} . Better results can be obtained with high precision frequency standards from atomic or quantum clocks (10^{-16} .. 10^{-18}). Present ground based clocks are reaching an accuracy of 10^{-17} , corresponding to sub- μm accuracy at distances up to 109 m. The technical development of precision frequency standards for space applications is currently under way. Nevertheless, from our simulations we find that even the simple additional introduction of a high-finesse cavity into the comb laser may be sufficient to improve the timing and phase noise to an accuracy level that would be reaching 50 nm at 10000 m.

3. Conclusion

We conclude that frequency combs can provide unprecedented absolute length measurements on a sub-micrometer scale over a wide range of distances. We have reviewed different schemes for measurements, and selected spectral interferometry as the method of choice for long distance measurements in space. Of the two main methods to obtain sub-wavelength resolution, temporal and spectral interferometry, the later one has the big advantage that no scanning or overlapping pulses are required. Because the spectral interferogram can be recorded single-pulse if necessary, it also allows to measure fast changing distances (e.g. between two or more moving satellites). From our simulations of spectral interferometry which are presented here we conclude that the uncertainty in determining a distance of 500 km could be better than 50 nm, provided that sufficiently accurate RF clocks are available in space.

Acknowledgements

The project »High Accuracy Long Distance Measurement with Frequency Combs« (Grant 03G0729F) is part of the R&D-Programme GEOTECHNOLOGIEN. GEOTECHNOLOGIEN is funded by the German Ministry of Education and Research (BMBF) and the German Research Foundation (DFG).

References

- [1] Udem T., Holtzwarth R., Hänsch TW. Nature 416, 6877 p233 (2002)
- [2] Minoshima K and Matsumoto H, Applied Optics 39 (30) 5512 (2000)
- [3] Matsumoto H, Minoshima K, Telada S, Proc SPIE 5190, 308 (2003)
- [4] Ki-Nam Joo and Seung-Woo Kim, OpticsExpress 14(13) 5954_ (2006)
- [5] Coddington, Nature Photonics 3,351 (2009)
- [6] Jun Ye, Optics Letters 29(10) 1153 (2004)
- [7] Cui M., Schouten RN, Bhattacharya N, van den Berg SA, J. Eur. Opt. Soc. Rapid Publ. 3, 08003 (2008)
- [8] Hyun S.,et al., Manufact. Techn. 59 (2010) 555-558
- [9] Lay OP, et al. Optics Letters 28(11), 890 (2003)

Quantum sensors for Earth observation

M. Gilowski and E.M. Rasel

Institut für Quantenoptik, Leibniz Universität Hannover, Welfengarten 1, 30167 Hannover, Germany

Abstract

We report on our development of various kinds of quantum sensors based on matter-wave interferometry for precise inertial sensing of Earth's rotation rate and gravity. By manipulating cold or ultra cold atoms with coherent light fields we realize several experimental platforms for the detailed investigation of different interferometer types and of their key technologies. In an atomic gyroscope using cold Rubidium atoms we demonstrate a sensitivity for rotations of 6×10^{-7} rad/s. In an atomic gravimeter, which is under construction, we study the source system based on ultra cold atoms in a Bose-Einstein condensate. Finally, a miniaturized and robust experiment using ultra cold atoms in a free fall environment is realized as a test-bed for matter-wave interferometry on long timescales. These experiments pave the way in the direction of utilizing the technology of matter-wave interferometry for future space applications.

Introduction

Atomic quantum sensors are a key-technology for the ultra-precise monitoring of accelerations and rotations. These sensors evolved from a new kind of optics based on matter-waves rather than light-waves. Matter-wave optics is still a young, but rapidly progressing science which recently generated sensational Nobel-prize awarded inventions such as laser cooling and atom lasers [1,2].

The applications of atomic quantum sensors are truly interdisciplinary, covering diverse and important topics such as tests of fundamental physics, the realization of SI-units, prospecting for resources, GALILEO technology, environment monitoring and major Earth-science the-

mes [3-8]. This field represents an emerging area of science quantum engineering, with a high potential for a future technology and multidisciplinary applications. Thanks to an impressive evolution and remarkable inventions, the *ultimate potential* of matter-wave sensors is still entirely open. For the closely related field of atomic clocks, the growth in performance was exponential during the last decades! This is the reason, why matter-wave sensors are considered as one of the *most promising fields to progress in metrology and fundamental tests*.

Atomic gyroscopes and gravimeters provide a new tool for the precise detection of tiny forces. The outstanding feature of these sensors is the precisely known scaling factor: there is no need for calibration which predestines these sensors for inertial references and for applications in the Système International.

The following report summarizes our activities and achievements in the field of matter-wave interferometry. We will describe the features of this technology by presenting three experiments which point out the development of atomic inertial sensors. The first one is an atomic gyroscope for the high-precision measurement of rotations. The second one is a dual atomic gravimeter, which is under construction and which provides a source of ultra cold atoms. The third one is a miniaturized transportable experiment with ultra cold atoms in a microgravity environment, which is performed in the drop tower facility (ZARM) in Bremen. These experiments are steppingstones in the direction of the realization of future inertial atomic sensors with sensitivities compared or even beyond current state-of-the-art devices.

The gyroscope

The interferometric measurement of rotations is based on the Sagnac-effect [9], which indicates that a phase shift is induced between two interferometer paths which enclose an area A , due to a rotation with the angular velocity Ω . This phase shift is then given by $\delta\phi_{\text{rot}} = 4\pi EA\Omega/hc$, where E is the energy of the wave, h the Planck's constant and c the speed of light. Since this relation is also valid for light as well as for matter-wave interferometers, the high potential of gyroscopes based on atoms is obvious. By comparing the phase shifts using the energies of matter and visible light, an improvement in the order of 10^{11} for atom interferometers is in principle possible. Furthermore, the sensor is also sensitive to accelerations [10]. In order to distinguish between phase shifts due to rotations and accelerations the sensor consists of two interferometers allowing a differential measurement [10]. The basic schematic of the atomic gyroscope is sketched in Fig. 1.

Two identical atomic sources [13] emit atoms on flat parabolic trajectories into the interferometer chamber, but with opposite launch directions. Each source consists of a two-dimensional magneto-optical trap (2D-MOT) loading

a subsequent 3D-MOT with a high flux of several 10^9 at/s. Using the moving molasses technique 10^8 atoms with a forward drift velocity of 2.8 m/s and a temperature of 8 μ K are launched in each interferometry pulse. In a next step the atoms are state- and velocity-selectively transferred into the magnetically insensitive hyperfine state $F = 1$, $m_F = 0$ (where F and m_F are the quantum numbers for the total angular momentum and the Zeeman sublevel, respectively) via a multi-stage preparation using precisely controllable laser manipulation.

In the interferometry section a symmetric Ramsey-Bordé interferometer configuration is realized by applying four so called $\pi/2$ -light pulses [14]. This coherent beam splitting processes are based on a Raman-transition between two hyperfine states which form the ground states of the interferometer. With these light pulses the matter-wave is split, redirected and finally recombined. In this way, the created interferometer paths enclose an area of 8.6 mm² leading to a high sensitivity for the Sagnac-effect. In this interferometer configuration phase shifts imprinted during the interferometric cycle are translated into a change of the distribution in the two ground states [14]. Thus, we finally obtain the phase shift of each interfero-

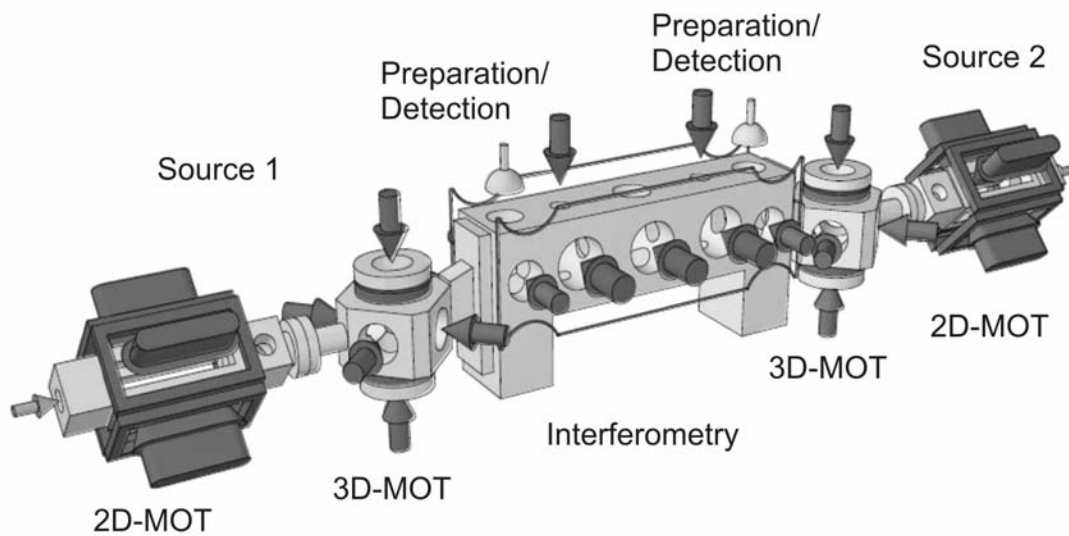


Figure 1: Schematic overview of the gyroscope with its key-element sections. Laser beams for cooling and trapping as well as for the preparation, the interferometry and the detection process are represented by the arrows. More details can be found in reference [11,12].

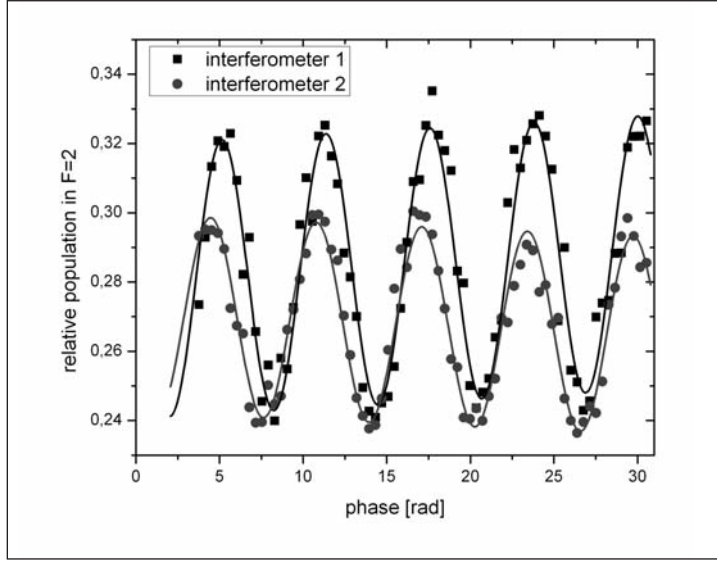


Figure 2: The Interference fringes of the two interferometers are obtained by sweeping the phase of the beam splitting light field before the last pulse is applied.

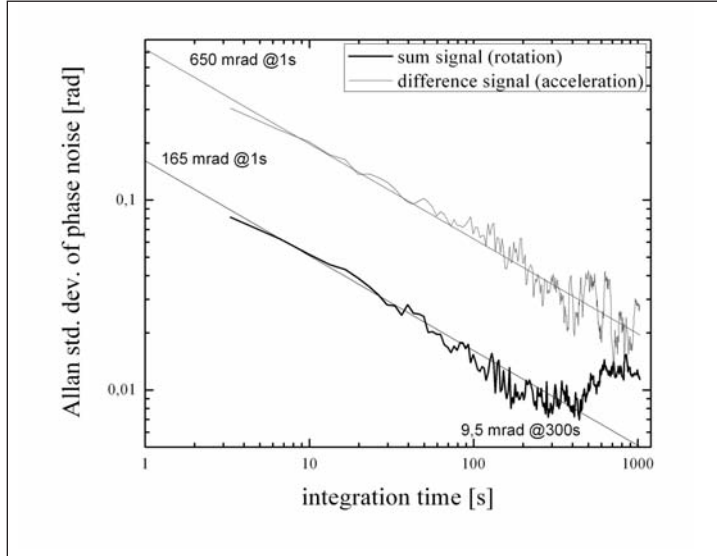


Figure 3: Allan standard deviation of the combined signals of the two interferometers.

meter by using a state-selective fluorescence detection, applied after the interferometry sequence. We detect in the gyroscope approximately several 10^7 atoms.

Typical interference patterns of the two interferometers of the gyroscope are shown in Fig. 2. We reach a contrast in the four pulse geometry of 11% and 16%. The reduced contrast can be attributed to a reduced efficiency of the beam splitting process, which depends on the one hand on the temperature and the spatial width of the atoms and on the other hand on the spatial intensity profile of the beam splitting light field. A further selection of velocity classes in the preparation stage will in future

gain the contrast of the interferometer signal. Furthermore, a reduction of the initial temperature of the ensemble would increase the efficiency of this process and thus motivates the use of ultra cold atoms (see below). The difference in contrast can be attributed to the alignment of the spatial interaction position, which is different for the four beam splitting pulses for the two interferometers, respectively.

Finally, we can infer the rotation sensitivity of the gyroscope by measuring the phase noise of the two interferometers. In Fig. 3 the Allan standard deviation for the combined signal of the two interferometers is shown. Here, the

rotation signal can be inferred from the sum of the two interferometer signals whereas the acceleration might be calculated from the differential signal. It is clearly visible that vibration noise coming from accelerations is highly suppressed due to the dual measurement scheme. After averaging the combined signal over 300 s a phase noise of 9.5 mrad is reached. This corresponds to a reached sensitivity in the gyroscope of 6×10^{-7} rad/s which is two orders of magnitude below the Earth rotation rate.

Currently, this sensitivity is limited by the noise of the detection process as well as inertial noise. The implementation of an optimized detection system and an improvement of the vibration isolation are under way and will further improve the sensitivity by at least one order of magnitude on the short-term scale. In combination with novel techniques like the transfer of large photon momentum leading to a larger transversal atomic velocity and thus to larger enclosed areas [15], the aimed sensitivity might reach the 10^{-10} rad/s level for integration times of 1000s. A further optimization is the reduction of the atomic temperature, which besides the increasing of the beam splitter efficiency would decrease systematic effects coming for instance from wave front distortions of the beam splitting light fields. The realization of such an ultra cold atomic source for atom interferometry is described in the following section.

The ultra cold atom source

In a second experiment a dual gravimeter based

on matter-wave interferometry is setup for the test of the Equivalence principle. For this purpose the free fall of two atomic species, Rubidium and Potassium, will be compared. In this experiment the aimed shot-noise limited sensitivity is 10^{-9} g. This corresponds to the highest sensitivity for the test of the Equivalence principle with laser cooled atoms so far [12].

One of the essential aspects of the dual gravimeter is the source of ultra cold atoms to reach the demanded accuracy. The first step in this direction was reached by creating a Bose-Einstein condensate (BEC) of ^{87}Rb atoms in a near-infrared single beam optical dipole trap (ODT). The ODT is formed from laser light with a wavelength close to $2 \mu\text{m}$. Furthermore, an additional constant confinement in the axial direction of the trap is provided by a magnetic quadrupole field with a rather weak gradient of 10 G/cm.

The experimental description starts from a double MOT source system, which is related to the one explained in the above section. Here, 5×10^8 atoms are trapped in the 3D MOT. In the next step, 2×10^6 atoms are transferred into a single beam ODT at an initial temperature of 35 μK and a corresponding initial phase space density of about $1\text{--}2 \times 10^{-5}$. By a following reduction of the ODT laser intensity at constant magnetic field gradient the evaporative cooling is achieved. This allows for the creation of a nearly pure condensate with 10^4 atoms every 20 seconds as it is shown in Fig. 4.

Furthermore, before starting the evaporation sequence laser cooling in the ODT provides atomic samples with very low initial tempera-

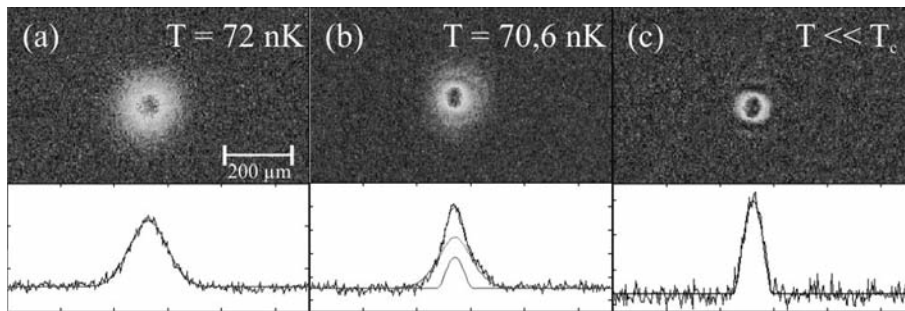


Figure 4: Absorption images of the atomic cloud in the weak hybrid trap at different temperatures and their corresponding density profiles after a time-of-flight of 21 ms, showing the phase transition from a thermal gas in (a) to a bimodal density distribution in (b) to a quasi pure BEC with 10^4 atoms in (c).

tures of about 2 μK and initial phase space densities as high as 10^{-2} . These very favorable initial values offer much potential for further improvement in the production of a BEC with respect to particle number and repetition rate. An adaption of the laser intensity ramp for forced evaporation to these strongly improved initial conditions offers great potential for this method to create BECs with particle numbers of more than 10^5 atoms with a substantially improved repetition rate. Moreover, this source scheme demonstrates a matter-wave interferometer source using ultra cold atoms.

Besides the ultra cold atoms for improving the accuracy of a matter-wave interferometer long interrogation times are preferable, since the induced inertial phase shifts in a matter-wave interferometer scale quadratically with the interrogation time for instance in a Mach-Zehnder configuration [14]. If not only the atoms but also the whole experiment itself would be in a free fall, the interrogation time could significantly be extended. And this is one of the motivations for the following experiment.

The BEC in microgravity – The QUANTUS project

The QUANTUS project (QUANTen Gase Unter Schwerelosigkeit) started as a feasibility study of a compact, robust and mobile experiment for the creation of a BEC in a weightlessness environment [16,12]. It was the drop tower in Bremen, which was chosen as the microgravity environment, since it provides both good accessibility and a better quality of microgravity than other platforms. This makes the experiment an ideal test bed for future space based missions with ultra cold atoms.

The capsule, which is released from the top of the evacuated tower, contains a complete BEC experiment as it is shown in Fig. 5. The realization of this experiment required a massive miniaturization of the setup, which was made possible by the development of atom chips [17]. We combine this technology with a mirror MOT, which is loaded with roughly 1.3×10^7 atoms of ^{87}Rb from the background gas.

After 10 s of loading, the capsule is released and is free falling over a time of 4.7 s. Within this time a BEC of about 10^4 atoms is produ-

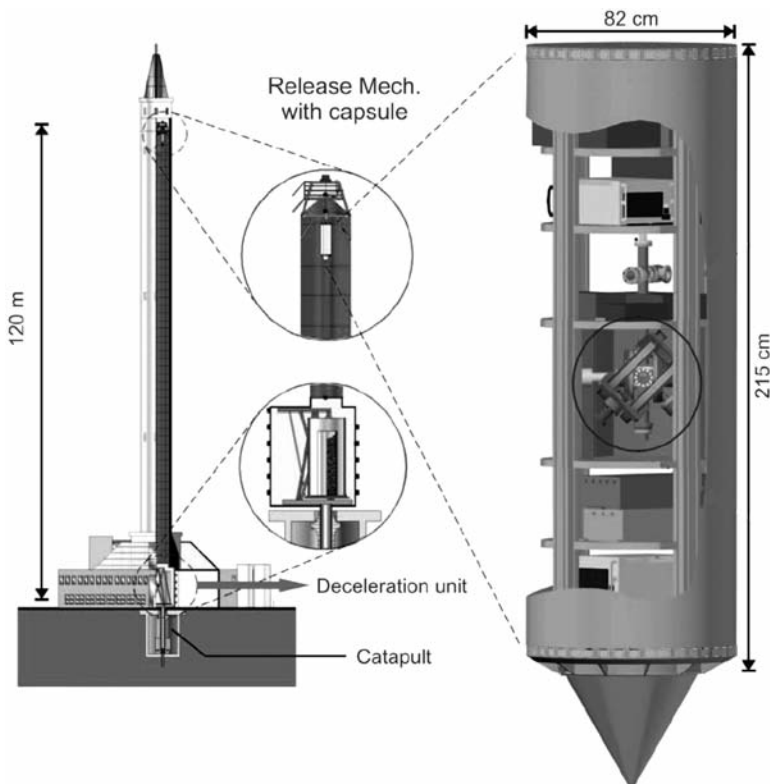


Figure 5: ZARM drop tower facility in Bremen (left). Capsule containing the BEC experiment (right). The future QUANTUS-II capsule will be launchable from a catapult. With this, the time of free fall can be almost doubled.

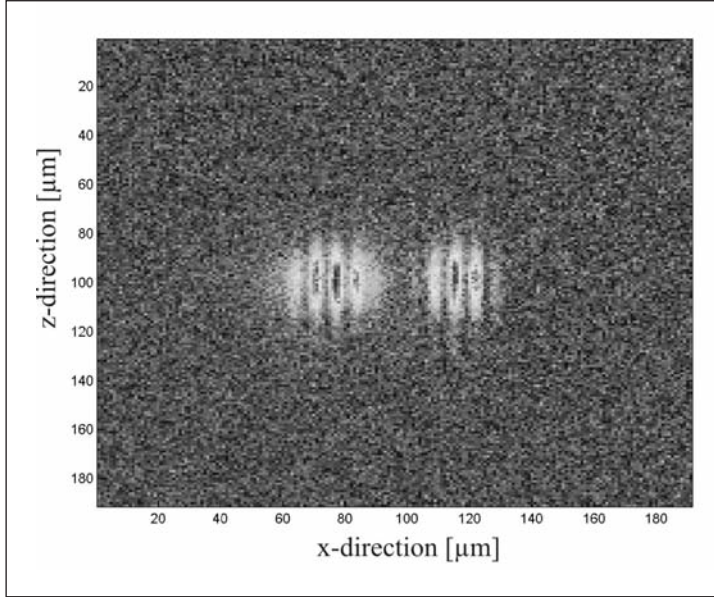


Figure 6: Interference pattern of a BEC in a two pulse interferometer on ground.

ced by the following procedure [16]: The atoms are further cooled in optical molasses and transferred to an Ioffe-Pritchard trap on the chip. By compressing the trap and radio frequency-induced evaporation a condensate in the hyperfine state $F = 2$, $m_F = 2$ is obtained. Finally, after switching off the current of the atom chip the BEC is released and can be observed by using the absorption imaging technique. During the long expansion over 1 s, the atoms form a giant coherent matter wave that is delocalized on a millimeter scale.

We have performed more than 190 experiments to demonstrate the feasibility of coherent matter-wave experiments in microgravity, thus enabling the realization of a robust atomic source, which is required for the implementation of an atom interferometer.

First interferometer experiments with this device on ground have already been demonstrated and will be performed in microgravity by the end of this year. Here, Bragg scattering is used as the coherent beam-splitting and mirror process. On ground, interferometer sequences in the Mach-Zehnder and Ramsey geometry have been realized so far (see Fig. 6).

The former being the candidate for high sensitivity measurements at long times while the latter is our candidate for coherence measurements. Since, our investigations aim at explo-

ring the usability of BEC as a source for matter-wave interferometry, the coherence of the chip-based BEC is an important property to be studied. Furthermore, the precise preparation in the nK regime developed in the expansion campaigns has to be proven sufficient for interferometry needs in increasingly long interferometer sequences. Here, the reproducibility of the interferometer over multiple drops is a major challenge which will be met with a more suitable choice of initial state. A coherent transfer of the BEC into the magnetically insensitive hyperfine state $F = 2$, $m_F = 0$ would avoid the influence of parasitic magnetic effects.

The implementation of this transfer is currently under way. The design and potential of this technique will be studied in various experiments in 2011. The results and experience will be extended to two species (Rubidium and Potassium) in a new chip based drop tower experiment which is under construction and provides improved atom flux and preparation.

Outlook

The reported activities on atomic quantum sensors in the Institute of Quantum Optics show the enormous potential of these devices for the future application in Earth observation and fundamental physics. The presented atomic sensors serve as a platform for experiments aiming

at studying the relevant systematic errors and limitations and in the next period to push these devices beyond current state-of-the-art. Furthermore, tests of new quantum sensor concepts and strategies (continuous cold atom sensors, sensors based on degenerate ensembles, novel topologies) are on the way.

Another important aim is a direct comparison of different atomic inertial sensors, combined with the use of the best currently available geophysical models for facilitating a precise evaluation of these instruments. The cooperation of experts on atom interferometer sensors with experts from the field of Earth observation will also permit the design and development of improved inertial quantum sensors specifically tailored for demanding applications in this field. The resulting advanced sensors will then offer many more exciting possibilities. In the long run the future devices will complement and can even replace the classical ones for monitoring mass changes in active regions (e.g. volcanoes) and also help to discriminate between man-made and natural effects (e.g. changing water reservoirs).

The isolation of the sensor from Earth's environment, will finally enhance the potential of matter-wave interferometry. In future satellite missions such instruments may test gravity fields as gravimeters or gradiometers with high accuracy. The in this report presented experiments are studies of this novel and promising approach.

Acknowledgements

The project »Zukunftskonzepte für Schwerefeld-satellitenmissionen« is part of the R&D-Programme GEOTECHNOLOGIEN.

GEOTECHNOLOGIEN is funded by the German Ministry of Education and Research (BMBF) and the German Research Foundation (DFG). We also thank the center for quantum engineering and space time research (QUEST). Furthermore, we are grateful to the German Aerospace Center (Deutsches Zentrum für Luft- und Raumfahrt e.V. – DLR).

References

- [1] W.D. Phillips, Rev. Mod. Phys., Nobel Lecture, 70, 3, (1998).
- [2] W. Ketterle, Rev. Mod. Phys., Nobel Lecture, 74, 4, (2002).
- [3] M. Cadoret, et al., Phys. Rev. Lett., 101, 230801, (2008).
- [4] A. Bertoldi et al., Eur. Phys. J. D, 40, 271, (2006).
- [5] P. Cheinet, et al., Dig. Conf. Precision Electromagnetic Measurements (CPEM) 2004, London, U.K., 60-61, (2004).
- [6] D. S. Durfee, et al., Phys. Rev. Lett., 97, 240801, (2006).
- [7] Dimopoulos, et al., Phys. Rev. Lett., 98, 111102, (2007).
- [8] G.M. Tino et al., Nuc. Phys. B, 166, 159-165, (2007).
- [9] M.G. Sagnac, Compt. Rend. Des Sc. D. l' Acad. D. Sc., 157, 1410, (1913).
- [10] T.L. Gustavson, et al., Class. Quantum Grav., 17, 2385, (2000).
- [11] T. Müller, et al., Eur. Phys. J. D, 53, 273–281, (2009).
- [12] The homepage of the Institute of Quantum Optics, <http://www.iqo.uni-hannover.de>, (August 2010).
- [13] T. Müller, et al., Phys. Rev. A, 76, 063611, (2007).
- [14] Ch.J. Bordé, Phys. Lett. A. 140, 10-12, (1989).
- [15] H. Müller, et al., Phys. Rev. Lett., 100, 180405, (2008).
- [16] Zoest, et al., Science 328 (5985), 1540-1543, (2010).
- [17] W. Hänsel, et al., Nature 413, 498, (2001).

Environmental Disturbance Modelling for Future Gravity Missions

Pelivan I., Theil S.

DLR Institute of Space Systems, Robert-Hooke-Str. 7, D-28359 Bremen, Email: Ivanka.Pelivan@dlr.de

1. Introduction

In order to carry out comprehensive simulation analyses for future gravity missions, a closed loop simulation that can be parameterized to different reference scenarios and environmental conditions is being established. Thereby, various mission concepts can be evaluated and compared against each other. A generic approach in mission modelling allows the consideration of various disturbance sources that are also subject of the analysis. Starting with initial disturbance modelling of external effects based on a first concept idea, the estimation of internal and external disturbances and disturbance coupling can be refined. This refers to external effects resulting from the spacecraft environment: A satellite in orbit is subject to atmospheric drag in low Earth orbit and electromagnetic radiation as well as magnetic field. Internal disturbances due to instrument noise also have to be taken into account.

In this paper, the approach to modelling of environmental forces and torques for future gravity missions is lined out in sections 2 and 3. The integration of the environment into a closed-loop simulation is considered in section 4 together with a few words on simulation analysis for future gravity missions. Section 5 concludes with a summary and an outlook towards modelling of the next disturbance class, the internal noise from controller components.

2. Environmental Modelling

For spacecraft orbiting the Earth, orbit disturbances result primarily from gravity, atmos-

pheric drag, solar radiation and magnetic field. For environmental modelling within this project, the library modules from HPS (High Performance Satellite Dynamics Simulator), developed in collaboration with ZARM, University of Bremen, are used. The library includes a comprehensive collection of environmental models, a dynamics sub-library, several actuator and sensor models, libraries for coordinate and date transformations and general mathematical calculations. Furthermore, a surface forces library module is provided which delivers the normalized force and torque that acts on a satellite due to a disturbance source like solar radiation depending on the incident direction, for example the Sun direction. The functionality of this module is outlined in section 4. Further information on all modules and application can be found in the HPS documentation.

All modules can be used in MiL (model-in-the-loop) and SiL (software-in-the-loop) applications, and several modules can be integrated into HiL (hardware-in-the-loop) environments. The gravity library contains three models for the calculation of gravitational acceleration and gravity gradients. A simple model including the first six zonal Earth harmonic field coefficients is available next to two higher order models up to degree and order 360 (customizable to higher order for the Earth Gravity Model 2008). The higher order gravity models distinguish in the way singularities, especially at the Earth's poles, are treated.

The atmosphere library contains the Harries-Priester, the NRLMSISE00, and the HWM93

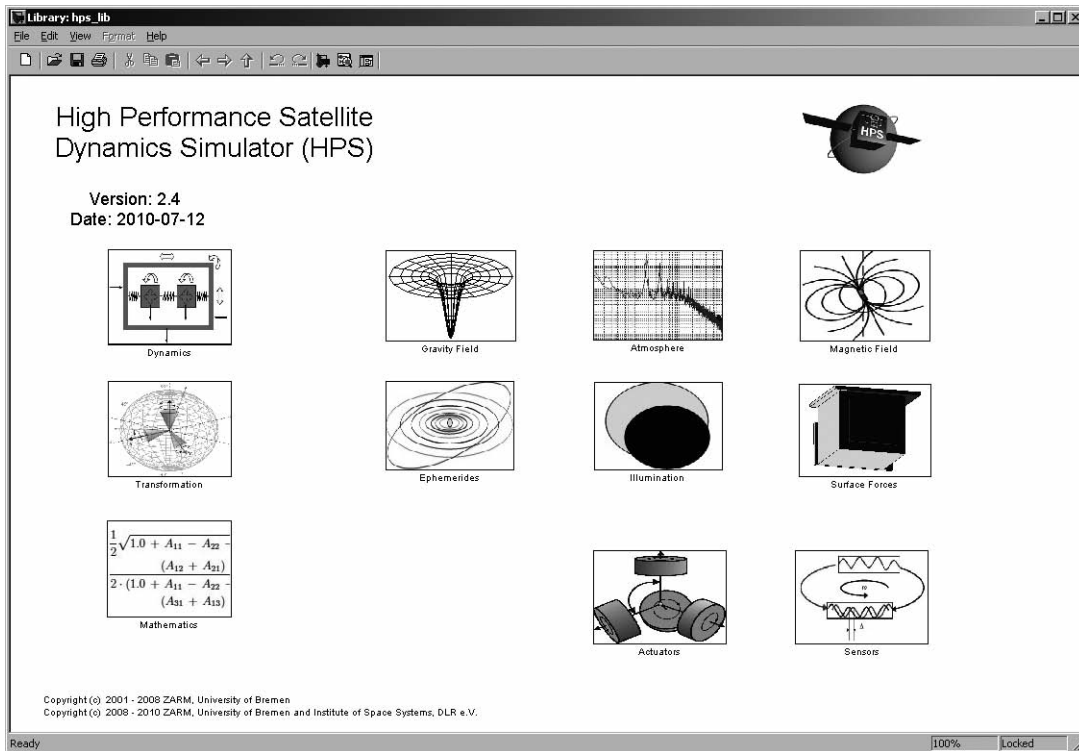


Figure 1: The High Performance Satellite Dynamics Simulator

wind models. The Harris-Priester density model is a simple model to determine the mass density of the upper atmosphere at a given point. It is based on the properties of the upper atmosphere as determined from the solution of the heat conduction equation under quasi hydrostatic conditions. The NRLMSISE00 is an empirical model for the atmosphere extending from the ground to the exosphere.

With the IGRF11 (International Geomagnetic Reference Field, 11th generation) the latest version of a standard mathematical description of the Earth's main magnetic field is incorporated. Furthermore, the magnetic field library contains the Tsyganenko models which are semi-empirical best-fit representations for the magnetic field, based on a large number of satellite observations.

The illumination library includes models for eclipse, solar radiation pressure, and albedo. The eclipse module can be used to determine the shadowing conditions for a constellation of three objects. For a spacecraft orbiting the Earth, the different eclipse conditions range from no eclipse to partial eclipse, annular eclipse, and total eclipse.

Two source descriptions for the calculation of the solar radiation pressure are provided, that is a point-like and a finite-disk source. The solar radiation pressure is computed considering the solar flux at average Earth distance from the Sun, and the distance between the satellite and the Sun.

The solar radiation reflected by the Earth, the Earth albedo, is calculated in the albedo module based on averaged satellite-measured data. The datasets used are measurements of the reflectivity of Earth's surface provided by the Total Ozone Mapping Spectrometer (TOMS).

The effects of most environmental disturbances depend on several factors:

- Sun, Earth, and spacecraft position
- the surface of the satellite that is exposed to the disturbance, thereby also the satellite attitude
- material properties of the satellite surface

For disturbances due to the magnetic field, volume instead of surface properties need to be considered.

For accurate modelling of environmental disturbances, thus, a model to calculate quantities such as solar radiation pressure or atmospheric density as well as a model of the satellite under consideration is necessary in order to evaluate the impact due to the spacecraft environment.

3. Environmental Pre-processing

For a rough estimation of spacecraft surface and volume forces and torques, a satellite reference surface or volume is considered with average volume or surface properties. A coarse calculation of disturbance forces due to solar radiation pressure for example would require a reference satellite area with average reflexion coefficients. For a more accurate analysis, a more detailed approach is required based on the spacecraft geometry and material properties. The geometrical model of the spacecraft has to be discretized into finite elements or volumes. Element or volume forces and torques for different environmental conditions are calculated in pre-processing since this is a rather time consuming task depending on the number of elements or volumes. The total forces and torques are obtained by summing up the element forces and torques. For a closed-loop simulation, total force and torque components are provided via look-up tables. In the following, the complete process is exemplary outlined for the disturbance force due to solar radiation pressure.

For solar radiation pressure, the disturbance force depends on several factors:

- the incident angle of the sunlight
- the affected area
- surface properties, that is coefficients of specular and diffuse reflexion
- value of solar pressure

In a first step, a structural model of the satellite is built. Thereby, the following considerations have to be taken into account: The greater the model detail, the more accuracy in results can be expected. An unfavourable effect accompanying the increase in model exactness, however, is the increase in computation time when calculating the environmental actions on the satellite. For details that cannot be neglected a compromise therefore has to be found. The same applies when discretizing the single areas into finite elements: The finer the grid, the more accurate are the results, yet the longer is the computation time. In figure 2, a simple GRACE-like structural model is displayed.

In the next step, to save computation time, a back-side and shadow determination algorithm is executed.

The higher the grid resolution, the better is the shadow line. However, this results in the aforementioned increase in computation time for repeated determination of illuminated, shadowed, and back-side elements for a specified range of incident angle of sunlight. The range step also influences the achieved accuracy with

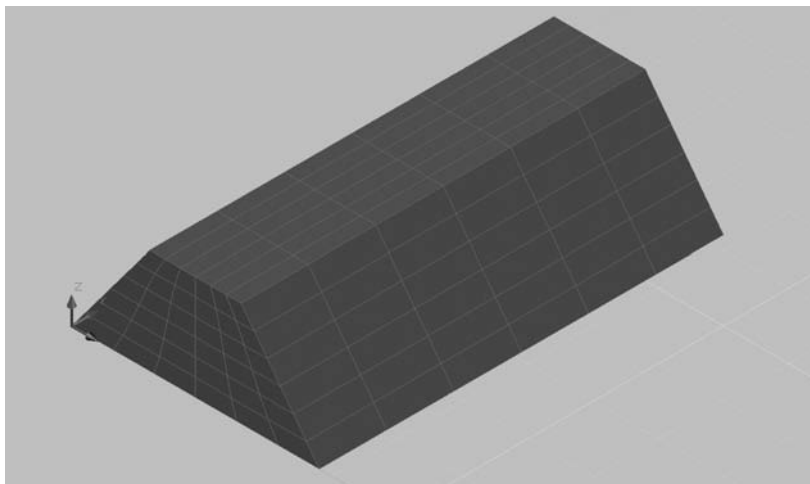


Figure 2: GRACE-like structural model

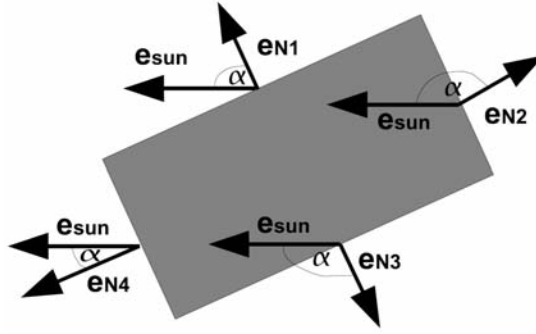


Figure 3: Back-side determination

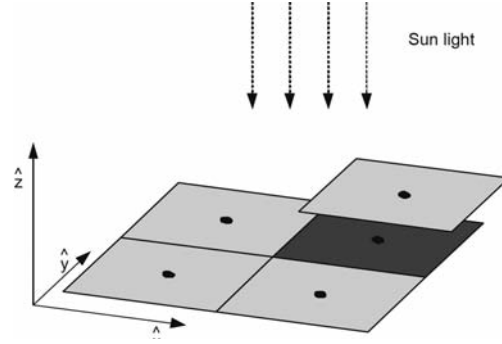


Figure 4: Shadow determination

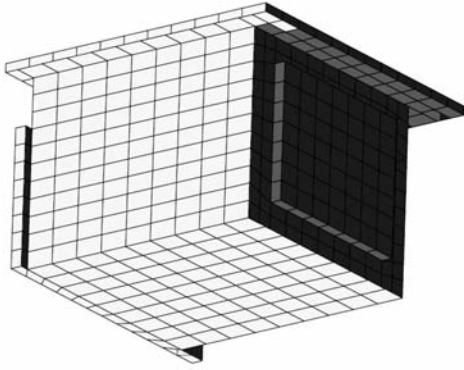


Figure 5: Example satellite after execution of back-side and shadow determination algorithms

adverse effect on computation time: The smaller it is, the more accurate are the results but the higher is the computation time for pre-processing. The increased accuracy in results refers to less interpolation necessary when integrating the pre-calculated values into the closed-loop simulation.

The computation of the illumination conditions is divided into two parts. First, all elements must be identified that are exposed to the Sun's radiation. Afterwards, the visible elements are examined again to distinguish whether they are shaded by other elements or not. For the first part, the angle between the incident sunray and the element normal is calculated (see figure 3). If the angle is larger than 90 degrees, the element is marked with a back-side flag and excluded from force and torque calculation for solar radiation.

With the back-side flag, all elements are grouped into the categories »visible« or »invisible«. After execution of the back-side algorithm, a

shadow algorithm is used to determine which elements are shielded from the Sun by other elements. The shadow algorithm is applied to visible elements only. The principle of operation is illustrated in figure 4. The algorithm does not produce a clear, sharp line of shadow, but it checks for each element whether it is shaded by another element or not. An element is considered as shaded if the projection of its centre point on the area of the elements in Sun direction is located inside this area, and is marked with a shadow flag.

Errors occur as half of the element area might actually not be shaded. Since this happens in both directions, the overall error is expected to be small. The error can be minimized by reducing the overall element size.

Figure 5 shows an image of an example satellite which geometry has undergone both the back-side and shadow determination checks. Elements that are visible are light grey, elements with the back-side flag are shown in dark grey and shaded elements have an intermediate grey scale value.

After the illumination conditions are checked, normalized surface forces are calculated for each element marked as visible by using

$$\vec{f}_i = -A_i[(1 - c_{si}) \cdot \vec{e}_{Sun} + 2(c_{si} \cos \alpha + \frac{1}{3}c_{di}) \cdot \vec{e}_N] \cos \alpha$$

where A_i is the reference area, \vec{e}_{Sun} is the Sun vector, \vec{e}_N is the element normal vector, α is the angle between the Sun and the element normal vectors, and c_{si} and c_{di} are the element coefficients of specular and diffuse reflexion respectively. The element torque is obtained by

taking the cross product of the element force and a corresponding lever arm to the satellite centre of mass. By summation of the element forces and torques respectively, the total normalized force and torque is obtained. Normalization in the case of solar radiation modelling means, that the total forces and torques are not yet multiplied with the solar radiation pressure calculated by one of the illumination library modules.

The above calculations are repeated for a range of illumination conditions. The total forces and torques are saved in lookup tables such that tabular or interpolated values are available for use in a closed-loop simulation. In a similar manner, other environmental disturbance forces and torques like those due to atmospheric drag can be computed.

4. Closed-loop Simulation and Simulation Analysis

The environmental forces and torques prepared in pre-processing are included inside a closed-loop simulator via the HPS Surface Forces library. This library contains look-up tables for each component of the force and the torque vectors. The look-up tables work with an interpolation/extrapolation method. During the simulation the force and torque is calculated for the incoming polar and azimuth angles which result from e.g. the sun vector expressed in the satellite body frame.

The forces and torques from the surface forces module are passed to a model for calculation of the satellite dynamics. Depending on the coordinates used a prior transformation may be necessary.

The HPS dynamics sub-library contains a simple and a multi-body simulation module. The simple satellite dynamics model can simulate a rigid body with six degrees of freedom. Due to its simplicity, this model is very usable for SiL and HiL applications for controller design. It may also be used to obtain a quick look into general system behaviour. The multi-body satellite dynamics allows for in-depth investiga-

tion of complex dynamics including instrument-spacecraft coupling. The multi-body dynamics core is highly accurate due to its completeness in accounting for dynamical and environmental effects. Since the motion of a satellite in Earth's orbit is mainly determined by the acceleration due to the Earth's gravity field, the calculation of the gravitational acceleration, the gravity-gradient and all resulting torques, is carried out within the multi-body dynamics. Thereby the gravitational acceleration is updated at every internal time step. Other external disturbances due to environmental effects are accounted for only at every external time step.

In order to close the loop, several control modules need to be developed. Compared to the generic dynamics, those are mission specific and have to be established considering all mission specifications.

The simulator is established to perform simulation analyses for a certain number of reference scenarios. Pre-processing has to be carried out individually for different satellite geometries and reference orbits. In lack of a final satellite geometry, simple geometries such as the GRACE-like model depicted in figure 2 are used.

For the reference scenarios under investigation, atmospheric drag and solar radiation pressure represent the largest disturbances. Those are currently under investigation for a number of reference orbits and preliminary simplified satellite geometries. Since no material properties are specified yet, reference values of common spacecraft materials are applied.

5. Outlook

Following the preliminary investigation outlined above, more definite results will be obtained upon agreement with respect to various points. For disturbance modelling due to environmental effects, the satellite orbit has to be known, furthermore the satellite geometry, spacecraft materials used and the corresponding coefficients in the space environment.

Since material properties are not always known under space conditions, some uncertainty will remain in the estimation of environmental effects.

Besides modelling of disturbances due to external environmental effects, the presence of instrument noise from the control loop, sensors, and actuators is of interest. Estimation of internal disturbances and disturbance coupling will be part of the simulation analyses in the future.

Acknowledgement

The models used for environmental disturbance modelling are part of the HPS library developed in a joint research project with ZARM, University of Bremen.

References

HPS Design Document, version 3.24, September 2010.

HPS User's Guide, version 4.31, September 2010.

Author's Index

A

Arras C. 46
Abrikosov O. 112

B

Baur O. 62
Bedrich S. 167
Beyerle G. 46
Bosch W. 52
Bouman J. 52
Brandt N. 152
Brieden P. 94, 134
Brockmann J.M. 70
Bruinsma S. 112

C

Cai J. 62

D

Dahle C. 3, 7, 112
Danzmann K. 160
Dehne M. 160
Denker H. 106
Doll B. 118

E

Eicker A. 22, 77
Elsaka B. 140

F

Fichter W. 152
Flechtner F. 3, 112, 146
Flury J. 31, 134
Fuchs M. 52
Förste C. 112

G

Gerberding O. 160
Gilowski M. 178
Grombein T. 84
Gruber T. 52

H

Hamoudi M. 35
Haser A. 46
Hayn M. 42
Heck B. 84
Heinzel G. 134, 160
Heise S. 46
Hirth M. 152
Holschneider M. 42
Holzwarth R. 172

I

Ihde J. 106
Iran-Pour S. 126

K

Kargoll B. 70
Klein V. 167
Köhl A. 101
König D. 7
Krasbutter I. 70
Kurtenbach E. 22, 77
Kusche J. 22, 77, 140

L

Lesur V.	35
Lezius M.	172
Liebsch G.	106
Lühr H.	35

M

Mahrdt C.	160
Marty J.-C.	112
Mayer-Gürr T.	22, 77
Michaelis I.	35
Müller J.	94, 134
Müller V.	160
Murböck M.	52

N

Neumayer K.H.	3, 13, 112, 146
--------------------	-----------------

P

Pail R.	52
Pelivan I.	185
Peterseim N.	31

R

Raimondo J.-C.	146
Rasel E.M.	178
Rauberg J.	35
Reubelt T.	126
Rother M.	35
Rülke A.	106
Rummel R.	52

S

Sand R.	118
Schachtschneider R.	42
Schall J.	22, 77
Schlicht A.	31
Schmidt M.	52
Schmidt T.	46
Schuh W.-D.	70
Seitz K.	84
Shabanloui A.	22, 77
Shako R.	112
Sheard B.	160
Siegismund F.	101
Sneeuw N.	62, 126
Stammer D.	101
Steinmetz T.	172
Stummer C.	52

T

Theil S.	185
---------------	-----

V

Voigt C.	106
---------------	-----

W

Wardinski I.	35
Wickert J.	46

Z

Zus F.	46
-------------	----

GEOTECHNOLOGIEN Science Reports – Already published/Editions

- No. 1** Gas Hydrates in the Geosystem – Status Seminar, GEOMAR Research Centre Kiel, 6–7 May 2002, Programme & Abstracts, 151 pages.
- No. 2** Information Systems in Earth Management – Kick-Off-Meeting, University of Hannover, 19 February 2003, Projects, 65 pages.
- No. 3** Observation of the System Earth from Space – Status Seminar, BLVA Munich, 12–13 June 2003, Programme & Abstracts, 199 pages.
- No. 4** Information Systems in Earth Management – Status Seminar, RWTH Aachen University, 23–24 March 2004, Programme & Abstracts, 100 pages.
- No. 5** Continental Margins – Earth’s Focal Points of Usage and Hazard Potential – Status Seminar, GeoForschungsZentrum (GFZ) Potsdam, 9–10 June 2005, Programme & Abstracts, 112 pages.
- No. 6** Investigation, Utilization and Protection of the Underground – CO₂-Storage in Geological Formations, Technologies for an Underground Survey Areas – Kick-Off-Meeting, Bundesanstalt für Geowissenschaften und Rohstoffe (BGR) Hannover, 22–23 September 2005, Programme & Abstracts, 144 pages.
- No. 7** Gas Hydrates in the Geosystem – The German National Research Programme on Gas Hydrates, Results from the First Funding Period (2001–2004), 219 pages.
- No. 8** Information Systems in Earth Management – From Science to Application, Results from the First Funding Period (2002–2005), 103 pages.
- No. 9** 1. French-German Symposium on Geological Storage of CO₂, Juni 21./22. 2007, GeoForschungsZentrum Potsdam, Abstracts, 202 pages.
- No. 10** Early Warning Systems in Earth Management – Kick-Off-Meeting, Technical University Karlsruhe, 10 October 2007, Programme & Abstracts, 136 pages.
- No. 11** Observation of the System Earth from Space – Status Seminar, 22–23 November 2007, Bavarian Academy of Sciences and Humanities, Munich, Programme & Abstracts, 194 pages.
- No. 12** Mineral Surfaces – From Atomic Processes to Industrial Application – Kick-Off-Meeting, 13–14 October 2008, Ludwig-Maximilians Universität, Munich, Programme & Abstracts, 133 pages.

- No. 13** Early Warning Systems in Earth Management – Status Seminar, 12–13 October 2009 Technische Universität München, Programme & Abstracts, 165 pages.
- No. 14** Die dauerhafte geologische Speicherung von CO₂ in Deutschland – Aktuelle Forschungsergebnisse und Perspektiven, Herausgegeben von: Ludwig Stroink, J. Peter Gerling, Michael Kühn, Frank R. Schilling, 140 Seiten.
- No. 15** Early Warning Systems for Transportation Infrastructures, Workshop 9-10 February 2009, Fraunhofer IITB Karlsruhe, Karlsruhe Institute of Technology (KIT), 160 p.
- No. 16** Mineral Surfaces – From Atomic Processes to Industrial Application, Status Seminar, 26-27 October 2010, Johannes Gutenberg-Universität Mainz, Programme & Abstracts, 204 p.

Notes

Notes

Notes



Observation of the System Earth from Space

Three joint interdisciplinary projects were launched in March 2009 in the framework of the R&D-programme GEOTECHNOLOGIEN.

Significant advances in the scientific use of space based data were achieved through a coordinated approach and prioritization in a joint programme of research centres and universities. The satellite missions CHAMP, GRACE and GOCE led to a quantum jump in research related to Earth's gravity and the magnetic fields, and to mass transport within the system Earth. The missions were and are instrumental to establish a new segment of the Earth system science. The main topic »Observation of the Earth system from Space« of the R&D programme GEOTECHNOLOGIEN allowed it to a large number of German scientists to be involved in the missions in leading positions. Germany is now an internationally recognized partner and leader in this field.

The R&D programme GEOTECHNOLOGIEN has allowed the stabilisation at the international global geodetic observing system. Based on the insight gained to the exploration and monitoring of changes related to the Earth's surface, the boundary layer between atmosphere and solid Earth, oceans and ice shields has been made possible. This boundary layer is our habitat and therefore at the focus of our interests. The Earth's surface is subject to anthropogenetic changes; changes driven by Sun, Moon and planets, and by changes caused by processes in the Earth system. These state parameters and their variability are best monitored from space. The theme »Observation of the System Earth from Space« offers comprehensive insight into a broad range of research topics relevant to society including geodesy, oceanography, atmosphere science (from meteorology to climatology), hydrology and glaciology.

This volume summarizes the scientific results presented during the status seminar at the Rheinische Friedrich Wilhelms University in Bonn, Germany in October 2010. The articles reflect the interdisciplinary approach of the research topic.



Bundesministerium
für Bildung
und Forschung

DFG

The GEOTECHNOLOGIEN programme is funded by the Federal Ministry for Education and Research (BMBF) and the German Research Foundation (DFG)

ISSN: 1619-7399